Fachbereich für Physik und Elektrotechnik
der Universität Bremen

The Atlantic Meridional Overturning Circulation in the North Atlantic, focussing on 47°N - variability, trends, and meridional connectivity

Dissertation zur Erlangung des akademischen Grades
Doktor der Naturwissenschaften (Dr. rer. nat.)

SIMON WETT

Universität Bremen

1. Gutachterin: PROF. DR. MONIKA RHEIN
2. Gutachter: PROF. DR. PAUL G. MYERS

Eingereicht: 23. Dezember 2023
Tag des Promotionskolloquiums: 04. März 2024

Abstract

The Atlantic Meridional Overturning Circulation (AMOC) plays a vital role in the climate of Europe and the North Atlantic region by redistributing heat and freshwater in the Atlantic. Climate model studies project an AMOC decline under global warming in the 21st century. However, they disagree on the magnitude and timescales of the weakening. Thus, monitoring AMOC changes remains essential to provide benchmarks for assessing climate models and understanding the physical processes determining AMOC variability.

In this thesis, basin-wide AMOC volume transports are calculated for the period 1993-2018. Measurements from moored instruments of the NOAC array at 47°N are combined with hydrography and satellite altimetry. Variability, trends, and meridional connectivity with the RAPID array at 26°N are analyzed. Within the study period, the AMOC volume transport at 47°N exhibits a mean strength of 17.2 Sv and substantial variability on interannual and seasonal timescales but no significant long-term trend. The unfiltered and the low-pass filtered NOAC AMOC shows a significant correlation with the RAPID AMOC when the NOAC AMOC leads by about one year, indicating meridional connectivity. An accompanying analysis of the AMOC at 47°N in different observation-based gridded data sets reveals a good representation of the AMOC, highlighting the value of these data sets in designing cost-efficient future AMOC monitoring arrays. However, the ARMOR3D data set exhibits weaknesses representing the recent AMOC increase after 2010. An analysis of the AMOC at the NOAC, RAPID, and OSNAP (52°N-60°N) lines in the high-resolution forced VIKING20X model simulation reveals a mean NOAC AMOC strength within the estimated error range of the NOAC observations. In disagreement with observations, the VIKING20X AMOC decreases after the mid-1990s until 2010 at all three array lines. This decrease coincides with a significant cooling and freshening in the subpolar North Atlantic, qualitatively resembling a pattern that has been associated with a decreasing AMOC. In agreement with the observations, VIKING20X shows meridional connectivity between the NOAC and RAPID AMOC when the NOAC AMOC leads by about one year, though less distinct. This agreement indicates a common mechanism, possibly large-scale wind field changes, determining the meridional connectivity in observations and VIKING20X. An analysis of different ANHA model simulations with varying resolution underlines the importance of model resolution for accurately representing the AMOC mean strength and variability but also stresses the need for model improvements beyond resolution.

This thesis presents the first observation-based AMOC estimate at 47°N. It highlights the value of continued observations as benchmarks to assess model performance and the need for model improvements to understand the physical mechanisms determining AMOC variability. These mechanisms must be understood and represented in climate models to make informed projections of the future AMOC and its role in the climate system.

Zusammenfassung

Durch die Umverteilung von Wärme und Frischwasser im Atlantik, spielt die Atlantische Meridionale Umwälzzirkulation (Atlantic Meridional Overturning Circulation, AMOC) eine wichtige Rolle für das Klima in Europa und im Nordatlantik. Klimamodellstudien prognostizieren einen Rückgang der AMOC durch den Einfluss der globalen Erwärmung. Daher ist die Beobachtung der AMOC von besonderer Bedeutung um Vergleichsgrößen für die Bewertung von Klimamodellergebnissen zu liefern und die physikalischen Prozesse zu verstehen, die die Variabilität der AMOC bestimmen.

In dieser Dissertation werden beckenweite AMOC Volumentransporte für den Zeitraum 1993-2018 berechnet. Verankerungsmessungen des NOAC Arrays bei 47°N werden kombiniert mit hydrographischen Daten und Satelliten-Altimetrie. Es werden Variabilität, Trends und der meridionale Zusammenhang mit dem RAPID Array bei 26°N analysiert. Im Beobachtungszeitraum zeigt der Volumentransport der AMOC eine mittlere Stärke von 17,2 Sv und erhebliche Variabilität auf mehrjährigen und saisonalen Zeitskalen, aber keinen signifikanten Langzeittrend. Die ungefilterte und die tiefpass-gefilterte NOAC AMOC Zeitreihe zeigt eine signifikante Korrelation mit der RAPID AMOC Zeitreihe, wenn die NOAC AMOC die RAPID AMOC um etwa ein Jahr anführt, was auf einen meridionalen Zusammenhang hindeutet. Eine begleitende Analyse der AMOC bei 47°N in verschiedenen beobachtungsbasierten gegitterten Datensätzen offenbart eine gute Darstellung der AMOC, was den Wert dieser Datensätze für das Entwerfen eines kosteneffizienten zukünftigen AMOC-Beobachtungsarrays unterstreicht. Der ARMOR3D Datensatz zeigt jedoch Schwächen bei der Darstellung des jüngsten Anstiegs der AMOC nach 2010. Eine Analyse der AMOC an den Positionen der NOAC, RAPID und OSNAP (52°N-60°N) Arrays in der hochaufgelösten, angetriebenen VIKING20X-Modellsimulation zeigt eine mittlere Stärke der NOAC AMOC, die innerhalb des abgeschätzten Fehlerbereichs der NOAC Beobachtungen liegt. Im Gegensatz zu den Beobachtungen nimmt die VIKING20X AMOC jedoch an allen drei Array-Positionen nach Mitte der 1990er-Jahre bis 2010 ab. Diese Abnahme deckt sich mit einer signifkanten Abkühlung und einer Abnahme des Salzgehalts im subpolaren Nordatlantik, die qualitativ einem Muster entspricht, welches mit einer Abnahme der AMOC assoziert wurde. In Übereinstimmung mit Beobachtungen, zeigt VIKING20X einen meridionalen Zusammenhang zwischen der NOAC und RAPID AMOC wenn die NOAC AMOC um etwa ein Jahr anführt, jedoch weniger deutlich. Diese Übereinstimmung deutet auf einen gemeinsamen Mechanismus hin, der den meridionalen Zusammenhang in Beobachtungen und VIKING20X bestimmt, möglicherweise großskalige Windfeld-Änderungen. Eine Analyse verschiedener ANHA Modellsimulationen mit variierender Auflösung unterstreicht die Wichtigkeit der Modellauflösung für eine genaue Darstellung der mittleren AMOC sowie der Variabilität, hebt aber auch die Notwendigkeit

von Modellverbesserungen jenseits der Auflösung hervor.

Diese Dissertation präsentiert die erste beobachtungsbasierte Abschätzung der AMOC bei 47°N. Sie betont den Wert kontinuierlicher Beobachtungen als Vergleichsgröße für die Bewertung der Leistung von Modellen und die Notwendigkeit von Modellverbesserungen um die physikalischen Mechanismen zu verstehen, die die Variabilität der AMOC bestimmen. Diese Mechanismen müssen verstanden und in Klimamodellen repräsentiert sein um informierte Vorhersagen über die Zukunft der AMOC und ihre Rolle im Klimasystem zu treffen.

Contents

"How inappropriate to call this planet Earth when it is quite
clearly ocean."

Arthur C. Clarke, *writer and physicist*

Chapter 1

Introduction

1.1 The overturning of the global ocean

The ocean plays a vital role in redistributing heat, freshwater, carbon, and nutrients around the globe. The Earth receives most incoming solar radiation at the equator due to its spherical shape and the orientation of its rotational axis, causing the spread of climate zones from tropical to polar across latitudes (Bryden & Imawaki, 2001). At the same time, the Earth emits longwave radiation back into space, which is also largest at the equator (Trenberth & Solomon, 1994). However, the latitudinal variations of the outgoing longwave radiation are smaller than those of the incoming shortwave radiation, creating an energy surplus at the equator and a deficit at the poles. This difference drives atmospheric and oceanic meridional heat transport (MHT) from the equatorial to the polar regions. A considerable portion of the combined ocean-atmosphere poleward heat transport in the subtropics is conducted by the ocean (Talley et al., 2011; Boccaletti et al., 2005; Trenberth & Caron, 2001). Balancing the solar radiation budget, this MHT strongly influences the global climate system.

The circulation of the global ocean is driven by the winds and density differences. While all ocean basins are exposed to wind forcing, the Atlantic Ocean plays an integral part in the oceanic heat distribution due to its geographic characteristics. The Atlantic exhibits an opening to the subpolar and polar ocean basins. Here, these waters are exposed to cold air temperatures, resulting in strong heat fluxes to the atmosphere. The waters cool, which increases their density and decreases the stratification of the water column. The

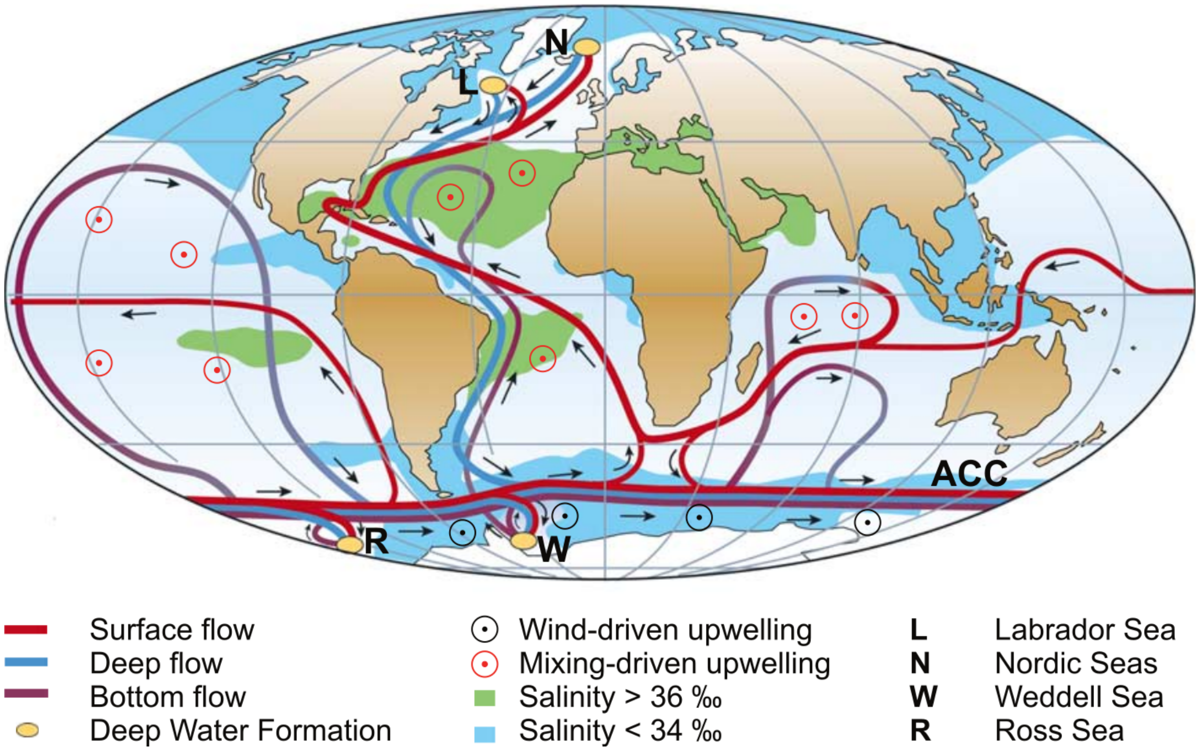

Figure 1.1: Schematic depiction of the global overturning circulation, indicating the upper and lower circulation branches, dense water formation, and upwelling regions. Figure from Kuhlbrodt et al. (2007), who modified it after Rahmstorf (2002).

waters overturn and form dense water masses (Talley et al., 2011). In both the Indian and the Pacific Ocean, the Asian continent and the Aleutian Islands, respectively, inhibit a substantial advection of waters to the high latitudes. In the Pacific, a small inflow into the Arctic exists via the Bering Strait. However, the Pacific lacks deep subpolar basins and marginal seas like the Labrador and Irminger Seas and the Iceland Basin in the subpolar North Atlantic, where local currents and wind forcing support the formation of dense water masses. Only the higher salinity of the Atlantic allows the formation of waters dense enough to reach into the deep ocean (Broecker, 1991). Therefore, the Atlantic is the only ocean in the northern hemisphere exhibiting such strong, dense water mass formation.

Through wind- and mixing-driven upwelling in different parts of the global ocean, the dense water masses formed in the subpolar and polar North Atlantic regain the potential energy lost during their formation, closing the loop of the overturning (Marshall & Speer, 2012). Without turbulent mixing, the overturning would be confined to a shallow surface layer but would not affect the deep ocean (Wunsch & Ferrari, 2004). Consequently, the wind forcing and turbulent mixing processes, initiated, for example, by breaking internal gravity waves (induced by wind and tides), drive the deep-reaching overturning of the Atlantic (Kuhlbrodt et al., 2007). This circulation is termed the Atlantic Meridional Overturning Circulation (AMOC).

The AMOC is responsible for the vast majority of the net MHT in the Atlantic (90 %, Trenberth & Solomon, 1994) and about a quarter of the global combined ocean-atmosphere MHT at 26°N (Johns et al., 2011; Ganachaud & Wunsch, 2003; Bryden & Imawaki, 2001). The currents of the Atlantic are part of a major current system connecting the global ocean basins. This global current system was first described by Broecker (1987) as the "global ocean conveyor" to describe the overturning on paleo-timescales, depicting a continuous, conveyor-belt-like system of currents that connects the global ocean basins. This concept became very popular in the oceanographic community and was modified, for example, by Rahmstorf (2002) and Kuhlbrodt et al. (2007) (Figure 1.1). However, this depiction is a strong simplification of the actual currents in the North Atlantic.

1.2 The circulation in the North Atlantic

The circulation in the North Atlantic is a complex system consisting of various individual currents (Figure 1.2). The dominant current in the North Atlantic is the Gulf Stream and its extension, the North Atlantic Current (NAC, Krauss, 1986). It is part of the subtropical gyre but extends northward, transporting warm and saline subtropical waters into the subpolar North Atlantic and further northeastward into the Nordic Seas as part of the AMOC (Figure 1.2). At the Northwest Corner at approximately 50°N, 43°W, the current detaches from the North American shelf. Subsequently, it crosses the Atlantic, determining the boundary between the subtropical origin waters and the subpolar gyre (Rossby, 1996). On its way across the Atlantic, the NAC divides into several branches, partly recirculating the subtropical origin water southward (Stendardo et al., 2020). More than half of the total northward volume transport of the NAC at 47°N is recirculated back southward next to the NAC (Rhein et al., 2019b; Mertens et al., 2014). Like many features of the North Atlantic circulation, the location of the NAC pathways is influenced by the North Atlantic Oscillation (NAO). The NAO is an index describing the atmospheric pressure difference between the subpolar and subtropical regions of the North Atlantic (Hurrell, 1995; Barnston & Livezey, 1987). Due to changing wind-forcing with the NAO, the NAC is located more southward or northward, resulting in a contraction and expansion of the subpolar gyre (Holliday et al., 2020). Thus, via a changing wind forcing, the NAO strongly influences the heat transport and the hydrographic properties throughout the subpolar North Atlantic.

Warm and saline subtropical origin waters are transported northward with the NAC and enter the subpolar North Atlantic. While parts of the warm and saline waters are transported further into the Nordic Seas through the Denmark Strait and over the Iceland-Scotland sill (Holliday et al., 2020), another branch recirculates with the subpolar gyre in the Iceland Basin and around the Irminger Sea (Figure 1.2). The strength of these

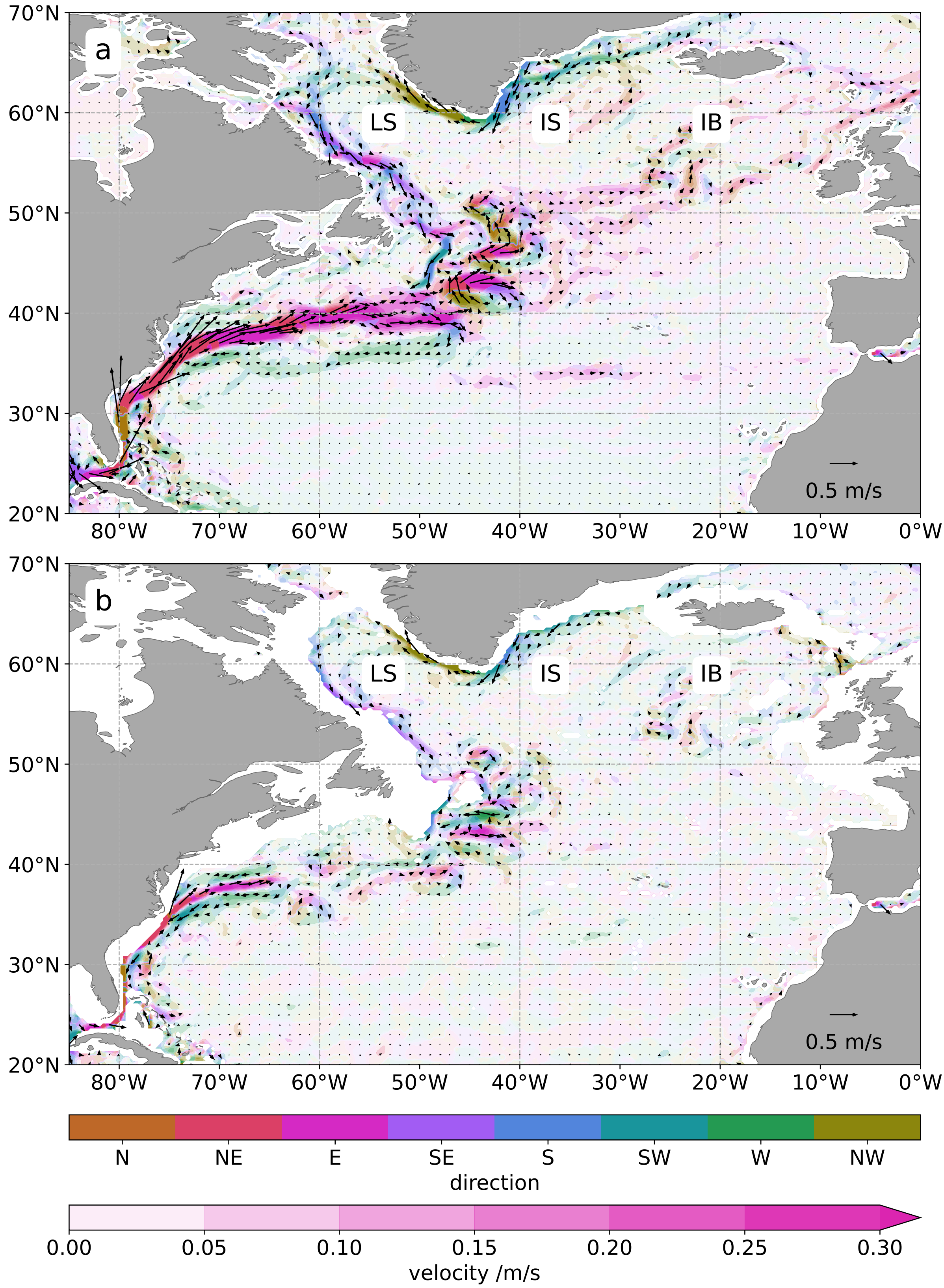

Figure 1.2: The time-mean geostrophic circulation in the North Atlantic in the upper 500 m (a) and below 1000 m (b), based on ARMOR3D. Colors denote the direction of the flow, while the transparency marks the total velocity. Arrows mark the strength and direction of the flow. The labels indicate the locations of the Labrador Sea (LS), Irminger Sea (IS), and Iceland Basin (IB).

branches is mediated by the NAO (Holliday et al., 2020). In the western Irminger Sea, the warm and saline waters flow southward alongside the polar waters in the East Greenland Current (Daniault et al., 2011) and around the southern tip of Greenland, where they continue as the boundary current, termed the West Greenland Current. Here, eddies are shed off from the boundary current (Hátún et al., 2007), influencing the stratification in the Labrador Sea by transporting heat and freshwater from the boundary current into the interior (Pennelly et al., 2019; De Jong et al., 2016). The boundary current rounds the Labrador Sea and returns southeastward with the Labrador Current. In the Labrador and Irminger Seas, the subtropical origin waters are exposed to cold temperatures, and as a result of the cooling of the saline waters, deep convection occurs (Spall & Pickart, 2001; Marshall & Schott, 1999). After convection, the dense water masses are exported southward along the Deep Western Boundary Current (DWBC) (Rhein et al., 2015; Myers & Kulan, 2012; Pickart, 1992), together with the overflows from the Nordic Seas (Hansen et al., 2016; Harden et al., 2016) feeding the lower limb of the AMOC.

Due to the large amounts of heat redistributed in the Atlantic, the AMOC is an integral mechanism for the global climate system. In combination with the prevailing westerly winds, the release of heat to the atmosphere in the subpolar North Atlantic contributes to the relatively warm climate of western Europe, compared to similar latitudes in North America and Asia (Buckley & Marshall, 2016; Seager et al., 2002). Furthermore, the AMOC influences many climate phenomena in the Atlantic region and on a global scale. These climate phenomena include regional temperature and precipitation (e.g., Jackson et al., 2015), tropical storm activity (e.g., Yan et al., 2017), regional sea level (e.g., Little et al., 2019) and the rate of uptake of anthropogenic carbon (e.g., Rhein et al., 2017). A change in the oceanic heat supply would have strong consequences for these connections and, thus, for regional and global climate.

1.3 The AMOC as a tipping element in the climate system

In climate models, the AMOC has been shown to be sensitive to freshwater forcing and was projected to weaken on decadal and longer timescales due to enhanced freshwater input into the subpolar North Atlantic via changes in the hydrological cycle and the melting of the Greenland ice sheet under global warming (Bakker et al., 2016). Simulations in forced ocean models have confirmed that the Greenland meltwater has contributed to a freshening trend in the Labrador Sea that could potentially suppress deep convection, though not yet showing an impact on the AMOC (Böning et al., 2016). There is considerable uncertainty regarding the magnitude and the timing of the AMOC decrease in climate models (IPCC, 2021; Jackson & Wood, 2018). Due to its strong influences on the redistribution of heat and freshwater in the climate system, it is thus of great importance to understand the sensitivity of the AMOC to these forcing mechanisms and their past and future changes, especially under global warming.

AMOC reconstructions based on proxy records

Paleoclimate records suggest that abrupt climate changes in the past were linked to AMOC variations (Lynch-Stieglitz, 2017). A weak AMOC was associated with strong northern hemisphere cooling and vice versa (Henry et al., 2016). Since about 8000 years before present, the AMOC has been relatively stable (Lippold et al., 2019), but multiple proxy records, based on sea surface temperature (SST) and regional sea level, indicate that the AMOC has weakened over the twentieth century due to anthropogenic warming (Zhu et al., 2023; Caesar et al., 2021, 2018; McCarthy et al., 2015a).

Present-day global surface temperature trends show warming in almost all regions of the world except in the subpolar North Atlantic (Figure 1.3 a). This feature is known as the North Atlantic warming hole and has been linked to a weakening of the AMOC (Caesar et al., 2018; Rahmstorf et al., 2015). Rahmstorf et al. (2015) calculated an AMOC index based on surface temperature differences between the whole northern hemisphere and the subpolar gyre (Figure 1.3 b). They found a stable AMOC over much of the past millennium and a weakening over the 20th century. Based on multiple proxy records, Caesar et al. (2021) argued that the current AMOC was the weakest in the last millennium. Based on density variations in the Irminger Sea, obtained from an ocean reanalysis, Chafik et al. (2022) estimated a reduction of the AMOC by 2.2 Sv since 1950. However, the trend remained insignificant due to strong inter-annual and decadal variability. There is still debate over whether these proxy records indicate a slowdown of the AMOC (Kilbourne et al., 2022) because other reconstructions, for example, based on hydrographic data, found no decline (Rossby et al., 2020). Further discussion concentrates on the question of whether the possible AMOC slowdown of the past century is driven by anthropogenic forcing or natural decadal variability (Caesar et al., 2018). Despite the uncertainties associated with the past AMOC evolution from proxy records, these findings raise concern about the ultimate fate of the AMOC in a warming climate.

The possibility of an AMOC collapse

Temperature and salinity influence the density of seawater in different ways (Stommel, 1961). While an increase in temperature results in a decrease in density, an increase in salinity increases the density. Thus, the advection of warm and saline subtropical waters into the subpolar North Atlantic introduces two different feedback mechanisms. A reduced supply of salinity into the subpolar North Atlantic with a decreasing AMOC decreases the surface density in the convection areas, slowing the AMOC and further reducing the

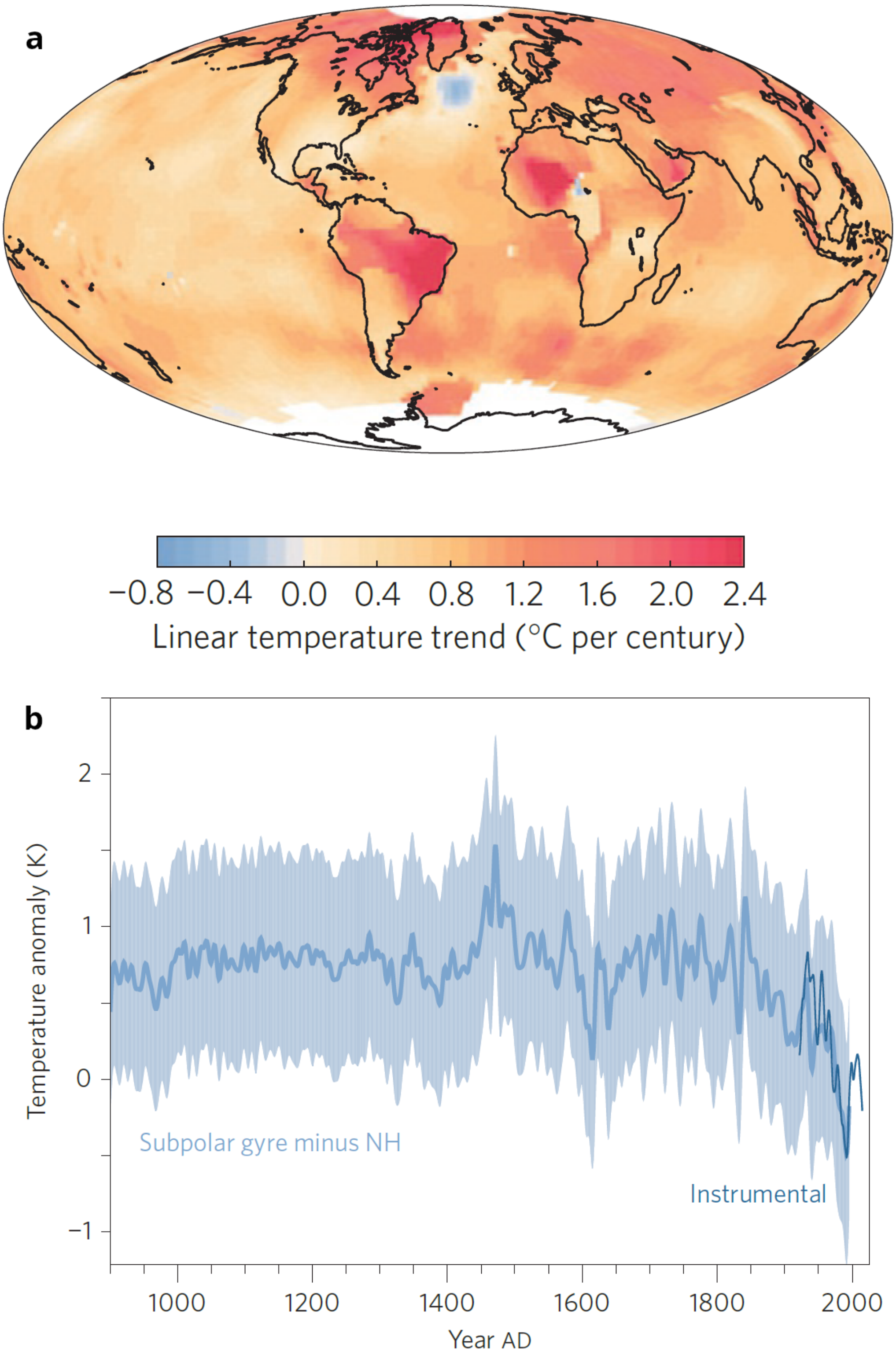

Figure 1.3: (a) Global surface temperature trends 1901-2013 (Hansen et al., 1999). Figure from Rahmstorf et al. (2015) (b) AMOC index, calculated by Rahmstorf et al. (2015), as the difference of the surface temperature anomalies between the whole northern hemisphere and the subpolar North Atlantic. The index is based on proxy reconstructions by Mann et al. (2009) and Mann et al. (2008) and instrumental records after 1922 (darker line, Morice et al., 2012). Figure from Rahmstorf et al. (2015).

inflow of saline subtropical waters. Physically, this positive feedback is counteracted by the negative temperature feedback (Griffies et al., 2009; Rahmstorf & Willebrand, 1995). The reduced inflow of warm waters into the subpolar North Atlantic increases the density, favoring convection, thus strengthening the AMOC. However, the temperature feedback is damped due to the transfer of heat from the ocean to the atmosphere, making the salinity feedback more important than the temperature feedback in influencing the AMOC.

It has been proposed using conceptual models (e.g., Weijer et al., 2019; Stommel, 1961) and forced model experiments (Lohmann & Ditlevsen, 2021) that the AMOC has a tipping point. A tipping point refers to a point where even a small change in the system can cause a shift to a different state (Lenton et al., 2008), that is, a complete shutdown of the AMOC. Consequently, the AMOC has been called a tipping element in the climate system (Lenton et al., 2008). Conceptual models (Stommel, 1961) and climate models (Drijfhout et al., 2010) have shown that the route towards a weakening and a possible shutdown of the AMOC is via a dominant salinity feedback. A reduced supply of saline subtropical waters into the subpolar North Atlantic with the AMOC further weakens the AMOC until it completely shuts down. Recent publications have reinvigorated the discussion about a forthcoming collapse of the AMOC (Ditlevsen & Ditlevsen, 2023; Boers, 2021). Based on a statistical analysis of SST in the North Atlantic, Ditlevsen & Ditlevsen (2023) projected a collapse of the AMOC around mid-century under a current emissions scenario. However, the connection between the AMOC and North Atlantic SST variability is associated with uncertainties, and SST is additionally influenced by factors not related to the AMOC (Menary et al., 2020; Keil et al., 2020). Roquet & Wunsch (2022) warned that the debate of a near AMOC shutdown and its consequences, though not negligible, might divert attention from other risks posed by continued anthropogenic emissions.

It is unclear whether a complete shutdown of the AMOC is possible in the real world. However, a slowdown, let alone a shutdown, of the AMOC would have implications for the global climate system by resulting in a substantial cooling of the subpolar North Atlantic Ocean and Northwestern Europe (e.g., Liu et al., 2017; Jackson et al., 2015; Rahmstorf, 2002, for further relevant references please see Section 1.1). The recent Intergovernmental Panel on Climate Change (IPCC) report stated that it is "very likely that the AMOC will decline in the 21st century" (IPCC, 2021). However, there is only low confidence in the associated timing and magnitude. Reasons for this low confidence are model biases that imprint on the mean strength and variability of the AMOC in response to anthropogenic climate change (Jackson et al., 2023). With medium confidence, a complete shutdown of the AMOC will not occur by 2100, according to the recent IPCC report (IPCC, 2021). However, the confidence in this statement was reduced from the previous report (IPCC, 2013) because recent studies suggest that the stability of the AMOC may be overestimated in climate models (Weijer et al., 2019; Liu et al., 2017). This overestimation of the

AMOC strength is presumably related to the coarse resolution of the ocean component used in climate models. Coarse-resolution ocean models tend to overestimate the heat and salt advection from the Indian Ocean to the Atlantic via the Aghulas Leakage at the southern tip of Africa, thereby supplying additional salt to the Atlantic and thus artificially strengthening the AMOC (Biastoch et al., 2018, 2008b; Beal et al., 2011). Due to these biases, there is debate over whether the confidence in the future weakening of the AMOC, based on modern climate models, should be revised. McCarthy & Caesar (2023) highlighted the problem of missing ice and freshwater dynamics originating from the melting Greenland ice sheet in climate models of the Climate Model Intercomparison Project (CMIP) 6. These biases stress the importance of continued model improvements.

1.4 AMOC observations

The discrepancies between models and observations highlight the importance of continued AMOC observations, providing important benchmarks to assess and improve model performance regarding mean strength, variability, and trends of the AMOC. The Rapid Climate Change - Meridional Overturning Circulation Heat Transport Array - Western Boundary Time Series (RAPID-MOCHA-WBTS, hereafter RAPID) at 26°N in the subtropical Atlantic (hereafter RAPID array), the longest observational AMOC record so far (e.g., Moat et al., 2020; McCarthy et al., 2015b; Cunningham et al., 2007), has been operational since 2004. Direct observations from purposefully designed AMOC monitoring arrays have changed the view of the AMOC since the RAPID array began its measurements in 2004.

Among the biggest surprises was the amount of observed variability detected by the observing systems, and that this variability varies with latitude (Frajka-Williams et al., 2019). While previously the perception of the AMOC was closely related to the picture of the conveyor belt, depicting a continuous, buoyancy-driven circulation, varying on decadal and longer timescales, the results from the RAPID array showed AMOC variability on timescales from days to decades (Cunningham et al., 2007) with strong influences of mesoscale eddies (Clément et al., 2014). Furthermore, the observations showed that the density-driven part of the AMOC cannot explain the observed high-frequency variability (Frajka-Williams et al., 2023; Buckley & Marshall, 2016) and that instead, the wind forcing dominates large parts of the high-frequency variability (Zhao, 2017; Zhao & Johns, 2014). The first results of the RAPID array showed a decline of the AMOC strength, exceeding the weakening predicted by climate models (Smeed et al., 2014), culminating in a minimum (including even a brief reversal of the AMOC) in 2009/2010, causing discussions about the anthropogenic influence and the future of the AMOC in a warming climate. However, the negative trend of the AMOC did not persist. The AMOC recovered and remained relatively constant after that (Smeed et al., 2018). The negative trend probably followed a previous strengthening of the AMOC as part of intrinsic decadal variability, related to strong dense water formation in the subpolar North Atlantic (Rhein et al., 2017; Kieke & Yashayaev, 2015; Lazier et al., 2002) rather than representing a long-term trend (Jackson et al., 2016). The minimum in 2009/2010 was related to a record negative NAO, imprinting on the wind-driven part of the AMOC (Srokosz & Bryden, 2015).

In the center of the subpolar North Atlantic, the Overturning in the Subpolar North Atlantic Program (OSNAP) array was established in 2014 (e.g., Li et al., 2021; Lozier et al., 2017). First results challenged the notion that deep convection in the Labrador Sea is the main contributor to setting the mean strength and inter-annual variability of the AMOC and indicated a more dominant role for the eastern Atlantic (Lozier et al., 2019). This finding is supported by recent observations, emphasizing a more dominant contribution of the Irminger Sea to setting AMOC variability (Sanchez-Franks et al., 2023; Chafik et al., 2022), possibly related to enhanced freshwater input into the Labrador Sea from melting glaciers in Greenland (Rühs et al., 2021). However, modeling studies highlight a relevant role of the Labrador Sea in low-frequency AMOC variability by contributing to the formation of dense Labrador Sea Water (LSW, Böning et al., 2023; Yeager et al., 2021; Feucher et al., 2019). The OSNAP array confirmed what had been established using ocean models before. AMOC variability on seasonal and inter-annual timescales is not coherent between the subtropical and the subpolar North Atlantic due to the larger influence of the local wind forcing on the AMOC variability compared to the buoyancy forcing on these timescales (Bingham et al., 2007; Biastoch et al., 2008a). To date, no correlation has been found between the OSNAP array AMOC variability and the RAPID array AMOC variability (Lozier, 2023).

AMOC observations at the boundary between subtropical and subpolar gyre

The North Atlantic Changes (NOAC) array was established north of the subtropical gyre and south of the region where water mass transformation from the upper to the lower limb of the AMOC occurs (Rhein et al., 2011) to study the exchange between these two regimes (Figure 1.4 a). The array's instrumentation was a combined effort of the University of Bremen and the Federal Maritime and Hydrographic Agency (BSH). The array was located at 47°N in the western Atlantic and followed the historical World Ocean Circulation Experiment (WOCE) hydrographic line A02 (Kieke et al., 2009; Koltermann et al., 1999) at about 48°N in the eastern Atlantic. Transport measurements in the western basin used in this thesis started in 2013. In 2016, the array was extended to the eastern basin. See Moritz et al. (2021b); Nowitzki et al. (2020); Rhein et al. (2019b) for exact deployment dates. Further efforts included validating and establishing the methods,

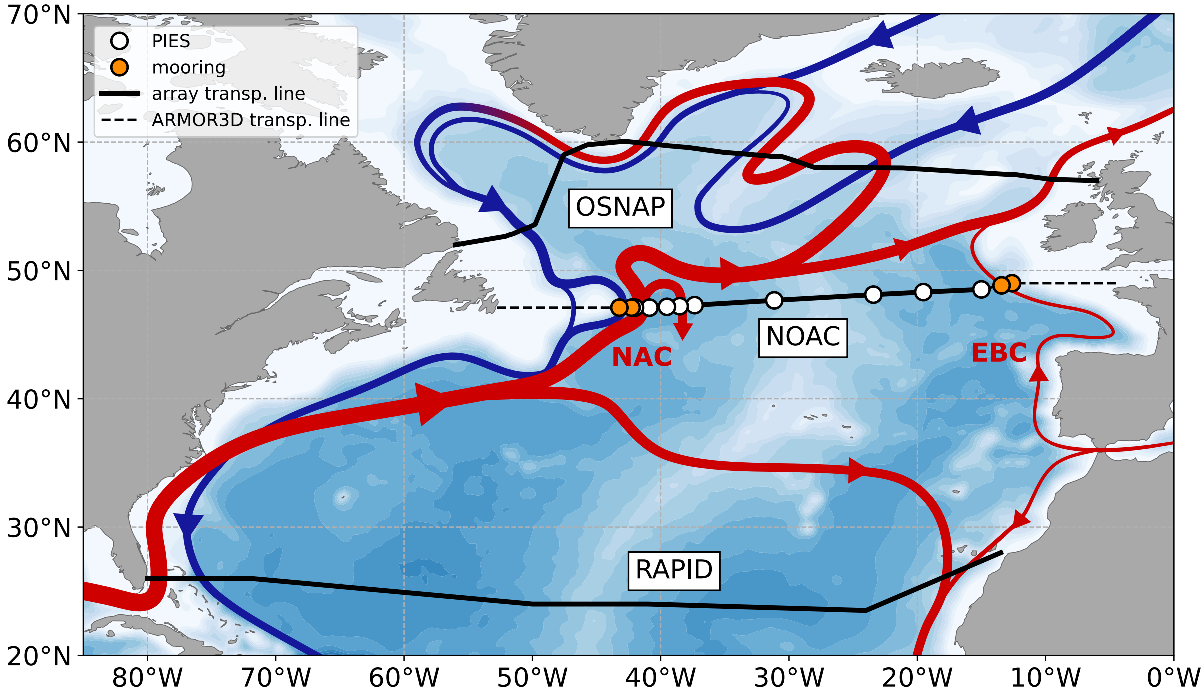

Figure 1.4: Schematic depiction of the major currents in the North Atlantic. Red (blue) arrows mark upper (deep) circulation pathways. Acronyms show the locations of the NAC and Eastern Boundary Current (EBC). Black lines indicate the transport lines of the NOAC, RAPID, and OSNAP arrays. For the NOAC array, parts of the section covered by ARMOR3D data are dashed. Pressure sensor-equipped Inverted Echo Sounder (PIES) locations are marked in white, moorings in orange. Topography is from Earth Topography (ETOPO) 2v2 (National Oceanic and Atmospheric Administration, NOAA, 2006).

extending the time series using satellite altimetry, and discussing the observed top-bottom transport time series of the AMOC components (Moritz et al., 2021b; Nowitzki et al., 2021; Rhein et al., 2019b; Roessler et al., 2015; Mertens et al., 2014) and a comparison with high-resolution ocean models (Breckenfelder et al., 2017; Mertens et al., 2014).

Volume transports of the NOAC array integrated from the ocean surface to the bottom in different parts of the section have been analyzed before. This work has shed light on the characteristics of the different current branches crossing 47°N at the boundary between the subtropical and the subpolar gyre. Mertens et al. (2014) used ship-board hydrographic data and mooring observations from the western boundary to study the transports in the DWBC. They found two distinct cores of southward DWBC transports: One at the continental slope with maximum velocities at mid-depth and another at the continental rise with bottom-intensified velocities. Rhein et al. (2019b) studied the transports in the western part of the section between 44°W and 31°W and found a significant decline in volume transport of 0.6 $\mathrm{Sv\,yr^{-1}}$, dominated by the southward flow east of 37°W, the major recirculation branch of the NAC. Based on sea surface height (SSH) data, they argued that this decrease most likely originates from regional warming differences between the coastal and interior parts of the western North Atlantic. Nowitzki et al. (2021) calculated estimates of the geostrophic transports at the NOAC array at 47°N in the Eastern subpolar North Atlantic. Additionally to the NAC pathway crossing 47°N in the western basin and subsequently the Mid-Atlantic Ridge, they found a more direct pathway of subtropical water crossing 47°N in the Eastern Atlantic. This pathway contributes about 22 % of the total inflow into the eastern subpolar basin. A positive trend of 2.0 Sv decade^{-1} was found in the meridional transport in the eastern part, which partly compensates for the negative trend in the western basin, found by Rhein et al. (2019b). At the eastern boundary, Moritz et al. (2021b) studied the offshore branch of the European Shelf Current based on mooring observations at the slope of the Celtic shelf. They found strong monthly to seasonal variability due to a dynamic eddy field.

This previous work at the NOAC array covers virtually the entire basin and thus allows the calculation of an AMOC estimate at 47°N, presented in Chapter 3. However, the Canadian and European shelves off Newfoundland and Ireland are not covered by moored instruments due to shallow waters and high fishing activity. Furthermore for a 180 km wide strip in the eastern Atlantic transports could not be calculated from moored observations due to a loss of mooring instruments (Section A.1). This thesis, therefore, relies on the observation-based gridded data set ARMOR3D (Section 2.2.1) to bridge these gaps and obtain a basin-wide AMOC estimate (Section 2.4.1).

The AMOC in Argo and gridded data sets

In the early 2000s, the global Argo program of freely drifting floats was established (Roemmich et al., 1998), providing a whole new platform for ocean observations. As a consequence of the launch of the Argo program and progress in ocean data assimilation, in the last decade, ocean reanalyses and gridded observational data sets have strongly improved and therefore gained attention in the climate science community (Storto et al., 2019; Balmaseda et al., 2015).

The opportunities arising from these novel approaches to ocean observations have not been extensively exploited. Willis (2010) calculated the AMOC at 41°N from Argo floats, applying a method, developed by Willis & Fu (2008) of estimating the circulation of the upper ocean. Their work was the first observational AMOC estimate at higher latitudes. Results showed a weaker AMOC than the RAPID measurements at 26°N and lower seasonal and inter-annual variability. Despite being a powerful tool for ocean observations due to the relatively good global observational coverage, Argo floats have some limitations. Most Argo floats are programmed to drift in a depth of 1000 m, diving to a depth of 2000 m every few days to measure a hydrographic profile. While this is sufficient to estimate the upper limb of the AMOC, the Argo floats do not wholly sample the lower AMOC limb in the deep ocean, which is known to be of major importance for the southward export of dense water masses and the meridional coherence of the AMOC (Hopkins et al., 2019; Zou et al., 2019, Section 1.6,). Additionally, due to the default drifting depth of 1000 m, the Argo floats cannot cover shallow ocean regions, limiting the analysis to regions where not large parts of the transports are situated over shallow topography (Willis, 2010). To minimize the influence of uncertainties in single gridded data sets, Desbruyères et al. (2019) combined different ocean reanalyses and observational data sets as an ensemble mean to calculate an AMOC estimate at 45°N. Like Willis (2010) at 41°N, they found a weaker mean AMOC strength than the RAPID measurements. The AMOC variability in their estimate exhibited a link to the water mass transformation in the eastern subpolar gyre with a five-year lag between the change in surface variables in the subpolar gyre and the associated AMOC variability.

Continued AMOC observations are of major importance for understanding the physical mechanisms of AMOC variability and serve as benchmarks for model evaluation. However, securing funding for expensive in-situ AMOC monitoring arrays is challenging. Therefore, gridded data sets provide the potential of cost-efficient AMOC estimates, possibly in combination with in-situ devices, where necessary. Section 3.8 analyzes the representation of the AMOC in gridded data sets. Based on these results, a cost-efficient future AMOC observing system is proposed in Chapter 6.

1.5 The AMOC in forced model simulations

In climate models, the key components of the climate system (e.g., atmosphere, ocean, cryosphere, biosphere) are simulated and coupled to exchange properties. These models are valuable tools to examine long-term responses of the climate system to external forcing, such as anthropogenic CO_2 on timescales from centuries to millennia. However, due to the computational costs of such long simulations, most coupled climate models are run with a relatively coarse ocean component (1°-0.25°, Heuzé, 2020), possibly causing uncertainties by not representing mesoscale eddies (Hirschi et al., 2020). Coupled model simulations are usually started from predefined initial conditions and then run freely. Consequently, different coupled models do not necessarily simulate the same events at the same time, limiting the comparability with observations.

So-called hindcast or forced ocean model simulations, usually starting in the mid-20th century or later, are forced with observational atmospheric forcing data sets. Since they simulate only specific climate system components, they can be run at higher spatial resolution compared to the ocean components in climate models. Forced ocean model simulations provide the opportunity to compare the model results directly with past observations. This assessment is essential to validating the model performance before using the model physics for future projections of climate parameters like the AMOC. The capability of hindcast simulations to realistically represent the AMOC in the North Atlantic has been claimed from a general agreement in terms of AMOC mean state and variability between different models of relatively coarse resolution (Danabasoglu et al., 2016) and in a comparison between observations at 26°N and 53°N and the high-resolution VIKING20X model (Biastoch et al., 2021). One major advantage of these hindcast simulations for representing AMOC variability is that due to the observational atmospheric forcing, one of the major driving forces of the AMOC, the wind, is realistically represented (Danabasoglu et al., 2016; Biastoch et al., 2008a).

Danabasoglu et al. (2016) showed that hindcast simulations exhibit similar inter-annual AMOC variability across different models. They generally find three different phases of AMOC evolution: A relatively constant AMOC from the late 1950s to the 1970s, A subsequent strengthening until the mid-1990s associated with enhanced dense water formation in the Labrador Sea (Rhein et al., 2017; Kieke & Yashayaev, 2015; Lazier et al., 2002), and a negative trend afterward. However, the consistent evolution across many ocean hindcast simulations does not necessarily imply a realistic representation because these agreements in variability include large differences in the mean state (Danabasoglu et al., 2014).

Despite a generally similar past evolution of the AMOC, some differences in decadal variability remain due to its sensitivity to numerical choices in the implementation (Biastoch et al., 2021; Hewitt et al., 2020). Specifically, the resolution and the quality of the atmospheric forcing data set are important for adequately representing the AMOC in forced ocean-only models (Biastoch et al., 2021). Large parts of the meridional volume, heat, and freshwater transports are influenced by mesoscale eddies (Frajka-Williams et al., 2019; Marshall et al., 2017; Clément et al., 2014; Wunsch, 1999). The radius of these eddies scales with the baroclinic Rossby radius, which depends on the topography, the stability of the water column, and the latitude. Garcia-Quintana et al. (2019) used a $^{1}/_{4}{}^{\circ}$ simulation of the Atlantic to compare the modeled AMOC at 26°N to observations at the same latitude. They found that the modeled AMOC properly represents the inter-annual AMOC variability. However, in the subpolar North Atlantic, the Rossby radius becomes smaller while the contribution of mesoscale eddies to the total heat and freshwater transport increases (Müller et al., 2019, 2017; Treguier et al., 2012). According to Hallberg (2013, their Figure 1), the resolution that is needed to adequately resolve mesoscale eddies in the subpolar North Atlantic is more than $^{1}/_{10}{}^{\circ}$. Such high resolution is required to resolve eddy processes and dynamic features, for example, at the Northwest Corner (Martin & Biastoch, 2023). The wind and buoyancy fluxes represent a strong influence of the atmosphere on ocean parameters as the AMOC. Thus, the realistic representation of the AMOC in hindcast simulations, additionally, strongly depends on the quality of the atmospheric forcing data set (Biastoch et al., 2021; Griffies et al., 2009).

While being able to simulate the past evolution of different ocean parameters, the missing influence of the ocean on the atmosphere via latent and sensible heat fluxes and freshwater fluxes induces artificial feedbacks in hindcast simulations that need to be accounted for. In forced models with a prescribed atmospheric component, the temperature feedback does not act as in the real world due to the limited surface heat fluxes in a forced model, where the atmosphere influences the ocean, but the ocean does not influence the atmosphere (Griffies et al., 2009). Thus, the sensitivity of the circulation in the North Atlantic and the AMOC to changes in the salinity is overestimated. Consequently, overly strong negative AMOC trends can occur (Biastoch et al., 2021). To account for this overly strong feedback, forced ocean models often use a salinity restoring mechanism, which sets the sea surface salinity (SSS) to observed values. However, this restoring cannot just be applied to the whole ocean domain since it would introduce errors where large amounts of freshwater enter the ocean, near river mouths or marine-terminating glaciers.

Forced model setups, simulating the past AMOC variability are the major tool to assess model performance and improve the representation and parameterization of key processes. Chapter 4 provides a detailed analysis of the representation of the AMOC in the North Atlantic, by comparing observations from AMOC monitoring arrays to the simulated AMOC in different model simulations.

1.6 Meridional Connectivity

As there are still uncertainties associated with modeling the AMOC of the past and future, observations remain an integral part of assessing the representation of the AMOC in model simulations. In the view of the AMOC as a conveyor belt, AMOC changes at any given latitude would be representative of the whole Atlantic by implying a continuous system of currents moving at a constant speed. If this were indeed true at all timescales, it would drastically reduce the necessity for direct AMOC observations at multiple latitudes, making monitoring the AMOC much more feasible by allowing to focus on possibly just a single monitoring system. However, it has been shown that there are meridional differences in the forcing and timescales of variability (Frajka-Williams et al., 2019). A lack of connectivity (also called coherence) of the AMOC at two latitudes implies convergence and divergence of ocean heat and freshwater content (Kelly et al., 2014). These redistributions impact oceanic and atmospheric dynamics, highlighting the importance of AMOC observations at different latitudes to understand the AMOC's role in the climate system.

Previous studies argued that subtropical AMOC variability is dominated by high-frequency wind forcing with low-frequency contributions by the buoyancy forcing (Jackson et al., 2022; Buckley & Marshall, 2016). However, low-frequency buoyancy forcing is more prominent in the subpolar North Atlantic. Due to these different timescales of the forcing mechanisms and the importance of buoyancy forcing for the subtropical and subpolar AMOC variability, meridionally coherent AMOC variability is expected on longer than decadal timescales (Gu et al., 2020). Such coherent decadal AMOC variability has also been found in a forced ocean model by Biastoch et al. (2021). Within the subtropical gyre, AMOC variability has been shown to be coherent on seasonal timescales, with the seasonal cycles being 180° out of phase between 26°N and 41°N (Mielke et al., 2013). However, meridional connectivity on inter-annual timescales, especially across gyres, is less clear (Gu et al., 2020; Bingham et al., 2007). Buckley & Marshall (2016) argued that due to the dominant influence of the wind-forcing on seasonal timescales, meridional connectivity on seasonal timescales is determined by the connectivity of the wind field (Buckley & Marshall, 2016).

Observational estimates and coupled ocean-atmosphere models disagree on the latitude ranges and timescales of meridional connectivity of the AMOC (Kostov et al., 2022; Gu et al., 2020; Frajka-Williams et al., 2018; Elipot et al., 2014). Due to the scarcity of direct AMOC observations, only a few studies analyze the connectivity between mooring array transport estimates in the North Atlantic. Within the subtropical gyre, observations of the RAPID and Meridional Overturning Variability Experiment (MOVE) arrays at 26°N and 16°N, respectively, showed opposing inter-annual variability (Frajka-Williams et al., 2018; Smeed et al., 2014; Send et al., 2011). However, Frajka-Williams et al. (2018) showed that these opposing trends were due to methodological differences and found coherence in the deep baroclinic circulation. Elipot et al. (2014) found coherent AMOC variability on semiannual and longer timescales between 41°N and 26°N, with the former leading by three months. Using the ECCO v4r3 state estimate (Forget et al., 2015), Han (2023) found in-phase meridional connectivity between the locations of the OSNAP and RAPID arrays and proposed a connection via adiabatic redistribution of waters, indicating that communication between latitudes does not need to be advective but can occur via isopycnal displacement.

A break in the connectivity is often found between the subpolar and the subtropical gyres at about 40°N due to the different mechanisms dominating the variability (Bingham et al., 2007). observational evidence for meridional connectivity beyond the subtropical gyre has not yet been found at the OSNAP array (Lozier, 2023), possibly due to the lmited length of the time series. At 47°N, the boundary between the subtropical and the subpolar gyre, the NOAC array can be extended until 1993 using direct AMOC transport measurements and satellite altimetry. This offers a timely opportunity to study the coherence of the AMOC between the subtropical gyre and the transition region to the subpolar gyre based on observations of the NOAC array (Section 3.7).

1.7 Thesis objectives

This thesis contributes to a better understanding of the AMOC variability and coherence in the North Atlantic. I discuss the observational inter-annual AMOC variability at the NOAC array and compare it to the variability from other AMOC estimates in the North Atlantic at the RAPID array and estimates from gridded data sets near the NOAC array. Furthermore, I use forced hindcast simulations to investigate the representation of the AMOC in numerical models at the locations of the observational estimates.

Basin-wide mooring-based AMOC estimates are still scarce due to the logistical and financial efforts associated, making these direct observations of the AMOC very valuable. Here, I present the first basin-wide AMOC estimate from the NOAC array at 47°N, the boundary between the subtropical and the subpolar gyre. I report the mean strength and variability of the AMOC observed at 47°N and compare it to other latitudes.

In recent years, the discussion about the meridional connectivity of the AMOC has gained more attention. Meridional connectivity of the AMOC on inter-annual timescales could have implications for designing a future AMOC observing system. If AMOC variations at a specific latitude partly represent changes at other latitudes, this connection could be used to infer the state of the AMOC from a reduced and thus more feasible set of mooring arrays. However, meridional connectivity of the inter-annual AMOC variability has not been intensively studied from direct observations due to a lack of observational AMOC time series with sufficiently long measuring periods. The basin-wide AMOC estimate of the NOAC array and the extension in time provide insights into the AMOC variability at the boundary between the subtropical and subpolar gyres. I analyze the coherence of the inter-annual variability with the longest available direct AMOC observational time series from the RAPID array and discuss the factors that influence the connectivity.

With the growing availability and quality of gridded data sets, these become more and more of interest for the oceanographic community to analyze subsurface parameters. These could provide a feasible alternative to classical mooring arrays, especially in designing a future AMOC monitoring system. I analyze the representation of the AMOC at 47°N in two different approaches, in the ARMOR3D data set and in a combination of different data sets, used in Desbruyères et al. (2019) and compare them to the AMOC estimate of the NOAC array.

As observations of the AMOC are limited in space and time, using numerical model simulations remains an essential part of the research on the AMOC as tools to better understand the physical mechanisms and project the future of the AMOC as a key parameter in the climate system. I analyze the AMOC in different forced model simulations at the locations of the observational estimates to investigate the representation of the AMOC in terms of mean state, variability, trends, and meridional connectivity. I compare them to the observational time series and explore reasons for similarities and differences. Additionally, I use model simulations with varying spatial resolution to shed light on the influence of resolution on the representation of the AMOC in forced model simulations.

The present thesis aims to answer the following research questions:

1. **What are the mean strength and variability of the AMOC at 47°N and how do these compare to other latitudes?** (Chapter 3)
2. **How coherent is inter-annual AMOC variability between the subtropical North Atlantic and the subpolar gyre boundary in observations and models?** (Chapter 3, Chapter 4)
3. **How useful are AMOC estimates from gridded data sets in designing a future AMOC monitoring system?** (Chapter 3)
4. **How well does the forced ocean model VIKING20X represent key characteristics of the observed AMOC?** (Chapter 4)
5. **What is the impact of model resolution on the representation of the AMOC in different simulations of the forced ocean model ANHA?** (Chapter 4)

The thesis is structured as follows: Chapter 2 presents the data used for the present thesis and describes the applied methodology. The analysis of the observational AMOC estimate at the NOAC array is presented in Chapter 3. The results from the model analysis are shown in Chapter 4. Chapter 5 summarizes the main findings and concludes the thesis. Finally, Chapter 6 puts the findings into a broader perspective and highlights questions for future research.

"I find the lure of the unknown irresistible."

Sylvia A. Earle, *marine biologist and oceanographer*

Chapter 2

Data and Methodology

This chapter covers the data and methods used in this thesis. Section 2.1 introduces the observational data used to calculate the basin-wide AMOC estimate at the NOAC array at 47°N. Section 2.2 describes the gridded data sets used for completing the observation-based NOAC AMOC estimate. In Section 2.3, the implementation of model simulations, discussed in this thesis, is described. Section 2.4 and Section 2.5 introduce the AMOC volume transport and MHT definitions. Finally, Section 2.6 explains the statistical methods used in this thesis.

2.1 Observational data

2.1.1 Measurement Principle of Pressure sensor-equipped Inverted Echo Sounders (PIES)

Many of the transport estimates discussed in this thesis are based on Pressure sensor-equipped Inverted Echo Sounders (PIES) measurements. These are moored devices, standing on the ocean bottom and measuring the round trip travel time τ of a sound pulse from the device to the sea surface, where it is reflected, and then back to the instrument (Chaplin & Watts, 1984; Watts & Rossby, 1977). Using the dependency of the sound velocity in seawater on the temperature and salinity, these measurements allow calculating the vertical distribution of temperature and salinity in the water column. From vertical distributions of temperature and salinity at two locations, horizontal density differences and the resulting geostrophic transport, representing the baroclinic component of the total geostrophic transport, can be calculated. Additionally, the PIES are equipped with a bottom pressure sensor. Changes in bottom pressure at the PIES location represent mass changes in the water column and, thus, the barotropic component of the total transport.

2.1.2 Transports from PIES measurements

In order to obtain transport time series from PIES measurements, several intermediate steps need to be taken. These include

1. creating a transfer function to obtain profiles of the specific volume anomaly (SVA) δ from measurements of the PIES travel time τ,
2. calculating the relative geostrophic velocity as the sum of the baroclinic and barotropic components,
3. referencing the relative geostrophic velocity to the geostrophic surface velocities from satellite altimetry to obtain the absolute geostrophic velocity.

The method applied to obtain profiles of temperature, salinity and SVA from the PIES travel time τ measurements follows Nowitzki et al. (2021); Roessler et al. (2015); Meinen et al. (2004). It is called the Gravest Empirical Mode (GEM) method and relies on hydrographic profiles of temperature and salinity (in this case Argo and shipboard Conductivity-Temperature-Depth probe, CTD, measurements, Section 2.1.6) taken in the vicinity of each PIES position. For each of these profiles the SVA δ and the corresponding travel time τ is calculated. Specific volume α is the reciprocal of the density and its anomaly is defined as

$$\delta = \alpha(S, T, p) - \alpha(35, 0, p) \tag{2.1}$$

After applying a few corrections (such as a latitude correction and a seasonal correction), the profiles are sorted by τ. Based on these data, an estimate of the temperature, salinity, and SVA profiles can be inferred from only the acoustic travel time τ, measured by the PIES.

Vertically integrating the SVA yields the geopotential anomaly (GPA) Φ,

$$\Phi = \int \delta \, dp \tag{2.2}$$

The baroclinic geostrophic velocity u_{bc} describes the geostrophic velocity due to horizontal density gradients between two stations A and B of known GPA. The baroclinic component of the geostrophic velocity can be calculated from the GPA as

$$u_{bc} = \frac{\Phi_B - \Phi_A}{f \cdot L}, \tag{2.3}$$

where Φ_A and Φ_B are the GPAs at the PIES positions, f is the Coriolis parameter and L is the distance between the two positions.

Fluctuations in the SSH (absolute dynamic topography, ADT) at the two positions A and B impact the geostrophic velocity. Their effect is called the barotropic component of the geostrophic velocity. After applying a drift correction to the measurements of the bottom pressure sensor of the PIES, the barotropic geostrophic velocity fluctuations can be calculated from the bottom pressure fluctuations at the PIES position as

$$u'_{bt} = \frac{\Delta p'}{\bar{\rho} \cdot f \cdot L}, \tag{2.4}$$

with the bottom pressure fluctuations of the two PIES $\Delta p'$ and the mean density of the reconstructed hydrographic profiles $\bar{\rho}$. Adding this to the baroclinic component yields the total relative geostrophic velocity.

Since geostrophy only yields velocity fluctuations, a known reference velocity is needed to obtain absolute velocities. Often, geostrophic velocities are calculated relative to a "level of no motion" at which the velocity is assumed to be zero. A better alternative is to use the geostrophic velocity at the ocean surface u_{alt} which is known from satellite altimetry as a "level of known motion". The altimetry-derived geostrophic surface velocity can be calculated via the geostrophic equations as

$$u_{alt} = -\frac{g \cdot \Delta\zeta}{f \cdot L}, \tag{2.5}$$

where $\Delta\zeta$ is the difference in SSH at the two stations. Given a high correlation between u_{alt} and the surface value of u_{bc}, the total relative geostrophic velocity from the PIES can be shifted by the mean difference between the surface values of u_{bc} and u_{alt}.

The combination of the relative geostrophic velocity obtained from the PIES and the altimetry-derived geostrophic surface velocity yields a more accurate estimate of the absolute geostrophic velocity and, thus, volume transport, compared to using a "level of no motion" at depth.

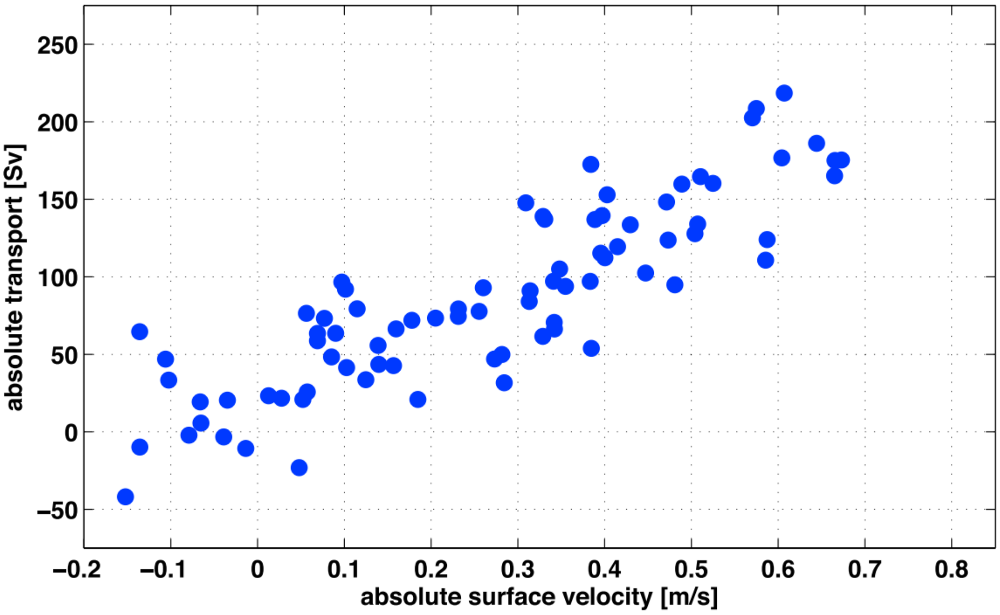

Figure 2.1: Correlation between values of the absolute transport, measured between PIES BP27 and BP28 of the NOAC array at 47°N in the western North Atlantic and the absolute surface velocity obtained from satellite altimetry, both in two-weekly resolution. Figure from Rhein et al. (2019b).

2.1.3 Extending transport time series in time using altimetry

Nowitzki et al. (2021), Moritz et al. (2021b), and Rhein et al. (2019b) showed that all individual flow components in the interior and the boundary currents at the NOAC array are significantly correlated with the SSH and follow roughly a linear relationship (Figure 2.1). This relationship enables extending the existing transport time series to the full altimetry period, starting in 1993, using the relationship obtained from the in-situ measurements and the altimetry.

For this purpose, the absolute transports are regressed onto the absolute surface velocities (Moritz et al., 2021b; Nowitzki et al., 2021; McCarthy et al., 2020; Rhein et al., 2019b; Roessler et al., 2015). The correlation between the barotropic transports and the surface velocity in the eastern Atlantic is not as strong as in the western Atlantic (Nowitzki et al., 2021). This introduces an uncertainty to the barotropic part of the extended transports in the eastern basin.

2.1.4 The North Atlantic Changes (NOAC) moored array

The NOAC array at about 47°N consisted of various moored sensors (Figure 1.4, Figure 2.4). In the ocean interior, geostrophic transports are calculated in eight segments from moored pressure-sensor-equipped inverted echo sounders (PIES, Nowitzki et al., 2021; Rhein et al., 2019b). At the western (Rhein et al., 2019b; Mertens et al., 2014) and eastern (Moritz et al., 2021b) boundaries, the transports are calculated from deep sea moorings equipped with acoustic current meters and profilers. The individual AMOC components calculated from moored instruments are extended back to 1993 by regressing absolute transports on the satellite altimetry-derived surface velocity field (Section 2.1.3).

Previous work at the NOAC array included estimates of the transports in the boundary current regions of the western (Mertens et al., 2014) and eastern (Moritz et al., 2021b) boundary current systems as well as the western (Rhein et al., 2019b) and eastern (Nowitzki et al., 2021) interior basin. These transport estimates cover large parts of the basin and allow the calculation of an observational, basin-wide AMOC estimate at 47°N. However, some regions along 47°N remain not covered by previous work. These regions include the Canadian and European shelves and a 180 km wide strip between Bremen PIES (BP) 32, the easternmost PIES, and EB3, the western mooring of the eastern boundary mooring array (Figure 1.4). In the final AMOC estimate at 47°N, geostrophic velocities from the ARMOR3D data set are used to estimate these transports. However, since data from BP32 and EB3 is available, calculating geostrophic transports in this 180 km wide region was attempted using the mooring and PIES data. However, calculating meaningful volume transports between BP32 and EB3 was impossible. Section A.1 describes the approach and explains why the decision to use ARMOR3D data instead of the mooring and PIES data was made.

Transports from the NOAC array have been calculated for the PIES segments in the western basin by Christian Mertens (University of Bremen, Rhein et al., 2019b), for the PIES segments in the eastern basin by Hannah Nowitzki (previously University of Bremen, Nowitzki et al., 2021), and for the Eastern Boundary (EB) moorings by Martin Moritz (BSH, Moritz et al., 2021b). In this thesis, the NOAC observational transports are combined with transports from ARMOR3D and wind stress data to yield a basin-wide AMOC estimate at 47°N.

2.1.5 Ekman transports from wind stress data

The velocities, measured by the moorings and PIES of the NOAC array, are based on geostrophy. These velocities and the resulting transports are responses to horizontal density differences and do not include the responses to local wind forcing. The Ekman transport due to the wind forcing can be calculated from the zonal wind stress. The wind stress data set used for the calculation of the Ekman transport is the IFREMER CERSAT Global Blended Mean Wind Fields (Desbiolles et al., 2017), comprising 6-hourly global surface wind data from satellite-borne scatterometry and radiometry on a $^1/_4°$ global grid (Bentamy et al., 2022; Bentamy, 2022). This data set is also used to link AMOC strength changes to wind stress changes (Section 3.5) and to calculate the Ekman transport at 45°N to accompany the AMOC calculations by Desbruyères et al. (2019, Section 3.8.2).

The wind stress values are interpolated onto the exact section of the NOAC array (Figure 1.4) and the Ekman transport along the NOAC array is calculated as

$$V_{Ek} = \frac{\tau_x}{\rho_0 f}, \tag{2.6}$$

where τ_x is the zonal wind stress, ρ_0 is the density of seawater, and $f = 2\,\Omega\,sin(\phi)$ is the Coriolis parameter at the latitude ϕ. $\Omega = \frac{2\pi}{T_{sid}}$ is the rotation rate of the Earth with the sidereal day $T_{sid} = 86164\,s$.

2.1.6 Hydrographic data

Hannah Nowitzki used hydrographic data to create a transfer function for obtaining the geostrophic transports from the PIES measurements of round-trip travel time. These data were obtained between 2015 and 2018 (see Nowitzki et al. (2021) for cruise details, their Tables 2 and 3). Additional hydrographic data was obtained from Argo floats near the respective PIES locations (Nowitzki et al., 2021, their Figure 3).

The calculation of the basin-wide AMOC volume transport at the NOAC array is based on the potential density (hereafter referred to as density) of the maximum stream function (Section 2.4.1). This density was obtained from lowered Acoustic Doppler Current Profiler (lADCP) sections along 47°N (see Rhein et al. (2019b) for cruise details, their Table 2). To use the maximum number of sections available, hydrographic data from four additional cruises after 2017 was included in the estimate of the density of the maximum stream function at 47°N.

2.1.7 Satellite altimetry

Besides in-situ observational data, satellite altimetry is used for this thesis. The Copernicus Marine Service supplies the data on a 1/4° global grid in daily resolution. Hannah Nowitzki used ADT data from 1993-2018 to calculate absolute transports from the PIES measurements. For this purpose, the geostrophic velocity, based on the ADT obtained from satellite altimetry, is calculated via the geostrophic equations (Equation 2.5) and compared to the geostrophic velocity from the PIES measurements. The geostrophic velocity from the PIES measurements is shifted accordingly (see Section 2.1.2).

The same data and method are applied, though unsuccessfully, to calculating geostrophic velocities and volume transports from the data obtained from the PIES BP32 and the mooring EB3 (Section A.1).

Additionally, the same data set is used to calculate linear trends of the SSH in the subpolar North Atlantic in Section 4.2.2.

2.2 Gridded data sets

2.2.1 ARMOR3D

For regions where there is no direct observational data available from the NOAC array (for example, the Canadian and European shelf regions), the ARMOR3D data set is used in this thesis to complete the basin-wide AMOC estimate at 47°N (Section 2.1.4). Furthermore, a basin-wide AMOC estimate at 47°N is calculated, entirely relying on ARMOR3D to assess the representation of the AMOC in ARMOR3D (Section 3.8.1).

ARMOR3D is supplied by the Copernicus Marine Service. ARMOR3D uses satellite altimetry, satellite measurements of SST and SSS, and in-situ measurements (obtained from CTD, Argo float, and mammal-borne sensor profiles). Hydrographic and velocity data from instruments of the NOAC array have not been used in ARMOR3D. The data set provides temperature, salinity, and geostrophic velocities on a global grid of $^1/_4$° lateral resolution (Figure 2.2 a) and weekly temporal resolution. The vertical resolution covers 41 levels down to 1500 m. Below 1500 m ARMOR3D consists of nine more vertical levels based on World Ocean Atlas (WOA) climatological values. The maximum depth, represented in ARMOR3D, is 5500 m.

ARMOR3D comprises only observational data, merged and gridded using statistical methods (Guinehut et al., 2012). This process includes three main steps. In the first step, the remote sensing parameters sea level anomaly (SLA), SST, and SSS are projected onto the vertical via multiple linear regression from the surface to 1500 m (Mulet et al., 2012). These synthetic profiles are then merged with the in-situ profiles from CTD, Argo, and mammal-borne sensor measurements in a second step (Bretherton et al., 1976). Finally, the combined profiles are extended to 5500 m using the WOA climatology. Geostrophic velocities are calculated using the thermal wind relation from the final, full-depth profiles. More information on the derivation and quality control of ARMOR3D can be found in Guinehut (2021), and Greiner et al. (2021).

ARMOR3D was chosen as the appropriate data set for the completion of the NOAC array transports because it is solely based on observational data and because of its relatively high spatial resolution, compared with other gridded data sets (for example, 1° in EN4, Section 2.2.2). ARMOR3D has been shown to yield comparable upper ocean heat content variability in the subpolar North Atlantic, in agreement with reanalyses (Iakovleva & Bashmachnikov, 2021). Furthermore, a detailed analysis by Wiegand (2023) revealed a good representation of the hydrography at the eastern Atlantic Repeat Hydrography 7 West section (AR7W) in the subpolar North Atlantic in ARMOR3D. However, it shall be noted that there are a few limitations to this data set. ARMOR3D has a horizontal resolution, generally capable of resolving the Rossby radius in the central North Atlantic at 47°N. However, especially on the shelves, the Rossby radius becomes smaller as a function of topography. Thus, on the shelves, ARMOR3D cannot resolve mesoscale eddies. Additionally, while ARMOR3D is gridded to a horizontal resolution of $^1/_4{}^\circ$, the actual resolution of the input data is different and depends on the available observational data. Generally, in the shelf regions, in-situ observations are scarce, primarily due to the shallow topography and the resulting lack of observations from Argo floats, which have a default drifting depth of 1000 m. Additionally, satellite altimetry data is not as reliable close to the coast (Benveniste et al., 2020). Consequently, though still completely observation-based, the ARMOR3D geostrophic velocities on the continental shelves and the resulting transports are subject to these uncertainties. Greiner et al. (2021) analyzed the global accuracy of ARMOR3D geostrophic velocities, finding that the geostrophic velocities are slightly too barotropic due to a dominance of the reference surface currents over the hydrographic structure during the application of the thermal wind equation. The bias due to this overestimation was found to be $0.06\,\mathrm{cm\,s^{-1}}$ at 1000 m (Greiner et al., 2021). This effect might be enhanced in the narrow boundary current due to the scarcity of in-situ data and thus result in an overestimation of the boundary current transports.

2.2.2 EN4

The EN4 data set (Good et al., 2013) was used by Desbruyères et al. (2019) in combination with ARMOR3D and two other data sets to estimate the AMOC at 45°N in the North Atlantic (Section 3.8.2). Additionally, the EN4 data set is used in this thesis to compare the upper ocean temperature and salinity trends in the North Atlantic to the trends found in the VIKING20X model simulation and ARMOR3D (Section 4.2.2, Figure A.7).

The EN4 version used in this thesis, EN4.2.1 (Desbruyères et al. (2019) used EN4.2.0), provides quality-controlled and bias-corrected objective analyses of ocean temperature and salinity (Gouretski & Reseghetti, 2010). The EN4 data set incorporates data from various types of instruments. The contributing data sources are the World Ocean Database, the Global Temperature and Salinity Profile Program, the Arctic Synoptic Basin Wide Oceanography, and Argo floats. The data is provided on a 1° grid (Figure 2.2 b) with 42 depth levels, spanning the period from 1990 to the present in monthly resolution.

2.3 NEMO model simulations

The Nucleus for European Modelling of the Ocean (NEMO) provides a framework for ocean model configurations. In this thesis, forced NEMO ocean model simulations are used to analyze the representation of the AMOC in forced ocean models.

The NEMO framework features three major components: The ocean dynamics and thermodynamic component, represented by the Ocean Engine (OCE, Madec et al., 2023), the sea ice component, represented by the large-scale Louvain-la-Neuve sea-Ice Model (LIM2, Bouillon et al., 2009), and the marine biogeochemistry component, represented by the Biogeochemistry with Light Iron and Nutrient limitation and Gases model (Galbraith et al., 2010). In this thesis, only results from the OCE, coupled with LIM2 are used, namely temperature, salinity, and meridional and zonal velocity.

In order to numerically derive the dynamics and thermodynamics of the ocean in a numerical model, a few assumptions need to be implemented. For the NEMO model, these include the following:

Spherical Earth approximation: The Earth is considered a sphere. Consequently, geopotential surfaces are spheres, and gravity acts perpendicular to the geopotential surfaces. Gravity is independent of latitude and longitude.

Thin-shell approximation: Due to the negligible ocean depth compared to the Earth's radius, the effects of ocean depth on gravity are neglected.

Turbulent closure approximation: The effects of turbulent fluxes from small-scale features are parameterized in large-scale features.

Boussinesq approximation: $\rho = \rho(S, T, p)$, density variations are only considered regarding the buoyancy force.

Hydrostatic approximation: $\frac{\partial p}{\partial z} = -\rho g$, the vertical momentum equation is expressed as a balance between the vertical pressure gradient and the buoyancy force (since this suppresses the representation of convection, convective processes are parameterized instead)

Incompressibility approximation: $\nabla \cdot \mathbf{u}$, the flow is assumed to be incompressible, the velocity vector $\mathbf{u}$ has no divergence.

Neglect of additional Coriolis terms: Coriolis terms, depending on the cosine of the latitude, are neglected.

With these approximations applied, the ocean dynamics and thermodynamics in NEMO are described with the primitive equations (Madec et al., 2023). These are the horizontal momentum balance (Equation 2.7), the heat and salt conservation equations (Equation 2.8, Equation 2.9), the hydrostatic equation (Equation 2.10), the incompressibility equation (Equation 2.11), and the equation of state (Equation 2.12):

$$\frac{\partial \mathbf{u}_h}{\partial t} = -\left[(\nabla \times \mathbf{u}) \times \mathbf{u} + \frac{1}{2}\nabla(\mathbf{u}^2)\right]_h - f\mathbf{k} \times \mathbf{u}_h - \frac{1}{\rho_0}\nabla_h p + D^U + F^U \tag{2.7}$$

$$\frac{\partial T}{\partial t} = -\nabla \cdot (T\mathbf{u}) + D^T + F^T \tag{2.8}$$

$$\frac{\partial S}{\partial t} = -\nabla \cdot (S\mathbf{u}) + D^S + F^S \tag{2.9}$$

$$\frac{\partial p}{\partial z} = -\rho g \tag{2.10}$$

$$\nabla \cdot \mathbf{u} = 0 \tag{2.11}$$

$$\rho = \rho(T, S, p) \tag{2.12}$$

In these equations, $\mathbf{u}$ is the three-dimensional velocity vector, and $\mathbf{u}_h$ denotes the horizontal component of it. T and S are the potential temperature and salinity. ρ is the in-situ density, ρ_0 is the reference density. p denotes the pressure and g the Earth's gravitational acceleration. $\mathbf{k}$ is the vertical unit vector perpendicular to the geopotential surface. The terms D^U, D^T, and D^S are parameterizations of small-scale features due to momentum, temperature, and salinity, respectively, while F^U, F^T, and F^S are surface forcing terms related to momentum, temperature, and salinity, respectively.

The ocean is confined by the coastline, the seafloor, and the sea surface. At these boundaries, exchanges of momentum, heat, and salt with other parts of the climate system occur. The parameters exchanged at these boundaries are either supplied by other model components (e.g., the sea ice model) or prescribed by forcing data sets at the respective boundaries (Madec et al., 2023):

Land-ocean interface: The most important exchang of properties at the land-ocean interface is freshwater imported into the ocean via river runoff and glacial meltwater. The freshwater from rivers and glaciers can strongly impact the local stratification and, thus, the circulation. These freshwater sources are incorporated in all model simulations discussed in this thesis.

Solid earth-ocean interface: Exchanges of heat and salt through the solid earth-ocean interface are small in the ocean and usually have only very local effects. They are neglected in all simulations discussed here. Thus, the bottom velocity is parallel to the ocean floor. Momentum exchange via friction at the sea floor is parameterized.

Atmosphere-ocean interface: The atmosphere-ocean interface is a relevant interface for driving the ocean circulation. The properties of the atmosphere invoke a vertical velocity at the ocean surface through changes in the SSH ζ, and the precipitation-evaporation budget $P-E$

$$w = \frac{\partial \zeta}{\partial t} + \mathbf{u}_h|_{z=\zeta} \cdot \nabla_h(\zeta) + P - E \tag{2.13}$$

Sea ice-ocean interface: Since the ocean is seasonally covered by sea ice in the high latitudes, another interface emerges between the ocean and the sea ice in these periods. When sea ice is present, the SST is set to the freezing point. The exchange of momentum, heat, and freshwater between the ocean and the sea ice is handled in the sea ice model (Bouillon et al., 2009).

This thesis discusses results from different model simulations based on the NEMO framework. In the following, the characteristics of the different simulations will be introduced.

2.3.1 VIKING20X

In order to investigate the representation of the AMOC in the North Atlantic, the VIKING20X model simulation (hereafter VIKING20X, Biastoch et al., 2021) is used (Chapter 4). VIKING20X features a high-resolution nest of the Atlantic Ocean (33.5°S to ~65°N) in a global $1/4°$ parent simulation (ORCA025, Barnier et al., 2006). Communication between the high-resolution and the low-resolution simulation is applied (two-way nesting). The simulation is evaluated on a curvilinear, tripolar Arakawa C-grid (Arakawa & Lamb, 1977). The tripolar grid design increases the resolution in the high latitudes, leading to a nominal resolution of $1/20°$ (Figure 2.2 c). The nest and the parent simulation have the same vertical axis consisting of 46 unevenly spread levels, ranging from 6 m at the surface to 250 m in the deep ocean.

The simulation discussed in this thesis is VIKING20X-JRA-OMIP (Biastoch et al., 2021), spanning 1958-2022. Following the Ocean Model Intercomparison Project (OMIP) protocol (Griffies et al., 2016), the model velocities are starting from a state of rest in 1958. Accordingly, the first years of the simulation are regarded as a spin-up period. Values before 1980 are not shown or discussed in this thesis because they are likely biased by the ocean approaching a quasi-stationary equilibrium (Arne Biastoch, personal communication). VIKING20X is forced from the atmospheric forcing data set JRA55-do (Tsujino et al., 2018). The forcing supplies atmospheric variables on a $1/2°$ grid with 3 hours temporal resolution. Additionally, the JRA55-do forcing includes river runoff and the runoff from ice sheets, representing the recent increase in the latter (Bamber et al., 2018). In order to reduce model biases related to the salt advection feedback from missing atmospheric feedbacks (Figure 1.3), SSS restoring is applied, restoring the SSS to climatological values, except where freshwater enters the ocean, like near river mouths or around Greenland.

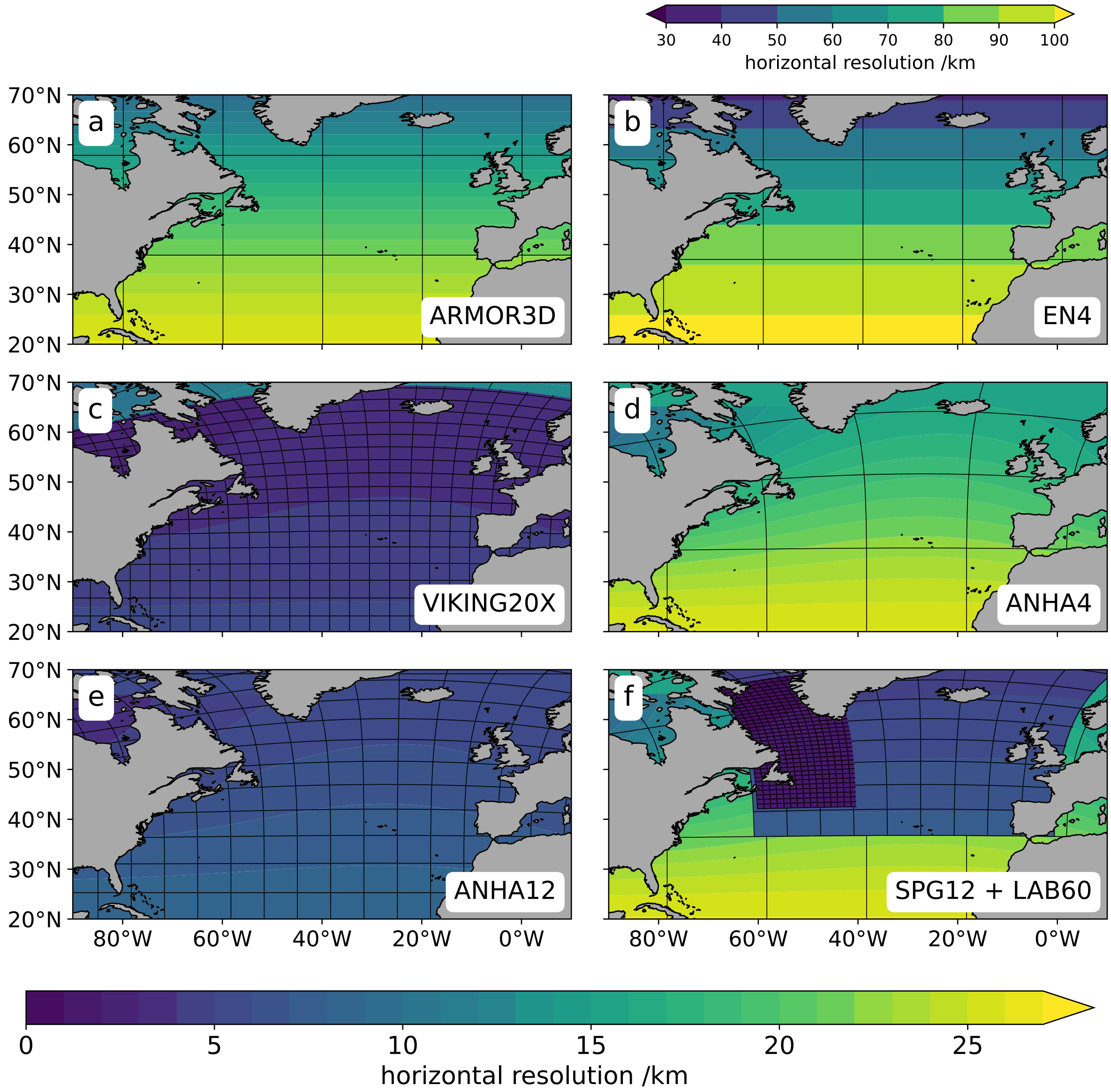

Figure 2.2: Horizontal resolution of the different data sets and model simulations used in this thesis. Note the different color scale for EN4 (b) due to the coarser resolution of this data set. The black lines denote every 80th grid line in each data set, except for EN4, where it denotes every 20th grid line.

2.3.2 ANHA

In addition to VIKING20X, a set of model simulations of the Arctic Northern Hemisphere Atlantic (ANHA) family is analyzed in this thesis to investigate the impact of ocean resolution in forced ocean models (Section 4.5). Three different simulations with varying nominal resolution, ranging from $^1/_4°$ (ANHA4, Figure 2.2 d), over $^1/_{12}°$ (ANHA12, both Hu et al., 2018, Figure 2.2 e) to a nested simulation with $^1/_{60}°$ resolution in the Labrador Sea (LAB60, Pennelly & Myers, 2020) are discussed.

Like VIKING20X, ANHA4 and ANHA12 (with $^1/_4°$ and $^1/_{12}°$ nominal resolution, respectively, Figure 2.2 d, e) represent subdomains of the global 1/4° ORCA025 simulation, covering most of the Atlantic (20°S to the north pole, including the whole Arctic Ocean and Canadian Archipelago). The vertical resolution is distributed over 50 depth levels, ranging from 6 m at the surface to 450 m in the deep ocean. Like in VIKING20X, the first years of the model simulation are not investigated due to possible effects associated with the model spin-up. This thesis discusses ANHA4 and ANHA12 in the period 2004-2018. They are forced from the Canadian Meteorological Centre Global Deterministic Prediction System reforecasts (CGRF) data set (Smith et al., 2014), providing hourly atmospheric parameters with 33 km horizontal resolution. Additionally, the simulation features river discharge (Dai et al., 2009) and freshwater runoff from Greenland (Bamber et al., 2012). In contrast to VIKING20X, no SSS restoring is applied in ANHA (Hu et al., 2018).

Additionally, a nested very-high-resolution simulation of the Labrador Sea (LAB60, Pennelly & Myers, 2022, 2020) with 1/60° nominal resolution is analyzed. In an ANHA4 configuration with 1/4° horizontal resolution, a nest with 1/12° resolution in the subpolar gyre region (SPG12) is implemented, spanning 36°N to 70°N (Müller et al., 2017). In the Labrador Sea and the adjacent North Atlantic, a second nest is implemented with 1/60° horizontal resolution (Figure 2.2 f), ranging from 42°N to 70°N and 70°W to 40°W, though not following a rectilinear grid. Two-way nesting is applied (Pennelly, 2021). All model domains share the same vertical grid with 75 depth levels, ranging from 1 m at the surface to 200 m in the deep ocean. In the period analyzed in this thesis, the model is forced by the DRAKKAR forcing set (DFS) (Dussin et al., 2016), supplying atmospheric data with 3-hourly (wind, temperature, and humidity) and daily (precipitation and radiation) temporal resolution while providing approximately 45 km spatial resolution in the Labrador Sea. The DFS provides data only until 2017. Therefore, after 2017, the forcing data set is switched to the ERA5 reanalysis (Hersbach et al., 2020).

2.4 Definition of the AMOC

The circulation in the Atlantic is a complex, three-dimensional field of ocean currents. Consequently, summarizing the evolution of this current system in one parameter, the AMOC requires an integrated view of the currents. For the overturning in the Atlantic, the meridional velocities v are relevant. Thus, the definition of the AMOC uses the zonally integrated meridional velocities. These zonally integrated velocities vary with depth. In order to quantify the volume transported northwards and detect the vertical level that separates the upper limb from the lower limb, the velocities are additionally integrated cumulatively over the vertical axis. The resulting quantity is called the overturning stream function (hereafter also referred to as the stream function, Figure 2.3) Ψ. Often, depth z is used as the vertical axis, resulting in a definition of the stream function as follows:

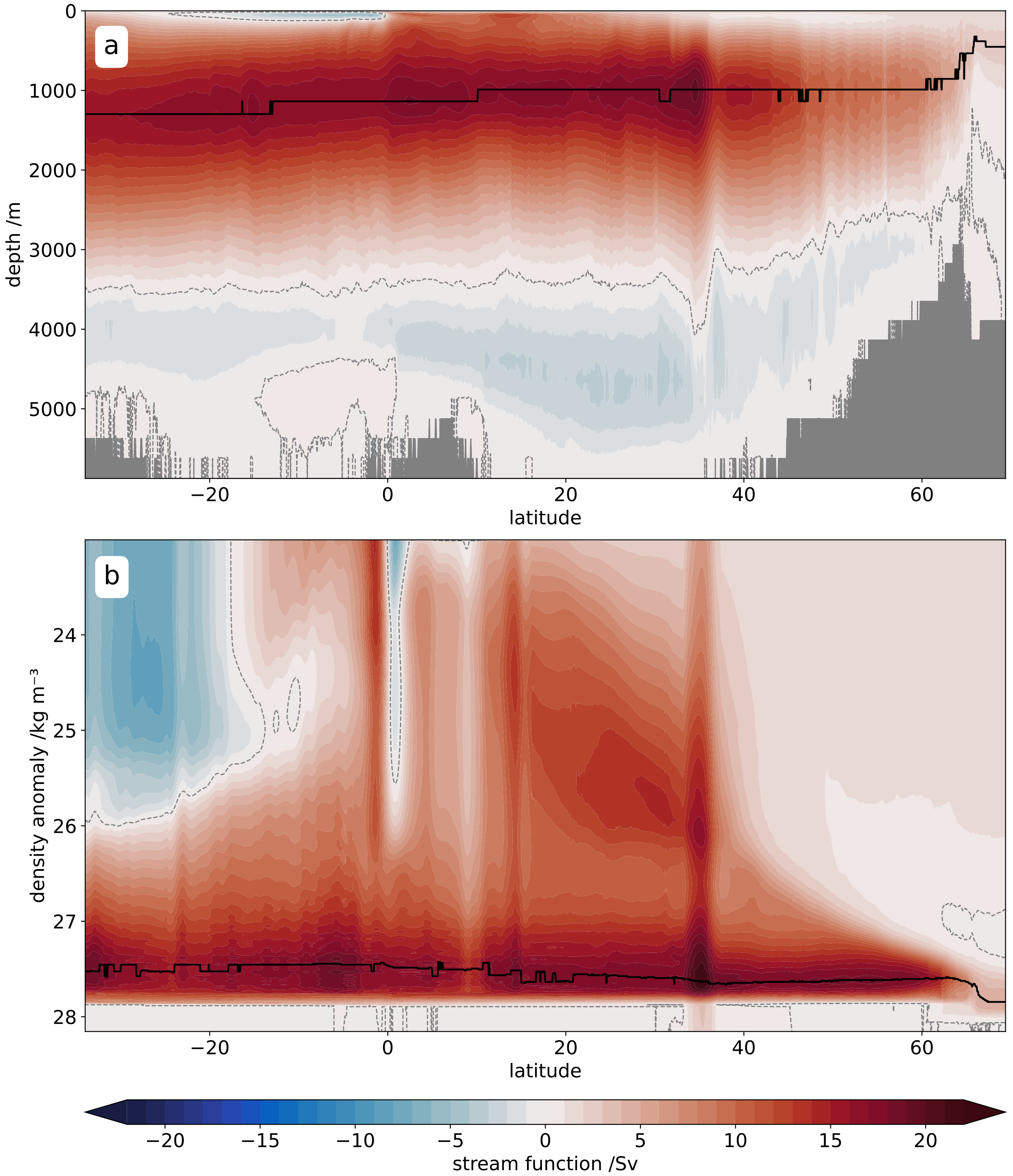

Figure 2.3: The Atlantic meridional overturning stream function over latitude in depth coordinates (a) and density coordinates (b) as simulated in VIKING20X (Section 2.3.1). The black solid line denotes the maximum of the overturning stream function over depth/density for each latitude. The dashed line denotes the zero contour.

$$\Psi(y, z) = \int_{x_W}^{x_E} \int_{z}^{\zeta} v \, dx \, dz. \tag{2.14}$$

Here, the meridional velocity v is integrated zonally from the western boundary x_W to the eastern boundary x_E and cumulatively from the sea surface ζ to the desired depth z. The AMOC at a given latitude y is defined as the maximum of the zonally and vertically integrated stream function Ψ.

However, the classical view of the AMOC as an upper limb flowing northward and a lower limb flowing southward does not hold in the subpolar North Atlantic due to inclined isopycnals. Therefore, in the subpolar North Atlantic, the potential density is chosen as the vertical axis for the calculation of the stream function:

$$\Psi(y, \sigma_\theta) = \int_{x_W}^{x_E} \int_{\sigma_{\theta,min}}^{\sigma_{\theta,max}} v \, dx \, d\sigma_\theta \tag{2.15}$$

While in the subtropical Atlantic, these definitions of the AMOC are identical (Moat et al., 2020; Wang et al., 2019), they more realistically depict the water mass transformation between density classes in the subpolar North Atlantic (Foukal & Chafik, 2022; Li et al., 2017). In Chapter 3, the AMOC at 47°N, calculated in density space (Section 2.4.1), is compared to the RAPID AMOC at 26°N (Moat et al., 2022), calculated in depth space. In the model simulations used in this thesis, the AMOC is calculated as in Equation 2.15. In none of the AMOC volume transport time series based on model simulations discussed in this work is the inflow through Bering Strait into the Arctic Ocean considered. Since in the observational estimates, a zero net throughflow through the respective section is assumed (Section 2.4.1), the AMOC at any given latitude in the Atlantic is overestimated in the models, compared to the observations by the amount of the Bering Strait inflow (1.0 Sv, Woodgate, 2018).

2.4.1 AMOC calculation at the NOAC moored array

Classically, the AMOC is defined via the stream function, integrated zonally and vertically over depth or density (Section 2.4). However, this method of defining the AMOC requires knowledge of the entire velocity field. Therefore, it is not applicable for a basin-wide mooring array with only a limited number of instruments, such as the NOAC array. Since the transport calculations of the NOAC array are based on geostrophy, only the transport between each pair of moored devices is known. Thus, the AMOC at the NOAC array at 47°N is viewed as the sum of different components. These components are the shelf regions, the Western Boundary Current (WBC), the NAC, the interior transport, and the EBC (Figure 2.4). Note that the term WBC is used here to describe the upper transports in the

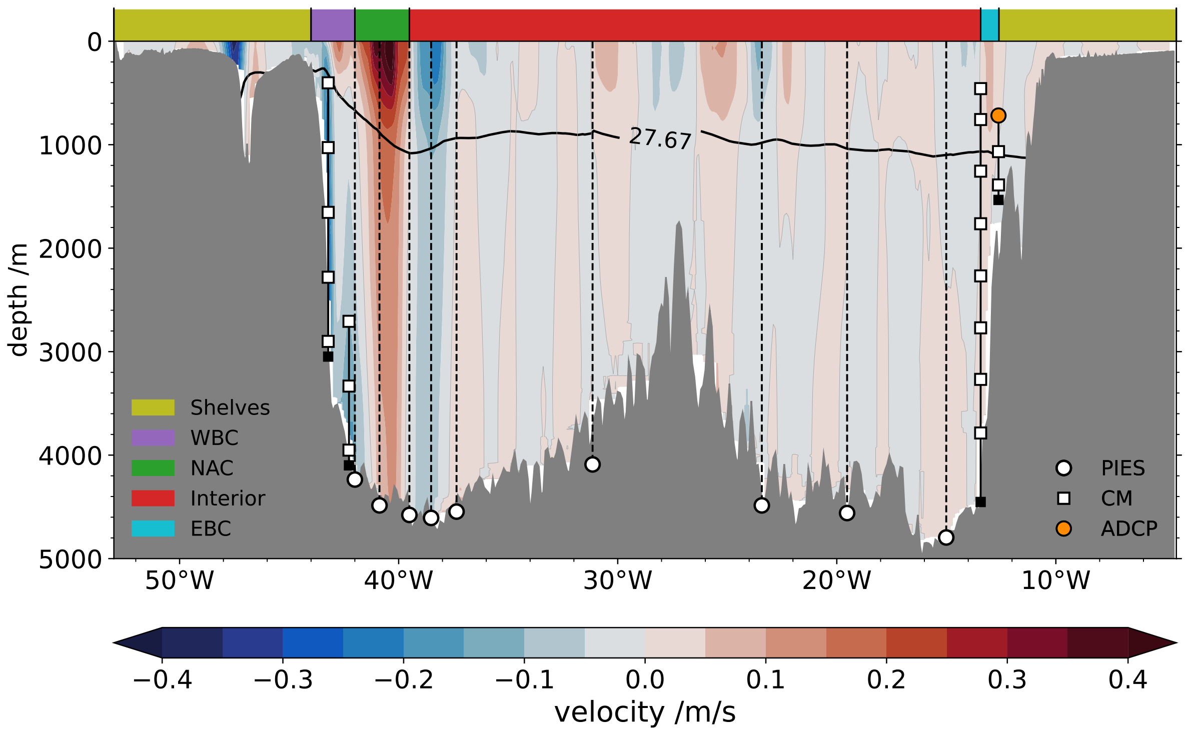

Figure 2.4: Mean geostrophic velocity along the NOAC array, based on CTD data and ARMOR3D (on the shelves), both 2003-2020. Markers indicate the positions of each PIES (white circles), single-point acoustic current meter (CM, white squares), and upward-looking Acoustic Doppler Current Profilers (ADCP, orange). The black line shows the mean depth of the $\sigma_\theta = 27.67\,kg\,m^{-3}$ isopycnal. Colors on top of the section indicate the geographical boundaries of the individual AMOC components (Figure 3.3). Topography is from ETOPO2v2 (NOAA, 2006)

DWBC region. The components are compiled from the transport measurements, described in Section 2.1.4. The interrelations of the individual components will be discussed in Section 3.4.

The NOAC AMOC in density space is calculated as the transport between the sea surface and the density of the maximum overturning stream function (Figure 2.4). This density is obtained from the mean of 16 lADCP and CTD sections as $\sigma_\theta = 27.67\,kg\,m^{-3}$ (all density values in this thesis are given as the density anomaly). It is similar to the density found by Li et al. (2021) for the full OSNAP array in 2014-2018 ($\sigma_\theta = 27.65\,kg\,m^{-3}$). At 47°N, the $\sigma_\theta = 27.67\,kg\,m^{-3}$ isopycnal lies at about 1100 m depth in the interior, rising to 300 m close to the Canadian continental slope (Figure 2.4).

A net-zero top-bottom transport is forced across the array by introducing a spatially uniform but temporally variable compensation velocity, calculated at monthly resolution and spread evenly across the whole basin, including the shelves. For comparison with the OSNAP and RAPID estimates, other mass exchanges, for example, the Bering Strait inflow into the Arctic Ocean (1.0 Sv, Woodgate, 2018) are not considered separately (Kanzow et al., 2010, 2009). This procedure yields a mean northward compensation transport of 3.3 Sv (standard error of the mean, SEM: 0.4 Sv). The basin-wide AMOC volume transport is calculated as the sum of the individual transport components of the NOAC array (Figure 2.4), the Ekman transport, and the compensation transport integrated from the surface to the density of $\sigma_\theta = 27.67\,kg\,m^{-3}$, respectively.

2.4.2 Assessing the NOAC AMOC calculation method using VIKING20X

The observational AMOC discussed in Chapter 3 is not defined via Equation 2.15, but via a modified approach as all transports above $\sigma_\theta < 27.67\,\mathrm{kg\,m^{-3}}$, which is the density of the maximum of the time-mean stream function obtained from multiple ship cruises along 47°N (Section 2.4.1). This approach, however, bears the risk of not representing a possible trend in the density of the maximum stream function. The number of basin-wide ship cruises is too low to allow for a time-dependent estimate of the stream function from the observations. However, VIKING20X offers the possibility of assessing the accuracy of the method against the classical approach via the time-varying stream function. Additionally, the model can be used to show the advantages of using the stream function in density coordinates in the subpolar North Atlantic over using the stream function in depth coordinates.

In VIKING20X at the NOAC line, the maximum stream function in depth coordinates lies at a mean depth of $1000\,m$ (Figure 2.5 a). However, this depth is not representative for the whole east-west extent of the basin since the isopycnals do not follow depth contours but are inclined. Thus, north of the subtropical gyre, the AMOC is best defined in density coordinates (Section 2.4). The maximum of the stream function in density coordinates lies at a density of $\sigma_\theta = 27.64\,\mathrm{kg\,m^{-3}}$ (Figure 4.1 a), which is similar to the value found from observations during ship cruises ($\sigma_\theta = 27.67\,\mathrm{kg\,m^{-3}}$). The depth of the maximum overturning stream function in depth space does not show a significant trend over the full period of VIKING20X (Figure 2.5 a). Similarly, the maximum of the stream function in density space does not show a significant trend over the NOAC observational period (Figure 2.5 b).

Figure 2.6 shows the AMOC calculated in VIKING20X as the maximum of the stream function in depth coordinates (cyan), as the maximum of the stream function in density coordinates (blue) and analogous to the calculation based on data from the NOAC array as all transports at densities $\sigma_\theta < 27.67\,kg\,m^{-3}$ (pink). There is very close agreement between the AMOC calculated in density coordinates as the maximum of the stream function and the AMOC calculated in density coordinates considering the transports at densities $\sigma_\theta < 27.67\,\mathrm{kg\,m^{-3}}$. The correlation of the time series is 0.98, both for the

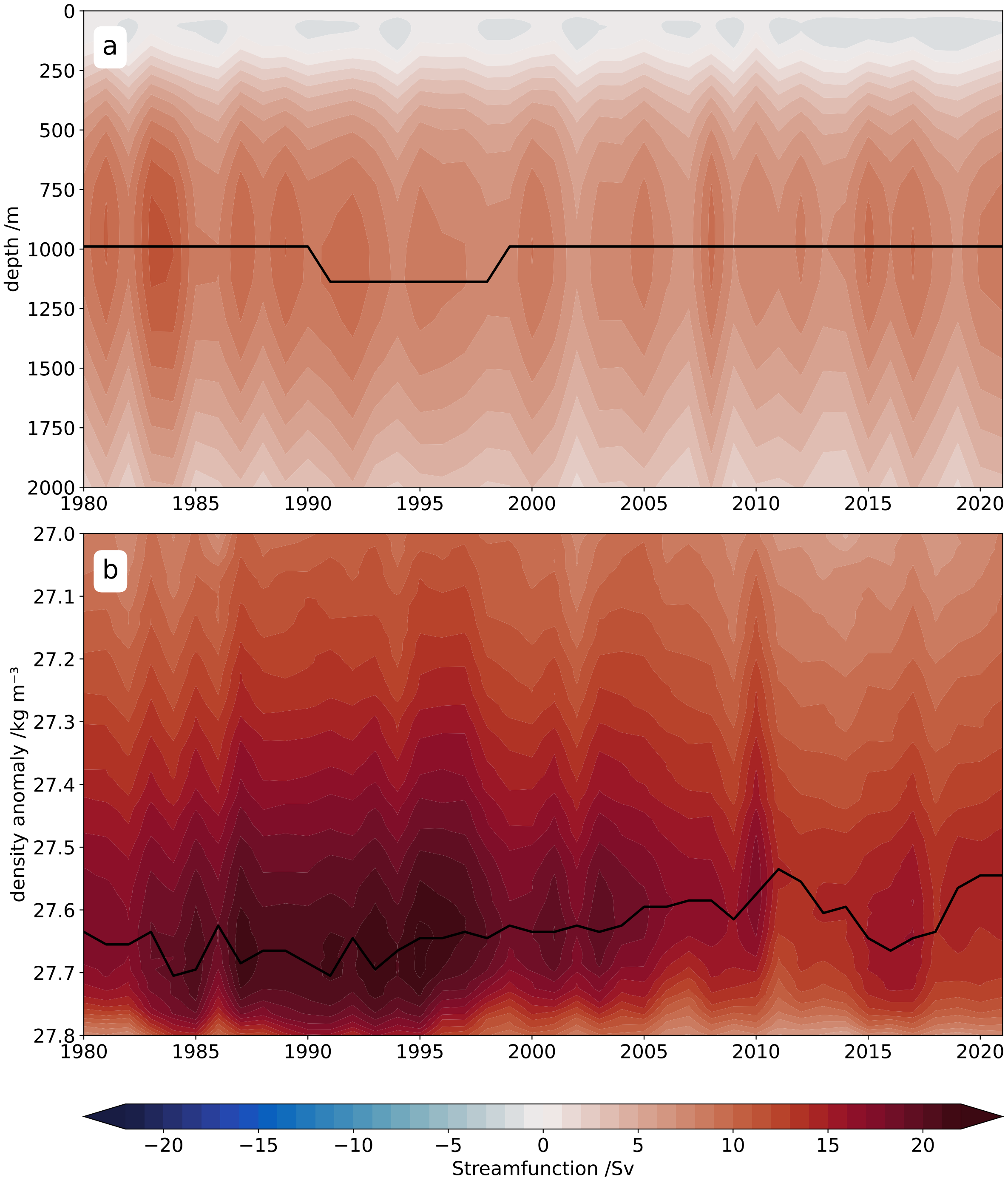

Figure 2.5: Annual averages of the Atlantic meridional overturning stream function at the NOAC line in depth coordinates (a) and density coordinates (b) as simulated in VIKING20X (Section 2.3.1). The black line denotes the maximum of the overturning stream function over depth/density.

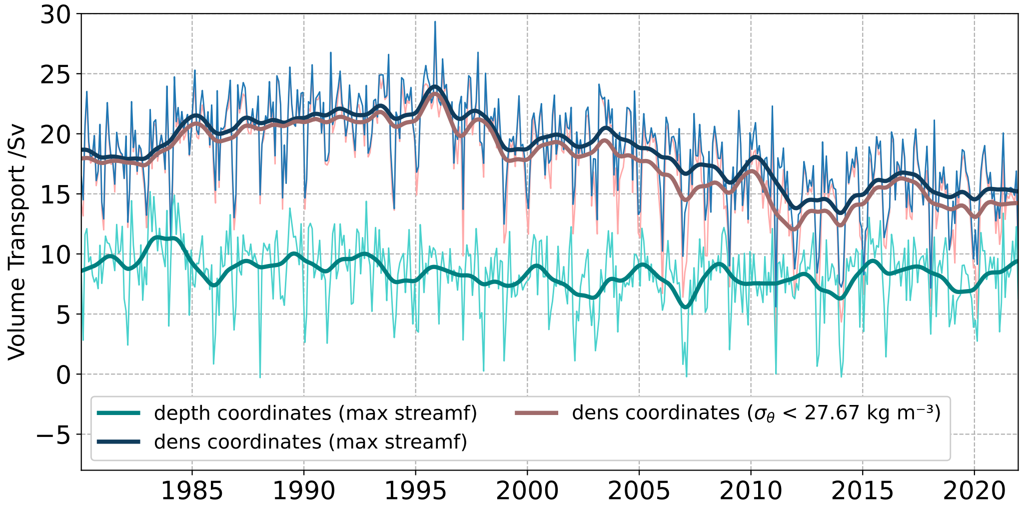

Figure 2.6: The AMOC in VIKING20X, calculated as the maximum of the overturning stream function in depth coordinates (cyan), as the maximum of the overturning stream function in density coordinates (blue), and analogous to the calculation from the NOAC data as all transports at densities $\sigma_\theta < 27.67\,kg\,m^{-3}$ (pink). The dark lines denote the low-pass filtered time series.

monthly values and for the low-pass filtered time series. Differences between the two time series appear stronger during strong AMOC trends (e.g. 1995-2010). The difference in the mean AMOC strength is 0.9 Sv, which is about 5% of the total AMOC value and can be explained by the difference in the density of the maximum stream function.

Most shipboard observations for the calculation of the maximum stream function were obtained in spring and summer, possibly introducing a seasonal bias. An analysis of the VIKING20X model simulation exhibits a significant seasonal cycle of the density of the maximum stream function with a maximum in summer and an amplitude of $0.09\,\mathrm{kg\,m^{-3}}$ (not shown), indicating a possible underestimation of the observed AMOC. The number of basin-wide observational transects is too low to allow for a time-dependent estimate. However, the effect would be small: a considerable density difference of, for example, $\Delta\sigma_\theta = 0.05\,kg\,m^{-3}$ would result in an AMOC difference of less than 2%, which is small, compared to other transport uncertainties (Section 3.6).

This analysis shows that using the density of the maximum of the mean stream function at 47°N in the North Atlantic as the lower limit for the transports contributing to the observational AMOC estimate of the NOAC array is a valid method of calculating the AMOC based on observations. The comparison with the AMOC calculated via the classical approach as the maximum of the time-varying stream function in VIKING20X shows a strong agreement with the method applied in the observations. The depth and the density of the maximum of the time-varying overturning stream function show no significant trend over the observational period. This analysis cannot fully exclude that, in reality, there is a drift in the density of the maximum stream function at 47°N that VIKING20X does not show. However, these results from a realistically forced ocean hindcast simulation provide a solid argument that this method of calculating the AMOC is valid.

2.5 Meridional heat transport (MHT) calculation

The MHT is the critical parameter determining the impacts of the AMOC on the climate. The geostrophic transport between two observational stations can be calculated using geostrophy. However, the MHT depends on the temperature and cannot be calculated analogously from observations (Section 4.4). In this thesis, the MHT is calculated based on VIKING20X and ARMOR3D, respectively, where the temperature at every gridpoint in space and time is given. The MHT Q is defined analogous to the AMOC volume transport (Equation 2.14) as the zonally and vertically integrated product of the meridional velocity v and the temperature T as

$$Q = \rho_0 \, c_p \int_{x_W}^{x_E} \int_{z}^{\zeta} v \, T \, dx \, dz, \tag{2.16}$$

where ρ_0 is the density of seawater and c_p is the specific heat of seawater.

2.6 Statistics

In this thesis, AMOC volume transports are generally presented at monthly resolution (Figure 3.2, Figure 4.2, Figure 4.14) and low-pass filtered with the commonly used Butterworth filter (2^{nd} order with a two-year cutoff period, hereafter simply low-pass filter). Rhein et al. (2019b) and Nowitzki et al. (2021) showed that the decorrelation timescales of the individual AMOC components at 47°N are around two months for the western and eastern transport components. Therefore, the Pearson correlation coefficients are calculated from unfiltered and low-pass filtered time series of two-month averages throughout this thesis. All correlations are tested for statistical significance at the 95%-level following Ebisuzaki (1997) (with 1000 surrogates) and previously applied by McCarthy et al. (2015a) and Diabaté et al. (2021). All time series are detrended prior to calculating correlations.

2.6.1 Correlation and coherence analysis

In order to compute the statistical significance of the correlation between two time series A and B, a non-parametric method proposed by Ebisuzaki (1997) is used. McCarthy et al.

(2015a) and Diabaté et al. (2021) previously used this method to estimate the statistical significance for correlations of serially correlated low-pass filtered time series.

This method evaluates the Fourier transform of the time series A and generates a large number (1000 in this case) of resampled time series with random phase while retaining the power spectrum. Thus, the resampled time series has similar spectral properties as the original time series. Subsequently, the Pearson correlation coefficient of the 1000 resamples of time series A with time series B is calculated. The significance level is then given by the percentage of the correlations of the resampled time series, which are lower than the correlation between the original time series A and B. Thus, in this approach using the 95% significance level, all correlations are significant, where this is the case for less than 5% of the resampled correlations.

The method described above is applied also to estimates of lag correlations. The Nyquist-Shannon sampling theorem states that the highest resolvable frequency of a time series is $0.5/dt$, where dt is the time step of the time series (Shannon, 1949). Accordingly, since low-pass filtered time series with a cutoff period of 2 years are presented, lag correlation coefficients are meaningful only every 12 months for the low-pass filtered time series. Lagged correlation coefficients of low-pass filtered time series are plotted as enlarged markers in Figure 3.4 and Figure 4.10. For the unfiltered time series, lag correlation coefficients are presented every two months.

In addition to calculating the lag correlation between the NOAC and RAPID AMOC volume transport time series, a multitaper coherence analysis is performed in Section 3.7 to calculate the cross-spectra and the squared coherence. This method provides a measure of the coherence of the two time series across different frequencies. Here, a multitaper method implemented in the jlab toolbox (Lilly & Elipot, 2021) is used to calculate the cross-spectral densities. Based on these, following Emery & Thomson (1998), the squared coherence $\gamma_{12}^2(f)$ is calculated as

$$\gamma_{12}^2(f) = \frac{|G_{12}(f)|^2}{G_{11}(f) \cdot G_{22}(f)} \tag{2.17}$$

and

$$\gamma_{12}(f) = |\gamma_{12}^2(f)|^{1/2} \cdot e^{-i\phi_{12}(f)} \tag{2.18}$$

where $G_{12}(f)$ is the cross-spectral density of the NOAC and RAPID AMOC time series, while $G_{11}(f)$ and $G_{22}(f)$, respectively, are the auto-spectral densities of the NOAC and RAPID AMOC time series. $\phi_{12}(f)$ denotes the phase lag between the two signals.

"We realized as never before how important it is to make repeated observations in the same spot, preferably throughout the year, if we want a complete picture of conditions in the sea."

J. Harland Paul, *ship's surgeon, in "The Last Cruise of the Carnegie" (1932)*

Chapter 3

The AMOC at 47°N from observations of the NOAC moored array

Due to the substantial logistical and financial efforts necessary to deploy and maintain an observational mooring array, direct observational estimates of the AMOC are rare. The most prominent arrays are the RAPID array at 26°N in the subtropical North Atlantic and the OSNAP array between 52°N and 60°N in the subpolar North Atlantic (see Section 1.4 for an overview of the AMOC monitoring arrays in the North Atlantic or Frajka-Williams et al., 2019). At 47°N, the boundary between the subtropical and the subpolar North Atlantic, the NOAC array was established as a result of cooperation between the University of Bremen and the BSH to monitor exchanges between the two regimes.

In this chapter, the individual NOAC AMOC components are combined to calculate the basin-wide observational AMOC volume transport at the NOAC array at 47°N. The transport time series are extended in time using satellite altimetry, yielding a 25-year AMOC time series from 1993-2018[1]. Measurement gaps are closed using the observation-based ARMOR3D data set. The NOAC AMOC mean state and trend are discussed in Section 3.1 and compared to other AMOC estimates in the North Atlantic. Section 3.2 and Section 3.3 discuss the seasonal cycle and the inter-annual variability of the NOAC AMOC. Section 3.4 investigates the interrelations between the individual NOAC AMOC components. The role of atmospheric drivers of AMOC variability is investigated in Section 3.5, while Section 3.6 provides an uncertainty estimate of the mean NOAC AMOC

---

[1] Rounding to an integer number of years, the time series is 25 years long. However, the first data is from 1993, and the last is from 2018. Thus, it is referred to as a 25-year time series from 1993-2018.

Table 3.1: Mean, SEM, and standard deviation (STD) of the NOAC AMOC at 47°N and the RAPID AMOC at 26°N in their respective full period and the measuring periods of the RAPID and OSNAP arrays. Note that for the RAPID values, the OSNAP period is 2014-2020, due to the longer RAPID time series, compared to the OSNAP time series.

	full period 1993-2018	RAPID period 2004-2018	OSNAP period 2014-2018 (2020)
NOAC mean	**17.2 Sv**, SEM: 0.4 Sv	**17.5 Sv**, SEM: 0.6 Sv	**18.4 Sv**, SEM: 1.3 Sv
NOAC STD	**5.2 Sv**	**5.5 Sv**	**6.4 Sv**
RAPID mean	**16.9 Sv**, SEM: 0.4 Sv	**16.9 Sv**, SEM: 0.4 Sv	**16.7 Sv**, SEM: 0.5 Sv
RAPID STD	**3.4 Sv**	**3.4 Sv**	**2.7 Sv**

transport. Finally, in Section 3.7, the meridional coherence of the NOAC AMOC with the RAPID AMOC at 26°N (Moat et al., 2022) is investigated. This chapter has been modified after a publication in the peer reviewed journal Geophysical Research Letters (Wett et al., 2023a). The basin-wide AMOC volume transport time series at 47°N is published as Wett et al. (2023b).

3.1 AMOC mean strength and variability at 47°N

The mean strength of the NOAC AMOC (1993-2018: 17.2, SEM: 0.4 Sv, 2004-2018: 17.5, SEM: 0.6 Sv) is close to that of the RAPID AMOC (2004-2018: 16.9, SEM: 0.4 Sv) and of other estimates from the subpolar region (OVIDE section (1997-2010: 18.1 Sv, Mercier et al., 2015), OSNAP array (2014-2018: 16.6 Sv, Li et al., 2021)). The mean NOAC AMOC strength in the OSNAP period (18.4 Sv, Table 3.1) is slightly larger compared to the full period but within the estimated uncertainty (Section 3.6). The mean AMOC transports of the NOAC, RAPID, and OSNAP arrays are not significantly different within their uncertainties. Other calculations based on altimetry and Argo data (41°N, 1993-2009: 15.5 Sv, Willis, 2010) and gridded data sets (45°N, 1993-2015: 14.3 Sv, Desbruyères et al., 2019, 1993-2017: 13.9 Sv, SEM: 0.4 Sv, with added Ekman transport, Section 3.8.2) yield 10-15% smaller mean AMOC volume transports, possibly due to methodological differences.

Previous studies found no significant long-term trend in subtropical AMOC estimates after 1981 (Worthington et al., 2021, based on an empirical model). The NOAC AMOC shows a non-significant linear trend of 0.03 $\mathrm{Sv\,yr^{-1}}$ over the study period (SEM: 0.04 Sv, representing a minimum uncertainty without accounting for auto-correlation). However, Rhein et al. (2019b) concluded that decadal trends in the individual AMOC components smaller than 10% cannot be resolved due to a possible change in the regression between

SSH and transports. The overall variability of the monthly NOAC AMOC (STD: 5.2 Sv) is 50% higher than that of the RAPID AMOC (STD: 3.5 Sv) and lower than the OSNAP AMOC variability (7.6 Sv, Baker et al., 2022). The different regional settings probably cause the different STDs at the NOAC and RAPID arrays. Stronger NAC variability at the NOAC array compared to the Florida Current at the RAPID array (Piecuch, 2020) explains a larger NOAC AMOC variability on seasonal time scales. The STDs of the low-pass filtered time series (NOAC: 1.7 Sv, RAPID: 1.5 Sv, both 2004-2018) are similar.

The mean NOAC compensation transport (3.3 Sv, SEM: 0.4 Sv, Section 2.4.1) lies within the range of values for the compensation transport for other observational AMOC estimates from -2.9 ± 1.8 Sv at the OSNAP array (Fu & Li, 2023) to approximately 10 Sv at the RAPID array (Danabasoglu et al., 2021). The NOAC AMOC estimate utilizes ARMOR3D (Section 2.2.1) to bridge gaps where geostrophic transports cannot be calculated from NOAC instruments, inducing further uncertainties. ARMOR3D only provides climatological values below 1500 m. Thus any inter-annual variability in the deep ocean is neglected. However, ARMOR3D is used only for the shelves (which are shallower than 1500 m) and a 180 km strip in the eastern basin. Thus, any uncertainty induced by using climatological ARMOR3D data is expected to be small compared to other uncertainties.

3.2 The seasonal cycle of the AMOC at 47°N

The AMOC volume transport at 47°N exhibits a significant seasonal cycle with a range of 6.0 Sv at monthly resolution (Figure 3.1 a), which is 35% of the AMOC's mean volume transport. However, the contribution of the seasonal cycle to the AMOC's total variability is small. Removing the seasonal cycle slightly reduces the STD, from 5.2 Sv to 4.8 Sv, a decrease of 8%. The strongest AMOC volume transports appear from August to November, the weakest in January. This agrees with other observations of the seasonal cycle in the subpolar North Atlantic at the OSNAP array (Fu et al., 2023), finding a minimum AMOC volume transport in winter (November-January). The shape of the seasonal cycle does not depend on whether it is calculated over the whole period, the RAPID measuring period, or the OSNAP measuring period (Figure 3.1 a). At shorter periods, larger uncertainties render the seasonal cycle insignificant.

The seasonal cycle at the RAPID array exhibits a different shape, with a maximum in December and a minimum in May. At the RAPID array, the contribution of the seasonal cycle to the total AMOC variability is larger than at the NOAC array. For RAPID, the STD of the full time series (3.5 Sv) is 20% larger than without the seasonal cycle (2.8 Sv).

Of the individual AMOC components at 47°N (Figure 3.1 b), only the NAC, shelves transport, and the Ekman transport show a significant seasonal cycle. Almost all individual AMOC components display a minimum in winter. Only the NAC shows an inverse

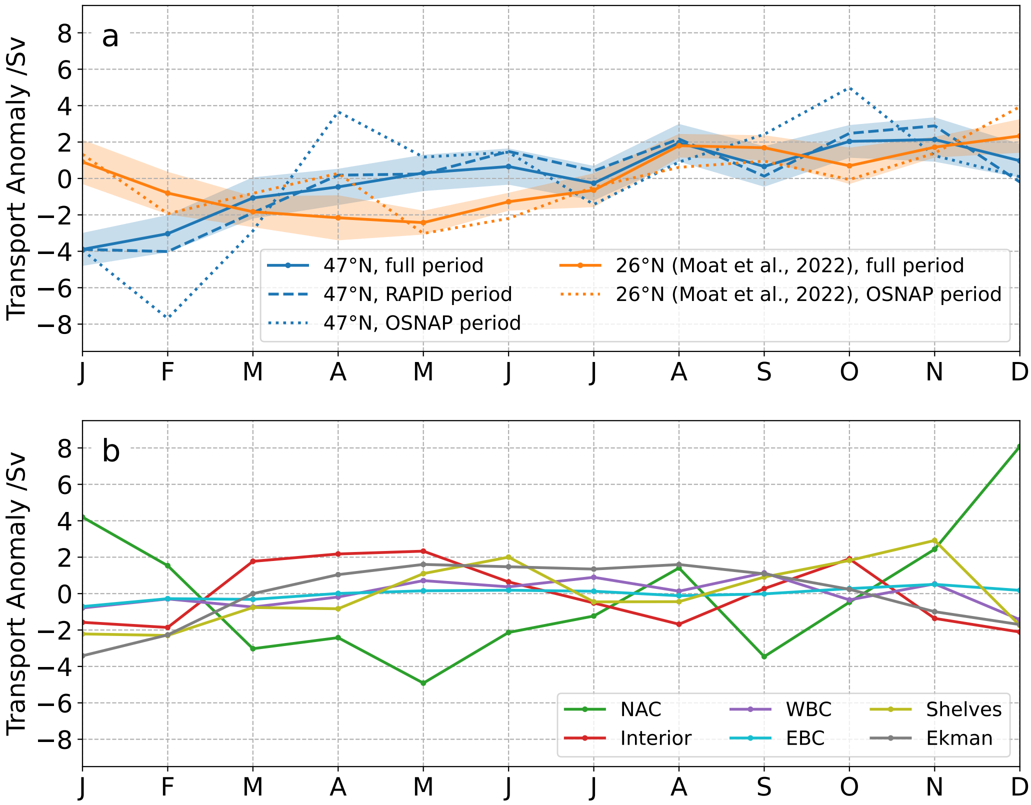

Figure 3.1: a) Seasonal cycle of the basin-wide AMOC volume transport anomaly at the NOAC array at 47°N and the RAPID array at 26°N (Moat et al., 2022). Displayed values are calculated as the mean transport for each month of the year in their respective full periods (NOAC: 1993-2018, RAPID: 2004-2018). Additionally, the seasonal cycle of the NOAC AMOC in the RAPID measuring period (2004-2018) and the seasonal cycles of both the NOAC and RAPID AMOC in the OSNAP measuring period (2014-2018) are displayed. The shaded area denotes the SEM for each month (for the full period of NOAC and RAPID). b) Annual cycle of the transport anomalies of the individual AMOC components at 47°N (1993-2018), calculated as in a). Only the NAC and shelves transport and the Ekman transport show a significant seasonal cycle, indicated by the SEM of each month (not shown).

behavior, with a maximum in December and a minimum in March, possibly related to the wind stress forcing, which exhibits a maximum in winter (not shown) and potentially influences the strength and position of the NAC via geostrophic adjustment. The wind-driven Ekman transport is in the opposite phase because it is strongest southward when the westerly winds are strongest.

Table 3.2: Comparison of different low-pass filters applied to the AMOC time series at 47°N and their effects on the (lag) correlation with the RAPID AMOC at 26°N Moat et al. (2022). Significant correlations at the 95%-level are marked in bold. Note that, due to the Nyquist-Shannon theorem, the corresponding lag can only be multiples of 12 months for the low-pass filtered time series.

Filtering method	Correlation	Lag corr. max.	corresponding lag
unfiltered two-month averages	0.14	**0.35**	12 months
1-year moving average (boxcar window)	0.45	**0.70**	12 months
2-year moving average (boxcar window)	0.71	**0.83**	12 months
2-year moving average (Hann window)	0.53	**0.74**	12 months
2nd order Butterworth filter (2-year cutoff period)	0.57	**0.72**	12 months

3.3 Inter-annual variability of the NOAC and RAPID AMOC

The 1990s and the preceding decades were characterized by increasing dense water formation in the subpolar North Atlantic (Rhein et al., 2017; Kieke & Yashayaev, 2015; Lazier et al., 2002), influencing the low-frequency variability of the AMOC (Danabasoglu et al., 2016). Accordingly, the AMOC volume transport of the NOAC array starts at relatively high values in 1993. Consistent with previous model studies (e.g., Yeager & Danabasoglu, 2014; Biastoch et al., 2008a) and observational estimates (e.g., Jackson et al., 2019; Mercier et al., 2015), a decreasing NOAC AMOC is found in the 1990s from 19 Sv in 1994 to 15 Sv in 2000, with the strongest decline between 1996 and 1998 (Figure 3.2 a and c, low-pass filtered). This decline ceases after 2002, when the NOAC AMOC increases, reaching the maximum of more than 20 Sv in late 2005. This maximum results from a strong NAC, not compensated by an average interior transport (Figure 3.3, Section 3.4). Following the 2005 maximum, the NOAC AMOC decreases with a minimum of less than 15 Sv reached in 2009. It strengthens afterward until 2018. Comparable multi-annual features are also observed in the RAPID AMOC: A maximum around 2005/2006 followed by a decline until about 2010, and a strengthening until 2018 (Moat et al., 2020).

Though the unfiltered and low-pass filtered NOAC and RAPID AMOC time series are not significantly correlated at zero lag, the correlation becomes statistically significant

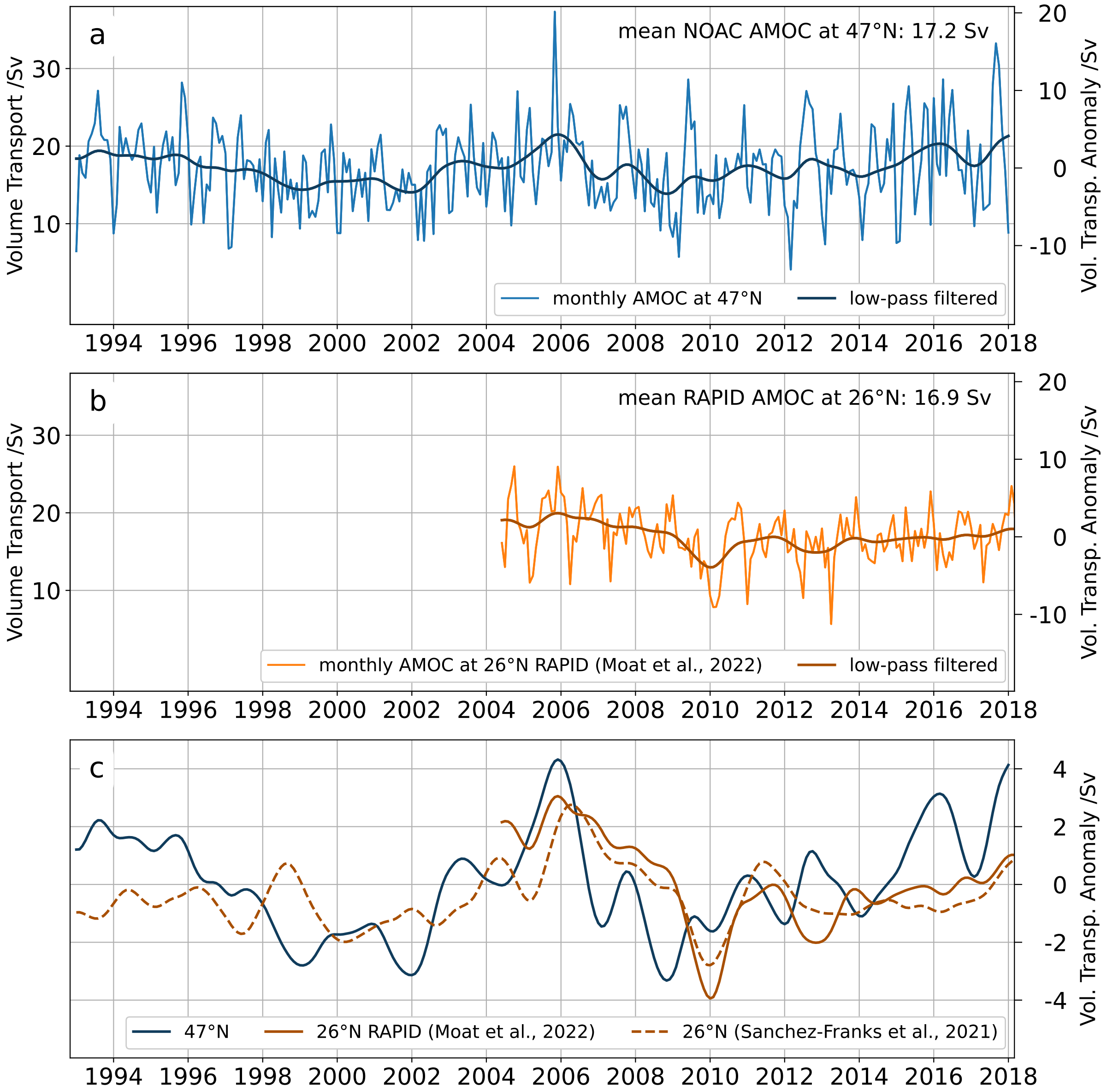

Figure 3.2: Monthly AMOC volume transport time series at the NOAC array at 47°N (a) and the RAPID array at 26°N (b) for the absolute transport (left y-axis) and the transport anomaly (with respect to each full-period mean, right y-axis). The dark lines represent the low-pass filtered AMOC. (c) Comparison of the low-pass filtered time series at NOAC (blue) and RAPID (brown). The dashed brown line shows the altimetry-based AMOC estimate at 26°N from Sanchez-Franks et al. (2021) with the same low-pass filter applied. Note that Sanchez-Franks et al. (2021) use a different low-pass filter in their Fig. 11.

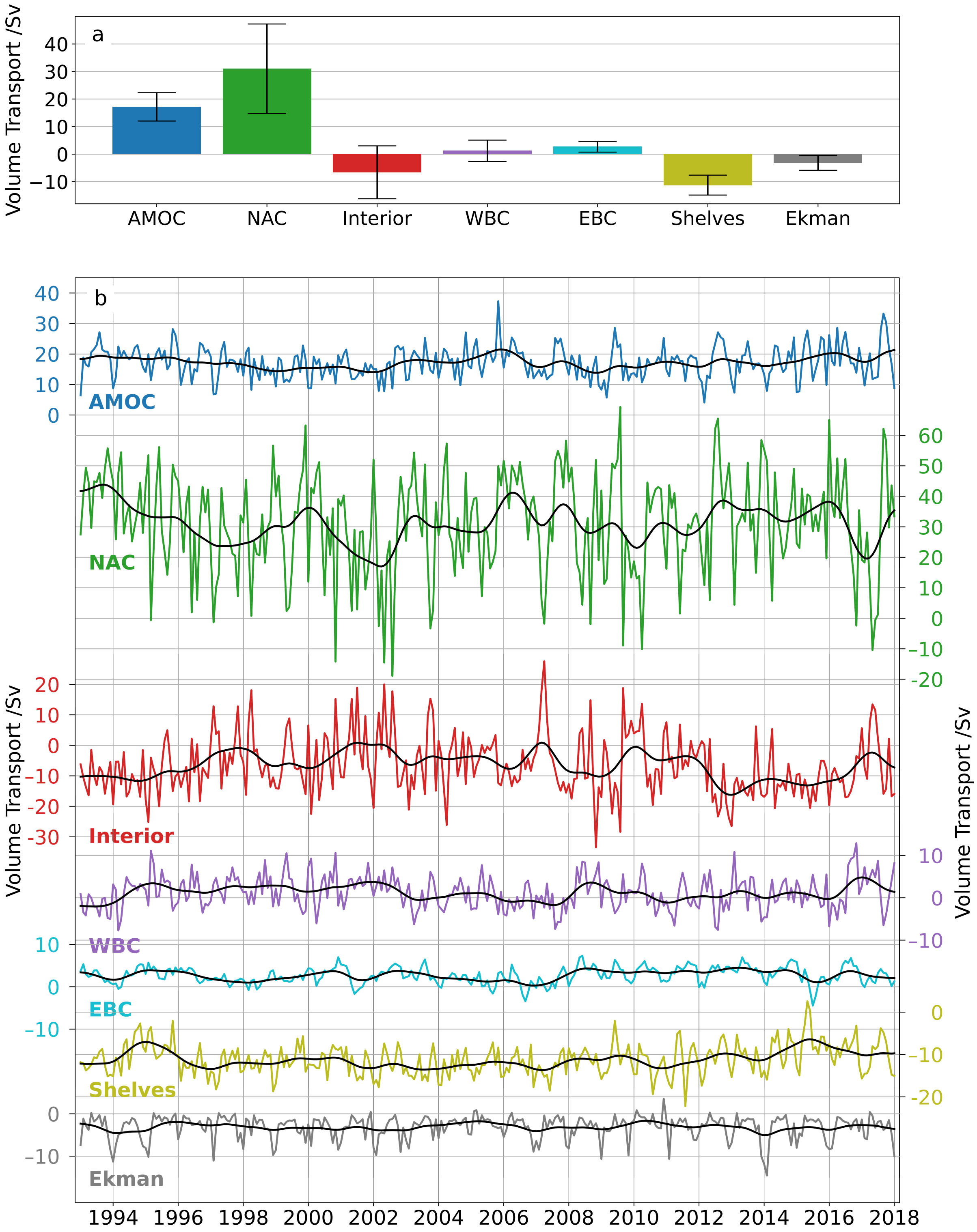

Figure 3.3: a) Mean and STD of the AMOC and each component of the basin-wide AMOC volume transport at 47°N. b) Monthly time series of the individual AMOC components at 47°N. The black lines represent the low-pass filtered time series. All curves are shifted gradually and correspond to their respective y-axis scale. Note the different scales for the WBC, EBC, Shelves, and Ekman components.

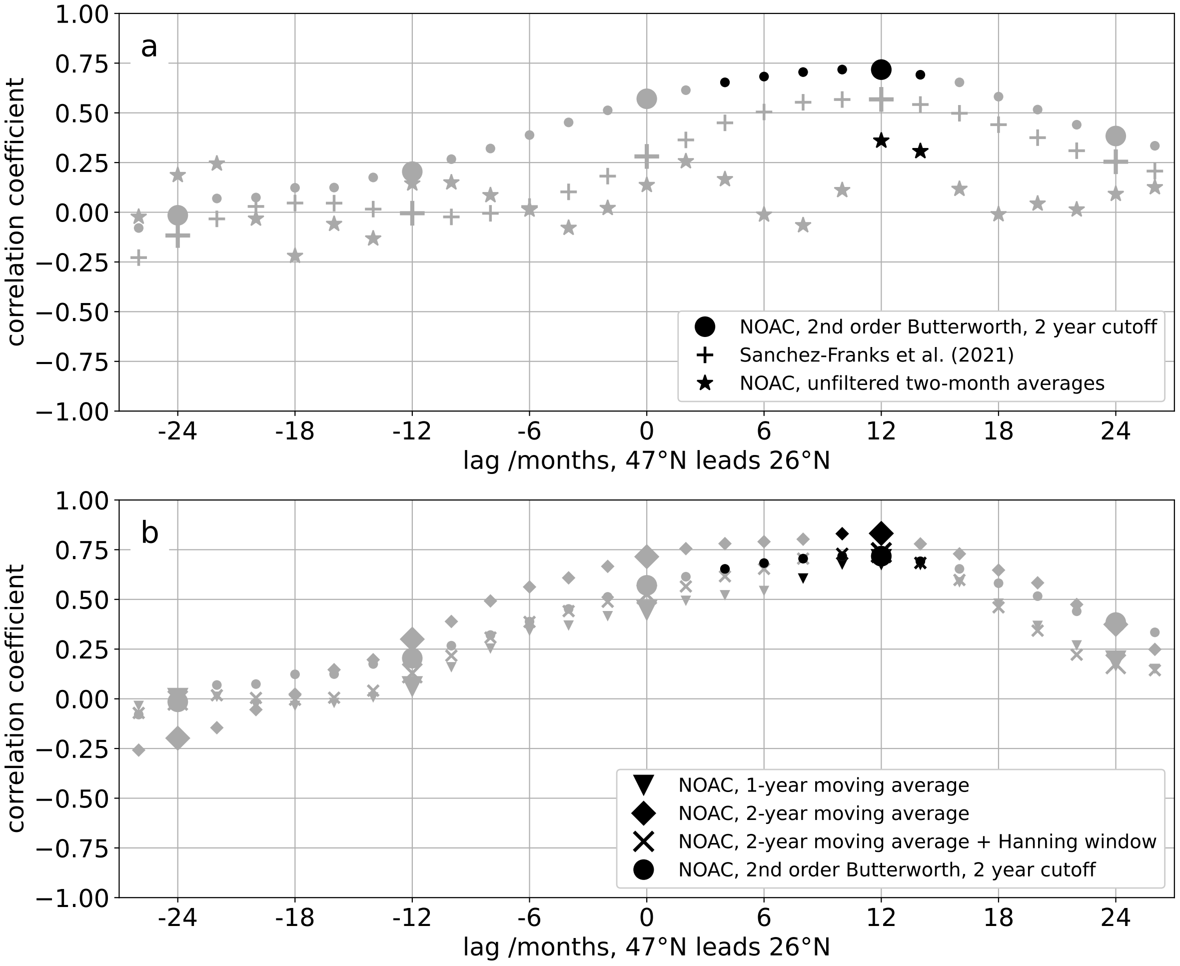

Figure 3.4: Lagged correlation coefficients between the low-pass filtered NOAC AMOC at 47°N and estimates of the AMOC at 26°N by Moat et al. (2022) and Sanchez-Franks et al. (2021) (a). Comparison of lagged correlation coefficients between the low-pass filtered AMOC at 47°N and the RAPID AMOC at 26°N Moat et al. (2022), using different filtering techniques (b). The 47°N AMOC leads. Significant correlations are plotted in black. For the low-pass filtered time series, values whose interpretation is valid according to the Nyquist-Shannon theorem (Section 2.6.1) are plotted as enlarged markers.

($r = 0.70 - 0.83$, depending on the filtering method) when the NOAC AMOC leads by about one year (Figure 3.4, Table 3.2). This significant correlation also holds for the unfiltered time series of two-month averages. A significant correlation larger than $r = 0.30$ is found when the NOAC AMOC leads by 12-14 months (Figure 3.4 a), persisting when the seasonal signal is removed from both time series ($r = 0.35$, 12 months lag, not shown). While the values of the correlation coefficients differ slightly, the statistical significance does not depend on the choice of the low-pass filter (Table 3.2).

Sanchez-Franks et al. (2021) extended the RAPID AMOC time series using satellite altimetry. Consistent with the NOAC AMOC, their time series exhibits an increase in 2000-2005, though their AMOC estimate shows no decline in the 1990s (Figure 3.2 c). The NOAC AMOC time series is compared to this estimate, and no significant correlation

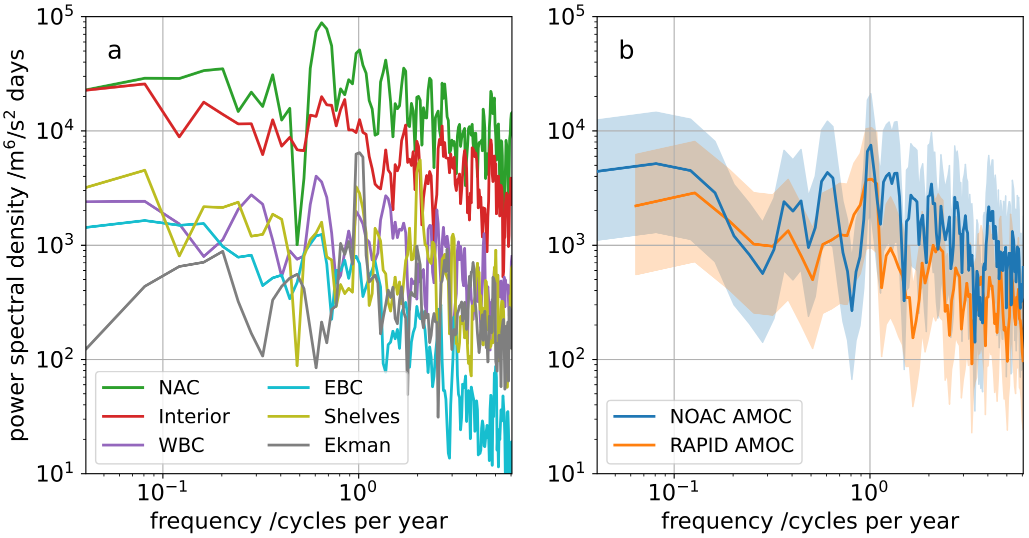

Figure 3.5: Multitaper spectral estimates for the individual AMOC components at 47°N (for the sake of clarity, uncertainty estimates are not shown) (a) and the NOAC and RAPID AMOC, including 95% uncertainty estimates (b) (time-bandwidth product P=2 for a and b). The calculation is based on code by Lilly (2022).

is found at any lag (Figure 3.4 a). At the 90% significance level, however, the correlation at about one year lag is significant. The absence of a significant correlation possibly originates from the low correlation before the RAPID measuring period. While different altimetry-based estimates of the 26°N AMOC correlate well with the RAPID measurements (Sanchez-Franks et al., 2021; Frajka-Williams, 2015), they show little agreement among themselves before, possibly due to overfitting during the RAPID array measuring period (Sanchez-Franks et al., 2021). For the RAPID measuring period (2004-2018), a significant lag correlation is found between the NOAC AMOC and the estimate by Sanchez-Franks et al. (2021) when the 47°N AMOC leads by about one year ($r = 0.68$).

3.4 Main AMOC components

At the RAPID array, the mid-ocean transport dominates the low-frequency (>1 year) variability of the AMOC (Moat et al., 2020). For the NOAC AMOC, the NAC and the interior transport dominate the variability on all timescales (Figure 3.3, Figure 3.5 a). Of all components, the NAC (mean: 31 Sv, SEM: 1.3 Sv) exhibits the strongest correlation with the basin-wide NOAC AMOC ($r = 0.61$, Table 3.3). In the subtropical North Atlantic, on seasonal timescales, the transport through Florida Strait and the upper mid-ocean transport compensate each other (Frajka-Williams et al., 2016; Kanzow et al., 2007). Consistent with Rhein et al. (2019b) and Mertens et al. (2014), a similar relationship is found at 47°N between the corresponding components of the NAC and the interior

Table 3.3: Correlation of two-month averages and low-pass filtered time series of individual components with the basin-wide NOAC AMOC and each other. Significant correlations are marked in bold.

2-month averages	AMOC	NAC	Interior	WBC	EBC	Shelves	Ekman
AMOC	×						
NAC	**0.61**	×					
Interior	**-0.41**	**-0.81**	×				
WBC	**-0.55**	**-0.74**	**0.30**	×			
EBC	0.19	0.05	**-0.24**	0.11	×		
Shelves	**0.47**	0.08	-0.22	0.10	**0.28**	×	
Ekman	**0.32**	-0.22	0.17	0.15	0.08	0.19	×
low-pass filtered	AMOC	NAC	Interior	WBC	EBC	Shelves	Ekman
AMOC	×						
NAC	**0.56**	×					
Interior	-0.38	**-0.75**	×				
WBC	-0.40	**-0.67**	0.17	×			
EBC	0.20	0.02	-0.42	0.22	×		
Shelves	0.32	0.32	**-0.65**	0.29	0.27	×	
Ekman	0.21	-0.23	0.28	-0.01	-0.03	0.23	×

transport. The net southward interior transport exhibits a mean of -6.6 Sv (SEM: 0.8 Sv). The interior transport is significantly anticorrelated with the NOAC AMOC ($r = -0.41$, Table 3.3) and the NAC ($r = -0.81$). The shelf transport is concentrated primarily over the western shelf with a mean southward transport of -11.2 Sv (SEM: 0.3 Sv). The Western Boundary Current (WBC), EBC, and the Ekman transport have mean values below 5 Sv and STDs of 2-4 Sv, with strong seasonal variability. The NAC dominates the upper transports in large parts of the western basin, including the region of the WBC component (Figure 2.4), resulting in a mean northward flow of the WBC component above $\sigma_\theta = 27.67\,kg\,m^{-3}$.

3.5 Atmospheric drivers of AMOC variability

Processes influencing the AMOC on multiple timescales include advection, direct wind forcing, geostrophic adjustments to wind forcing by waves, or surface buoyancy fluxes (e.g., Kostov et al., 2022, 2021; Buckley & Marshall, 2016; Robson et al., 2016; Wang et al., 2015). Despite the limited influence of the wind-driven Ekman transport on the

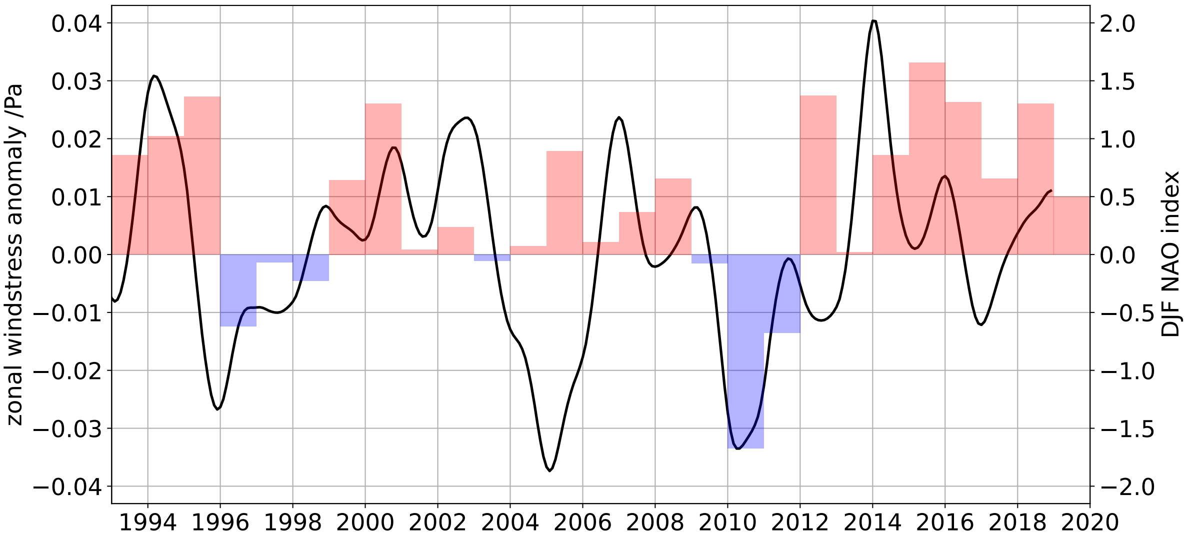

Figure 3.6: Deseasonalized zonal wind stress anomaly at 47°N ± 5°, calculated as a basin-wide average and low-pass filtered from monthly data. The blue and red bars show the NAO index, averaged over December, January, February (DJF), assigned to the year of the respective January and February, based on Barnston & Livezey (1987).

AMOC (Figure 3.3), inter-annual AMOC variability in the subpolar North Atlantic partly results from wind stress anomalies (e.g., Jackson et al., 2022; Kostov et al., 2021; Buckley & Marshall, 2016). At 47°N, strong AMOC phases, for example, around 1993/1994, 2005/2006, and 2015/2016 (visible in the low-pass filtered time series, Figure 3.2 a and c) are accompanied by a strong NAC (Figure 3.3), a relationship also found by other studies (Smeed et al., 2018, 2014). These phases coincide with sharp transitions in the local wind stress anomaly (Figure 3.6), possibly linked to changes in atmospheric pressure patterns resulting in NAO anomalies or meridional shifts of the pressure systems (Iqbal et al., 2019; Buckley & Marshall, 2016).

Recalculating the NOAC AMOC with one component held constant at its mean value allows investigation of their contribution to the total AMOC. In these strong AMOC phases, the AMOC with a constant NAC is about half as strong as with a varying NAC, indicating that a strong NAC has driven these strong AMOC phases. The contribution of the Ekman transport to the AMOC is not exceptionally strong in these phases (not shown). This leads to the conclusion that large-scale wind field changes in the North Atlantic have partly driven the strong NOAC AMOC periods around 1993/1994, 2005/2006, and 2015/2016, possibly via changes in the geostrophic adjustment, resulting in a strong NAC that additionally may have shifted zonally.

The primary non-seasonal atmospheric mode in the North Atlantic is the NAO, affecting wind stress and surface buoyancy fluxes. Here, the monthly mean NAO index from the U.S. National Oceanic and Atmospheric Administration (NOAA) is used based on orthogonally rotated principal components (Barnston & Livezey, 1987). The correlation between the low-pass filtered NOAC AMOC and the NAO index with the same filter applied is insignificant. However, the positive NAO phase from 2014 to 2018 coincides with an AMOC increase of about 1 Sv at the RAPID array (Figure 3.6, note that the figure shows the December, January, February (DJF) NAO). At the NOAC array, the increase in this period is even more substantial (over 2 Sv), suggesting that a long-lasting positive NAO phase drives an increased AMOC volume transport. This also holds for the strong NOAC AMOC phase in 1993/1994, a period of persistent positive NAO (Buckley & Marshall, 2016).

3.6 Uncertainty of the absolute mean AMOC transport

The mean basin-wide AMOC volume transport at 47°N is subject to uncertainties. These uncertainties include random errors, such as the uncertainty in the measurements of acoustic travel time by the PIES and the determination of geopotential anomalies from these as well as latitudinal differences between the PIES locations when calculating the Coriolis parameter. Additional systematic errors are possible misinterpretations of long-term trends in bottom pressure as sensor drift. The above uncertainties of the PIES transport estimates have been discussed in Nowitzki et al. (2021); Rhein et al. (2019b); Roessler et al. (2015). Errors could also arise from the uncertainty of the absolute geostrophic surface velocities obtained from altimetry. Those velocities are used as a level of known motion to calculate absolute transports (Section 2.1.2) and to extend the time series in time (Section 2.1.3). The accuracy of the geoid used to calculate absolute surface velocities from altimetry is in the range of a few centimeters (Morrow et al., 2023) and could induce considerable uncertainty in the absolute mean AMOC transport. Overall, the uncertainty of the mean AMOC transport is expected to be comparable to the magnitude of the compensation transport, designed to eliminate errors in the mass conservation across the array (3.3 Sv, SEM: 0.4 Sv).

For the RAPID array, Sinha et al. (2018) performed a comprehensive model study of the accuracy of the AMOC. They compared the AMOC derived in the model using the same method as the RAPID observations. Their study suggests the RAPID method underestimates the mean AMOC strength by about 1.5 Sv. This result can not easily be transferred to the NOAC array since the method of calculating the AMOC is different. For instance, at the NOAC array, the altimetry-derived geostrophic surface velocity is used as the level of known motion. In contrast, a level of no motion at depth is assumed at the RAPID array. In general, however, the bias at 47°N is expected to be of the same order of magnitude as at the RAPID array.

3.7 Meridional connectivity between the AMOC at 47°N and 26°N

The significant correlation between the low-pass filtered NOAC AMOC and the RAPID AMOC with a lag of about one year possibly indicates a southward communication of transport signals (e.g., Zhang, 2010; Biastoch et al., 2008a). Although advective southward communication is possible on these timescales, the lag correlations of the southward AMOC transport components at 47°N (interior transports, shelves, Ekman transport) with the RAPID AMOC (not shown) are statistically insignificant. Thus, the southward communication of anomalies cannot be attributed to a single component. The southward communication is possibly maintained by other mechanisms, for example, large-scale atmospheric dynamics or advection in the lower AMOC limb (Zou et al., 2019).

Wind-stress variations drive coherent AMOC variability across latitudes on inter-annual timescales (Elipot et al., 2017). The wind forcing results in the Ekman transport, oriented northward at 26°N and southward at 47°N. This inverse behavior could reduce the correlation between the NOAC AMOC and the RAPID AMOC. However, the Ekman transport additionally influences the AMOC via the compensation transport. To eliminate the direct influence of the Ekman transport on meridional connectivity, the correlation between the NOAC AMOC and the RAPID AMOC is computed with the NOAC Ekman component held constant at its mean value. Consistent with model studies (Wang et al., 2019; Bingham et al., 2007), an increased and significant correlation is found between the low-pass filtered NOAC AMOC and the RAPID AMOC at zero lag ($r = 0.66$), indicating that meridional connectivity is maintained by other processes, possibly still due to wind forcing, for example, geostrophic adjustment to large-scale wind field changes (Elipot et al., 2017).

While a lag correlation analysis focuses on the time domain of the connection between the signals, a coherence analysis provides insights into the shared behavior of the time series in the frequency domain. Using a multitaper estimate (Figure 3.7), coherence is found between the two signals, exceeding the 95% confidence level at periods of about seven years. Here, the phase lag is about 50°, indicating a time lag of about one year. This signal might correspond to the decrease following the 2005/2006 maximum and the subsequent increase after 2010, visible in both AMOC time series. However, the time series length limits the analysis, and the coherence might extend to lower frequencies, which are not resolved due to the limited overlap of the time series. The number of frequency bands exceeding the 95% confidence level is too low to exclude statistically that any coherence occurs by chance. However, the correlation analysis shows that the time series are related.

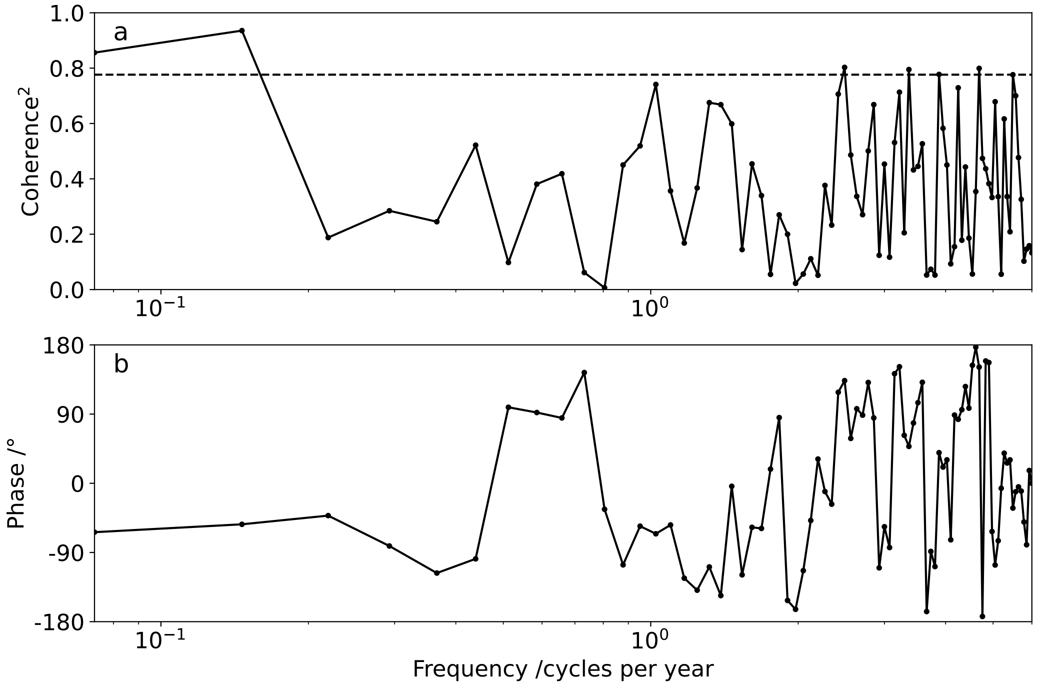

Figure 3.7: Multitaper coherence squared estimate of the NOAC and RAPID AMOC time series (a) and the corresponding phase lag between the signals (b). The dashed line denotes the 95% confidence level.

This chapter has presented the first observation-based basin-wide AMOC volume transport estimate at the NOAC array at 47°N, the boundary between the subtropical and subpolar gyre. The AMOC exhibits a mean value of 17.2 Sv and substantial variability on inter-annual and seasonal time scales. Meridional connectivity is found between the NOAC AMOC and the subtropical RAPID AMOC when the NOAC AMOC leads by about one year. The question of the driving mechanisms of this connectivity on inter-annual time scales remains unanswered. Although advective communication on the time scales of the found connectivity would be possible, correlations between the basin-wide RAPID AMOC and individual southward NOAC AMOC components are insignificant (not shown). Thus, the connectivity cannot be attributed to advection in a single component. However, the connectivity might also be a lagged reaction to changes in the large-scale wind field or advection in the lower limb of the AMOC. As the number and length of direct observational AMOC estimates are limited, exploring the meridional connectivity and its driving mechanisms beyond array-based AMOC observations could benefit from novel approaches to estimating the AMOC from other available observational tools, such as gridded observational data sets.

3.8 AMOC from gridded data sets

The increasing availability of ocean observations from satellites and autonomous in-situ platforms like Argo floats, and gliders have increased the quality of gridded observation-based data sets (e.g., Meng et al., 2021; Gasparin et al., 2020). These developments raise the question of how well gridded data sets can represent the variability of the AMOC and what role they could play in designing a future observing system that will need to be both accurate and feasible.

For the RAPID array, Frajka-Williams et al. (2023) argued that the current Argo fleet could not substitute moorings because of the scarcity of Argo measurements in the direct vicinity of the array at a single point in time. Despite the large global number of Argo floats, this number is still far too small to capture the high-frequency variability of the AMOC. Additionally, the salinity measurements of individual Argo floats can include biases (Wong et al., 2020), which are large enough to introduce significant uncertainties in the resulting AMOC transport (Frajka-Williams et al., 2023).

Despite the difficulties arising with attempts to calculate the AMOC from individual Argo floats, Frajka-Williams et al. (2023) highlighted the potential of combining different observations from remote and in-situ platforms to multi-observational approaches. Such combinations of data were previously used to analyze AMOC variability at the RAPID array at 26°N (Sanchez-Franks et al., 2021) and in the northern subtropical gyre at 45°N (Desbruyères et al., 2019). One such data set, combining observational data from satellite altimetry and in-situ measurements to yield a gridded field of hydrographic variables and geostrophic velocities while being completely observation-based, is ARMOR3D (Section 2.2.1). In the following, the AMOC estimate at 47°N, based on ARMOR3D, is discussed and compared to the estimate at 45°N by Desbruyères et al. (2019).

3.8.1 AMOC estimate at 47°N based on ARMOR3D

The AMOC estimate at 47°N based on ARMOR3D is calculated analogously to the AMOC from the NOAC array as the sum of all transports across the section above the density of the maximum stream function. The density of the maximum stream function in ARMOR3D is found to be $\sigma_\theta = 27.69\,kg\,m^{-3}$, which is in close agreement with the density obtained from lADCP measurements along the NOAC array ($\sigma_\theta = 27.67\,kg\,m^{-3}$, Section 2.4.1).

Additionally to the transports obtained from the geostrophic velocities in ARMOR3D, the Ekman transport, calculated based on atmospheric wind stress data (Section 2.1.5), is added. Analogous to the NOAC AMOC estimate, for ARMOR3D, a compensation transport is added to account for instantaneous mass imbalances across the section. On average,

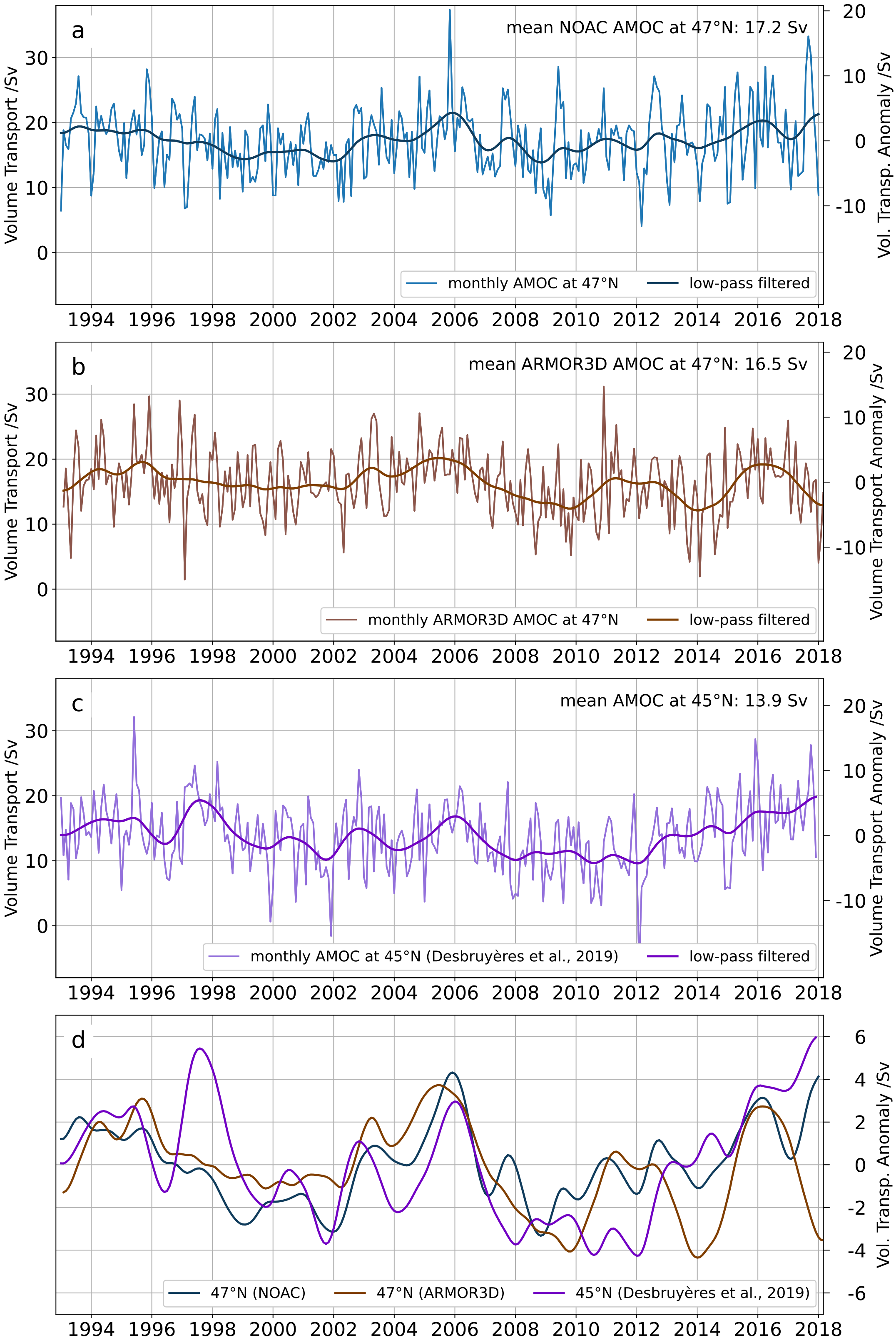

Figure 3.8: Monthly AMOC volume transport time series from the NOAC array at 47°N (a), based on ARMOR3D at 47°N (b), and the estimate at 45°N from Desbruyères et al. (2019) (with added Ekman transport) for the absolute transport (left y-axis) and the transport anomaly (with respect to each full-period mean, right y-axis). The dark lines represent the low-pass filtered AMOC. (d) Comparison of the volume transport anomaly of the low-pass filtered time series.

Table 3.4: Correlations between AMOC estimates in the vicinity of the NOAC array and the NOAC AMOC. The estimates considered are from ARMOR3D (47°N) and from Desbruyères et al. (2019) (45°N with added Ekman transport, referred to as D19). Correlations are shown for the two-month averages and the low-pass filtered time series, as well as for the full period of overlap (1993-2017) and the period 1993-2008. Significant correlations are marked in bold.

	ARMOR3D vs. NOAC		D19 vs. NOAC		ARMOR3D vs. D19	
	full	93-08	full	93-08	full	93-08
2-month averages	**0.49**	**0.49**	**0.34**	0.22	0.20	0.16
low-pass filtered	**0.73**	**0.81**	**0.60**	0.54	**0.39**	**0.51**

the transports in ARMOR3D (including the Ekman transport) are well balanced. The mean compensation transport is small (-0.4 Sv, SEM: 0.3 Sv), but its temporal variability (monthly STD: 3.6 Sv) underlines the importance of incorporating the compensation transport in the basin-wide AMOC estimate for the AMOC variability.

In the study period (1993-2017), the mean AMOC volume transport in ARMOR3D at 47°N (16.5 Sv, SEM: 0.4 Sv, Figure 3.8 b) is slightly smaller than the AMOC of the NOAC array at 47°N (17.2 Sv, SEM: 0.4 Sv, Figure 3.8 a). However, given the SEM of the two time series, the mean values are not significantly different. The AMOC variability in ARMOR3D in monthly resolution (STD: 4.9 Sv) and that of the low-pass filtered time series (STD: 2.0 Sv) resembles that of the NOAC AMOC (monthly STD: 5.2 Sv, low-pass filtered STD: 1.7 Sv). As the AMOC time series of the NOAC array, the ARMOR3D AMOC estimate does not show a significant trend over the study period.

The AMOC estimate at 47°N, based on ARMOR3D, exhibits high correlations with the NOAC AMOC, especially in the first part of the time series, 1993-2008. The two-month averages are significantly correlated with 0.49 for both the full period and the first part, 1993-2008 (Table 3.4). For the low-pass filtered time series, these correlations increase to 0.73 for the full period and 0.81 for the first part, 1993-2008.

The ARMOR3D AMOC time series captures the relatively strong AMOC in the mid-1990s and the following decrease until the early 2000s, as observed at the NOAC array (Figure 3.8). Likewise, it represents the observed overall maximum in the mid-2000s and a subsequent decrease until 2010, possibly associated with a strong negative NAO. Unfortunately, the ARMOR3D AMOC estimate fails to reproduce the increase of the AMOC transport after 2010, measured by the NOAC array. The period after the strong negative NAO in 2010 was associated with a dominance of positive NAO, inducing stronger winds over the North Atlantic. These winds are a possible driver of the increasing AMOC after 2010. Instead, the ARMOR3D AMOC shows two occurrences of strong AMOC decrease in 2013 and 2017, the former coinciding with a local minimum of smaller amplitude in

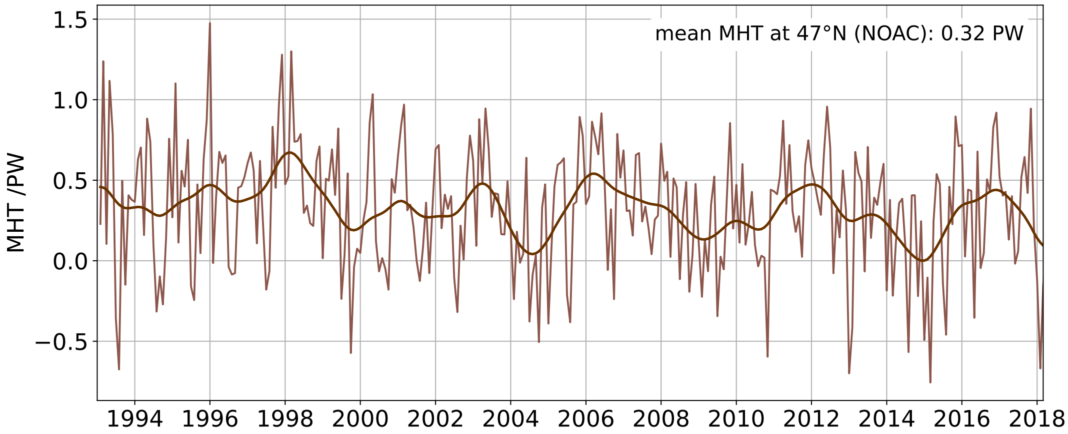

Figure 3.9: MHT at 47°N based on ARMOR3D at monthly resolution. The darker line denotes the low-pass filtered time series.

the NOAC AMOC time series at the same time. However, such strong inter-annual variability of the AMOC was not observed at the NOAC array in this period. 2013/14 was a period of exceptionally strong winds and respectively strong increase before at 47°N (Figure 3.6). The relationship between zonal wind stress and the AMOC, established in Section 3.5, explains a weak AMOC as a response to the wind forcing. However, this only holds for the weak AMOC in 2014. In 2018, no exceptional wind forcing is visible at 47°N. Wiegand (2023) analyzed the representation of hydrographic properties in ARMOR3D at eastern AR7W, finding an overall good agreement between ARMOR3D and ship-based in-situ data. In periods with higher observational coverage, the agreement was found to be notably better. However, this would explain differences in the early periods of the analyzed time series due to a lack of in-situ data, not a difference in the recent years. Thus, the origin of the AMOC anomaly in 2018 in ARMOR3D is unclear.

Data from moorings and PIES of the NOAC array is not included in ARMOR3D. However, for the NOAC AMOC and ARMOR3D, the same satellite altimetry measurements are a pivotal part of calculating the geostrophic velocities. This holds especially for the period 1993-2012. In this period, the AMOC estimate at the NOAC array is extended in time based on the linear relationship between the absolute geostrophic transport, measured by the PIES, and the absolute surface velocity, inferred from satellite altimetry (Section 2.1.3). Accordingly, the ARMOR3D and NOAC AMOC estimates are not independent. Thus, variations in the SSH measurements, which are a major source for the calculation of the geostrophic transports in ARMOR3D as well as the AMOC volume transport at the NOAC array, could be driving the high correlations between the AMOC time series obtained from both ARMOR3D and the NOAC array.

In contrast to station-based observations at the NOAC array, a gridded data set including continuous temperature fields, like ARMOR3D, offers the opportunity to additionally

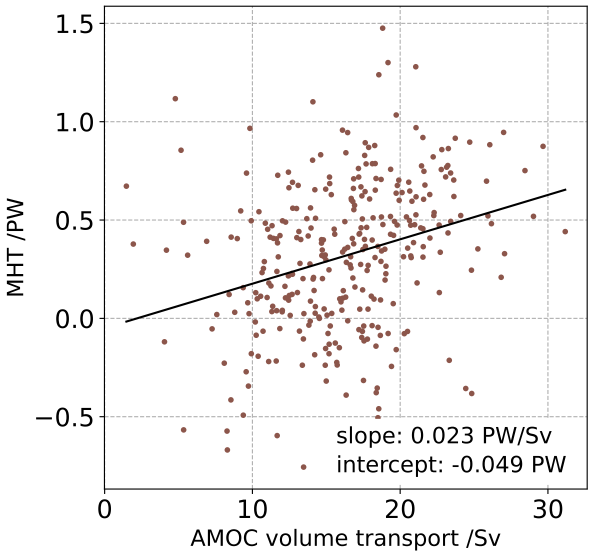

Figure 3.10: AMOC volume transport at 47°N based on ARMOR3D (Figure 3.8 b), plotted against the MHT at 47°N based on ARMOR3D (Figure 3.9). The black line denotes the linear regression. Slope and intercept are given in the lower right corner.

calculate the MHT. The MHT in ARMOR3D is calculated as defined in Section 2.5. However, since mass balance across the section is not necessarily given, the velocity used for the calculation is a compensated velocity, including a spatially constant compensation velocity, accounting for instantaneous mass imbalances across 47°N in ARMOR3D.

The mean MHT at 47°N, based on ARMOR3D is 0.32 PW (SEM: 0.03 PW, 1 PW = 10^{15} W, Figure 3.9). This value is lower than the value estimated at the same latitude during the WOCE (0.6 PW, Ganachaud & Wunsch, 2003), though these values were obtained over different periods. The value is lower than the mean MHT obtained from VIKING20X at the NOAC line (0.63 PW, SEM: 0.01 PW, Section 4.4, Figure 4.11) and lower than the reconstructed MHT at the NOAC array, using the linear relationship between AMOC volume transport and MHT from VIKING20X (0.59 PW, SEM: 0.01 PW, Figure 4.13). Unsurprisingly, ARMOR3D shows better agreement with the NOAC observations regarding the AMOC volume transport than the MHT. Temperatures at depth can only be inferred from scarce in-situ measurements, inducing uncertainties. Additionally, ARMOR3D only includes climatological data below 1500 m, possibly missing temperature trends in the deep ocean.

Generally, there exists a strong correlation between the AMOC volume transport and the MHT (Buckley & Marshall, 2016; Johns et al., 2011), following roughly a linear relationship. At 47°N, in ARMOR3D, the correlation between the AMOC volume transport and the MHT is significant but weak (0.28). The spread of the individual values around the regression line is large (Figure 3.10), explaining the differences between the AMOC and

MHT variability in ARMOR3D. Conclusively, though ARMOR3D partly represents the AMOC volume transport at 47°N, the discrepancy in the MHT indicates that it is not suitable for estimates of the MHT, highlighting the importance of model simulations for this purpose.

3.8.2 AMOC estimate at 45°N by Desbruyères et al. (2019)

Desbruyères et al. (2019) estimated the AMOC at 45°N in the North Atlantic based on a combination of four different data sets (Section 1.4): ARMOR3D (Section 2.2.1), EN4 (Section 2.2.2), ISHII (Ishii et al., 2003), and CORA (Tanguy et al., 2023). They independently calculated the AMOC in the different data sets and combined them as an ensemble mean, finding a mean AMOC volume transport of 14.3 Sv in 1993-2017. Following Mercier et al. (2015), Desbruyères et al. (2019) reconstruct the upper AMOC, assuming mass balance for the ensemble mean estimate (Damien Desbruyères, personal communication) and thus not applying a compensation transport. Their estimate is purely based on geostrophic velocities and does not include the wind-driven Ekman transport. Here, the Ekman transport at 45°N in the North Atlantic is calculated as described in Section 2.1.5 and added to the AMOC time series by Desbruyères et al. (2019) (Figure 3.8 c). In the following, this time series, including the Ekman transport, will be referred to as the estimate by Desbruyères et al. (2019).

The AMOC time series at 45°N, including the southward Ekman transport, exhibits a mean AMOC strength of 13.9 Sv (SEM: 0.4 Sv). This mean value is significantly lower than the mean values at the NOAC array and based on ARMOR3D at 47°N. However, the monthly STD (5.2 Sv) is in good agreement with the NOAC and ARMOR3D AMOC estimates.

The AMOC estimate at 45°N exhibits inter-annual variability similar to the NOAC AMOC and the ARMOR3D AMOC estimate. A maximum in the late 1990s and the subsequent decrease are represented, as well as the maximum in the mid-2000s, the decrease until 2010, and the increase after that (Figure 3.8 c). The correlations with the NOAC AMOC are significant for the full period (two-month averages: 0.34, low-pass filtered: 0.60, Table 3.4) but remain smaller compared to the correlations of the ARMOR3D AMOC estimate with the NOAC AMOC. However, in contrast to the ARMOR3D AMOC estimate, the 45°N estimate reproduces the recent increase in the AMOC strength observed at the NOAC array after the minimum in 2010. This might be a benefit of not completely relying on only one data set.

ARMOR3D is included in the combination of data sets used by Desbruyères et al. (2019) to estimate the AMOC at 45°N. Thus, their estimate suffers to some degree from the same problem of relying on the altimetry data, which is an important component for calculating and extending transports at the NOAC array. Despite the lower correlations with the NOAC AMOC compared to the ARMOR3D AMOC estimate, the AMOC estimate at 45°N by Desbruyères et al. (2019) seems to reproduce the inter-annual variability of the observed NOAC AMOC, including the increase after the minimum reached in 2010. This trend is not captured by the AMOC estimate based on ARMOR3D. The ARMOR3D AMOC estimate is based entirely on a single observation-based data set. However, Desbruyères et al. (2019) combined multiple observation-based data sets and reanalyses to yield an ensemble mean AMOC strength at 45°N. The use of multiple data sets could hold potential for future AMOC observation approaches that rely only partly or not at all on direct AMOC observations from mooring arrays.

The NOAC array was designed for different purposes, analyzing individual flow components at 47°N. An array serving the sole purpose of monitoring the AMOC could be operational with a reduced number of in-situ devices, covering the most dynamic western parts of the basin and relying on a combination of in-situ devices and different gridded data sets in the ocean interior. A detailed discussion of such a reduced array is provided in the outlook (Chapter 6).

"You have to know the past to understand the present."

Carl E. Sagan, *astronomer and science communicator*

Chapter 4

The AMOC in the North Atlantic in high-resolution ocean models

Observational estimates of the AMOC are available only since the RAPID array at 26°N was deployed in 2004 as the first in-situ AMOC monitoring array. The absence of direct observational estimates from before that time means that reliable AMOC time series are only just reaching lengths at which the inter-annual to decadal variability can be discussed. Due to the limited length of observational AMOC time series, model simulations remain an important tool for investigating the past and future AMOC. Assessing the performance of these model simulations against observations is a vital process to understand the AMOC and the robustness of model results.

Forced ocean models can simulate the past on various timescales. Thus, they can provide time series that are substantially longer than the observational time series (42 years for VIKING20X). These longer time series provide a more robust database for analyzing variability and trends and for statistical analyses. In Section 4.1, the mean strength, variability, and trends of the AMOC in VIKING20X at the positions of the NOAC, RAPID, and OSNAP arrays are investigated and compared to observational estimates. Section 4.2 explores the causes and imprints of the modeled AMOC trends in VIKING20X. The longer VIKING20X time series compared to observations is a great advantage for studying the meridional connectivity, which is investigated in Section 4.3. The MHT can be estimated from the observing systems only under certain assumptions, if at all possible, Section 4.4 analyzes the MHT in VIKING20X at the locations of the NOAC, RAPID, and

Table 4.1: Mean, SEM, and STD of the AMOC volume transport in VIKING20X and observations at the locations of AMOC monitoring arrays in the North Atlantic. The periods refer to the full model period without the spin-up period (1980-2021) and the observational period of the respective array (NOAC: 1993-2018, RAPID: 2004-2018, OSNAP: 2014-2018). Observational values are from Chapter 3 (NOAC), Moat et al. (2022, RAPID), and Baker et al. (2022, OSNAP).

	NOAC			RAPID			OSNAP		
	mean	SEM	STD	mean	SEM	STD	mean	SEM	STD
VIKING20X (full period)	18.6 Sv	0.2 Sv	3.8 Sv	18.4 Sv	0.2 Sv	3.0 Sv	18.9 Sv	0.2 Sv	3.0 Sv
VIKING20X (obs. period)	18.4 Sv	0.3 Sv	3.9 Sv	16.8 Sv	0.3 Sv	2.6 Sv	15.8 Sv	0.4 Sv	2.2 Sv
Observations	17.2 Sv	0.4 Sv	5.2 Sv	16.9 Sv	0.4 Sv	3.4 Sv	16.6 Sv	0.7 Sv	7.6 Sv

OSNAP arrays. One key parameter determining the performance of numerical models is the horizontal resolution. While it comes at additional computational costs, sufficiently high resolution is a prerequisite to represent mesoscale features of the circulation and their effects on the AMOC. The effect of model resolution on the representation of the AMOC in different ANHA simulations is explored in Section 4.5.

4.1 The AMOC in VIKING20X at NOAC, RAPID, and OSNAP

The performance of VIKING20X (model description in Section 2.3.1) in representing the observed AMOC at the NOAC, RAPID, and OSNAP AMOC monitoring arrays in the North Atlantic is analyzed. VIKING20X resolves the mesoscale in the subtropical and subpolar North Atlantic (Biastoch et al., 2021). The applied JRA55-do atmospheric forcing is a state-of-the-art data set to force ocean hindcast model simulations. In contrast to coupled climate models, these hindcast simulations rely on a realistic atmospheric forcing to simulate past ocean and climate parameters like the AMOC. The role of the atmospheric forcing is particularly important in realistically representing the AMOC in hindcast simulations, especially since the wind is one of the driving forces of the AMOC. Furthermore, VIKING20X represents the thermohaline component of the AMOC by simulating key aspects such as convection, overflows, and entrainment (Biastoch et al., 2021). VIKING20X offers a horizontal resolution of $^1/_{20}$°, resulting in less than 5 km in the subpolar North Atlantic (Figure 2.2). In total, 42 years of model data are used to analyze the AMOC variability, excluding the spin-up period.

For a comparison with observations, the VIKING20X AMOC is calculated at the positions of the AMOC monitoring arrays in the North Atlantic, the NOAC, RAPID, and OSNAP arrays. Hereafter, these locations of the arrays in model simulations are referred to as the NOAC, RAPID, and OSNAP lines. In VIKING20X, the AMOC is calculated as the time-varying maximum of the overturning stream function in density coordinates (Section 2.4). The mean density of the maximum stream function in VIKING20X at the NOAC line is $\sigma_\theta = 27.64\,kg\,m^{-3}$ (Figure 4.1 a). This value is in close agreement with the density of the maximum stream function obtained from observations at 47°N ($\sigma_\theta = 27.67\,kg\,m^{-3}$). A sensitivity analysis in VIKING20X yields only small differences between the AMOC definition via the time-varying stream function and via the transports above $\sigma_\theta = 27.67\,\mathrm{kg\,m^{-3}}$, analogous to the AMOC definition in the observations of the NOAC array (Section 2.4.2). At the RAPID line, the density of the maximum stream function is lower ($\sigma_\theta = 27.56\,kg\,m^{-3}$). At the OSNAP line, the density of the maximum stream function is $\sigma_\theta = 27.60\,kg\,m^{-3}$, which is also in good agreement with the observed maximum at the OSNAP array ($\sigma_\theta = 27.66\,kg\,m^{-3}$, Lozier et al., 2019).

NOAC (47°N)

At 47°N, at the NOAC line, the VIKING20X AMOC has a mean strength of 18.6 Sv (18.4 Sv in the NOAC observing period, Table 4.1, Figure 4.2). The mean AMOC strength in the observational period is larger than in the NOAC observations (17.2 Sv, Table 3.1) but generally falls within the estimated error range of the observational estimate (3.3 Sv, Section 3.6). Increasing throughout the 1980s, the VIKING20X AMOC at 47°N reaches a maximum in the mid-1990s associated with excessive convection in the Labrador Sea in the 1990s (Rhein et al., 2017; Kieke & Yashayaev, 2015; Lazier et al., 2002). Unsurprisingly, a very similar decadal variability was found by Böning et al. (2023) at the very close latitude of 48°N in VIKING20X. After the maximum in the 1990s, the AMOC volume transport in VIKING20X decreases with a significant trend of -0.3 $\mathrm{Sv\,yr^{-1}}$ until 2010. After 2010 the VIKING20X AMOC volume transport remains relatively constant at about 15 Sv.

The decreasing AMOC volume transport found in VIKING20X at 47°N after the maximum in the 1990s differs from observations of the NOAC array (Chapter 3). In observations, the AMOC volume transport exhibits an insignificant trend of 0.03 $\mathrm{Sv\,yr^{-1}}$ over the period 1993-2018. The AMOC decrease in VIKING20X appears to be influenced by a negative salinity feedback of reduced inflow of saline waters into the subpolar North Atlantic (Section 1.5, Martin & Biastoch, 2023), possibly a result of the slowdown of the AMOC after the peak convection in the mid-1990s. Ocean-only models and the associated modeled AMOC trends are known to be very sensitive to numerical choices, especially regarding the freshwater budget (Biastoch et al., 2021; Behrens et al., 2013), making it difficult to differentiate between actual AMOC variability and model-related trends. In order to correct for missing feedbacks with the atmosphere, in VIKING20X SSS restor-

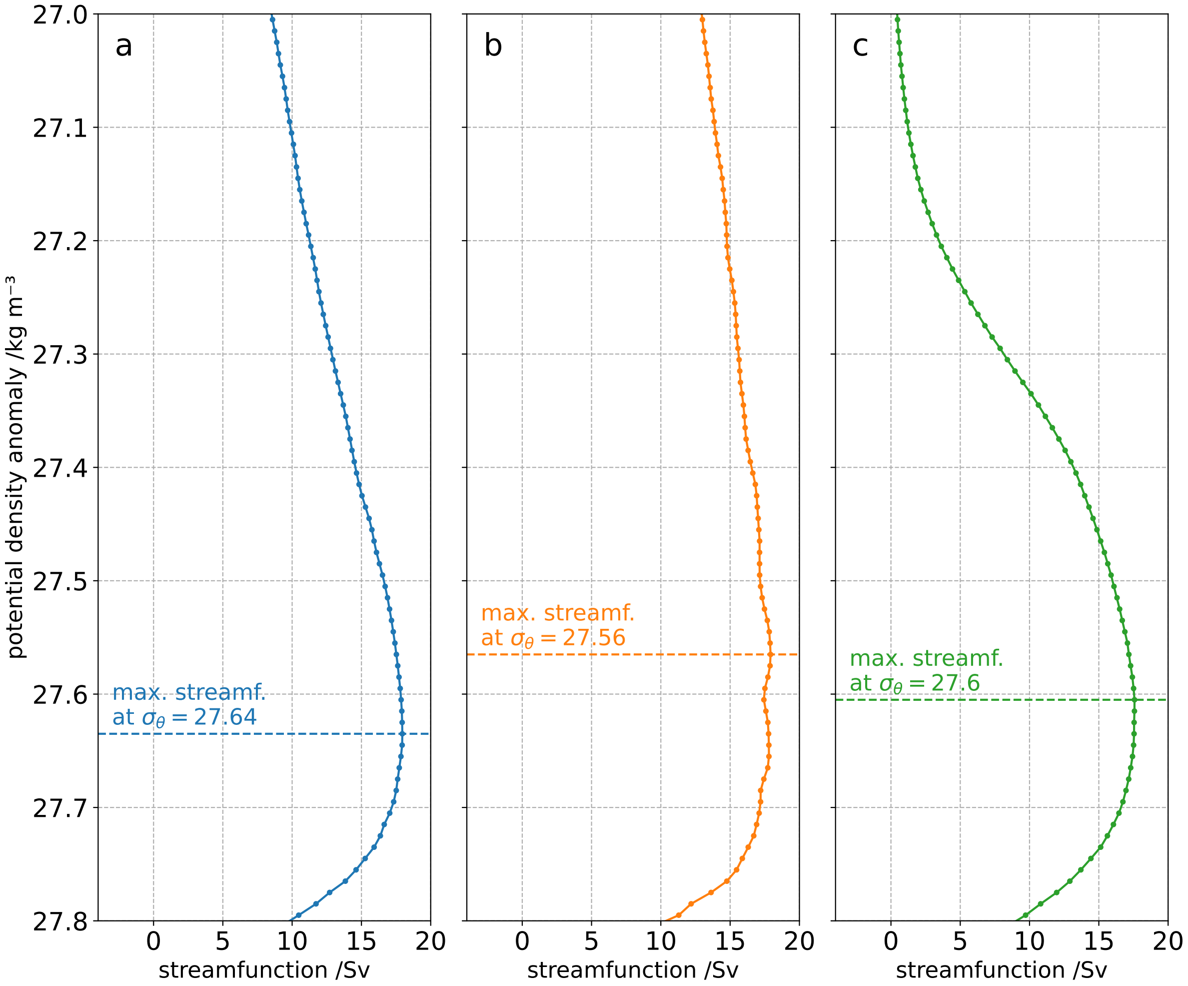

Figure 4.1: The mean meridional overturning stream function in density coordinates at the NOAC (a), RAPID (b), and OSNAP (c) lines as simulated in VIKING20X. The horizontal lines mark the density of the maximum overturning stream function. Note that the panels are not ordered by latitude.

ing to climatological values is implemented (Section 2.3.1). Biastoch et al. (2021) showed that the SSS restoring influences the modeled AMOC trend. They found a weaker AMOC trend at 26°N in simulations with stronger SSS restoring.

Despite the high correlation of AMOC variability between VIKING20X and observations at the RAPID array in the subtropical North Atlantic (Biastoch et al., 2021), the correlation of the AMOC volume transport between VIKING20X and the NOAC observations at 47°N is 0.44 and not significant on inter-annual timescales in the period of overlap. This is possibly due to the stronger variability at 47°N, dominated by the NAC, only partly represented by VIKING20X (Section 4.1.1).

RAPID (26°N)

With 18.4 Sv, the mean AMOC volume transport in VIKING20X at the RAPID line has a similar magnitude as the VIKING20X AMOC at the NOAC line (Table 4.1). The

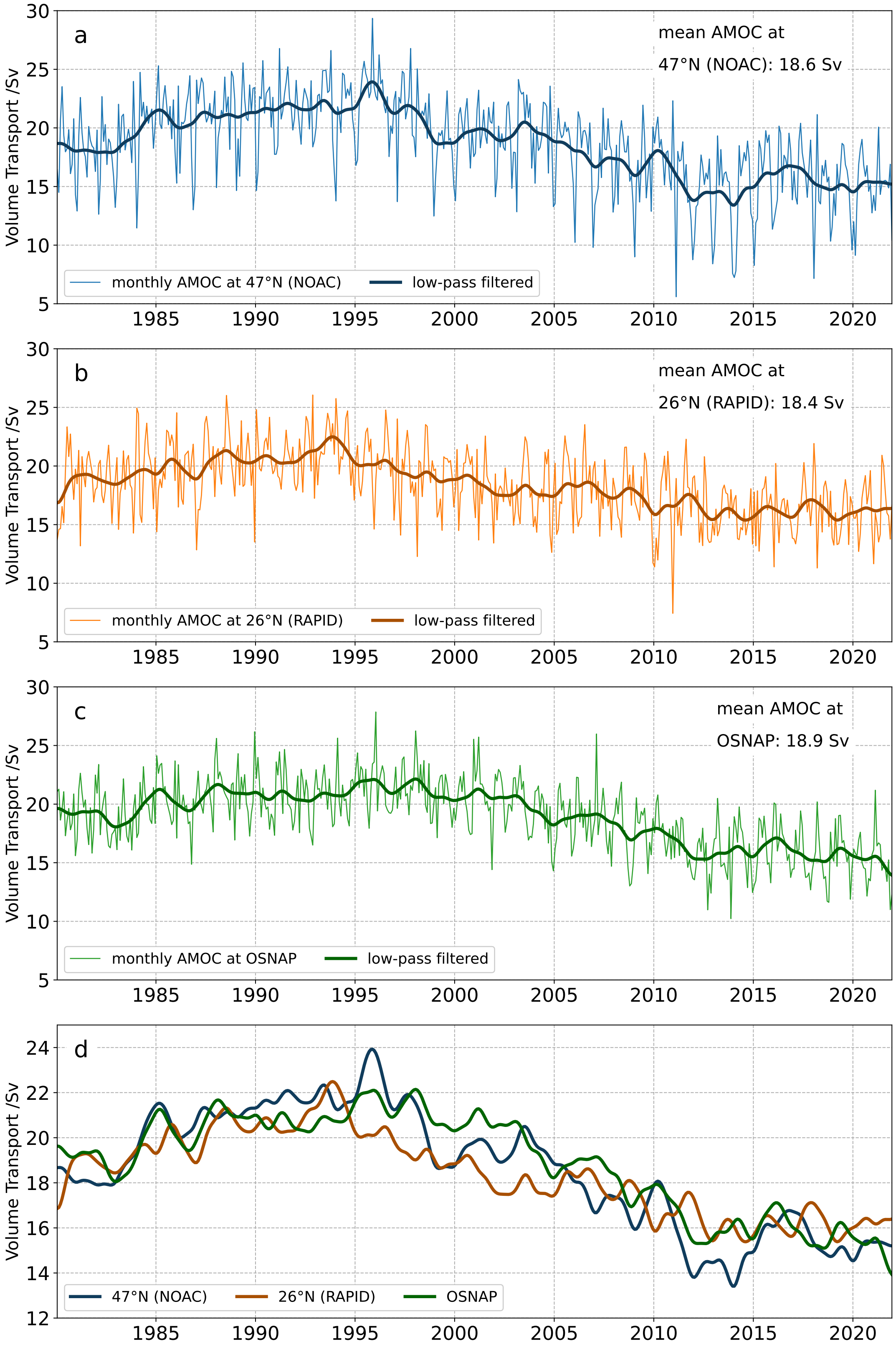

Figure 4.2: Monthly AMOC time series in VIKING20X calculated at the NOAC (a), RAPID (b), and OSNAP (c) lines. The dark lines denote the low-pass filtered time series. (d) Comparison of the low-pass filtered time series at NOAC, RAPID, and OSNAP. Note that the panels are not ordered by latitude.

mean AMOC in VIKING20X in the RAPID observational period (16.8 Sv) is in very good agreement with the RAPID observations (16.9 Sv). Subtropical AMOC variability on inter-annual timescales is primarily driven by the wind forcing (Buckley & Marshall, 2016). Driven by a realistic atmospheric forcing and representing mesoscale features, VIKING20X exhibits strong correlation with the RAPID array measurements at 26°N (Biastoch et al., 2021). VIKING20X shows the 26°N AMOC maximum in the mid-1990s and a subsequent decrease of AMOC volume transport with -0.2 Sv yr^{-1}. Observations showed that the RAPID AMOC at 26°N was in a state of reduced overturning after 2008 compared to 2004-2008 (Smeed et al., 2018). This negative trend is also visible in VIKING20X. However, in the model, this decrease is part of an overall negative trend of the AMOC volume transport after the mid-1990s, while observations indicated a strengthening of the AMOC after 2010 (Moat et al., 2020).

VIKING20X captures the generally larger variability at the NOAC line compared to the RAPID line in the center of the subtropical gyre at 26°N, which is driven by the stronger variability of the NAC, compared to the Florida Current (Piecuch, 2020). However, it underestimates the overall STD by about 24 % for 26°N (RAPID: 3.4 Sv, VIKING20X: 2.6 Sv in the observation period, Table 4.1) and 25 % for 47°N (NOAC: 5.2 Sv, VIKING20X: 3.9 Sv in the observation period, Table 4.1). This behavior of underestimating the AMOC variability is known from climate models and associated with an underrepresentation of the low-frequency variability (Yan et al., 2018).

OSNAP

The mean AMOC strength of VIKING20X at the OSNAP line over the full period (18.9 Sv) is very similar to the mean values in VIKING20X at the RAPID and NOAC lines from that period (Table 4.1). The observational estimates of the AMOC volume transport at the OSNAP array are available only after 2014, and thus, the observational period is shorter than for the NOAC and RAPID lines. However, the mean AMOC strength in VIKING20X in the observational periods (15.8 Sv) agrees well with the observations (Baker et al., 2022, 16.6 Sv). However, the model appears to underestimate the mean variability. In VIKING20X, the STD in the observational period of OSNAP is 2.0 Sv, while Baker et al. (2022) report 7.6 Sv monthly variability from the OSNAP observations (Table 4.1). In VIKING20X, at the OSNAP line, the decadal variability with a maximum in the 1990s and a subsequent significant decrease with -0.3 Sv yr^{-1} is evident. While recent studies showed that in the subpolar North Atlantic, the bulk of the overturning occurs in the Eastern Atlantic rather than in the Labrador Sea (Lozier et al., 2019), different modeling studies showed a connection between decadal AMOC variability and LSW production (Böning et al., 2023; Yeager et al., 2021). This low-frequency variability is represented in the modeled AMOC. However, on shorter timescales, the modeled variability in VIKING20X is smaller than the observed variability (Fu & Li, 2023). On these

Table 4.2: Correlation of the AMOC volume transport and the individual components at the NOAC line between VIKING20X and observations for the two-month averages and the low-pass filtered time series and for the upper and top-bottom components. Significant correlations are marked in bold (there are none).

	2-month averages		low-pass filtered	
	upper	top-bottom	upper	top-bottom
AMOC	0.2	×	0.45	×
NAC	-0.02	-0.04	0.07	0.07
Interior	0.06	-0.02	0.39	0.12
WBC	0	-0.07	-0.28	-0.30
EBC	-0.06	0.01	-0.14	-0.07
Shelves	-0.14	0.08	-0.01	0.30
western components	-0.13	-0.16	-0.33	-0.26

timescales, the AMOC is primarily forced by the winds, possibly indicating a connection to the model response to the wind forcing.

Modeling (Bingham et al., 2007) and observational studies (Mielke et al., 2013) have shown that AMOC variability on inter-annual timescales is not coherent between the subtropical and the subpolar gyre. In the subpolar gyre, low-frequency buoyancy forcing dominates the variability, while higher-frequency wind forcing dominates in the subtropics, although the subtropics are also influenced by low-frequency buoyancy variations (Jackson et al., 2022; Bingham et al., 2007). Such behavior is also found in VIKING20X, indicated by the stronger high-frequency variability at the RAPID line compared to the OSNAP line. The decadal evolution in VIKING20X at the OSNAP line is very similar to the decadal evolution in VIKING20X at the RAPID and NOAC lines, with a minimum in the 1970s, a maximum in the mid-1990s and a subsequent decrease of the AMOC volume transport. However, given the strong influence of the wind forcing on the AMOC and the opposing wind fields in the North Atlantic due to the NAO, opposing inter-annual variability in the subtropical and subpolar AMOC has been found in model studies (Gu et al., 2020). The connectivity of inter-annual AMOC variability in VIKING20X is discussed in Section 4.3.

4.1.1 Volume transports of NOAC AMOC components in VIKING20X and observations

In observational estimates, the basin-wide AMOC is often subdivided into individual components of the AMOC (Chapter 3, Moat et al., 2020; Frajka-Williams et al., 2016) to investigate the lateral flow compensation. Variability in one component that is com-

Table 4.3: Correlation of the two-month averages and low-pass filtered time series of the individual AMOC components with the basin-wide AMOC volume transport at 47°N and each other in VIKING20X. Significant correlations are marked in bold.

2-month averages	AMOC	NAC	Interior	WBC	EBC	Shelves
AMOC	×					
NAC	0.15	×				
Interior	0.05	**-0.89**	×			
WBC	0.02	**-0.51**	**0.26**	×		
EBC	0.12	0.05	**-0.26**	0.07	×	
Shelves	0.09	-0.01	-0.04	-0.11	-0.11	×
low-pass filtered	AMOC	NAC	Interior	WBC	EBC	Shelves
AMOC	×					
NAC	**0.61**	×				
Interior	-0.35	**-0.85**	×			
WBC	-0.05	**-0.52**	0.27	×		
EBC	0.15	-0.07	-0.22	0.23	×	
Shelves	-0.42	-0.14	-0.08	-0.21	-0.07	×

pensated by another component does not imprint on the AMOC variability. In the following, the AMOC volume transport in VIKING20X at the NOAC line is compared to the observations using the same definitions. This allows more detailed investigation of the circulation in VIKING20X at the NOAC line. These volume transport components are defined by fixed geographic boundaries and the depth of the density of the maximum overturning stream function (Figure 2.4). For comparisons of top-bottom transports, see Figure A.5 and Figure A.6.

In VIKING20X at the NOAC line, the individual components are calculated as the transports above the density of the maximum stream function ($\sigma_\theta = 27.64\,kg\,m^{-3}$). Here, the individual components show only insignificant correlation <0.39 with the respective components from the NOAC array observations (Table 4.2). In the NOAC observations, most of the individual AMOC components (two-month averages) exhibit significant correlations with the basin-wide AMOC (Table 3.3). However, in VIKING20X, the correlations of the individual components (two-month averages) remain insignificant (Table 4.3). In VIKING20X, for most components, the correlation (or anticorrelation) of the low-pass filtered time series is larger compared to the two-month averages, though only the NAC correlates significantly (Table 4.3). In contrast, the observational individual components at the NOAC array exhibit lower correlations for the low-pass filtered time series compared to the two-month averages (Table 3.3). These differences indicate that in the observations, the correlation with the basin-wide AMOC is based on the seasonal variability, possibly the seasonal cycle, while in VIKING20X, it is based on the inter-annual variability. This might be a result of underestimated seasonal AMOC variability in VIKING20X.

The individual AMOC components in VIKING20X (Table 4.3) have similar interrelations as the observational AMOC components at the NOAC array (Table 3.3). The model shows similar anticorrelations of the NAC with the southward transports of the Interior and WBC transports. In VIKING20X and observations, this connection holds for the two-month averages and the low-pass filtered time series, indicating a correlation on multiple timescales. The strong anticorrelation between the NAC and the Interior transports (-0.89 and -0.85 for the two-month averages and the low-pass filtered time series, respectively, Table 4.3) is even slightly stronger in VIKING20X than in the observations (-0.81 and -0.75 for the two-month averages and the low-pass filtered time series respectively, Table 3.3). Furthermore, in VIKING20X, the southward components of the Interior and WBC transports are significantly correlated, as they are in the observations.

Though the mean basin-wide NOAC AMOC volume transports are very similar between VIKING20X and observations (Table 4.1), the individual components show differences in the mean volume transports (Figure 4.3). Additionally, the volume transport trends differ in the sign for the basin-wide AMOC and most of the individual AMOC components between VIKING20X and the NOAC observations. A previous comparison of VIKING20X transports with observations of the DWBC at 53°N (Zantopp et al., 2017) in Biastoch et al. (2021) yielded a close representation (within 0.1 $\mathrm{Sv\,decade^{-1}}$) of the DWBC transport trends in VIKING20X. Similarly, the trends found in the upper transports of the WBC component at 47°N differ by 0.04 $\mathrm{Sv\,yr^{-1}}$ (0.4 $\mathrm{Sv\,decade^{-1}}$, Figure 4.3 c). However, the transport comparison in this component exhibits differences between the observed and modeled variability. Differences in the mean transport and trends in the individual transport components at 47°N probably arise from the static definitions of the components at 47°N. The geographical boundaries of the flow components are fixed in space and are not sensitive to zonal shifts of the currents. However, these differences do not contradict the significant correlations and anticorrelations between the individual components because the mean value and trend do not influence the correlation.

Rhein et al. (2019b) found a negative trend in the top-bottom western AMOC components at 47°N. A similar decrease is also visible in the western AMOC components, that is, the upper western transports, in VIKING20X (Figure 4.4). The trends of the summed transports of the western components (western shelf, WBC, and NAC, Figure 4.4) agree better than the trends of the individual components, considered separately. This agreement is another argument supporting the statement that the static geographical boundaries applied to both the observations and VIKING20X do not account for temporal shifts of

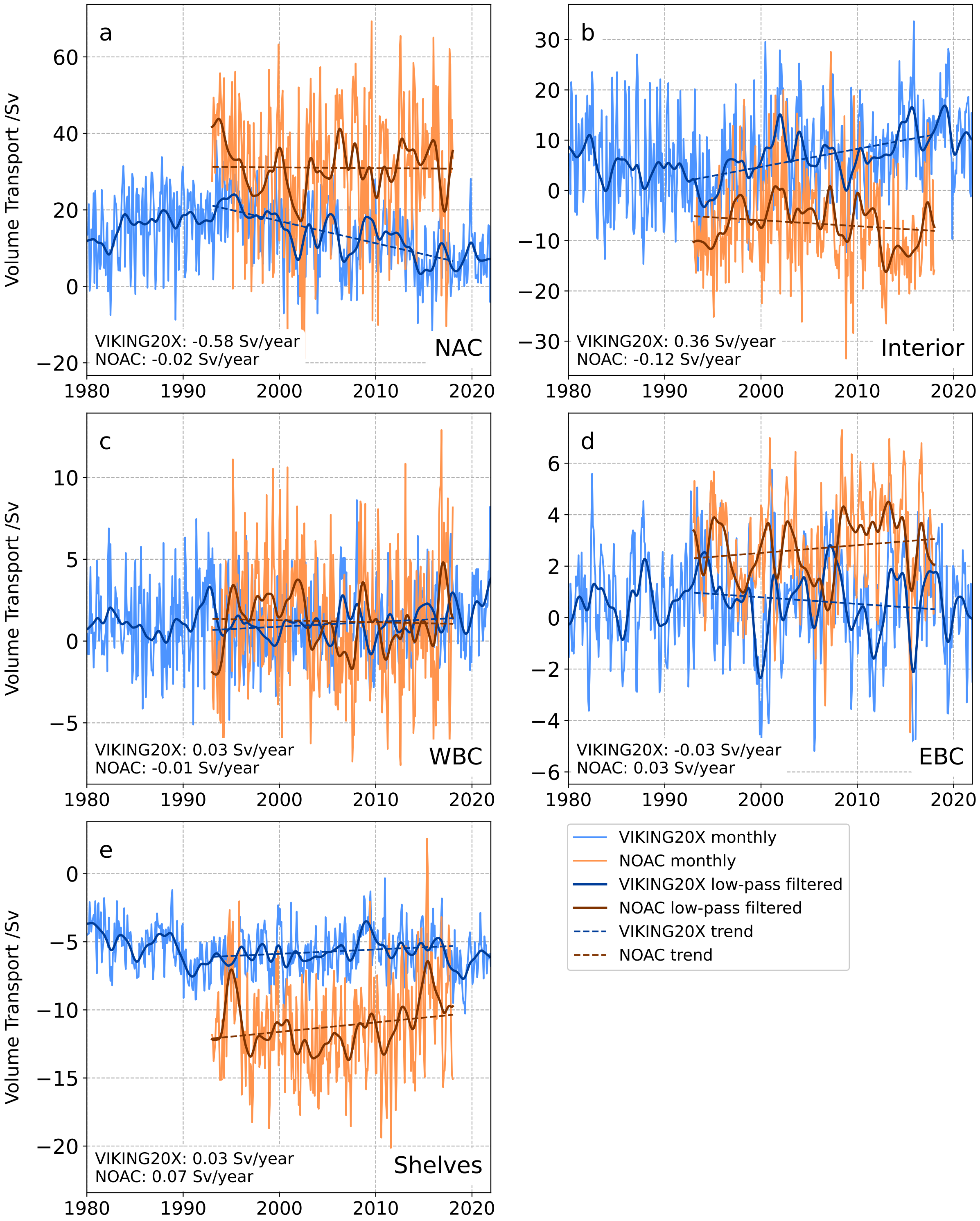

Figure 4.3: Volume transport comparison between individual AMOC components at the NOAC line from VIKING20X and observations of the NOAC array. Individual components are defined in the same way as shown in Figure 2.4 as transports above the density of the maximum overturning stream function. These components include the NAC, interior transport, WBC, EBC, and shelves transport. VIKING20X transports are in blue, NOAC transports are in orange. The dark lines denote the low-pass filtered time series. The dashed lines denote the trend over the observation period (1993-2018). The magnitude of these trends is given in the lower left corner of each subplot.

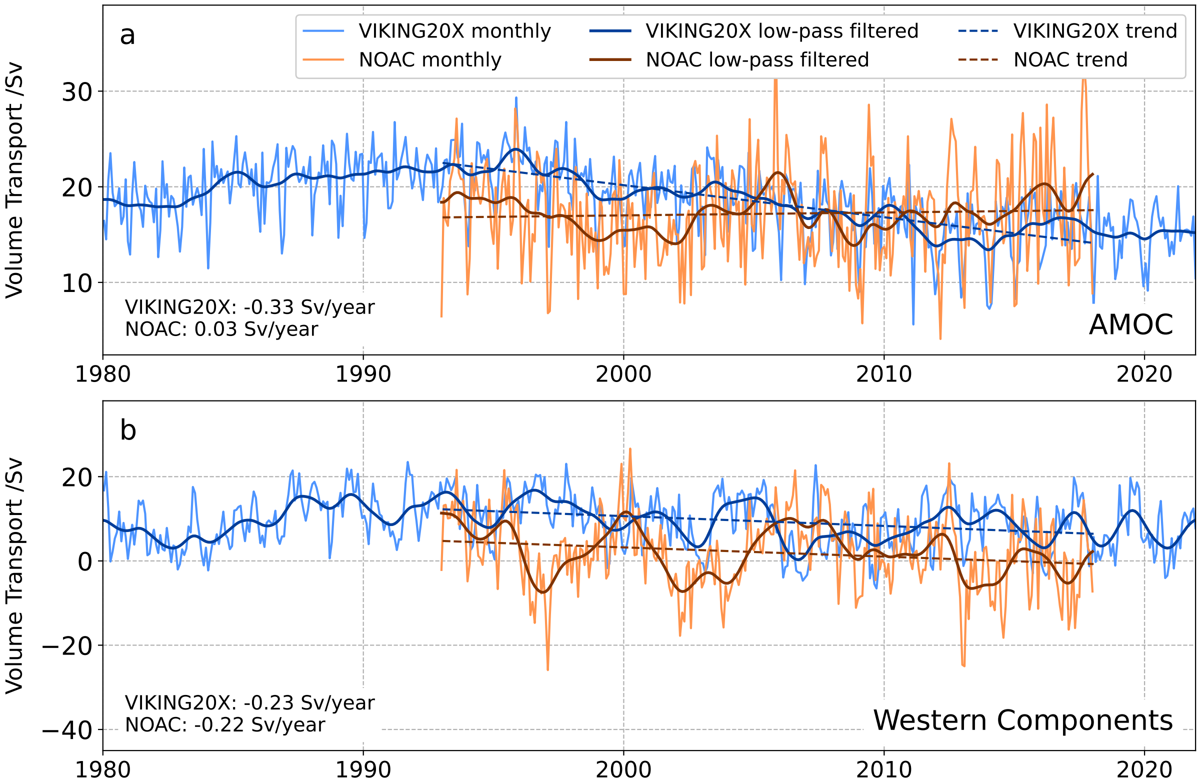

Figure 4.4: Volume transport comparison for the basin-wide AMOC and the sum of the upper transports of the western components (western shelf, WBC, NAC) at the NOAC line between VIKING20X and observations of the NOAC array. Individual components are defined in the same way as shown in Figure 2.4 as transports above the density of the maximum overturning stream function. VIKING20X transports are in blue, NOAC transports are in orange. The dark lines denote the low-pass filtered time series. The dashed lines denote the trend over the observation period (1993-2018). The magnitude of these trends is given in the lower left corner of each subplot.

the currents and thus result in differences between VIKING20X and observations. These shifts are accounted for when summing adjacent transport components, resulting in a better agreement of the trends. However, the static definition of the components is not the only reason for the differences between VIKING20X and the observations. Figure 4.3 and Figure 4.4 show that the decrease in the western components and, in VIKING20X, the AMOC is driven by different components. Rhein et al. (2019b) showed that the decrease of the interior transports in the western Atlantic is driven mostly by the transports east of 37°W (which is part of the interior transport component in this thesis). Meanwhile, the decrease of the western components and the basin-wide AMOC, as seen in VIKING20X, is driven by a decrease in the NAC. The dominant role of the NAC in setting the AMOC volume transport at 47°N in VIKING20X is also evident from the spectral estimates of the individual AMOC components at 47°N (Figure 4.5). Together with the interior transport, the NAC dominates the variability on all timescales.

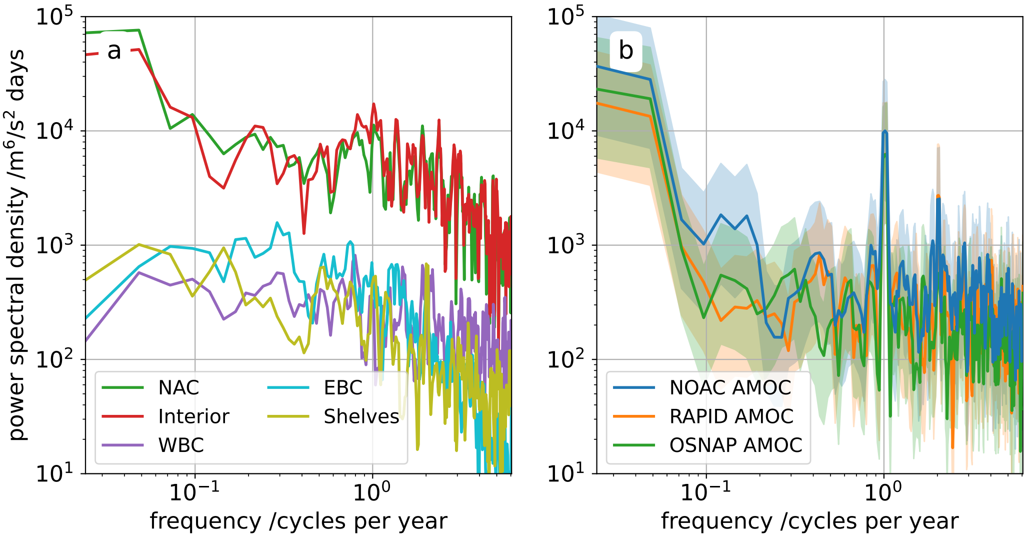

Figure 4.5: Multitaper spectral estimates for the individual AMOC components at the NOAC line in VIKING20X (for the sake of clarity, uncertainty estimates are not shown) (a) and the basin-wide AMOC estimates at the NOAC, RAPID, and OSNAP lines, including 95% uncertainty estimates (b) (time-bandwidth product P=2 for a and b). The calculation is based on code by Lilly (2022).

The different evolution of the NAC in VIKING20X and observations appears to stem from a physical difference between the model and the observations since the NAC does not show a decrease in the observations (Figure 4.3). As described in Section 4.1, the decreasing AMOC in VIKING20X in the recent decades, dominated by a decrease of the NAC volume transport, is probably related to decadal variability arising from decreasing convection activity after the 1990s maximum and salinity feedback of the forced model. In the following section, the reasons for this decreasing AMOC will be investigated in more detail.

4.2 Reasons for a decreasing AMOC in VIKING20X

Forced model simulations can be used to investigate past AMOC variability. In VIKING20X, the AMOC shows a weakening trend from the mid-1990s until 2010 (Section 4.1). However, such a consistent weakening is not visible in the AMOC observations at the NOAC array at 47°N (Chapter 3) or the RAPID array at 26°N (Moat et al., 2020). In the following, the reasons and basin-wide imprints of the weakening AMOC in VIKING20X are discussed and compared to the observation-based ARMOR3D data set.

4.2.1 VIKING20X

The period of the strongest negative trend in the AMOC volume transports in VIKING20X coincides with the observational period of the NOAC array (1993-2018). Thus, to ensure the best comparability with observations, the trends of the upper ocean parameters temperature, salinity, potential density, and SSH are analyzed in VIKING20X in 1993-2018.

Figure 4.6 (a) shows the upper 700 m temperature trends in the North Atlantic. In the central subpolar North Atlantic, along the pathway of the NAC, a significant cooling (exceeding -0.2 °C yr^{-1} in some regions) is visible while the rest of the North Atlantic is warming. This pattern of anomalies in VIKING20X is also reported by Fox et al. (2022), who attribute the exceptional cooling to reduced Labrador Sea surface heat loss. The strongest warming trends are found in the Gulf Stream region along the North American coast. This warming along the coast is probably due to a northward shift of the Gulf Stream, which has been associated with a decreasing AMOC in models (Joyce & Zhang, 2010) and observations (Smeed et al., 2018; Caesar et al., 2018). Qualitatively, this fingerprint of a slowdown of the AMOC is in line with the findings by Caesar et al. (2018). They found a widespread cooling of SSTs in the central subpolar North Atlantic over almost 150 years and attributed it to a weakening of the AMOC by about 3 Sv since the mid-20th century. Similarly, VIKING20X shows a significant cooling in the central subpolar North Atlantic (Figure 4.6 a), mostly along the NAC pathway. Though Caesar et al. (2018) used a much longer time series of almost 150 years (while only 25 years are analyzed in VIKING20X) and reported a much weaker trend, the resulting pattern is similar.

The cooling in the subpolar North Atlantic in VIKING20X coincides with a widespread significant freshening of more than -0.03 PSU yr^{-1} in the subpolar North Atlantic (Figure 4.6 b). In contrast to the cooling, the freshening is more widespread and significant throughout the subpolar North Atlantic. This indicates that the freshening of the North Atlantic is not purely driven by a decreasing NAC but also by other factors influencing the salinity in the subpolar North Atlantic, for example, freshwater input from melting glaciers in Greenland, which has been shown to potentially induce a future AMOC decline (Bakker et al., 2016). In a precursor of VIKING20X, Böning et al. (2016) showed that the freshwater supplied by the enhanced melting of Greenland glaciers influences the surface salinity of the Labrador Sea, though they could not yet detect an influence on the present AMOC. Martin & Biastoch (2023) analyzed the effect of enhanced Greenland freshwater runoff in model experiments. They found that in coupled and forced models, the response to enhanced Greenland runoff is a widespread freshening of the subpolar North Atlantic. In the forced model experiments they found a stronger freshening than in the coupled experiments due to the stronger decline of the AMOC in these experiments that is driven

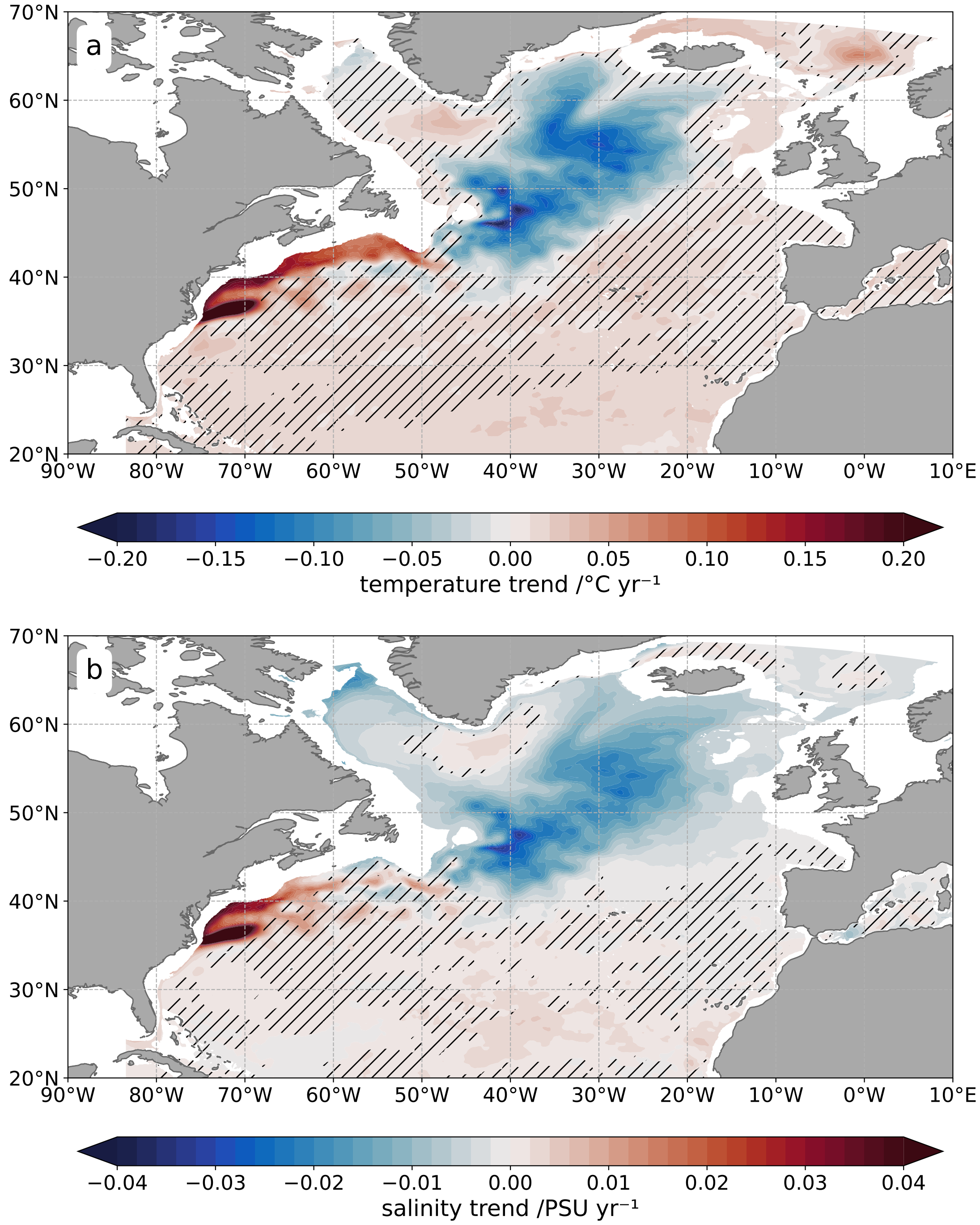

Figure 4.6: 1993-2018 temperature (a) and salinity (b) trends in the upper 700 m in the North Atlantic from VIKING20X. Only trends for regions with depths >700 m are shown. Regions with insignificant trends are hatched.

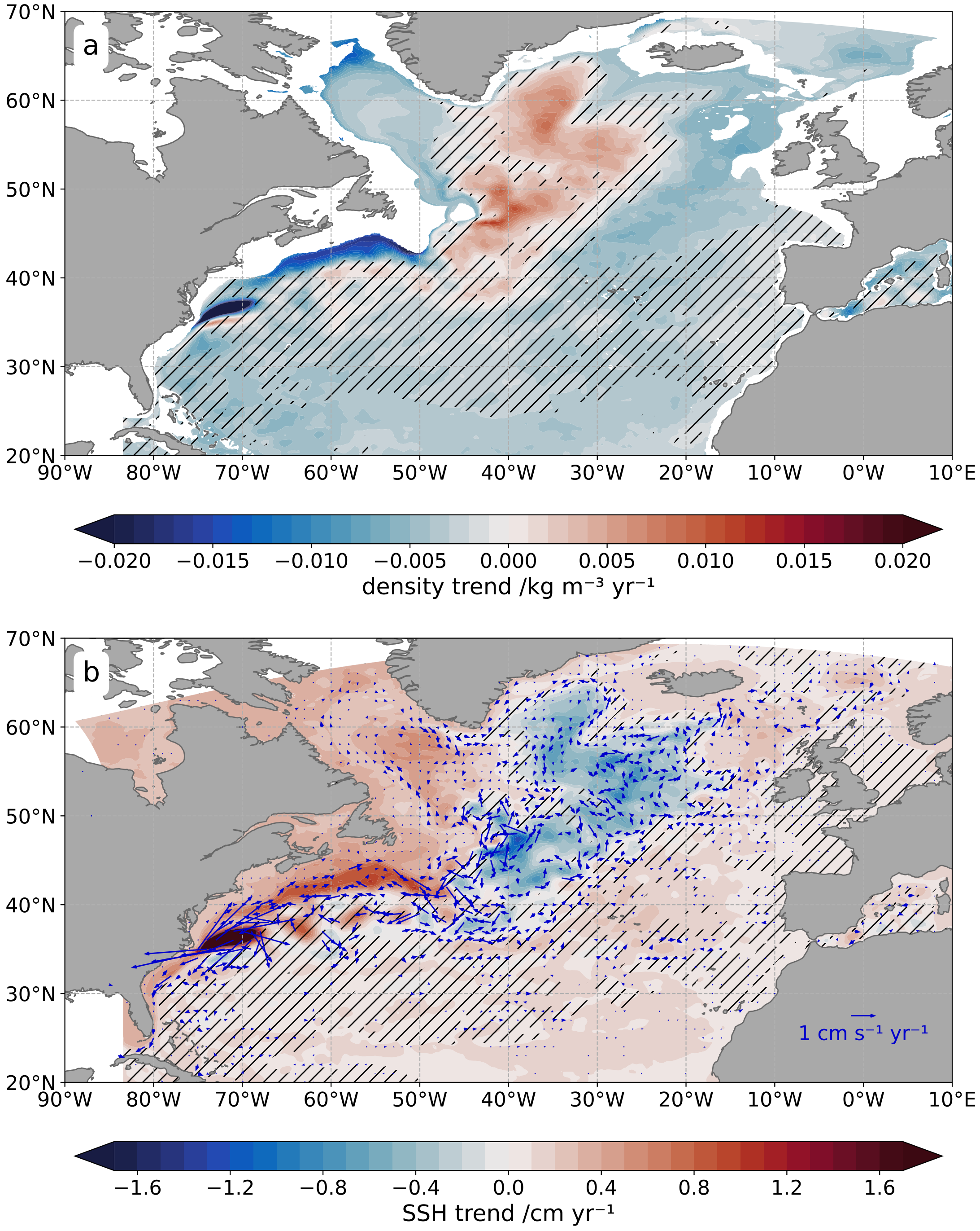

Figure 4.7: (a) 1993-2018 trends of upper 700 m density from VIKING20X. Only trends for regions with depths >700 m are shown. Regions with insignificant trends are hatched. (b) 1993-2018 trends of SSH in the North Atlantic from VIKING20X. Regions with insignificant trends are hatched. Blue arrows denote upper 700 m velocity trends. Only significant velocity trends are shown.

by the stronger sensitivity of forced models to a positive salinity feedback.

As the cooling, the freshening in VIKING20X is strongest along the pathway of the NAC (Figure 4.6 b). This indicates that the reduction of the AMOC and the associated decrease in salinity imported into the subpolar North Atlantic is responsible for the strong freshening. The reduction of the AMOC volume transport is likely a result of the salinity feedback, which is known to affect forced model simulations (Section 1.5).

The resulting density pattern (Figure 4.7 a), determined by temperature and salinity, resembles the inverse of the temperature pattern with significant positive density trends in the central subpolar North Atlantic along the pathway of the NAC and significant density decrease in the Labrador Sea and in the Eastern subpolar North Atlantic. The density pattern allows the determination of the dominance of temperature or salinity on the density. While the density changes in the central subpolar North Atlantic (where the temperature and the salinity are decreasing) might be driven by a combination of temperature and salinity changes, the density changes in the remainder of the North Atlantic (where only the temperature is weakly increasing) are driven by temperature rather than salinity.

Rhein et al. (2019b) analyzed the top-bottom transport decline in the western Atlantic at 47°N and found that the decline was linked to trends in the SSH pattern (their Figure 11). This pattern shows a relatively strong increase of the SSH at the western boundary along the North American coast, a weaker but positive trend at the eastern boundary, and insignificant, slightly negative trends in the interior. Häkkinen et al. (2016) compared SSH and ocean heat content (OHC) data, finding a similar pattern in the OHC. This indicates that the pattern of differential evolution of the SSH in the North Atlantic is a result of differential warming of the ocean. The pattern of SSH trends in VIKING20X (Figure 4.7 b) strongly resembles the inverse pattern of the temperature trends (Figure 4.6 a), indicating that, in VIKING20X, the change in SSH is indeed driven by the change in OHC. This SSH pattern is closely related to the decrease in the NAC volume transport imprinting on the basin-wide AMOC volume transport in VIKING20X. However, from this analysis, it is not possible to determine if the cooling in the subpolar North Atlantic is driven by the slowdown of the AMOC, vice versa, or a mixture of both.

The decrease of the AMOC after the 1990s is dominated by a decreasing NAC volume transport (Figure 4.3). Such behavior is not visible in the observations at the NOAC array (Figure 3.3). In VIKING20X, this slowdown of the NAC is responsible for the strong temperature and salinity trends in the subpolar North Atlantic along the pathway of the NAC. The velocity trends in the North Atlantic, primarily determined by the SSH trend, also show the slowdown of the NAC (Figure 4.7 b). This slowdown is visible as velocity trends pointing in the opposite direction as the flow path of the NAC. Especially in the Northwest Corner, there are strong indications for a slowdown. These trends propagate further into the subpolar North Atlantic and manifest as a slowdown of the flow around the Reykjanes ridge and the east Greenland current. However, in the Gulf Stream region south of Nova Scotia and Newfoundland, no significant slowdown is visible in VIKING20X. Instead, at the northern edge of the Gulf Stream pathway, a small but significant positive trend of the northeastward velocities is visible, possibly associated with a broadening of the Gulf Stream path. At Cape Hatteras, where the Gulf Stream detaches from the North American coast, a strong warming and salinity increase is associated with the formation of an eddy just east of Cape Hatteras. Since the NAC shows a slowdown along its pathway in the Northwest Corner and downstream from there, but no slowdown and even a slight increase in velocities upstream of the Northwest Corner, the excess water needs to be exported out of the Gulf Stream pathway. This export occurs south of Nova Scotia and Newfoundland, where an increased recirculation is visible in the velocity trends that transports the water back southward with the subtropical gyre.

The AMOC at the RAPID line in VIKING20X shows a similar negative trend since the mid-1990s, though not as strong as at the NOAC line. However, at 26°N, the upper 700 m velocity trends (Figure 4.7 b) do not show any significant decrease at specific locations, as they do for the NAC in the subpolar North Atlantic. Without having analyzed the individual components of the AMOC volume transport at the RAPID and OSNAP lines, it is possible to speculate that the change in the AMOC at the RAPID line in VIKING20X is probably widespread over the full basin and cannot be attributed to a single component of the upper 700 m.

4.2.2 Comparison with ARMOR3D

In contrast to the AMOC in VIKING20X at the NOAC line, the AMOC, calculated from ARMOR3D at the same latitude, does not show a significant negative trend (Section 3.8.1). For a comparison with observations, the same analysis of the trends throughout the North Atlantic in the NOAC observational period is done for the observation-based ARMOR3D data set.

Like VIKING20X, ARMOR3D exhibits a cooling of the central subpolar North Atlantic. However, the cooling has a much smaller magnitude and is found in a more confined area (Figure 4.8 a). The pattern also shows the warming in the Gulf Stream region, indicating a northward shift and broadening of the Gulf Stream. Like in VIKING20X, the pattern of the temperature trends qualitatively agrees with the pattern found by Caesar et al. (2018). Compared with VIKING20X, the cooling in the central subpolar North Atlantic and the warming in the Gulf Stream region is less pronounced, not exceeding 0.1 °C yr^{-1}. A very similar pattern is found for the ARMOR3D salinity trends (Figure 4.8 b) with a freshening in the central subpolar North Atlantic and an increase in salinity in the Gulf

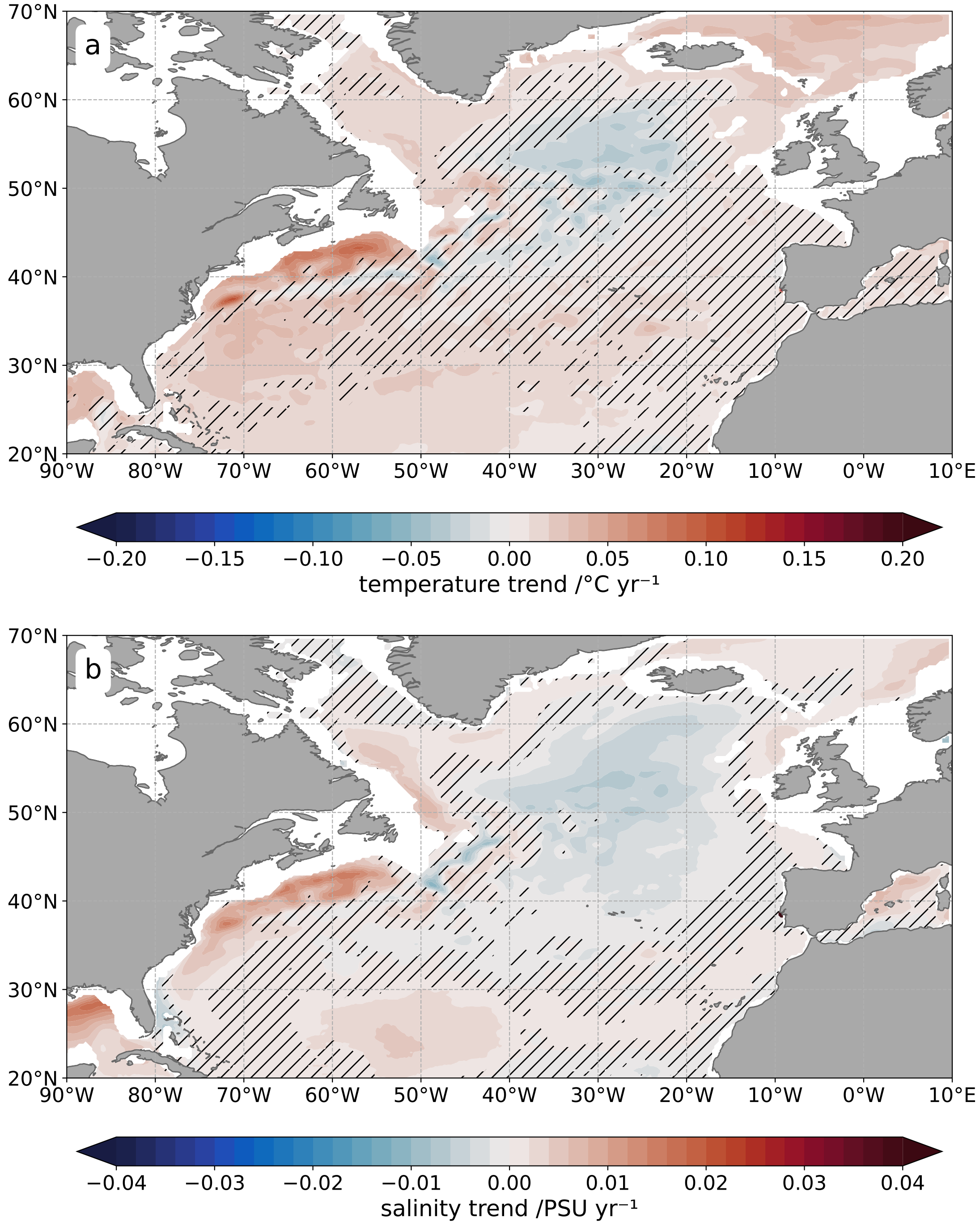

Figure 4.8: 1993-2018 temperature (a) and salinity (b) trends in the upper 700 m in the North Atlantic from ARMOR3D. Only trends for regions with depths >700 m are shown. Regions with insignificant trends are hatched.

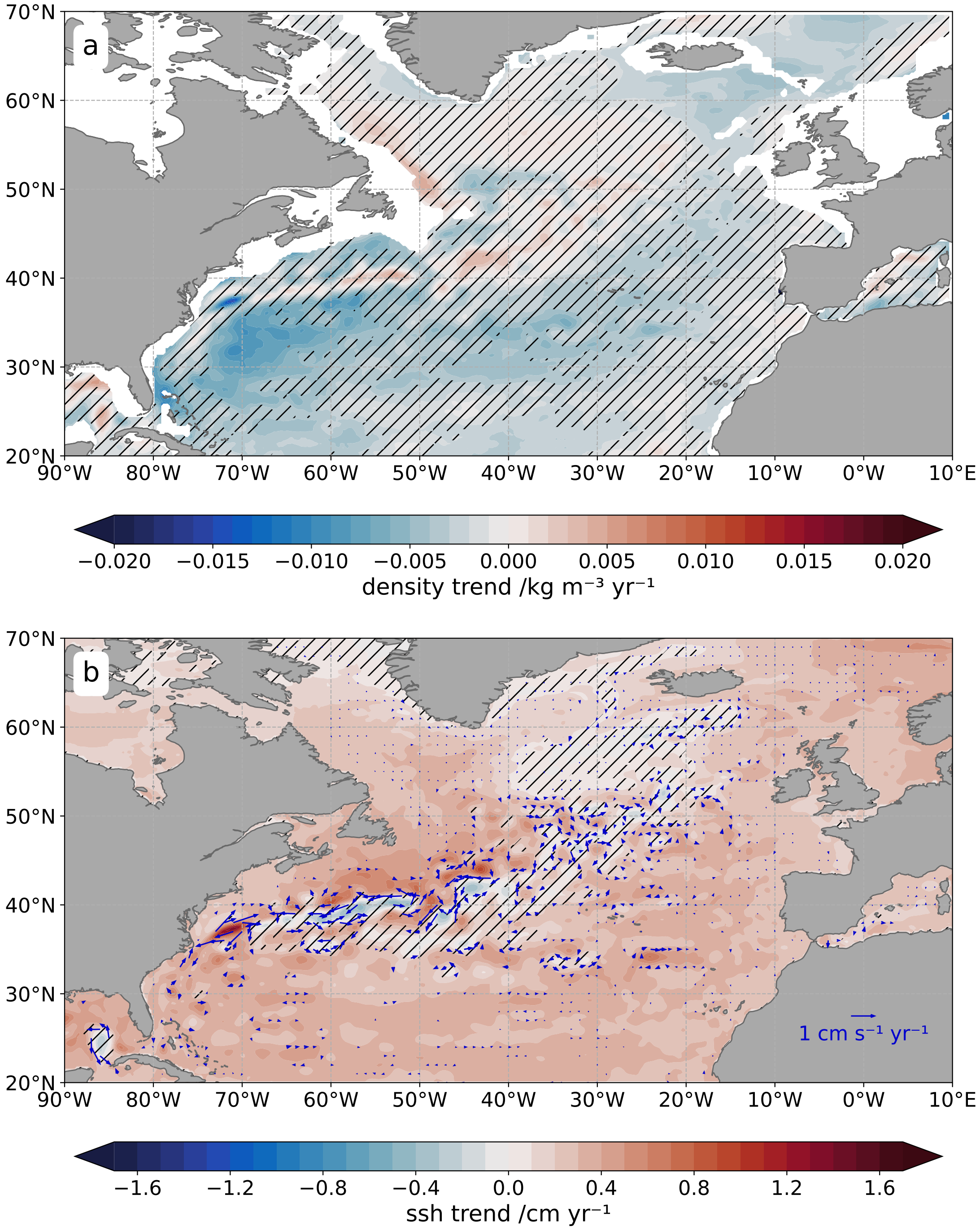

Figure 4.9: (a) 1993-2018 trends of upper 700 m density from ARMOR3D. Only trends for regions with depths >700 m are shown. (b) 1993-2018 trends of SSH in the North Atlantic. Regions with insignificant trends are hatched. Blue arrows denote upper 700 m ARMOR3D geostrophic velocity trends. Only significant velocity trends are shown.

Stream region. However, as for the ARMOR3D temperature trends, the magnitude and extent of the freshening and salinity increase (not exceeding 0.1 PSU yr^{-1}) is lower than in VIKING20X.

The ARMOR3D density pattern in the North Atlantic does not show a widespread significant trend (Figure 4.9 a). A pattern is visible similar to the one found in VIKING20X with small regions of significant density trends. However, the density trends in the subpolar North Atlantic are largely insignificant. Due to the smaller magnitude of the temperature and salinity trends, the changes in the density are too small to be statistically significant. The SSH trends show a similar evolution of the SSH in the North Atlantic as in VIKING20X (Figure 4.9 b). However, the negative trends in the central subpolar North Atlantic are insignificant and not as widespread as in VIKING20X since the SSH is influenced by the temperature (Häkkinen et al., 2016), and VIKING20X appears to overestimate the cooling in the subpolar North Atlantic. However, the SSH pattern explains the decrease of top-bottom volume transports in the western components, as reported in Rhein et al. (2019b). The influence of the SSH pattern on the velocity can be directly seen from the ARMOR3D velocity trends (Figure 4.9 b, note that for ARMOR3D these are only the geostrophic transports). The SSH changes in the Gulf Stream region south of Nova Scotia and Newfoundland, at about 40°N, coincide with southwestward velocity trends. However, these trends are likely not a direct indication of a weakened Gulf Stream but an imprint of a shifted and broadened Gulf Stream pathway. The significant velocity trends are mostly localized between the observational arrays at 26°N and 47°N. In line with the observations at the NOAC array at 47°N, the velocity trends at the NOAC array do not show a clear weakening signal in Figure 4.9 (b). Significant trends at 47°N are focused on the interior, pointing in multiple directions. A weakening of the NAC at 47°N or of the circulation in the Northwest Corner, as in VIKING20X, is not visible in the ARMOR3D velocity trends.

VIKING20X exhibits a strong and persistent AMOC weakening in 1993-2018 and the associated fingerprint throughout the North Atlantic (Figure 4.6). This fingerprint includes a cooling in the central subpolar North Atlantic and a northward shift of the Gulf Stream (Caesar et al., 2018). The cooling coincides with a freshening and an increase in density in the central subpolar gyre. A similar pattern, but with a smaller magnitude, is visible in the observation-based ARMOR3D data set (Figure 4.8) over the same period. Additionally, this pattern is consistent with the pattern of trends in the EN4 data set (Figure A.7).

The temperature and salinity trends seen in ARMOR3D are small, and negative trends are significant only in the center of the subpolar gyre. The pattern of these trends exhibits qualitative similarities with trend patterns associated with an AMOC decrease based on proxy observations and models (Caesar et al., 2018; Drijfhout et al., 2012). However, these proxy observations and models are associated with uncertainties (Menary et al., 2020; Little et al., 2020). The shape of the ARMOR3D temperature and salinity patterns indicates a reduced northward transport of warm and saline waters with the NAC. This decrease could be interpreted as an indication of a weakening AMOC in the recent decades. However, while in VIKING20X, the basin-wide AMOC at different latitudes in the North Atlantic, as well as the NAC at 47°N, show a weakening over the recent decades, the AMOC calculated based on ARMOR3D does not exhibit a decrease of the AMOC volume transport (Figure 3.8 b).

As of now, AMOC monitoring arrays and estimates based on gridded data sets do not show a persistent weakening trend, neither in the subtropical gyre (RAPID, Moat et al., 2020), the subpolar gyre (OSNAP, Lozier, 2023) or the boundary between the two regimes (NOAC, ARMOR3D, estimate by Desbruyères et al. (2019), Chapter 3). However, the strength of the variability on a multitude of timescales surprised scientists since direct observations of the AMOC started at the RAPID array in 2004. After all, the AMOC is influenced by many factors on multiple spatial and temporal scales. Possible trends in the AMOC volume transport as found by Caesar et al. (2018) are very small (3 Sv over 147 years) and thus masked by strong inter-annual and decadal variability of different origin. Thus, the absence of a detectable trend in direct AMOC observations does not disagree with weak proxy trends over a much longer time associated with anthropogenic warming (Jackson et al., 2022).

4.3 Meridional Connectivity in VIKING20X

The NOAC AMOC observations reveal a significant lagged correlation with the RAPID AMOC observations, indicating meridional connectivity (Section 3.7). However, the analysis of meridional connectivity in the observations is limited by the length of the observational time series. Generally, models offer the chance to analyze the meridional connectivity in greater detail, especially for longer time series. AMOC connectivity in models has been shown to originate from coherent buoyancy forcing on longer than decadal timescales (Biastoch et al., 2021; Gu et al., 2020). However, on inter-annual timescales, connectivity is less clear (Bingham et al., 2007).

Biastoch et al. (2021) analyzed inter-annual and decadal AMOC coherence in VIKING20X using Hovmöller diagrams across the full latitude range of the Atlantic. In agreement with earlier studies (Yeager & Danabasoglu, 2014; Biastoch et al., 2008a), they found a coherent signal at decadal timescales. AMOC anomalies on shorter timescales merely add noise to the picture. Generally, anomalies propagate from the subpolar to the subtropical North Atlantic within a few months in VIKING20X (Biastoch et al., 2021). However, between about 40-50°N, a significant delay in the coherence is visible due to the complex

Table 4.4: Correlation of the AMOC volume transport time series at the NOAC, RAPID, and OSNAP lines in VIKING20X for the two-month averaged and the low-pass filtered time series. Significant correlations are marked in bold.

	NOAC vs. RAPID	OSNAP vs. NOAC	OSNAP vs. RAPID
2-month averages	0.13	**0.42**	0.04
low-pass filtered	**0.70**	**0.85**	0.60

interaction of the subtropical and the subpolar gyre (Zou et al., 2019, in a precursor of VIKING20X).

In the following, the meridional connectivity of the AMOC in VIKING20X at the NOAC, RAPID, and OSNAP lines is analyzed. A striking feature of the AMOC volume transport time series at the NOAC, RAPID, and OSNAP lines is the similar decadal variability with a minimum in the 1970s, a maximum in the 1990s, and a decrease after that (Figure 4.2). This similarity aligns with the findings of Biastoch et al. (2021), who found coherent decadal AMOC evolution in VIKING20X throughout the Atlantic. The instantaneous correlations of the two-month averages of the AMOC at the different array lines are low (Table 4.4). Biastoch et al. (2021) noted the appearance of the strongest AMOC anomalies in the subpolar gyre. This is reflected in the correlations, which are highest between the NOAC and OSNAP lines (0.42). In fact, for the two-month averages, this is the only significant correlation between the different mooring positions. The low-pass filtered time series of the AMOC transport at the different mooring lines are significantly correlated, except between OSNAP and RAPID (NOAC vs. RAPID: 0.7, OSNAP vs. NOAC: 0.85, OSNAP vs. RAPID: 0.6, Table 4.4). The correlation is strongest between the OSNAP and NOAC lines in the subpolar North Atlantic (closest to each other) and weakest between the OSNAP and RAPID lines (farthest from each other). The correlations are even stronger and remain significant when the filtering window is enlarged (not shown).

In the observational AMOC estimate of the NOAC array, a significant lag correlation was found with the RAPID AMOC estimate, where AMOC anomalies at the NOAC array preceded those at the RAPID array (Section 3.7). In the following, VIKING20X is investigated to assess whether this lag between NOAC and RAPID is reproduced and whether the lag extends further north to the OSNAP line. The lag correlations are calculated between the NOAC, RAPID, and OSNAP lines and displayed for all combinations (i.e., NOAC leads RAPID, OSNAP leads NOAC, and OSNAP leads RAPID). The unfiltered monthly AMOC time series show increased lag correlation every 12 months (Figure 4.10 a). This correlation is due to the seasonal cycle in all three time series. These maxima in the lag correlations are shifted due to the shift of the seasonal cycles between the different positions of NOAC, RAPID, and OSNAP, possibly similar to the out-of-phase connectivity found by Mielke et al. (2013) within the subtropical gyre. When the seasonal

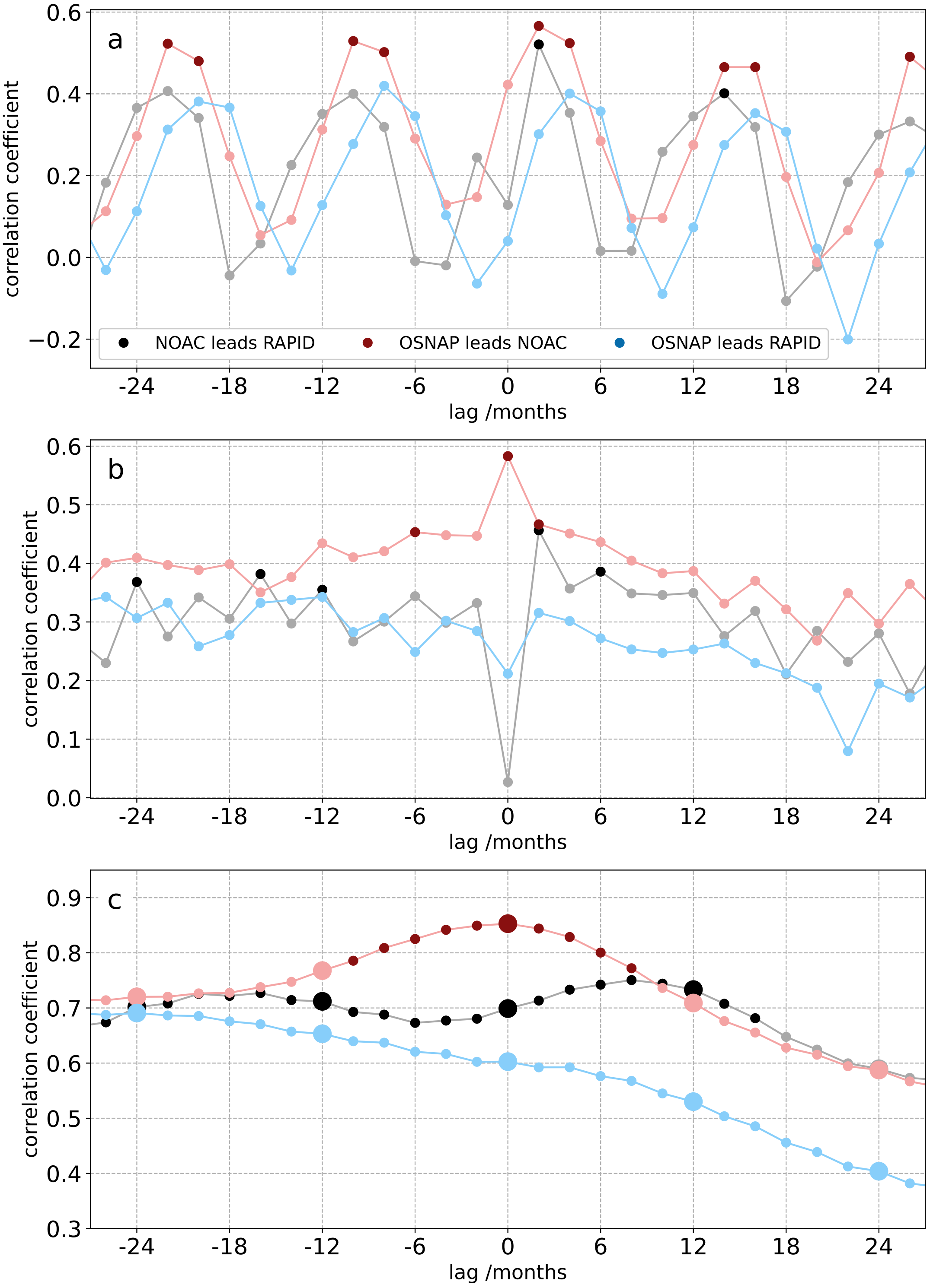

Figure 4.10: Lag correlations of the AMOC time series from VIKING20X, calculated at the NOAC, RAPID, and OSNAP lines. The panels show the unfiltered time series (a), the unfiltered time series with the seasonal cycle removed (b), and the low-pass filtered time series (c). For the low-pass filtered time series, values whose interpretation is valid according to the Nyquist-Shannon theorem (Section 2.6.1), are plotted as enlarged markers. Significant correlations are denoted as dark colors. Note the different y-axis scales for (a), (b), and (c).

cycle is removed from the data, there is hardly any lagged meridional connectivity visible in the unfiltered data (Figure 4.10 b). However, the correlation between the AMOC at the NOAC and the OSNAP line at lag zero remains high when the seasonal cycle is removed, indicating increased instantaneous connectivity in the subpolar gyre compared to the instantaneous connectivity between the NOAC and RAPID lines.

In agreement with observations, VIKING20X exhibits increased significant lag correlation of the low-pass filtered time series at the NOAC and RAPID lines when the NOAC AMOC leads by about one year (Figure 4.10 c). Though the lag correlations of the two-month averages are also significant at 14 months lag between NOAC and RAPID (Figure 4.10 a), this significant correlation is caused by the shifted seasonal cycles and vanishes when the seasonal cycle is removed. However, the low-pass filter used has a cutoff period of two years, thus removing influences of the seasonal cycle. The correlations between the locations of the other arrays do not show increased correlations at specific lags. However, the correlation between the low-pass filtered AMOC time series at the OSNAP and NOAC lines in VIKING20X at zero lag is particularly high.

Models offer the chance to investigate the connectivity and the associated timescale of the AMOC in more detail and disentangle the physical processes that connect the AMOC between different latitudes. VIKING20X exhibits connectivity of the two-month averages due to a shift of the seasonal cycles. However, this connectivity vanishes when the seasonal cycle is removed. The lag correlation of the low-pass filtered time series exhibits a significant maximum between the NOAC and RAPID AMOC when the NOAC AMOC leads by about one year. This agrees with the results from the observations (Section 3.7). However, in VIKING20X, the maximum is not as distinct as in the observations, and high and significant correlations are found over a range of lags.

The similarities found in the connectivity analysis in observations and VIKING20X indicate that the lagged correlation between NOAC and RAPID is induced by a physical mechanism present in the observations and the model. Possibly, a lagged response to interannual large-scale wind field changes or advection in the lower limb of the AMOC could be driving the connectivity. Further work on VIKING20X, including a detailed analysis of the individual mechanisms driving AMOC variability and the associated timescales, could answer this question. However, the remaining differences between VIKING20X and observations regarding the meridional connectivity highlight the importance of continuous AMOC observations at different latitudes to validate model experiments and subsequently use observations and models to understand the physical processes determining AMOC connectivity across latitudes.

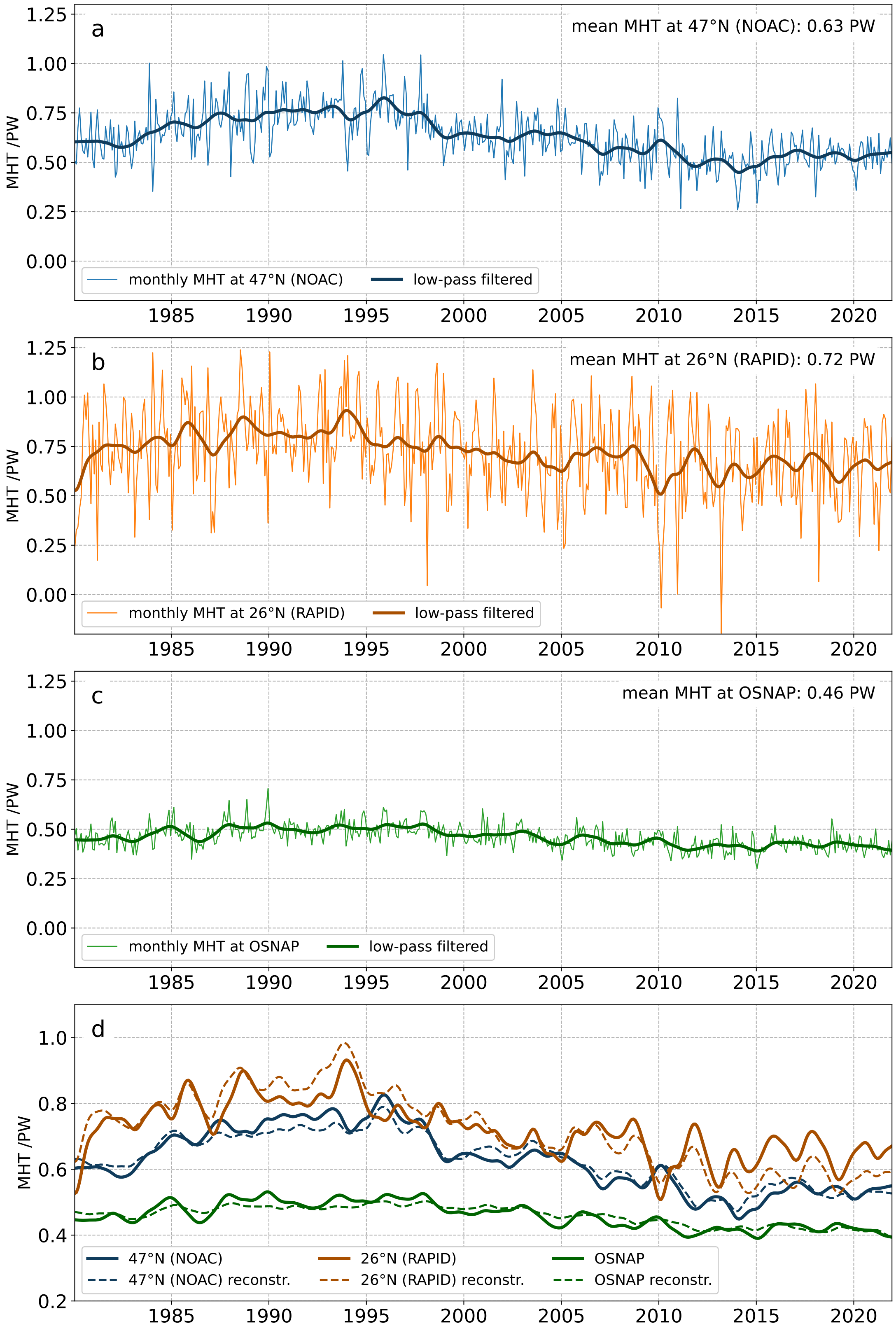

Figure 4.11: Monthly time series of MHT from VIKING20X calculated at the NOAC (a), RAPID (b), and OSNAP (c) lines. The dark lines denote the low-pass filtered time series. (c) Comparison of the low-pass filtered time series at NOAC, RAPID, and OSNAP. The dashed lines denote the reconstruction of the MHT based on a linear regression with the AMOC volume transport. Note that the panels are not ordered by latitude.

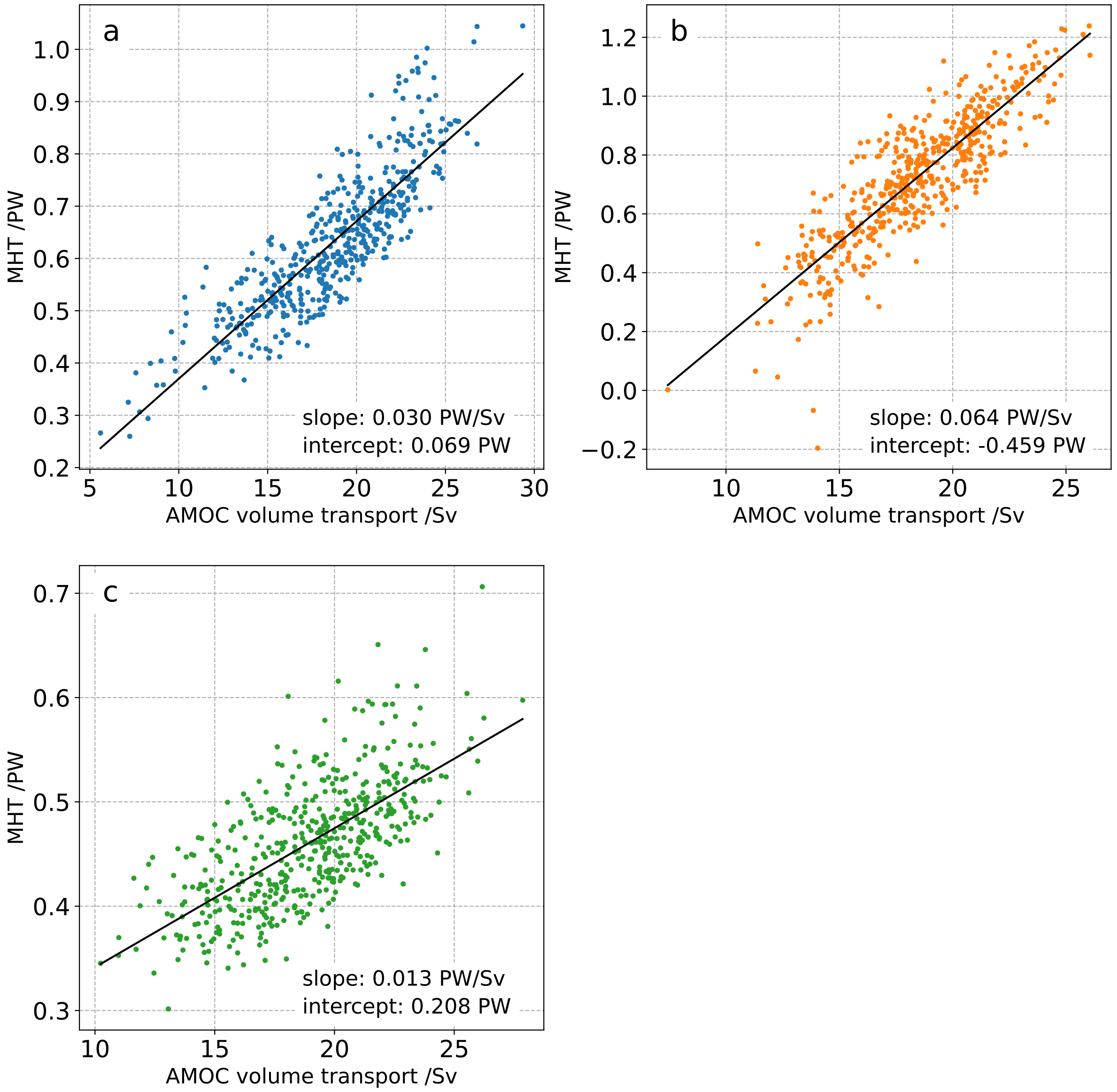

Figure 4.12: AMOC volume transport in VIKING20X at the NOAC (a), RAPID (b), and OSNAP (c) lines, plotted against the respective MHT. The black line denotes the linear regression. Slope and intercept are given in the lower right corner. Note the different scales of the axes on each subplot and that the panels are not ordered by latitude.

4.4 MHT in the North Atlantic in VIKING20X

While AMOC volume transport is a widely discussed climate parameter, the transported quantities like salinity and temperature strongly influence the ocean and atmosphere. The warm water flowing northwards in the Atlantic releases heat to the atmosphere and, together with the prevailing westerly winds, results in comparatively mild temperatures in Europe. Thus, the MHT is of particular interest for European and global weather.

Using the concept of geostrophy, a moored observing system is capable of monitoring the

Table 4.5: Correlation of the MHT and the AMOC volume transport at the NOAC, RAPID, and OSNAP lines in VIKING20X for the two-month averages and the low-pass filtered time series. Significant correlations are marked in bold.

	NOAC	RAPID	OSNAP
2-month averages	**0.64**	**0.63**	0.3
low-pass filtered	**0.95**	**0.88**	**0.83**

volume transports across the Atlantic with relatively few instruments placed over a large distance. However, monitoring the MHT on a basin scale cannot be done in the same way. In contrast to the volume transport, where the measurements from two moorings allow calculating the net volume transport between them, calculating the MHT requires knowledge of the velocity and the temperature over the entire section at high resolution in space and time. Thus, estimates of the MHT in the North Atlantic either rely on a high coverage of the section with hydrographic data (e.g., Johns et al., 2011) or require the temperature and velocity fields obtained from ocean models (e.g., Msadek et al., 2013) or gridded data sets like EN4 or ARMOR3D. Thus, VIKING20X offers the chance to investigate the MHT and its connection with the AMOC at the latitudes of the observational arrays in the North Atlantic.

The low-pass filtered MHT at all three array lines shows a maximum in the mid-1990s (Figure 4.11). After that maximum, the MHT decreases until about 2010 and remains constant after that. Generally, at the NOAC, RAPID, and OSNAP lines, the inter-annual evolution of the MHT is closely linked to the AMOC volume transport in VIKING20X (Figure 4.12). The mean MHT is strongest at the RAPID line (0.72 PW, SEM: 0.01 PW), followed by the NOAC line (0.63 PW, SEM: 0.01 PW, larger than the MHT at 47°N, based on ARMOR3D) and the OSNAP line (0.46 PW, SEM: $<$0.01 PW). A similar behavior of stronger correlation between the MHT and the AMOC volume transport in the subtropical North Atlantic, compared to the subpolar regime, was found by Biastoch et al. (2008a) in a precursor of VIKING20X. They associated this with the stronger baroclinicity of the subtropical Atlantic with weaker zonal temperature differences.

The MHT variability in VIKING20X varies with latitude. The strongest seasonal variability is found at the RAPID line (STD: 0.22 PW), followed by the NOAC line (STD: 0.13 PW), where decadal variability is more pronounced, and OSNAP (STD: 0.06 PW), where weaker variability on inter-annual and seasonal timescales is visible. Given the important role of the AMOC for the MHT this is in line with statements by Buckley & Marshall (2016) and Jackson et al. (2022). They stated that seasonal AMOC variability is dominant in the subtropics, while decadal variability dominates the AMOC in the subpolar regions. The fact that this connection is more obvious in the MHT than it is in the volume transports (Figure 4.2) indicates that the MHT at the RAPID line is more

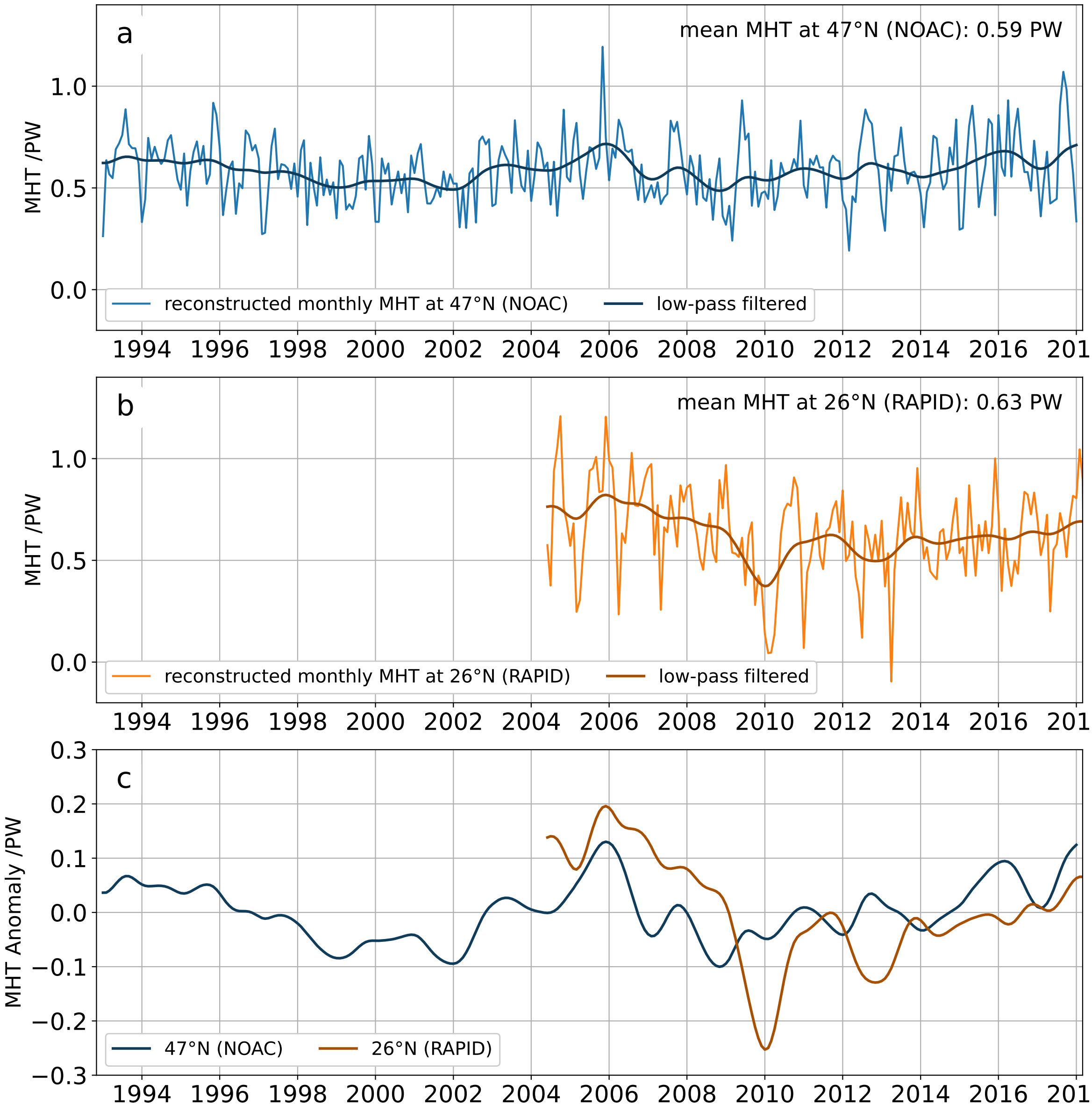

Figure 4.13: Reconstructed MHT at 47°N (NOAC) (a) and at 26°N (RAPID) (b), based on the linear relationship between volume transport and MHT, found in the VIKING model and the volume transport measurements at both arrays. The dark lines represent the low-pass filtered AMOC. (c) comparison of the MHT anomaly of the low-pass filtered time series.

dominated by the variations in the temperature rather than in the volume transport.

However, the MHT in VIKING20X at the RAPID line also significantly correlates with the AMOC volume transport. The correlations between the monthly MHT and the AMOC volume transport are ≥ 0.63 and significant at the NOAC and RAPID lines and 0.3 and insignificant at the OSNAP line (Table 4.5). The correlations of the low-pass filtered time series are even higher and ≥ 0.88 at the three array lines, indicating that the variability of the MHT and the AMOC volume transport are closely related in VIKING20X.

The close connection between the AMOC volume transport and the MHT is also reported in the literature (Buckley & Marshall, 2016; Johns et al., 2011). To first order, there is a linear relationship between the AMOC volume transports and the MHT, which can be modeled using a linear regression model. Figure 4.12 shows the AMOC volume transport at the NOAC, RAPID, and OSNAP lines in VIKING20X, plotted against the MHT. For the NOAC and RAPID lines, the MHT correlates well with the AMOC volume transport. Thus, the scattered dots follow a straight line in the Figure, though with different slopes and intercepts. At the OSNAP line, the linear relation is less clear due to the insignificant correlation (Table 4.5). Based on these values, slope, and intercept, the parameters of the linear regression model can be determined, enabling a reconstruction of the MHT given only the volume transport. The accuracy of the linear regression model is given by the correlation between the MHT and the AMOC volume transport at each array line (Table 4.5). Thus, the accuracy is best for the RAPID line (Figure 4.12 b), followed by the NOAC line (Figure 4.12 a). To test the accuracy of the reconstruction of the MHT, the MHT in VIKING20X is calculated from the volume transport using the linear regression model (Figure 4.11 d, dashed lines) and compared to the MHT, calculated from the full velocity and temperature field (Figure 4.11 d, solid lines). Notably, at the NOAC line, the error of the MHT reconstruction is strongest in times of strong AMOC values, like in the early and mid-1990s, while the agreement is closer during times of medium and low AMOC values. In contrast, at the RAPID line, the opposite is the case. Here, the error is strongest in weak AMOC phases, for example, after 2010. This is because, for these strong (weak) AMOC values, the relationship between the AMOC volume transport and the MHT at the NOAC (RAPID) line deviates from the strait line of the linear regression model (Figure 4.12). However, for most of the AMOC values, the linear regression model is a suitable approximation.

Though the given observation system does not allow a direct estimate of the MHT, the same linear regression model can be utilized to reconstruct the MHT from the NOAC observations (Figure 4.13). As expected from a linear model, the MHT reconstructed from the AMOC volume transport follows the variability of the AMOC volume transport. The reconstruction yields almost identical mean MHT at the NOAC (0.59 PW, SEM: 0.01 PW) and RAPID (0.63 PW, SEM: 0.02 PW) lines. Unsurprisingly, due to the good agreement in the mean AMOC volume transport, this is in line with the mean MHT values found in VIKING20X at the NOAC (0.63 PW, SEM: 0.01 PW) and RAPID (0.72 PW, SEM: 0.01 PW) lines. However, these numbers are somewhat smaller than the MHT calculated in different studies at the RAPID array (Johns et al. (2011): 1.35 PW in 2004-2007, McCarthy et al. (2015b): 1.25 PW in 2004-2012, Trenberth & Fasullo (2017): 1.00 PW in 2004-2013) and an estimate from the WOCE program (Ganachaud & Wunsch (2003): 1.27 PW). At the NOAC line, the VIKING20X MHT (0.63 PW) and the reconstructed

MHT (0.59 PW) agree closely with observational values for the MHT at the same latitude (0.6 PW, Ganachaud & Wunsch, 2003).

Models tend to yield lower MHT values than observations (Sinha et al., 2018; Stepanov et al., 2016; Msadek et al., 2013; Hui-Er & Yong-Qiang, 2012). The reasons for these discrepancies are not yet fully understood. Stepanov et al. (2016) suggested an underestimation of the southward recirculation in the upper-mid ocean transport from the RAPID methodology, which would impact the RAPID estimate of the MHT. However, whether or not the mean value of the MHT is correctly represented in VIKING20X and thus correctly reconstructed from the observed AMOC volume transport, the present analysis shows the strong linear connection between the AMOC volume transport and the MHT. Thus, a change in the AMOC volume transport will have direct implications for the MHT, making the MHT the key parameter determining the impact of the AMOC on the local climate in North America and Europe (Sutton & Hodson, 2005; Knight, 2005).

4.5 The effect of model resolution on the AMOC in the ANHA model simulations

In climate models, the representation of the AMOC at 26°N and the rate of AMOC weakening has been shown to depend on model resolution. In an analysis of Coupled Model Intercomparison Project (CMIP) Phase 6 models, Roberts et al. (2020) showed that generally, a higher resolution of the ocean models results in a stronger AMOC at 26°N, agreeing closer with RAPID observations. Jackson et al. (2020) showed that climate models with higher spatial resolution additionally exhibited a stronger AMOC weakening compared to coarser resolution models due to a more realistic representation of the circulation and, thus, more advection of saline subtropical waters. Additionally, the water mass transformation, linked to the AMOC, was shown to be more accurate in climate models with higher resolution ocean components (Oldenburg et al., 2022). These studies indicate the need for high-resolution ocean models to represent the AMOC accurately.

Models offer the possibility to investigate a specific aspect in different simulations. Since the AMOC is sensitive to small changes in the model environment, it is useful to run the desired experiments with the same configuration, varying only a single aspect whose influence on the AMOC shall be investigated. The ANHA simulations exist in different setups, where the resolution varies between ANHA4 and ANHA12. Here, the AMOC at the NOAC, RAPID, and OSNAP lines in the period 2004-2018, as well as the respective seasonal cycle, is discussed in ANHA4 and ANHA12 (Figure 4.14).

The findings from the modeled AMOC at the NOAC, RAPID, and OSNAP lines in ANHA4 and ANHA12 confirm the findings of Roberts et al. (2020) at 26°N: A higher

Table 4.6: Mean AMOC volume transport, SEM, and STD of the two-month averages in the different configurations of the ANHA NEMO model simulations at the NOAC, RAPID, and OSNAP lines. The values are calculated in the period of overlap between the model simulations and the observational period of the respective array (NOAC, RAPID: 2004-2017 for ANHA4 and ANHA12, 2007-2018 for LAB60+SPG12, OSNAP: 2014-2017 for ANHA4 and ANHA12). The OSNAP observational values cover 2014-2018 since they were obtained as values and not as a time series. Observational values are from Chapter 3 (NOAC), Moat et al. (2022, RAPID), and Baker et al. (2022, OSNAP). Note that the observational mean values are not adjusted to the different period covered by the LAB60+SPG12 simulation. However, the adjusted values are not significantly different from the values given below.

location and setup	NOAC				RAPID			OSNAP		
	1/4°	1/12°	1/60°	Obs.	1/4°	1/12°	Obs.	1/4°	1/12°	Obs.
mean /Sv	20.0	19.5	17.6	17.5	22.5	19.7	16.9	19.2	16.6	16.6
SEM /Sv	0.3	0.4	1.1	0.6	0.4	0.3	0.4	0.4	0.4	0.7
STD /Sv	3.2	3.5	8.6	5.5	3.4	2.9	3.4	2.1	2.0	7.6

ocean resolution leads to a more realistic mean AMOC strength. The same is valid at the NOAC and OSNAP lines. However, in contrast to the results of Roberts et al. (2020), the AMOC in ANHA is overestimated in the coarser resolution models. Generally, ANHA4 and ANHA12 both overestimate the mean AMOC strength at the positions of the three array lines. However, increasing the horizontal resolution from 1/4° to 1/12° yields a more realistic mean AMOC strength at the three array lines, reducing the mean AMOC strength over the full analysis period from 20.0 Sv to 19.5 Sv (NOAC), 22.5 Sv to 19.7 Sv (RAPID) and 19.2 Sv to 16.6 Sv (OSNAP), all being closer to the mean AMOC strength of the observations at the respective array (Table 4.6), though still overestimating the observational mean AMOC strength. The improvement of the mean AMOC strength is dominated by a better representation after 2009. No compensation transport is applied in the model simulations discussed here (Section 2.4). The resulting overestimation of the AMOC in the models by the amount of the inflow through the model's open boundary in the Bering Strait (1.0 Sv, Woodgate, 2018) partly explains the differences between observations and models. The change in model resolution only slightly affects the mean variability of the AMOC for the NOAC, RAPID, and OSNAP lines, exhibiting no clear improvement compared to the observations (Table 4.6). The correlation with the observations increases from ANHA4 to ANHA12 for all three arrays, though only the correlation between the ANHA12 RAPID AMOC and the RAPID observations is significant (Table 4.7). This is possibly related to the comparatively short time series. In agreement with observations, both model configurations do not show a significant overall trend of the AMOC transports at any of the array positions. This disagreement with VIKING20X presumably relates to numerical differences in the simulations (see Chapter 5).

Table 4.7: Correlations of low-pass filtered time series of the AMOC volume transports from the ANHA NEMO model simulations in different setups (ANHA4, ANHA12, LAB60+SPG12) at the NOAC, RAPID, and OSNAP lines. The last line shows the correlation with the RAPID and NOAC observations, respectively. Significant correlations are marked in bold.

location and setup		NOAC			RAPID		OSNAP	
		1/4°	1/12°	1/60°	1/4°	1/12°	1/4°	1/12°
NOAC	1/4°	×						
	1/12°	0.60	×					
	1/60°	-0.15	-0.16	×				
RAPID	1/4°	0.06	-0.41	0.25	×			
	1/12°	-0.21	0.29	-0.53	-0.29	×		
OSNAP	1/4°	**0.68**	0.51	-0.47	-0.16	0.09	×	
	1/12°	0.15	0.70	-0.18	-0.38	0.30	0.49	×
Obs.		0.43	0.59	0.09	-0.14	**0.79**		

The AMOC at the NOAC line at 47°N shows a more realistic mean value in ANHA12 compared to the ANHA4 simulation (Table 4.6). The modeled AMOC at the NOAC line shows no significant correlation with the RAPID AMOC, neither in ANHA4 nor ANHA12. In both ANHA4 and ANHA12, the inter-annual AMOC variability at the NOAC line shows a similar evolution as the observations with a strong AMOC in the mid-2000s, a minimum in 2008/09, a subsequent decrease and an increase after 2014, possibly associated with a strong NAO in that period (Figure 4.14 a). The correlation with observations increases from 0.43 in ANHA4 to 0.59 in ANHA12, though both remain insignificant.

In both ANHA4 and ANHA12, at the NOAC line, the AMOC exhibits a pronounced seasonal cycle with maximum transports in October (ANHA4) and April (ANHA12), while the observations show a maximum AMOC in November (Figure 4.15 a). In contrast to the mean AMOC strength, increasing the resolution from ANHA4 to ANHA12 does not lead to a better representation of the seasonal cycle at the NOAC line. Instead, the shape of the seasonal cycle agrees better with observations in ANHA4. This might be associated with overly strong Ekman transports in the fall, dominating the seasonal cycle. While in observations, the seasonal cycle is dominated by the geostrophic transport of the NAC and the interior transport (Section 3.2, Figure 3.1 b), model studies showed an overestimation of the Ekman contribution compared to observations (Dong et al., 2014). An investigation of the relative contributions of the geostrophic and Ekman components to the seasonal cycle of the AMOC at 47°N, though beyond the scope of this thesis, could

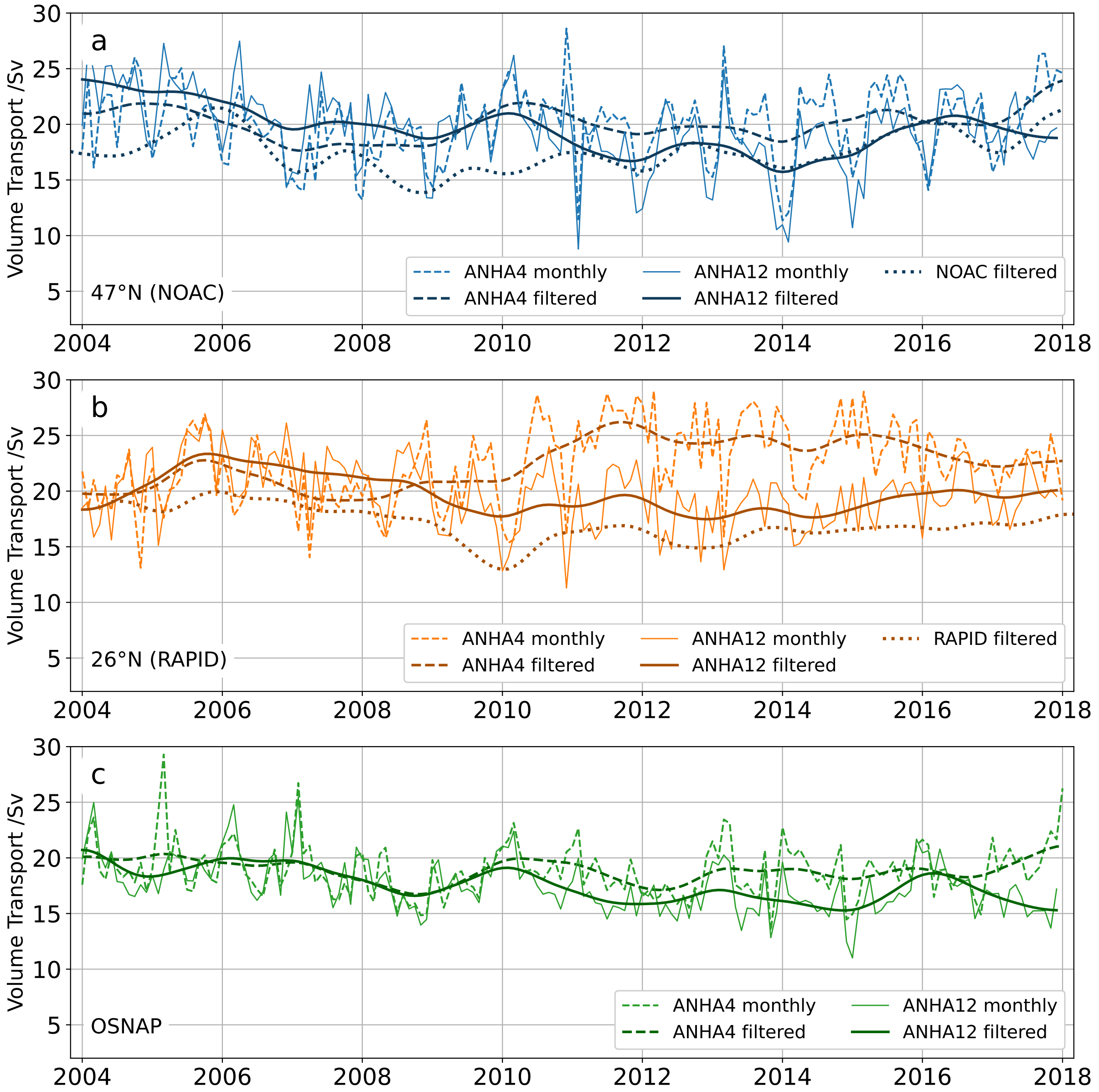

Figure 4.14: AMOC volume transport in ANHA4 (dashed lines) and ANHA12 (solid lines) at the NOAC (a), RAPID (b), and OSNAP (c) lines. The bold lines denote the low-pass filtered time series. The dotted lines denote the low-pass filtered observational time series from the NOAC and RAPID arrays. Note that the panels are not ordered by latitude.

test this hypothesis.

At the RAPID line, ANHA4 and ANHA12 simulate similar high-frequency variability (Figure 4.14 b), including the decrease in 2009, associated with a strongly negative NAO. However, after 2009, they exhibit different inter-annual variability. Following the 2010 minimum, the ANHA4 AMOC increases to a mean strength of about 25 Sv until 2016, while, in closer agreement with the RAPID observations, the ANHA12 AMOC remains at a mean strength of about 18 Sv in the same period. This deviation between ANHA4 and ANHA12 is possibly related to high-frequency and large amplitude wind-driven AMOC os-

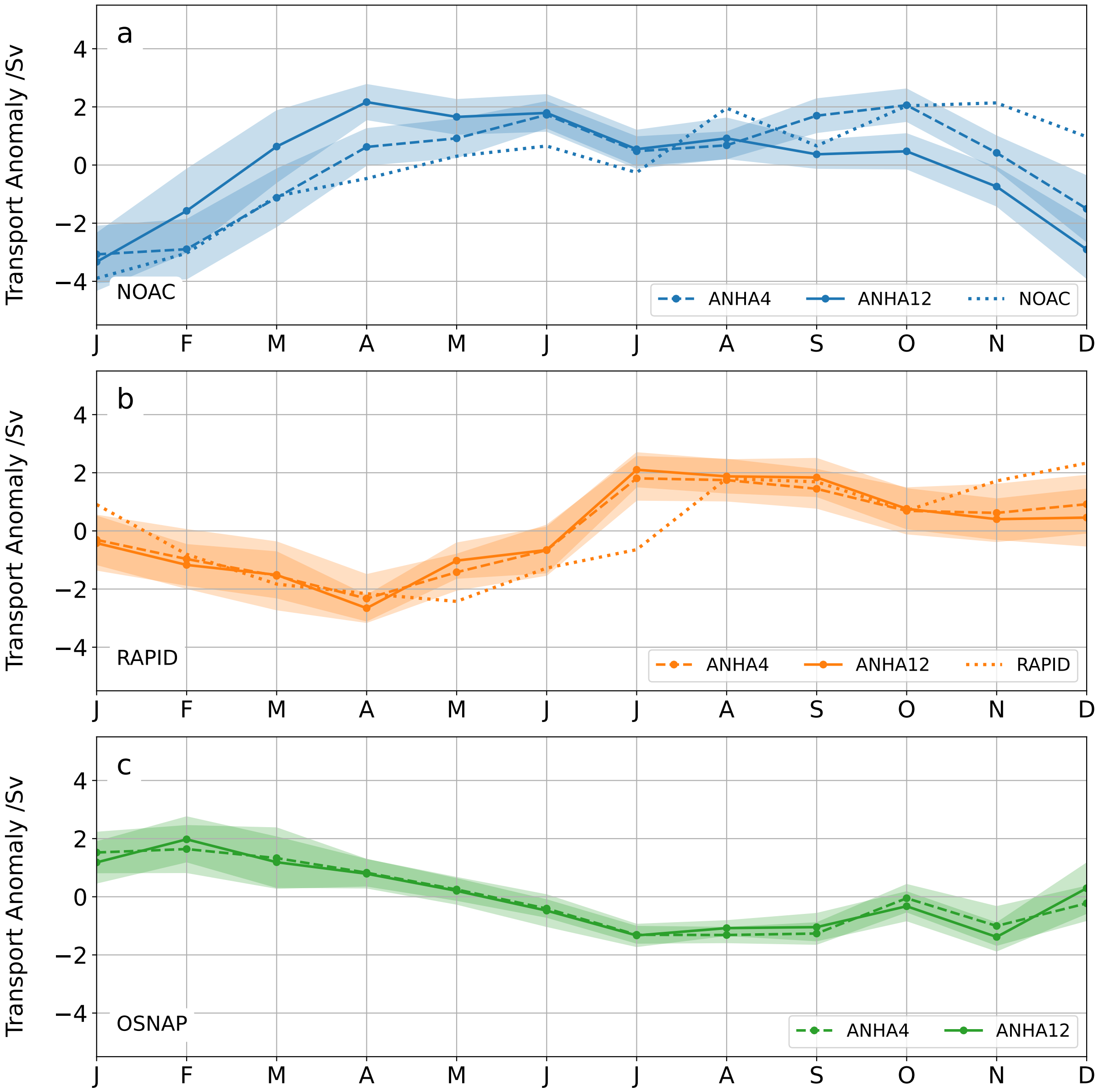

Figure 4.15: The seasonal cycle of the AMOC volume transport in ANHA4 (dashed lines) and ANHA12 (solid lines) at the NOAC (a), RAPID (b), and OSNAP (c) lines. The shaded area denotes the SEM for each month. The dotted lines represent the seasonal cycle from observations of the NOAC and RAPID arrays. Note that the panels are not ordered by latitude.

cillations, described in a $^1/_4$° NEMO model simulation by Blaker et al. (2021). The timing of this deviation of the ANHA4 inter-annual AMOC variability from the observed RAPID AMOC agrees with a strong increase of the gross northward and southward transports, visible in ANHA4 at the southern boundary of the model domain and the equator (Paul G. Myers, personal communication). Meridional propagation of these equatorial oscillations possibly influences the inter-annual AMOC variability in ANHA4 at the RAPID line. Similar behavior with similar timing yet weaker amplitude is also visible at the NOAC and OSNAP lines, possibly indicating meridional communication of these oscillations. However, a detailed analysis of these oscillations and their effect on the AMOC at different latitudes is beyond the scope of this thesis.

With a strong AMOC in summer and fall and a weak AMOC in spring, the modeled seasonal cycle at the RAPID line is in good agreement with the seasonal cycle observed at the RAPID array and does not show a significant difference between ANHA4 and ANHA12 (Figure 4.15 b). In both ANHA4 and ANHA12, maximum transports are visible in July, while the observations at the RAPID array exhibit the maximum AMOC in December due to the wind forcing (Kanzow et al., 2010). Generally, the shape of the seasonal cycle in ANHA4 and ANHA12 at the RAPID line is similar to the observed seasonal cycle at RAPID. However, the transition from a low AMOC in the spring to a strong AMOC in the summer and fall in the modeled seasonal cycle leads the same transition in the observations, possibly indicating a faster response to the wind forcing in the ANHA4 and ANHA12 simulations.

At the OSNAP line, the increased resolution of ANHA12 results in a better representation of the mean AMOC strength (Table 4.6). Similar to the NOAC line, the variability is similar between ANHA4 and ANHA12, with differences in the mean AMOC strength after 2010. However, the overlap of the OSNAP observational period with the model period is not long enough to meaningfully compare the inter-annual behavior in ANHA4 and ANHA12 with observations.

In the observations, most of the overturning occurs at the eastern part of the OSNAP line (Lozier et al., 2019), but models often assign a more dominant role to the Labrador Sea for determining the strength of the AMOC (Yeager et al., 2021; Zhang et al., 2019), possibly due to a too coarse resolution, not resolving mesoscale dynamic features (Pennelly et al., 2019; Saenko et al., 2014). The AMOC at OSNAP west has been analyzed by Hoshyar et al. (2024). Here, ANHA4 and ANHA12 overestimate the AMOC, while the high-resolution nest of the Labrador Sea, LAB60, strongly improves the representation of the AMOC at OSNAP West.

Additionally to the ANHA4 and ANHA12 simulations, this high-resolution simulation of the Labrador Sea with $^1/_{60}°$ resolution (LAB60) is combined with its parent nest SPG12 to calculate a basin-wide AMOC estimate at 47°N with the highest possible resolution in the ANHA simulations (hereafter LAB60+SPG12).

The mean AMOC volume transport at the NOAC line in LAB60+SPG12 (17.6 Sv, Table 4.6) is even closer to the observed NOAC AMOC than the value in ANHA12, which was already an improvement over ANHA4. This indicates an advancement in simulating the mean AMOC using a high-resolution Labrador Sea nest. However, the AMOC at the NOAC line, calculated from the highest available resolution version of the ANHA models, exhibits unrealistically strong seasonal variability (Figure 4.16). The mean variability in

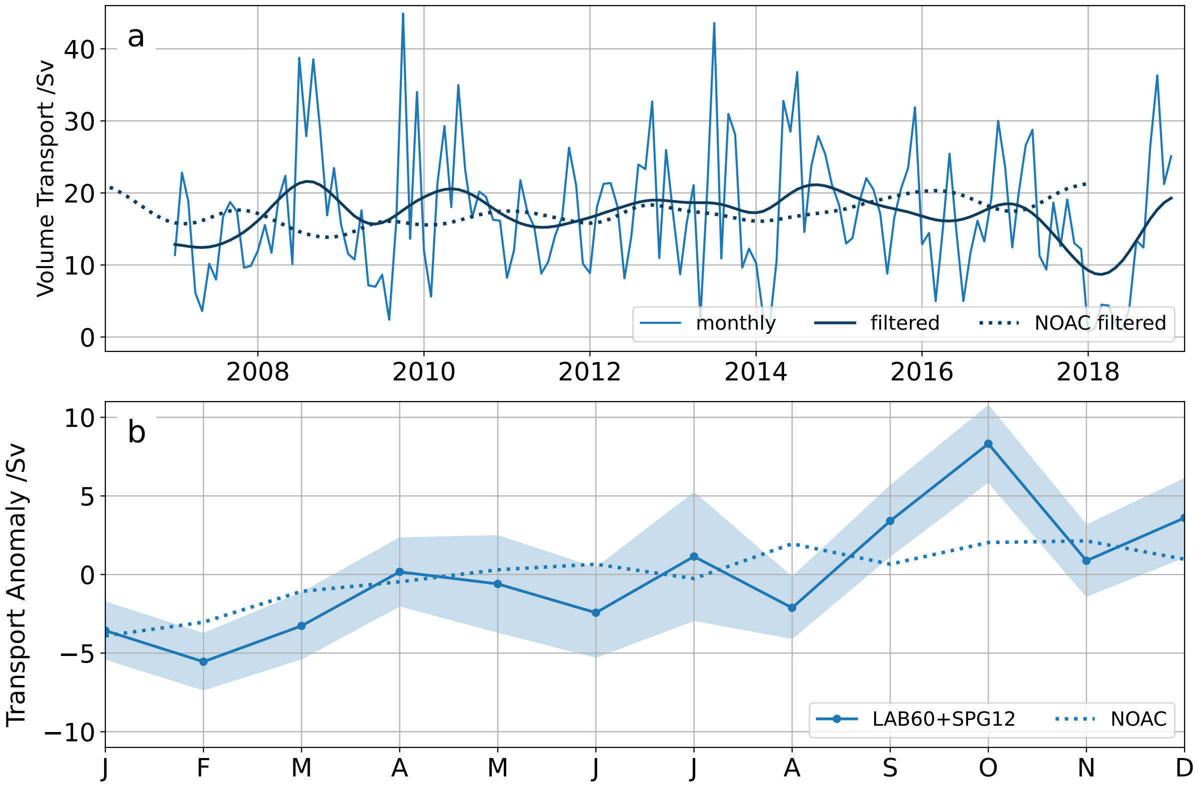

Figure 4.16: (a) AMOC volume transport in LAB60+SPG12 at the NOAC line. The bold line denotes the low-pass filtered time series. The dotted line denotes the low-pass filtered observational time series from the NOAC array. (b) Seasonal cycle of the AMOC volume transport in LAB60+SPG12. The shaded area denotes the SEM for each month. The dotted line represents the seasonal cycle from observations of the NOAC array. Note the different scale of the y-axis compared to Figure 4.14 and Figure 4.15.

LAB60+SPG12 (STD: 9.0 Sv, Table 4.6), strongly overestimates the observed variability at the NOAC array (STD: 5.2 Sv). This strong variability might result from the nested simulation, which is used to calculate the AMOC at the NOAC line. The westernmost part of the section is covered by the high-resolution LAB60 nest, while the eastern parts are covered by the parent SPG12 nest (Figure 2.2 f). Possibly the interaction of the high-resolution LAB60 nest and the underlying SPG12 simulation cause unrealistically strong transport fluctuations at the boundary between the two nests. Additionally, the density of the maximum stream function might vary, inducing unrealistic variability. However, despite the overestimation of the variability, the general shape of the seasonal cycle of the AMOC in LAB60+SPG12 with a maximum in October agrees with the observations (Figure 4.16).

Further investigation would be necessary to detect the sources for the strong variability using the LAB60+SPG12 simulation. However, these results indicate that for basin-wide AMOC estimates, a combination of AMOC estimates from nests with different horizontal resolutions might not be a desirable scenario. Currently, the ocean modeling group at the

University of Alberta is running a $^1/_{60}$° pan-Arctic NEMO simulation, ARC60, covering the OSNAP line (Paul G. Myers, personal communication). Comparing the AMOC at the OSNAP line in ARC60 with observations could assess the model performance and possibly allow insights into the subpolar AMOC evolution beyond the OSNAP observational period.

Increasing the resolution from $^1/_4$° in ANHA4 to $^1/_{12}$° in ANHA12 and $^1/_{60}$° in the Labrador Sea in LAB60+SPG12 improves the representation of the mean AMOC strength, which agrees closer with the observations for higher resolutions. These results support recent studies that an increased model resolution in the North Atlantic helps better represent key features of the Atlantic Ocean dynamics, like the AMOC and LSW formation (Roberts et al., 2020; Garcia-Quintana et al., 2019). Being able to better resolve these with increased resolution enables more accurate simulation of the AMOC. A good representation of the AMOC is necessary to trust these simulations for making projections of the future evolution of the AMOC.

However, the discrepancies that remain between the modeled AMOC and the observations, especially in the LAB60+SPG12 simulation, also highlight that modeling the inter-annual variability of the AMOC remains an important task that will require more effort than increasing the model resolution, like continuous observations as benchmarks for testing model performance. Additionally, since resolution will never resolve all relevant small-scale processes, improved parameterizations will be needed to account for unresolved processes, even in high-resolution models.

"The sea, the great unifier, is man's only hope. Now, as never before, the old phrase has a literal meaning: we are all in the same boat."

Jacques Yves Cousteau, *oceanographer and filmmaker*

Chapter 5

Summary and Conclusions

This thesis presents a detailed analysis of the observed and modeled AMOC mean state, variability, and trends of the past decades at 47°N in the North Atlantic, the boundary between the subtropical and the subpolar gyre. Furthermore, the meridional connectivity of the 47°N AMOC is investigated. In the following, the findings of this thesis are summarized, and the research questions posed in Section 1.7 are answered. Conclusions are drawn based on the results.

1. What are the mean strength and variability of the AMOC at 47°N and how do these compare to other latitudes?

A 25-year (1993-2018) observational AMOC record based on the NOAC array at 47°N with a mean AMOC strength of 17.2 Sv is presented in Chapter 3. The mean strength of the NOAC AMOC agrees well with the AMOC at the subtropical RAPID array at 26°N and other estimates in the subpolar North Atlantic: the OSNAP array (Li et al., 2021), an AMOC estimate at 45°N (Desbruyères et al., 2019), and the OVIDE section (Mercier et al., 2015). Models often indicate a maximum of the AMOC at latitudes around 35°N to 45°N (e.g., Biastoch et al., 2021). Being closer to this latitude range, a larger AMOC at 47°N could be expected. Indeed, the observations of the NOAC (17.5 Sv) and RAPID arrays (16.9 Sv) show a larger mean AMOC strength at the NOAC array in the RAPID observational period. However, the mean AMOC strength is not significantly different between the two arrays. The variability is larger at the NOAC array (STD: 5.5 Sv) compared to the RAPID array (STD: 3.4 Sv). This is due to the larger variability of the NAC at 47°N, compared to the Florida current at 26°N (Piecuch, 2020). In agreement with other observational estimates (Worthington et al., 2021; Willis, 2010), the AMOC estimate at the NOAC array does not exhibit a significant overall trend.

As discussed in Jackson et al. (2022), the inter-annual variability of AMOC transport time series at 41°N (Willis, 2010), 50°N (Jackson et al., 2019), and the OVIDE section (Mercier et al., 2015) differ substantially. These differences possibly originate from the different methods and data sets used (e.g., choice of the reference level, compensation transport). All these estimates suffer from undersampling of the strong and narrow boundary currents, especially at the western continental slope and rise (e.g., Mertens et al., 2014), while the NOAC array at 47°N was specifically designed to resolve the boundary currents.

The NAC and the interior transport dominate the AMOC variability at the NOAC array on all timescales. A large portion of the NAC volume transport is compensated by the interior transport. The two-month averages of the NAC and the interior transport are significantly anticorrelated. This behavior is consistent with other studies at the RAPID array, where the corresponding component of the upper mid-ocean transport compensates the Florida Current transport (Frajka-Williams et al., 2016; Kanzow et al., 2007).

Decadal AMOC variability is driven by the buoyancy forcing in the subpolar North Atlantic (Jackson et al., 2022; Biastoch et al., 2008a). However, on inter-annual timescales also the wind forcing contributes to driving the AMOC variability in the subpolar North Atlantic. In agreement with the literature (Jackson et al., 2022; Buckley & Marshall, 2016), the inter-annual AMOC variability at the NOAC array at 47°N is partly driven by large-scale wind field changes. Phases of strong AMOC volume transport coincide with transitions in the local wind stress anomaly. These transitions are possibly related to changes in the NAO and meridional shifts of the atmospheric pressure systems.

Starting from high AMOC volume transports in the 1990s, associated with decadal AMOC variability due to enhanced dense water formation in the 1990s (Rhein et al., 2017; Kieke & Yashayaev, 2015; Lazier et al., 2002), the AMOC decreases until 2002 and increases after that. This increase culminates in the overall AMOC maximum of the observed period in 2005. Driven by the large-scale wind field reacting to changes in the NAO, the overall AMOC minimum is reached in 2009 and followed by a steady increase until the end of the observational period in 2018, possibly related to a consistently positive NAO after 2014.

2. How coherent is inter-annual AMOC variability between the subtropical North Atlantic and the subpolar gyre boundary in observations and models?

The coherence of AMOC variability throughout the Atlantic on different timescales is a prevailing topic in the literature (e.g., Gu et al., 2020; Frajka-Williams et al., 2018; Bingham et al., 2007) due to its possible application in inferring the AMOC at different latitudes from a limited number of observational arrays. Section 3.7 discusses the meridional connectivity of the AMOC time series at the NOAC array at 47°N with the subtropical RAPID array and the associated timescales of communication. In Section 4.3, the meridional connectivity between the NOAC, RAPID, and OSNAP lines is investigated in VIKING20X.

Jackson et al. (2022) noted the correlation between the AMOC time series at 26°N and 41°N (Willis, 2010), and associated both with the subtropical regime. The authors assigned the AMOC estimates from 45°N (Desbruyères et al., 2019) and 50°N (Jackson et al., 2019) to the subpolar regime because they did not appear to be correlated with the subtropical AMOC. However, the NOAC and RAPID AMOC exhibit enhanced significant correlation (r=0.72) when the NOAC AMOC leads by about one year. This finding either points to an extended subtropical regime reaching as far north as 47°N or challenges the notion that the subtropical and subpolar regimes are decoupled on inter-annual timescales. This finding is additionally supported by the significant correlations between the NOAC AMOC time series and the 45°N AMOC estimate by Desbruyères et al. (2019) with added wind-driven Ekman transport. Increased coherence of the NOAC and RAPID AMOC is found at periods of about seven years with a phase lag of about one year. However, the number of frequency bands exceeding the 95% confidence level is too low to exclude random coherence. The present observational time series are too short to resolve coherence on decadal or longer timescales.

What determines the meridional connectivity between 47°N and 26°N in the observations of the NOAC array remains an open question. The higher correlation between both time series when the 47°N Ekman transport variability is removed from the NOAC AMOC indicates the potential impact of other wind-driven mechanisms, for example, geostrophic adjustment. Kostov et al. (2022) proposed a southward communication of subpolar AMOC variability via passive advection of buoyancy anomalies and boundary waves that impact subtropical AMOC variability. Though advective communication is possible on the timescales of the meridional connectivity found between NOAC and RAPID, the lag correlations of the individual components of the NOAC AMOC with the RAPID AMOC remain insignificant. Thus, an advective southward communication in a single component cannot be found at the NOAC array. Instead, other mechanisms like boundary waves, wind field changes, or advection in the lower limb of the AMOC could be more dominant in communicating AMOC anomalies between NOAC and RAPID.

In agreement with observations, VIKING20X shows meridional connectivity of the AMOC, indicated by increased significant correlations of the AMOC at the NOAC and RAPID lines when the NOAC AMOC leads by about one year. This finding indicates that the connectivity between those latitudes is determined by a common physical mechanism present in observations and VIKING20X. A detailed analysis in VIKING20X regarding the meridional connectivity over multiple latitudes, timescales, and possible forcing mechanisms could help determine the processes responsible for AMOC connectivity. Such analysis could shed light on whether the connectivity is maintained via advective pathways or a response to large-scale changes, for example, in the wind-forcing.

VIKING20X exhibits instantaneous connectivity between the NOAC AMOC and the OSNAP AMOC on seasonal and inter-annual time scales. The question of how far the meridional connectivity extends northward beyond 47°N in observations remains to be answered. Addressing this question requires more observational efforts to separate regional from methodological differences in the AMOC time series (Danabasoglu et al., 2021; Frajka-Williams et al., 2018) and a deeper understanding of the involved processes. Both objectives highlight the importance of long-term observations, especially AMOC time series and near-realistic high-resolution models. The OSNAP array in the center of the subpolar gyre will provide a valuable tool to study the meridional connectivity into the central subpolar gyre once its AMOC time series is sufficiently long.

3. How useful are AMOC estimates from gridded data sets in designing a future AMOC monitoring system?

The recent IPCC report downgraded the confidence in an AMOC decrease since 1850 due to discrepancies between climate models and multiple (proxy) observations (IPCC, 2021). These discrepancies highlight the importance of continued AMOC observations. In times when these observations need to be both accurate and feasible, gridded observational data sets could play a role in designing a future AMOC monitoring system. In Section 3.8, the ARMOR3D observation-based gridded data set is used to estimate the AMOC at 47°N and compared to the approach by Desbruyères et al. (2019), who used an ensemble mean of different data sets at 45°N (EN4, CORA, ISHII, and ARMOR3D).

The AMOC at 47°N based on ARMOR3D exhibits a similar mean strength (16.5 Sv) and is significantly correlated (r=0.73) with the observed AMOC at the NOAC array. This correlation is largest in the first period of observations (1993-2008, r=0.81). Desbruyères et al. (2019) estimated the AMOC at 45°N combining different data sets as an ensemble mean. This approach is widely used in climate model ensemble simulations (IPCC, 2021) and has been shown to outperform individual models in terms of reducing the uncertainty (Foley et al., 2013; Rinke et al., 2006). The comparison of the AMOC in ARMOR3D and the approach by Desbruyères et al. (2019) reveals differences to the observed AMOC at the NOAC array. The AMOC estimate, based on ARMOR3D fails to reproduce the steady increase of the AMOC in the recent years, following the minimum in 2009. The approach by Desbruyères et al. (2019) exhibits a significantly lower mean AMOC strength (13.9 Sv) and a significant but weaker correlation (r=0.6). However, their estimate includes an increasing AMOC after 2009, in accordance with the NOAC observations.

Both ARMOR3D and the NOAC AMOC strongly rely on the same satellite altimetry data, rendering these estimates not independent. Thus, the high correlations between the ARMOR3D AMOC and the NOAC AMOC might be artificially enhanced. The velocities in ARMOR3D might be additionally biased by scarce observations from Argo floats in the narrow boundary currents and the climatological fields below 1500 m. However, these uncertainties cannot explain the different evolution of the NOAC AMOC and the estimate from ARMOR3D in the recent years. The increasing AMOC volume transport after 2013 is evident in the NOAC and RAPID observations and is visible in the estimate by Desbruyères et al. (2019). It coincides with a period of continuously positive NAO, explaining the increasing AMOC with increased wind forcing in the North Atlantic. Though an explanation for the difference between the ARMOR3D AMOC estimate and the NOAC AMOC is not found in the present thesis, more trust is put into the NOAC estimate and the estimate by Desbruyères et al. (2019) because of the mutual agreement and the coinciding NAO variability. A detailed analysis of the performance of an ensemble of different observational data sets and reanalyses could resolve the weaknesses and strengths of individual data sets. Such an approach will prove valuable in designing a future AMOC monitoring system that is both accurate and feasible. A proposal for such a monitoring system is described in the outlook (Chapter 6).

4. How well does the forced ocean model VIKING20X represent key characteristics of the observed AMOC?

Due to the scarcity of observational AMOC monitoring arrays and the short time series obtained from these, interpreting results from numerical models is an essential part of understanding past and future AMOC variability. The characteristics of the AMOC in the high-resolution forced ocean model VIKING20X have been analyzed in Section 4.1.

VIKING20X represents the mean AMOC strength at the NOAC (18.4 Sv in the observational period), RAPID (16.8 Sv in the observational period) and OSNAP (15.8 Sv in the observational period) lines. The mean AMOC strengths obtained at the three array lines lie within the estimated error range of observations and model. The individual components of the AMOC at 47°N in VIKING20X are generally weaker correlated compared to the observations of the NOAC array. The low-pass filtered time series of the AMOC at 47°N exhibits a significant correlation only with the NAC, indicating a dominance of the NAC on inter-annual timescales. This dominance is supported by the decline of the AMOC in VIKING20X after the mid-1990s, which is driven by a decreasing NAC volume transport. Additionally, the spectra of the components reveal that on all timescales, the AMOC variability is dominated by the NAC and the interior transport.

The AMOC in VIKING20X at the NOAC, RAPID, and OSNAP lines exhibits coherent decadal variability. The AMOC exhibits a maximum in the mid-1990s in VIKING20X at all three observational array lines. Afterward, the AMOC volume transport continuously decreases until 2010, which is a disagreement with observations. The strongest decrease is found at the NOAC line at 47°N (-0.3 Sv yr^{-1}). In this period, the upper 700 m temperature, and salinity trends reveal a strong cooling and freshening in the subpolar North Atlantic along the pathway of the NAC. This is a consequence of the AMOC weakening being dominated by a decreasing NAC, bringing less heat and salt towards the subpolar latitudes. This conclusion is also evident from analyzing the NAC transport trends and basin-wide upper 700 m velocity trends. A comparison with the ARMOR3D upper 700 m temperature, and salinity trends exhibits a similar pattern of cooling and freshening in the subpolar North Atlantic. However, the magnitude of the observed trends is not as strong.

The cooling pattern in VIKING20X in the subpolar North Atlantic qualitatively resembles the pattern described by Caesar et al. (2018) as an SST imprint of a decreasing AMOC. However, they reported a much weaker amplitude. While the AMOC in VIKING20X shows a decrease after the 1990s, such a trend is not visible in the ARMOR3D AMOC. However, like VIKING20X, ARMOR3D shows a similar yet weaker cooling in the subpolar North Atlantic. Caesar et al. (2018) interpreted this (in their case, SST) trend as a sign of an already weakening AMOC. The NOAC AMOC estimate does not show a significant trend over the same period. While there is debate over whether the pattern found by Caesar et al. (2018) indicates a weakening AMOC (e.g., Kilbourne et al., 2022), the observational AMOC has been shown to exhibit strong variability on multiple timescales (Srokosz & Bryden, 2015). In an analysis of 147 years of SST data, Caesar et al. (2018) found a decreasing AMOC of 3 Sv, that is a trend of about -0.2 Sv decade^{-1}. Given the monthly STD of the observed NOAC AMOC (5.2 Sv), such small trends are masked by the strong AMOC variability on multiple timescales.

5. What is the impact of model resolution on the representation of the AMOC in different simulations of the forced ocean model ANHA?

One essential requirement for a realistic representation of the AMOC in ocean and climate models is a sufficient ocean resolution to resolve mesoscale features (Biastoch et al., 2021; Hallberg, 2013). In climate models, an increased resolution has been shown to result in improved representation of the subtropical AMOC (Roberts et al., 2020). In order to investigate the representation of the AMOC at different latitudes, AMOC time series at the NOAC, RAPID, and OSNAP lines have been analyzed in different resolutions of the ANHA NEMO model in Section 4.5.

Increasing the horizontal resolution from $^1/_4$° in ANHA4 to $^1/_{12}$° in ANHA12 decreases the mean AMOC strength at all three latitudes investigated, resulting in a closer agreement with the respective observed mean AMOC strength (mean VIKING20X AMOC:

NOAC: 19.5 Sv, RAPID: 19.7 Sv, OSNAP: 16.6 Sv, in the respective model-observations overlap period). The high-frequency variability, including the seasonal cycle, does not show strong differences between ANHA4 and ANHA12. This is generally reassuring since most climate models use a relatively coarse ocean component. However, the inter-annual variability does exhibit differences, especially at the RAPID line. Here, the AMOC variability is possibly influenced by high-frequency and large-amplitude equatorial oscillations in ANHA4.

In agreement with observations at the NOAC, RAPID, and OSNAP arrays, none of the ANHA NEMO model configurations show a long-term trend. This is in contrast to VIKING20X, exhibiting a negative trend after the mid-1990s. The representation of the AMOC in forced ocean models is very sensitive to numerical choices, especially those related to the freshwater fluxes (Biastoch et al., 2021). Differences between the ANHA simulations and VIKING20X include the SSS restoring, the forcing data set, and various other numerical choices. In ANHA, no SSS restoring is implemented. Thus, the reasons for the different AMOC trends in the ANHA simulations and VIKING20X are presumably differences in the implementation of these forcing parameters in the respective models. These differences among different forced models, as well as between models and observations, highlight the importance of model intercomparison projects, like the OMIP (Griffies et al., 2016), providing a protocol for approaches to investigate the reasons and influences of model biases. Continuously analyzing the effects of different implementations will advance the representation of the AMOC in numerical models.

The AMOC calculated from a combination of the high-resolution $^{1}/_{60}{}^{\circ}$ LAB60 simulation and the parent nest of $^{1}/_{12}{}^{\circ}$ SPG12 further improves the representation of the mean AMOC strength at the NOAC line (17.6 Sv in the model-observations overlap period), compared to observations. However, in this simulation, the variability is strongly overestimated. The reason for this disagreement could be interactions between the two nests at the boundary of the LAB60 domain, inducing unrealistically strong variability. Currently, a $^{1}/_{60}{}^{\circ}$ resolution simulation of the Arctic basin is conducted by the ocean modeling group at the University of Alberta (ARC60, Paul G. Myers, personal communication). This simulation covers the full OSNAP line. A high-resolution nest of the Labrador Sea (LAB60) strongly improved the representation of the AMOC at OSNAP west (Hoshyar et al., 2024). An analysis of the OSNAP AMOC in the pan-Arctic high-resolution ARC60 simulation and a comparison with the OSNAP observations could explore if the advantages of increased resolution in improving the representation of the AMOC apply to a basin-wide estimate at $^{1}/_{60}{}^{\circ}$ resolution.

A realistic representation of the AMOC in ocean and climate models is essential for making projections of future climate states and the AMOC itself. The present thesis analyzes the characteristics of the AMOC in the North Atlantic in observations and models. It adds to a more complete understanding of the observed AMOC variability at the NOAC array at 47°N, the boundary between the subtropical and the subpolar gyre. The NOAC AMOC estimate provides an additional benchmark for the comparison between models and observations to further improve models and yield a more realistic representation of the AMOC. Thus, the results of this thesis are of specific interest to the observational and modeling community.

On inter-annual timescales, similar meridional connectivity is found between the NOAC AMOC variability and the RAPID array in observations and VIKING20X. This connectivity indicates that inter-annual variability is communicated southward from 47°N to 26°N to some degree. The findings of this thesis highlight the value of continued observational AMOC estimates. However, in times when it is increasingly difficult to secure the funding for AMOC monitoring arrays, studies of the meridional connectivity can potentially indicate optimal latitudes for AMOC observations and reduce the costs of maintaining multiple observing arrays. Additionally, the costs for AMOC observing arrays could be lowered further by using novel instrumentation and increasingly accurate observation-based gridded data sets and ocean reanalyses. A proposal for such a reduced array is described in the outlook (Chapter 6).

AMOC variability and trends have strong influences on the relatively mild climate in Europe and global weather patterns. Understanding this complex system is of major importance to recognize early warning signs of change and adapt to these changes. However, observational AMOC time series are short and dominated by large seasonal and inter-annual variability. Climate models project a weakening of the AMOC with global warming (IPCC, 2021). However, these models are subject to biases, arising, for example, from an overly strong salt advection feedback (Griffies et al., 2009). Forced hindcast simulations provide a basis for understanding the underlying physical mechanisms related to the AMOC. These mechanisms include the relationship between dense water formation and the AMOC (Garcia-Quintana et al., 2019) or the relevance of the Labrador Sea convection and the convection in the eastern subpolar gyre (Yeager et al., 2021). Attempts to overcome or correct model biases rely on accurate observational estimates as benchmarks to assess the accuracy of the AMOC representation in forced simulations. This thesis provides a 25-year observational AMOC estimate at 47°N, at the boundary between the subtropical and subpolar North Atlantic, as a new observational latitude to compare modeled AMOC variability with observations.

“In the end we will conserve only what we love, we will love only what we understand, and we will understand only what we are taught."

Baba Dioum, *forestry engineer*

Chapter 6

Outlook

In 2024, the RAPID array will complete its second decade of direct AMOC observations, while the OSNAP array will complete its first decade of observations. The extension of the NOAC observational period using satellite altimetry yields an even longer time series of 25 years. Despite the limited length of the observational time series, the observation and interpretation of decadal variability are possible to some degree. These continued AMOC observations are accompanied by atmospherically forced model simulations providing high-resolution data of the simulated AMOC. However, despite the advances in observing and modeling the AMOC, uncertainties in the observations and biases in the models remain. There are many open questions that require answering to better understand the role of the AMOC in the climate system and its future evolution. A few of these questions shall be discussed in the following.

How can the AMOC at 47°N be observed cost-efficiently?

This thesis has shown that despite advances in modeling the AMOC in the North Atlantic, continued observational estimates of the AMOC from in-situ mooring arrays are still needed to obtain a complete picture of the AMOC trends and variability on multiple timescales. Additionally, these observations serve as important benchmarks for assessing model performance. However, proposing to simply continue the measurements at the existing arrays does not account for the increasing challenge of obtaining sufficient funding and personnel for the expensive maintenance of basin-wide AMOC observatories (Frajka-Williams et al., 2023). Novel approaches to estimating the AMOC at different latitudes, not relying on a large number of in-situ devices, are required (Jackson et al., 2022).

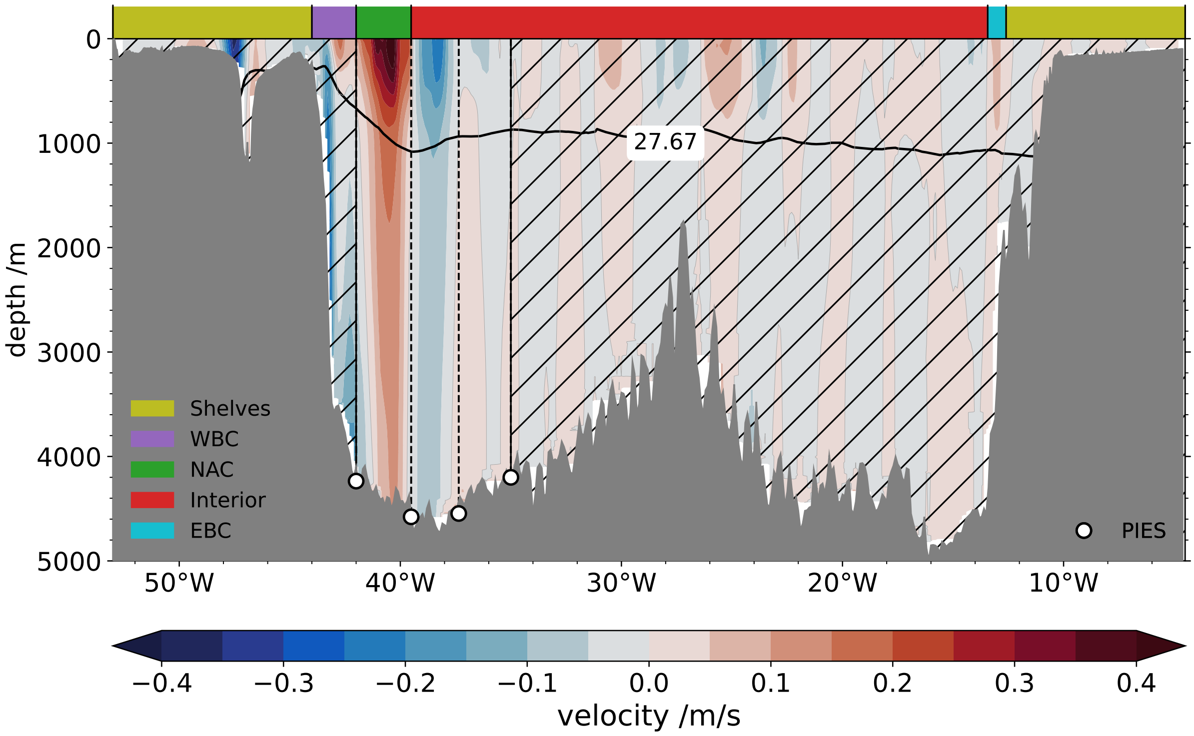

Figure 6.1: Proposal for a feasible AMOC monitoring array at 47°N in the North Atlantic. PIES are marked as white dots. Areas covered by gridded data sets are hatched. The remaining features depicted are the same as in Figure 2.4.

The latitude of 47°N represents an important location for the AMOC at the boundary between the subtropical and the subpolar North Atlantic, close to the latitudinal maximum of the overturning as obtained from model simulations (Biastoch et al., 2021). In this thesis, transport estimates from in-situ measuring devices have been extended using satellite altimetry, yielding 25 years of AMOC estimates from 1993 to 2018. Today, the NOAC array is not active anymore. However, the previous work has established the methodology of obtaining transport estimates from the combination of PIES, moorings, and altimetry using the GEMS method and estimating the AMOC from individual transport measurements across the basin (Moritz et al., 2021b; Nowitzki et al., 2021; Rhein et al., 2019b; Roessler et al., 2015; Mertens et al., 2014). Building on this experience and the conclusions from this thesis, here, an approach for a cost-efficient, minimal array is proposed to capture the AMOC variability at 47°N. This array combines in-situ measurements from PIES, satellite altimetry, atmospheric wind stress data to calculate the Ekman transport, and gridded observational data sets.

Results of this thesis have shown that in observations and models, the AMOC variability on all timescales is dominated by the NAC and the interior transport, defined as all transports between the NAC and the Eastern boundary current (Figure 3.5, Figure 4.5). The two-month averages of the sum of these components are significantly correlated with the AMOC volume transport (r=0.59). The proposed array of estimating the AMOC at 47°N builds on this dominance by capturing the transport of the NAC and the largest recirculation branch by a set of four PIES (Figure 6.1). Three PIES are located at former NOAC array PIES positions at 42°W, 39.5°W and 37.4°W. These three PIES capture the most dominant parts of the NAC and interior transport. For redundancy, an additional PIES is added at 35°W, capturing another important recirculation branch of the NAC. Should one of the three easternmost PIES fail, transport calculations, incorporating satellite altimetry, could still capture the NAC and most important parts of the interior transport. Using the PIES measurements and hydrographic data (from Argo and shipboard CTD measurements) from the vicinity of the PIES locations, the transfer functions to obtain accurate transports from the travel time measurements of the PIES (Section 2.1.2) could be updated regularly.

This proposed instrumentation leaves large parts of the basin uncovered by in-situ measurements. However, the analysis of gridded observational data sets in this thesis has shown that these are generally capable of reproducing the variability observed by the NOAC array (Section 3.8). Uncertainties associated with relying on a single data set (e.g., ARMOR3D) could be minimized by applying an ensemble mean approach to a combination of multiple available data sets and ocean reanalyses (Section 3.8). Thus, to construct a feasible AMOC monitoring array, the transports in the parts of the basin not covered by in-situ instruments (hatched areas in Figure 6.1) are proposed to be obtained from gridded data sets. An assessment of different observational data sets and ocean reanalyses could reveal which data should be included in this approach and how they should be processed (e.g., regarding the compensation transport and the inclusion of the Ekman transport from atmospheric wind stress data) and combined. Given the past transport time series from the individual instruments of the NOAC array, the accuracy of the AMOC estimate of the proposed array could be compared to the full NOAC array AMOC by including NOAC data only from the PIES positions proposed here (except the one not included in NOAC) and obtaining the remaining transports from gridded data sets. However, this analysis is beyond the scope of this thesis.

Many of the existing observation-based gridded data sets and ocean reanalyses rely, to a large extent, on observations from Argo floats. One key limitation of the Argo floats is that their diving depth is limited to 2000 m, which does not resolve the lower limb of the AMOC. Accordingly, for example, in ARMOR3D, only climatological values are provided. However, in the recent years, progress has been made in the development of a deep Argo fleet, an extension of the existing Argo program. This fleet incorporates floats that can dive substantially deeper than most Argo floats today (Roemmich et al., 2019). The deep Argo fleet will help sample the deep ocean in higher spatial and temporal resolution without the need for research vessels. Integrating deep Argo profiles in observational data sets will improve the uncertainties associated with the undersampling of the deep ocean.

With such data sets, more trust could be put into the corresponding AMOC estimates based on these data sets.

The array, proposed here, could capture the dominant variability of the AMOC at 47°N from in-situ PIES measurements. Additionally, including the transports from observation-based data sets and ocean reanalyses, the mean AMOC strength and trends could be estimated. In order to gain confidence in trend estimates, the PIES could be equipped with novel drift-free bottom pressure sensors (Frajka-Williams et al., 2023). Bottom pressure sensors in classical PIES only provide information about the pressure fluctuations because each pressure sensor is subject to a unique sensor drift (Hughes et al., 2018), which is usually removed in data processing (Nowitzki et al., 2021; Roessler et al., 2015; Watts & Kontoyiannis, 1990). However, this makes it impossible to detect long-term trends in the bottom pressure. The novel drift-free bottom pressure sensors overcome this issue by incorporating a second pressure sensor held at constant atmospheric pressure in an additional pressure housing. In data processing, the drift of this second pressure sensor can be removed from the bottom pressure, measured by the classical pressure sensor, thus conserving possible trends in the bottom pressure. Equipping the two outermost positions (Figure 6.1) with drift-free bottom pressure sensors would allow estimating trends in the barotropic component of the velocities and associated trends in the AMOC.

Assuming a price of 40,000 EUR for a classical PIES and about 100,000 EUR for PIES including the drift-free bottom pressure sensors, the proposed array instrumentation would cost less than 300,000 EUR, which is substantially lower compared to a basin-wide mooring array involving considerably more instruments (e.g., 70 moorings in the OSNAP array, Fu & Li, 2023). Additionally, maintenance costs could be kept minimal because PIES can measure up to five years without needing battery replacement, depending on the sampling frequency. If data retrieval is desired in the meantime, the PIES could additionally be equipped with multiple pop-up data shuttles (Jeon et al., 2021). These are buoyant devices able to save the PIES data and ascend to the surface, where they can transmit the data via satellite telemetry. However, these devices would come at additional costs. Since all in-situ instruments of the array are located in the western Atlantic, maintenance could be conducted in short cruises from the port of St. John's, Newfoundland, without crossing the whole basin for array maintenance. The port of St. John's is frequently visited by oceanographic research vessels. Instrument replacement and data retrieval could occasionally be done in cooperation with colleagues working in the region.

What are the dominant processes determining AMOC variability and meridional connectivity on multiple timescales?

While proxy observations indicate a decrease of the AMOC over the last century, possibly forced by anthropogenic carbon emissions (Caesar et al., 2021, 2018), observational AMOC estimates do not show a trend over the last decades (Chapter 3, Worthington et al., 2021). This is possibly due to the large variability of the AMOC on multiple timescales, masking minimal trends proposed, for example, by Caesar et al. (2018). Thus, it is important to understand the forcing and timescales of the AMOC variability in order to be able to differentiate internal variability from long-term trends (Jackson et al., 2022).

As observations are naturally incomplete and models are naturally imperfect, answering this question requires a comprehensive approach, combining observational and modeling efforts. Given the limited time series of observational AMOC estimates, investigating AMOC variability on multiple timescales requires the use of numerical model simulations. These models need a sufficient resolution to most realistically represent mesoscale features and thus produce realistic AMOC variability. This thesis has shown the value of direct AMOC observations at 47°N, providing a benchmark for assessing the representation of the AMOC at the boundary between the subtropical and the subpolar gyre in model simulations.

A detailed analysis of the different forcing parameters in such model simulations can shed light on the relevance of the respective influences on past variability of the AMOC, including the relative importance of wind forcing and buoyancy forcing and the connection between the formation of LSW and the AMOC (Garcia-Quintana et al., 2019; Rhein et al., 2017; Yashayaev & Loder, 2017). Models additionally allow the analysis of AMOC variability at multiple latitudes and comparisons with observations where these exist. Studying the causes for variability at multiple latitudes will help identify the processes determining AMOC connectivity and possibly allow the determination of optimal latitudes for AMOC observations.

How can the discrepancies between observations and models regarding past AMOC variability and trends be overcome?

Apart from uncertainties associated with the observational AMOC estimates, differences between observed and modeled AMOC variability and trends are possibly related to model biases due to incorrectly represented (or parameterized) atmosphere-ocean feedbacks, mesoscale eddies, and overflows from the Nordic Seas (Fox-Kemper et al., 2019).

These model biases highlight the importance of continued observations to assess model performance. Based on such assessments, model performance can be enhanced. One approach is to increase horizontal and vertical model resolution. This thesis and previous work (Roberts et al., 2020) have shown that increasing ocean model resolution results in a better representation of the AMOC in forced ocean models and climate models, possibly due to the enhanced representation of mesoscale eddies and their associated heat and freshwater transport. This is especially important as climate models usually have rather coarse-resolution ocean components. However, increasing the resolution comes with increased computational costs and will naturally not resolve all relevant small-scale processes. Thus, higher resolution will generally need to be accompanied by additional efforts. These efforts include increasing the resolution in specific regions of importance, for example using unstructured grids (e.g., in ICON and FESOM, Danilov, 2013) or nested simulations (e.g., Pennelly & Myers, 2020), and improved parameterization of unresolved small-scale processes (Jackson et al., 2023).

The AMOC is of major importance in the climate system, globally shaping climate and weather patterns that, for example, sustain the relatively mild climate in Europe. Changes to this system would have drastic consequences for the lives of millions of people. In order to make informed projections about the future of the AMOC and the climate system on a warming planet, we rely on numerical simulations. However, observational time series are needed as benchmarks to assess the performance of these simulations. This thesis has highlighted the need for both continued AMOC observations and improvements in modeling the AMOC and provided routes to approach these tasks. However, to minimize the risk of strong change in the AMOC and the climate system in the coming century, the only way is to drastically cut anthropogenic greenhouse gas emissions.

Appendix

A.1 Transports between BP32 and EB3 in the eastern basin

Generally, calculating geostrophic transports between a PIES and a mooring can be done analogously to calculating transports between two PIES, given that the mooring is equipped with temperature and salinity recording devices. Here, the approach of calculating transports between the NOAC positions BP32 and EB3 for a 180 km wide strip in the eastern Atlantic (Figure 1.4, Figure 2.4) is described. Reasons for not using the available NOAC data and instead relying on transports obtained from ARMOR3D are explained.

The PIES data was processed by Hannah Nowitzki as described in Section 2.1.2 and supplied as profiles of temperature and salinity binned to 10 dbar steps. In order to calculate geostrophic transports between BP32 and EB3, the temperature and salinity recorders of the EB3 mooring are used. The EB3 mooring was equipped with 23 temperature recorders between 455 m and 3775 m nominal depth[1] and 5 salinity recorders between 460 m and 1710 m nominal depth[2]. However, the upper 450 m of the water column remained unsampled to prevent mooring loss due to high fishing activity in the region. Note that the shallowest instrument recording temperature was at 455 m depth while the shallowest instrument recording salinity was at 460 m. However, for simplicity, this will be referred to

---

[1] temperature recorders were located at the following nominal depths: 455 m, 460 m, 495 m, 525 m, 555 m, 585 m, 615 m, 705 m, 755 m, 1005 m, 1255 m, 1310 m, 1710 m, 1760 m, 2260 m, 2760 m, 2970 m, 3020 m, 3070 m, 3120 m, 3170 m, 3270 m, and 3775 m.

[2] salinity recorders were located at the following nominal depths: 460 m, 705 m, 1005 m, 1310 m, and 1710 m.

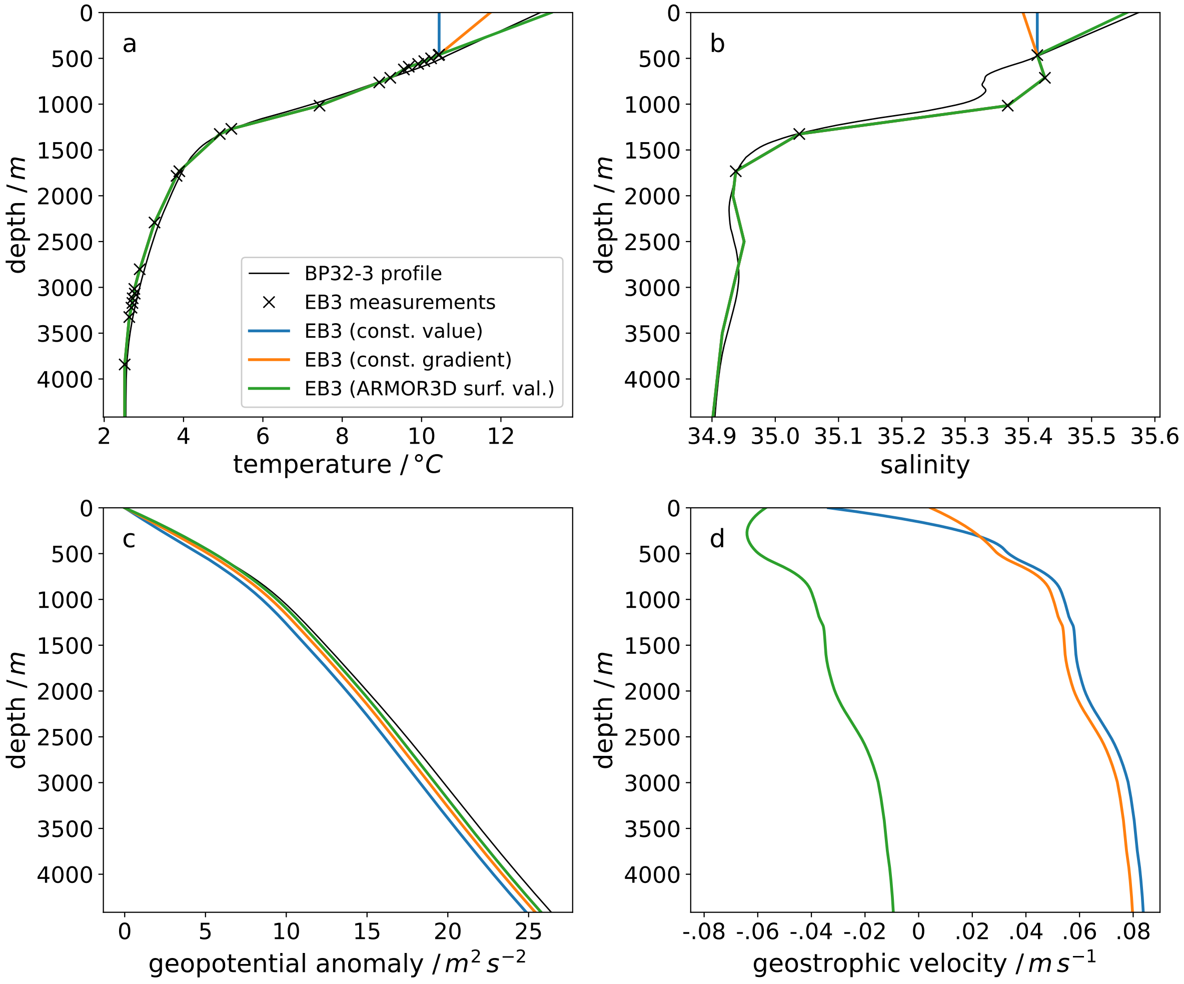

Figure A.1: Example profiles of temperature (a), salinity (b), GPA (c), and geostrophic velocity (d) at BP32-3 and EB3 from June 10, 2018. The different colors highlight different approaches taken to extrapolate the EB3 profiles to the surface and the resulting geopotential anomalies and geostrophic transports between BP32-3 and EB3.

as 450 m for both the temperature and the salinity recorder. Unfortunately, this mooring design was at the cost of not resolving the surface signal of temperature and salinity.

Additionally, the water column between 1700 m and the bottom was not sampled with salinity recorders. The salinity profile is extended to the bottom using ARMOR3D. However, since ARMOR3D consists of climatological values below 1500 m, no temporal variation in salinity is resolved here.

To address the issue of the unsampled upper 450 m, different approaches are taken to extrapolate the temperature and salinity to the surface (Figure A.1).

(a) Assuming a constant temperature and salinity in the upper 450 m, the temperature and salinity values, measured at 450 m, are continued to the surface.

(b) Assuming a constant gradient of temperature and salinity in the upper water col-

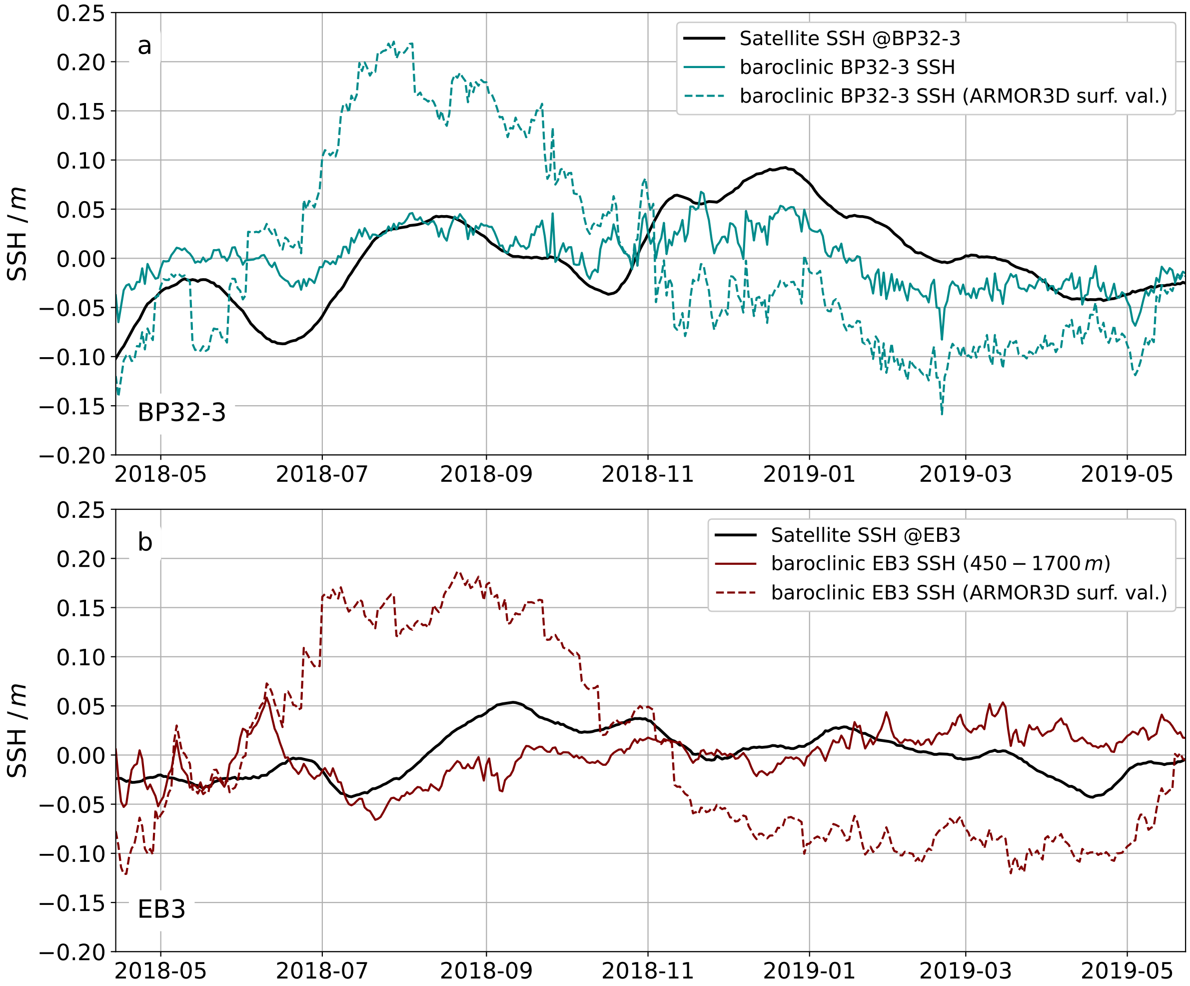

Figure A.2: Normalized SSH at BP32-3 (a) and EB3 (b) in the period of overlap. The black line shows the SSH at the respective positions obtained from satellite altimetry. The solid colored lines indicate the baroclinic SSH from BP32-3 and EB3, based only on the available data from the PIES and mooring, respectively. The dashed lines show the baroclinic component of the SSH derived from the BP32-3 (values between 450 m and the surface are cut) and EB3 data respectively and interpolated to ARMOR3D surface values.

umn, the temperature and salinity gradient between the last instrument at 450 m and the instrument below (at 460 m depth for temperature, at 705 m depth for salinity) is continued to the surface.

(c) The values for temperature and salinity are linearly extrapolated between the instruments at 450 m and the surface values obtained from ARMOR3D. These surface values are linearly interpolated to the exact location of the mooring.

Extrapolating the EB3 data from 450 m to the surface assuming a constant value or a constant gradient results in strong mean differences between the geostrophic surface velocities obtained from EB3 and the satellite-based geostrophic surface velocities. As a consequence, the profiles of the geostrophic velocity from these approaches are shifted

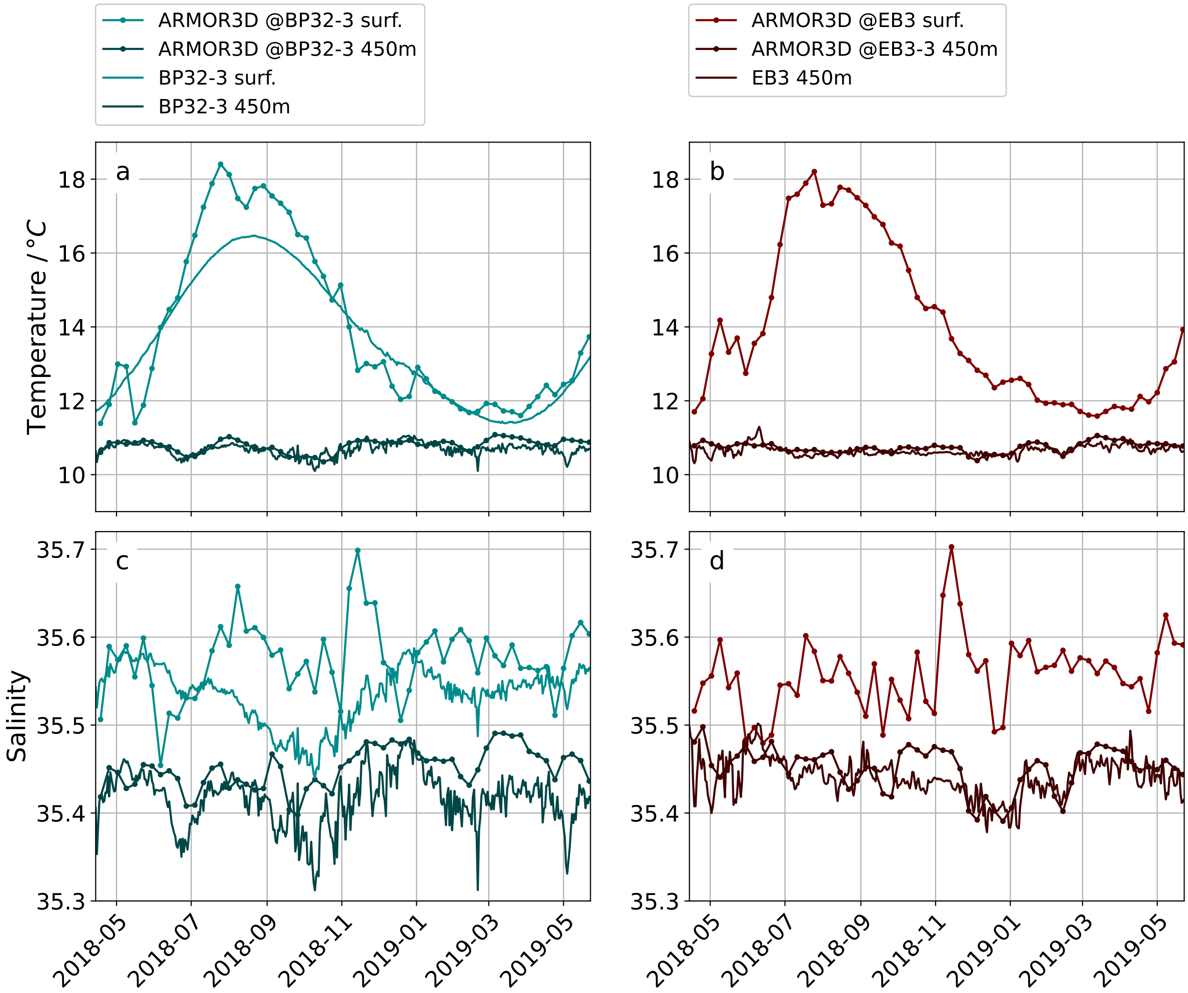

Figure A.3: Time series of temperature (a, b) and salinity (c, d) at the BP32-3 (a, c) and EB3 (b, d) locations at the surface and at 450 m, the depth of the shallowest recording device at EB3. The solid lines with dots show ARMOR3D time series linearly interpolated to the exact locations of BP32-3 and EB3 in weekly resolution, the solid lines are obtained from BP32 and EB3, respectively. Bright colors mark surface values, while dark colors refer to the depth of 450 m.

by a large value, resulting in the maximum velocity occurring right above the seafloor (Figure A.1 d). Due to this unrealistic behavior of the geostrophic velocity, the two approaches of assuming a constant value or a constant gradient at EB3 between 450 m and the surface are not considered further. Instead, the analysis focuses on extrapolating the EB3 data on the ARMOR3D surface values.

Nowitzki et al. (2021) showed that the baroclinic SSH fluctuations at different PIES locations (including BP32 in 2016/2017) are highly correlated ($r \geq 0.85$) with the corresponding SSH fluctuations obtained from satellite altimetry (their Figure 9). Such a high correlation is desirable when calculating absolute transports from PIES measurements and altimetry SSH. With $r = 0.78$, the correlation of the SSH at BP32-3 derived from PIES measurements with the satellite SSH is lower than in 2016/2017. However,

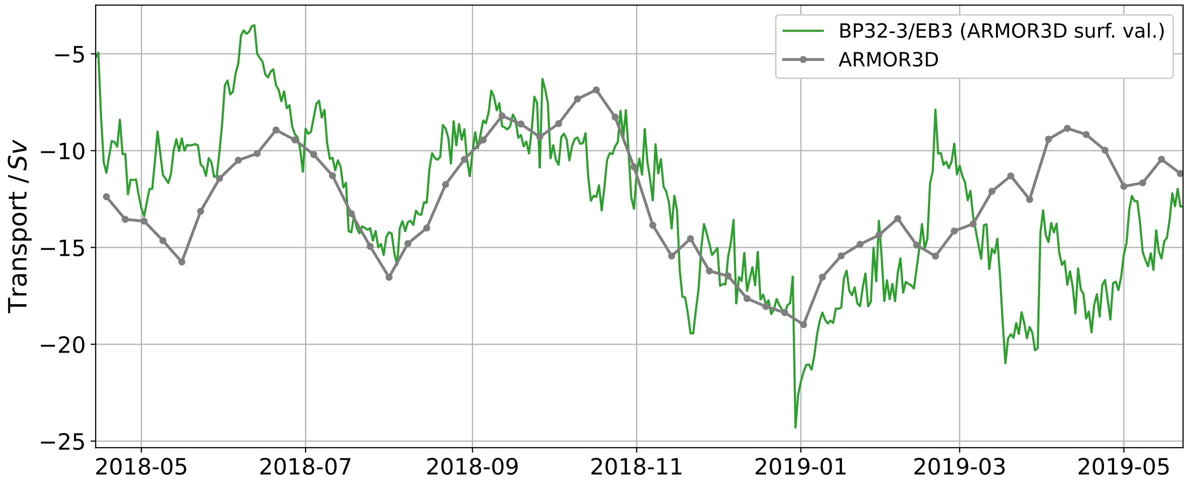

Figure A.4: Geostrophic top-bottom transports between BP32-3 and EB3. The green line shows the geostrophic transports calculated from the measurements of BP32-3 and EB3 (the missing values between 450 m and the surface at EB3 are extrapolated to ARMOR3D surface values). The grey line indicates the geostrophic transport, calculated from ARMOR3D. Note that the temporal resolution is smaller for the ARMOR3D time series as this data set is provided in weekly resolution.

a meaningful transport between two stations could still be calculated with such a correlation. The problem for calculating the geostrophic transports lies in the low coverage of instruments at the EB3 mooring. The correlation between the altimetry SSH and the SSH derived from the available EB3 data between 450 m, and 1700 m is low ($r = 0.15$) and insignificant. The reason for this low correlation is the missing data between 450 m and the surface, where the strongest variability in the geostrophic velocity occurs. To get an estimate of the upper 450 m, the temperature and salinity values at the EB3 mooring are interpolated onto ARMOR3D surface values of temperature and salinity. With this approach, the correlation with the altimetry SSH increases to $r = 0.4$ but remains insignificant. This increased yet still insignificant correlation indicates that the upper 450 m are crucial to achieving a high correlation with the altimetry SSH and calculating accurate geostrophic velocities. However, the extrapolation to ARMOR3D surface values is not sufficient to resolve this surface signal. To further investigate the behavior of the correlation when extrapolating to ARMOR3D surface values, the values between 450 m and the surface at BP32-3 were cut and extrapolated to ARMOR3D surface values. As a result, the correlation with the altimetry SSH drops to $r = 0.27$ (insignificant). This indicates that the extrapolation to ARMOR3D surface values might also worsen the correlation at the EB3 mooring.

Extrapolating the EB3 values between 450 m and the surface to ARMOR3D surface values overestimates the SSH in late summer and early fall (July-October) 2018 compared to the SSH obtained from altimetry (Figure A.2). This overestimation introduces strong horizontal gradients of geopotential anomalies and thus might introduce unrealistic geostrophic transports. The overestimation coincides with a difference in SST and SSS, derived from the PIES measurements and from ARMOR3D (Figure A.3 a, c), while the differences in 450 m depth are smaller.

Based on these findings, the approach of extrapolating the EB3 measurements and calculating geostrophic velocities from these was not pursued further. Instead, for the sake of simplicity, the geostrophic transports between BP32-3 and EB3 used to obtain a basin-wide AMOC estimate were fully calculated from ARMOR3D. As depicted in Figure A.4, the geostrophic transports between the BP32-3 and EB3 calculated from the PIES and mooring measurements as well as from ARMOR3D are generally comparable. Small differences in the magnitude of these transports will likely have a minor effect on the basin-wide AMOC estimate.

A.2 Additional figures

Here, additional figures complementing the main text are shown. The individual Figures are described briefly in the following.

Figure A.5 and Figure A.6 show the top-bottom volume transport for the individual transport components of the AMOC at 47°N individually and as the combined transport of the western components.

Figure A.7 shows the upper 700 m trends of temperature and salinity in the North Atlantic in 1993-2018 in the EN4 reanalysis.

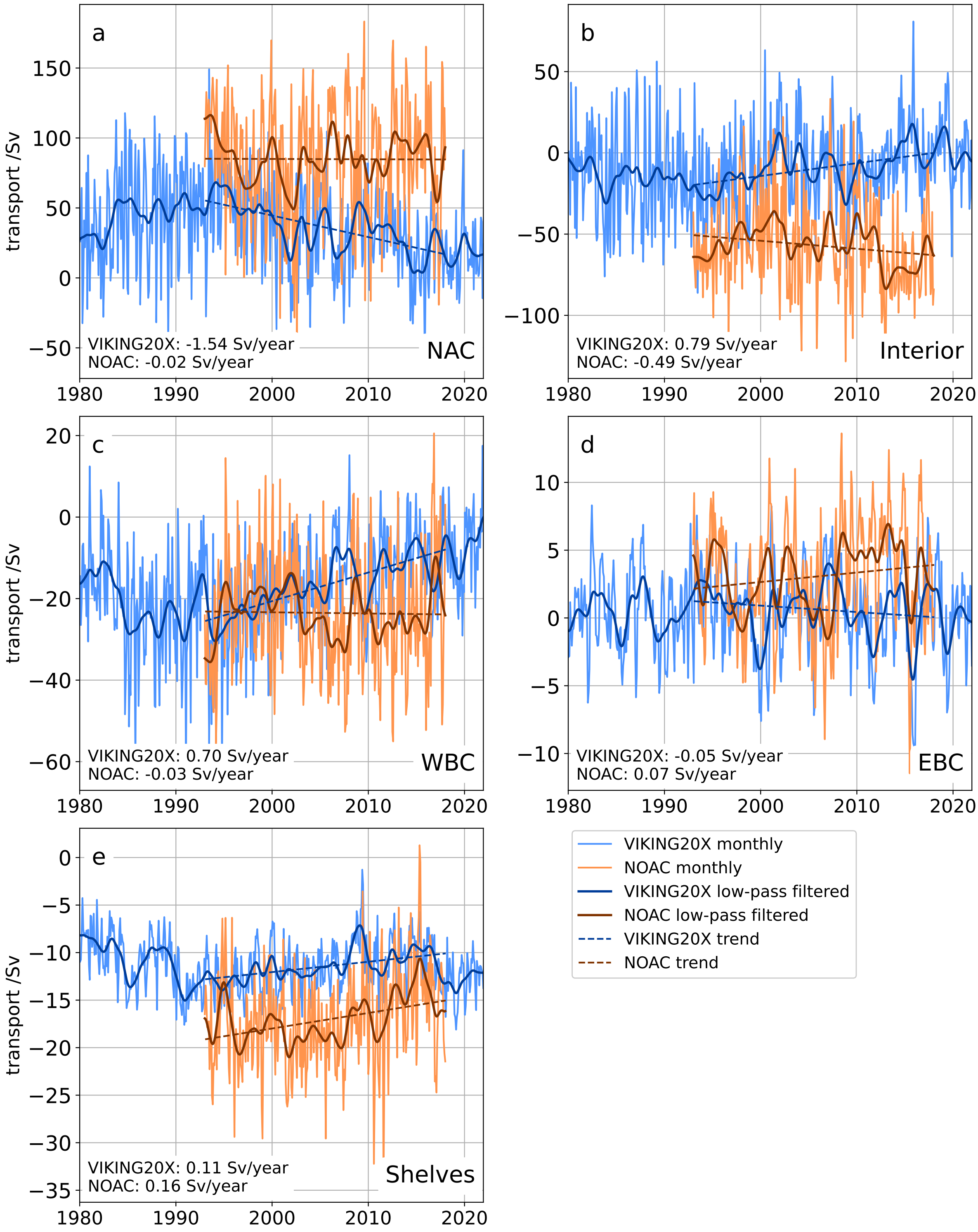

Figure A.5: Similar to Figure 4.3 but for top-bottom transports. Volume transport comparison between top-bottom transports of individual AMOC components at the NOAC line from VIKING20X and observations of the NOAC array. Individual components are defined in the same way as shown in Figure 2.4. These components include the NAC, interior transport, WBC, EBC, and shelves transport. VIKING20X transports are in blue, NOAC transports are in orange. The dark lines denote the low-pass filtered time series. The dashed lines denote the trend over the observation period (1993-2018). The magnitude of these trends is given in the lower left corner of each subplot.

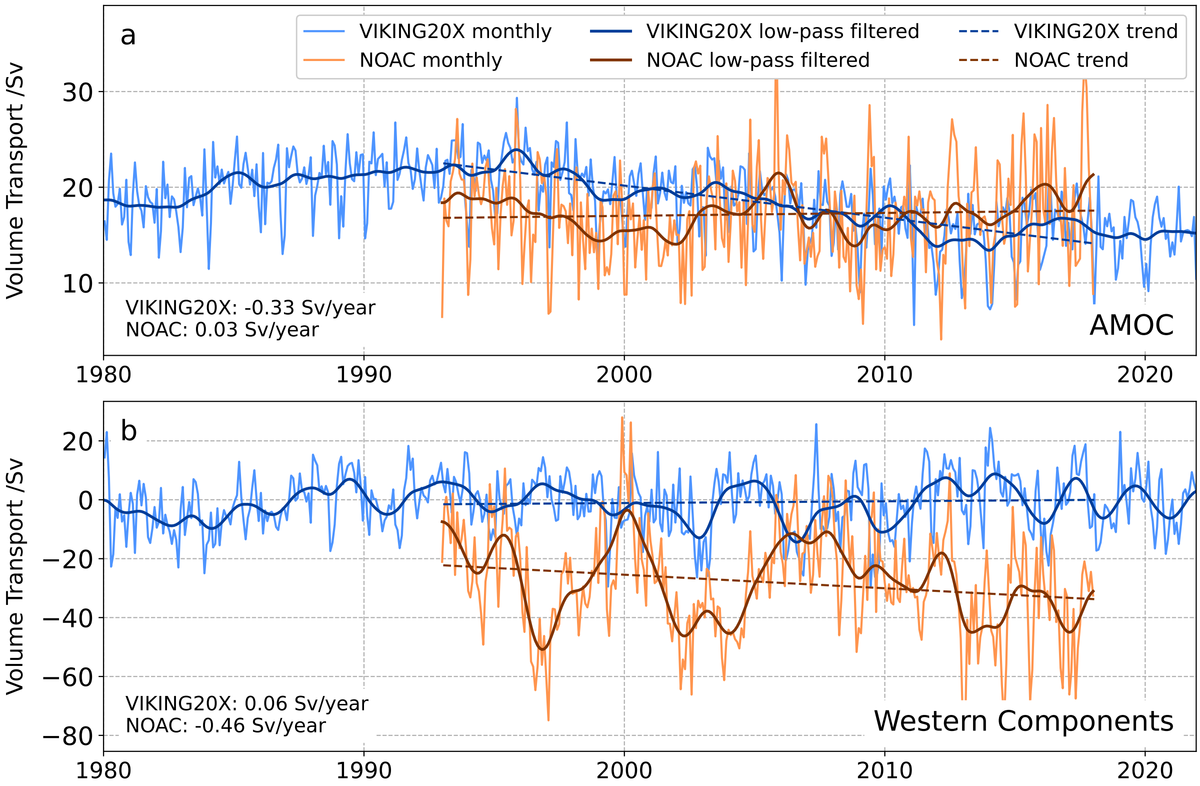

Figure A.6: Similar to Figure 4.4 but for top-bottom transports of the western components. Volume transport comparison between the basin-wide AMOC (as defined in Section 2.4.1, thus not top-bottom) and the sum of the top-bottom transports of the western components (western shelf, WBC, NAC) at the location of the NOAC array from VIKING20X and observations of the NOAC array. Individual components are defined in the same way as shown in Figure 2.4. VIKING20X transports are in blue, NOAC transports are in orange. The dark lines denote the low-pass filtered time series. The dashed lines denote the trend over the observation period (1993-2018). The magnitude of these trends is given in the lower left corner of each subplot.

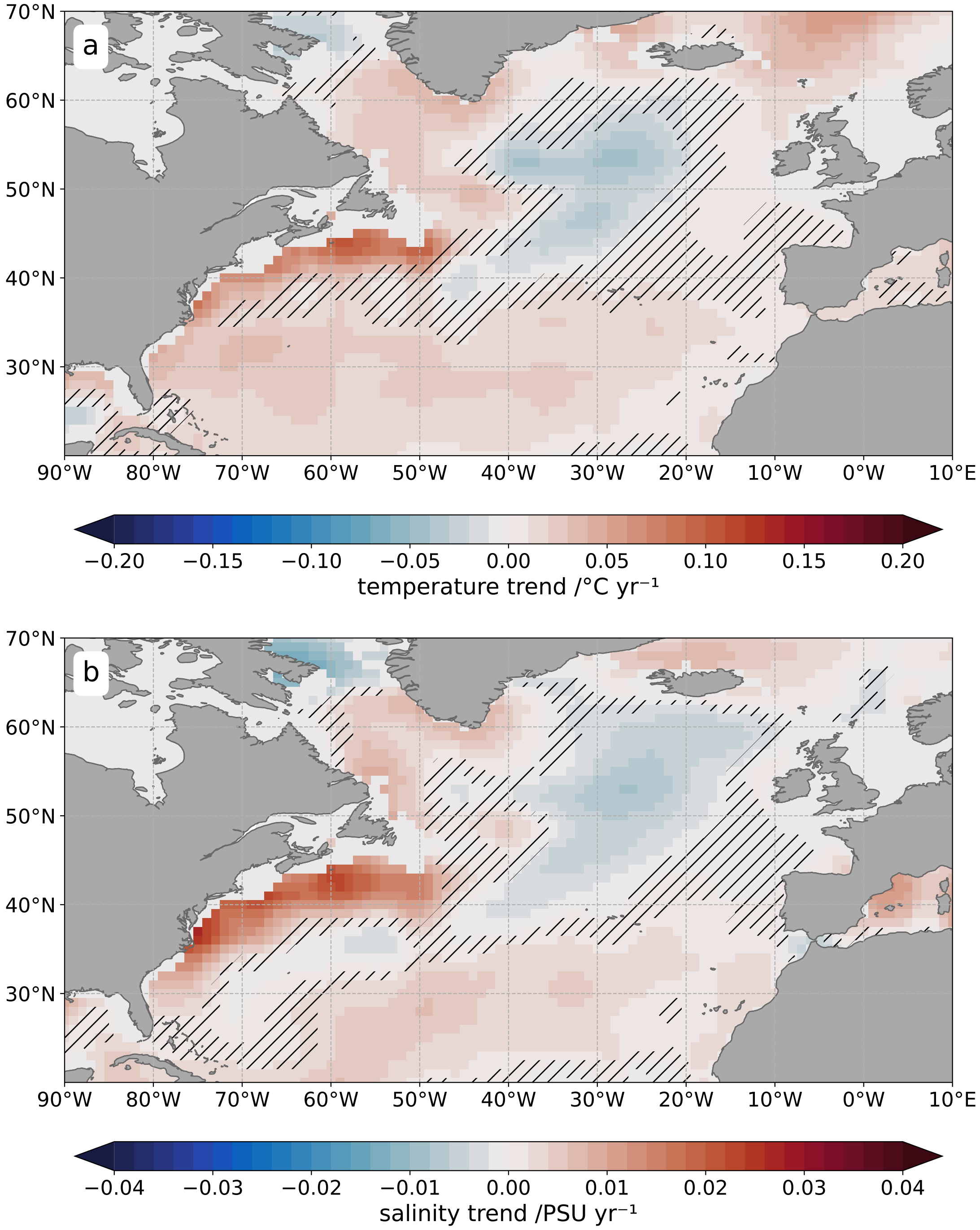

Figure A.7: Similar to Figure 4.8 but for EN4. 1993-2018 temperature (a) and salinity (b) trends in the upper 700 m in the North Atlantic from EN4. Only trends for regions with depths >700 m are shown. Regions with insignificant trends are hatched.

Acronyms

ADT	Absolute dynamic topography
AMOC	Atlantic Meridional Overturning Circulation
ANHA	Arctic Northern Hemisphere Atlantic
ANHA4	ANHA simulation with $^1/_4$° resolution
ANHA12	ANHA simulation with $^1/_{12}$° resolution
AR7W	Atlantic Repeat Hydrography 7 West section
BP	Bremen PIES
BSH	Bundesamt für Seeschifffarhrt und Hydrographie (Federal Maritime and Hydrographic Agency)
CGRF	Canadian Meteorological Centre Global Deterministic Prediction System reforecasts
CMIP6	Coupled Model Intercomparison Project Phase 6
CORE	Coordinated Ocean Reference Experiment
CTD	Conductivity-Temperature-Depth probe
DFS	DRAKKAR Forcing Set
DWBC	Deep Western Boundary Current
EB	Eastern Boundary
EBC	Eastern Boundary Current
ETOPO	Earth Topography
GEM	Gravest Empirical Mode
GPA	Geopotential anomaly
IPCC	Intergovernmental Panel on Climate Change
IRTG	International Research Training Group
JRA55-do	Forcing data set based on the Japanese 55-year Atmospheric Reanalysis
LAB60	nested ANHA simulation with $^1/_{60}$° resolution in the Labrador Sea
lADCP	lowered Acoustic Doppler Current Profiler
LSW	Labrador Sea Water
MHT	Meridional heat transport
MOVE	Merdional Overturning Variability Experiment
NAC	North Atlantic Current
NAO	North Atlantic Oscillation
NEMO	Nucleus for European Modelling of the Ocean
NOAA	National Oceanic and Atmospheric Administration

NOAC	North Atlantic Changes
OCE	NEMO Ocean Engine
OHC	Ocean heat content
OMIP	Ocean Model Intercomparison Project
OSNAP	Overturning in the Subpolar North Atlantic Program
PIES	Pressure sensor-equipped Inverted Echo Sounder
RAPID	(RAPID-MOCHA-WBTS) Rapid climate change - Meridional Overturning Circulation Heat Transport Array - Western Boundary Time Series
SEM	Standard error of the mean
SLA	Sea level anomaly
SPG12	parent nest of the subpolar gyre with $^{1}/_{12}^{\circ}$ resolution for LAB60 in the ANHA simulations
SSH	Sea surface height
SSS	Sea surface salinity
SST	Sea surface temperature
STD	Standard deviation
SVA	Specific volume anomaly
WOA	World Ocean Atlas
WOCE	World Ocean Circulation Experiment

List of Figures

List of Tables

Bibliography

Arakawa, A. & Lamb, V. R. (1977). Computational Design of the Basic Dynamical Processes of the UCLA General Circulation Model. *Methods in Computational Physics: Advances in Research and Applications*, volume 17, 173–265. Elsevier. `https://doi.org/10.1016/B978-0-12-460817-7.50009-4`

Baker, J., Renshaw, R., Jackson, L., Dubois, C., Iovino, D., & Zuo, H. (2022). Overturning variations in the subpolar North Atlantic in an ocean reanalyses ensemble. *Journal of Operational Oceanography, Copernicus Marine Service Ocean State Report*, (6), 16–20. `https://doi.org/10.1080/1755876X.2022.2095169`

Bakker, P., Schmittner, A., Lenaerts, J. T. M., Abe-Ouchi, A., Bi, D., Van Den Broeke, M. R., Chan, W., Hu, A., Beadling, R. L., Marsland, S. J., Mernild, S. H., Saenko, O. A., Swingedouw, D., Sullivan, A., & Yin, J. (2016). Fate of the Atlantic Meridional Overturning Circulation: Strong decline under continued warming and Greenland melting. *Geophysical Research Letters*, 43(23). `https://doi.org/10.1002/2016GL070457`

Balmaseda, M., Hernandez, F., Storto, A., Palmer, M., Alves, O., Shi, L., Smith, G., Toyoda, T., Valdivieso, M., Barnier, B., Behringer, D., Boyer, T., Chang, Y.-S., Chepurin, G., Ferry, N., Forget, G., Fujii, Y., Good, S., Guinehut, S., Haines, K., Ishikawa, Y., Keeley, S., Köhl, A., Lee, T., Martin, M., Masina, S., Masuda, S., Meyssignac, B., Mogensen, K., Parent, L., Peterson, K., Tang, Y., Yin, Y., Vernieres, G., Wang, X., Waters, J., Wedd, R., Wang, O., Xue, Y., Chevallier, M., Lemieux, J.-F., Dupont, F., Kuragano, T., Kamachi, M., Awaji, T., Caltabiano, A., Wilmer-Becker, K., & Gaillard, F. (2015). The Ocean Reanalyses Intercomparison Project (ORA-IP). *Journal of Operational Oceanography*, 8, 80–97. `https://doi.org/10.1080/1755876X.2015.1022329`

Bamber, J., Van Den Broeke, M., Ettema, J., Lenaerts, J., & Rignot, E. (2012). Recent large increases in freshwater fluxes from Greenland into the North Atlantic. *Geophysical Research Letters*, 39(19), 2012GL052552. `https://doi.org/10.1029/2012GL052552`

Bamber, J. L., Tedstone, A. J., King, M. D., Howat, I. M., Enderlin, E. M., Van Den Broeke, M. R., & Noel, B. (2018). Land Ice Freshwater Budget of the Arctic and North Atlantic Oceans: 1. Data, Methods, and Results. *Journal of Geophysical Research: Oceans*, 123(3), 1827–1837. `https://doi.org/10.1002/2017JC013605`

Barnier, B., Madec, G., Penduff, T., Molines, J.-M., Treguier, A.-M., Le Sommer, J., Beckmann, A., Biastoch, A., Böning, C., Dengg, J., Derval, C., Durand, E., Gulev, S., Remy, E., Talandier, C., Theetten, S., Maltrud, M., McClean, J., & De Cuevas, B. (2006). Impact of partial steps and momentum advection schemes in a global ocean circulation model at eddy-permitting resolution. *Ocean Dynamics*, 56(5-6), 543–567. `https://doi.org/10.1007/s10236-006-0082-1`

Barnston, A. G. & Livezey, R. E. (1987). Classification, Seasonality and Persistence of Low-Frequency Atmospheric Circulation Patterns. *Monthly Weather Review*, 115(6), 1083–1126. https://doi.org/https://doi.org/10.1175/1520-0493(1987)115<1083:CSAPOL>2.0.CO;2

Beal, L. M., De Ruijter, W. P. M., Biastoch, A., Zahn, R., SCOR/WCRP/IAPSO Working Group 136, Cronin, M., Hermes, J., Lutjeharms, J., Quartly, G., Tozuka, T., Baker-Yeboah, S., Bornman, T., Cipollini, P., Dijkstra, H., Hall, I., Park, W., Peeters, F., Penven, P., Ridderinkhof, H., & Zinke, J. (2011). On the role of the Agulhas system in ocean circulation and climate. *Nature*, 472(7344), 429–436. https://doi.org/10.1038/nature09983

Behrens, E., Biastoch, A., & Böning, C. W. (2013). Spurious AMOC trends in global ocean sea-ice models related to subarctic freshwater forcing. *Ocean Modelling*, 69, 39–49. https://doi.org/10.1016/j.ocemod.2013.05.004

Bentamy, A. (2022). Quality Information Document For the Global Ocean Wind Products WIND_glo_wind_l4_rep_observations_012_006. *Copernicus Marine Service*, (1.4), 23.

Bentamy, A., Piollé, J. F., Prevost, C., & Giesen, R. (2022). Product User Manual for Wind Product WIND_glo_wind_l4_rep_observations_012_006. *Copernicus Marine Service*, (1.3), 26.

Benveniste, J., Birol, F., Calafat, F., Cazenave, A., Dieng, H., Gouzenes, Y., Legeais, J. F., Léger, F., Niño, F., Passaro, M., Schwatke, C., & Shaw, A. (2020). Coastal sea level anomalies and associated trends from Jason satellite altimetry over 2002–2018. *Scientific Data*, 7(1), 357. https://doi.org/10.1038/s41597-020-00694-w

Biastoch, A., Böning, C. W., Getzlaff, J., Molines, J.-M., & Madec, G. (2008a). Causes of Interannual–Decadal Variability in the Meridional Overturning Circulation of the Midlatitude North Atlantic Ocean. *Journal of Climate*, 21(24), 6599–6615. https://doi.org/10.1175/2008JCLI2404.1

Biastoch, A., Böning, C. W., & Lutjeharms, J. R. E. (2008b). Agulhas leakage dynamics affects decadal variability in Atlantic overturning circulation. *Nature*, 456(7221), 489–492. https://doi.org/10.1038/nature07426

Biastoch, A., Schwarzkopf, F. U., Getzlaff, K., Rühs, S., Martin, T., Scheinert, M., Schulzki, T., Handmann, P., Hummels, R., & Böning, C. W. (2021). Regional imprints of changes in the Atlantic Meridional Overturning Circulation in the eddy-rich ocean model VIKING20X. *Ocean Science*, 17(5), 1177–1211. https://doi.org/10.5194/os-17-1177-2021

Biastoch, A., Sein, D., Durgadoo, J. V., Wang, Q., & Danilov, S. (2018). Simulating the Agulhas system in global ocean models – nesting vs. multi-resolution unstructured meshes. *Ocean Modelling*, 121, 117–131. https://doi.org/10.1016/j.ocemod.2017.12.002

Bingham, R. J., Hughes, C. W., Roussenov, V., & Williams, R. G. (2007). Meridional coherence of the North Atlantic meridional overturning circulation. *Geophysical Research Letters*, 34(23). https://doi.org/10.1029/2007GL031731

Blaker, A. T., Hirschi, J. J.-M., Bell, M. J., & Bokota, A. (2021). Wind-Driven Oscillations in the Meridional Overturning Circulation near the equator. Part I: Numerical Models.

Journal of Physical Oceanography, 51(3), 645–661. https://doi.org/10.1175/JPO-D-19-0296.1

Boccaletti, G., Ferrari, R., Adcroft, A., Ferreira, D., & Marshall, J. (2005). The vertical structure of ocean heat transport. *Geophysical Research Letters*, 32(10), 2005GL022474. https://doi.org/10.1029/2005GL022474

Boers, N. (2021). Observation-based early-warning signals for a collapse of the Atlantic Meridional Overturning Circulation. *Nature Climate Change*, 11(8), 680–688. https://doi.org/10.1038/s41558-021-01097-4

Bouillon, S., Morales Maqueda, M. A., Legat, V., & Fichefet, T. (2009). An elastic–viscous–plastic sea ice model formulated on Arakawa B and C grids. *Ocean Modelling*, 27(3-4), 174–184. https://doi.org/10.1016/j.ocemod.2009.01.004

Breckenfelder, T., Rhein, M., Roessler, A., Böning, C. W., Biastoch, A., Behrens, E., & Mertens, C. (2017). Flow paths and variability of the North Atlantic Current: A comparison of observations and a high-resolution model. *Journal of Geophysical Research: Oceans*, 122(4), 2686–2708. https://doi.org/10.1002/2016JC012444

Bretherton, F. P., Davis, R. E., & Fandry, C. (1976). A technique for objective analysis and design of oceanographic experiments applied to MODE-73. *Deep Sea Research and Oceanographic Abstracts*, 23(7), 559–582. https://doi.org/10.1016/0011-7471(76)90001-2

Broecker, W. S. (1987). The biggest chill. *Natural History Magazine*, 97, 74–82.

Broecker, W. S. (1991). The Great Ocean Conveyor. *Oceanography*, 4(2), 79–89. https://doi.org/10.5670/oceanog.1991.07

Bryden, H. L. & Imawaki, S. (2001). Chapter 6.1 Ocean heat transport. *International Geophysics*, volume 77, 455–474. Elsevier. https://doi.org/10.1016/S0074-6142(01)80134-0

Buckley, M. W. & Marshall, J. (2016). Observations, inferences, and mechanisms of the Atlantic Meridional Overturning Circulation: A review. *Reviews of Geophysics*, 54(1), 5–63. https://doi.org/10.1002/2015RG000493

Böning, C. W., Behrens, E., Biastoch, A., Getzlaff, K., & Bamber, J. L. (2016). Emerging impact of Greenland meltwater on deepwater formation in the North Atlantic Ocean. *Nature Geoscience*, 9(7), 523–527. https://doi.org/10.1038/ngeo2740

Böning, C. W., Wagner, P., Handmann, P., Schwarzkopf, F. U., Getzlaff, K., & Biastoch, A. (2023). Decadal changes in Atlantic overturning due to the excessive 1990s Labrador Sea convection. *Nature Communications*, 14(1), 4635. https://doi.org/10.1038/s41467-023-40323-9

Caesar, L., McCarthy, G. D., Thornalley, D. J. R., Cahill, N., & Rahmstorf, S. (2021). Current Atlantic Meridional Overturning Circulation weakest in last millennium. *Nature Geoscience*, 14(3), 118–120. https://doi.org/10.1038/s41561-021-00699-z

Caesar, L., Rahmstorf, S., Robinson, A., Feulner, G., & Saba, V. (2018). Observed fingerprint of a weakening Atlantic Ocean overturning circulation. *Nature*, 556(7700), 191–196. https://doi.org/10.1038/s41586-018-0006-5

Chafik, L., Holliday, N. P., Bacon, S., & Rossby, T. (2022). Irminger Sea Is the Center of Action for Subpolar AMOC Variability. *Geophysical Research Letters*, 49(17), e2022GL099133. https://doi.org/10.1029/2022GL099133

Chaplin, G. & Watts, D. (1984). Inverted Echo Sounder Development. *OCEANS 1984*, 249–253. https://doi.org/10.1109/OCEANS.1984.1152347

Clément, L., Frajka-Williams, E., Szuts, Z. B., & Cunningham, S. A. (2014). Vertical structure of eddies and Rossby waves, and their effect on the Atlantic meridional overturning circulation at 26.5°N. *Journal of Geophysical Research: Oceans*, 119(9), 6479–6498. https://doi.org/10.1002/2014JC010146

Cunningham, S. A., Kanzow, T., Rayner, D., Baringer, M. O., Johns, W. E., Marotzke, J., Longworth, H. R., Grant, E. M., Hirschi, J. J.-M., Beal, L. M., Meinen, C. S., & Bryden, H. L. (2007). Temporal Variability of the Atlantic Meridional Overturning Circulation at 26.5°N. *Science*, 317(5840), 935–938. https://doi.org/10.1126/science.1141304

Dai, A., Qian, T., Trenberth, K. E., & Milliman, J. D. (2009). Changes in Continental Freshwater Discharge from 1948 to 2004. *Journal of Climate*, 22(10), 2773–2792. https://doi.org/10.1175/2008JCLI2592.1

Danabasoglu, G., Castruccio, F. S., Small, R. J., Tomas, R., Frajka-Williams, E., & Lankhorst, M. (2021). Revisiting AMOC Transport Estimates From Observations and Models. *Geophysical Research Letters*, 48(10). https://doi.org/10.1029/2021GL093045

Danabasoglu, G., Yeager, S. G., Bailey, D., Behrens, E., Bentsen, M., Bi, D., Biastoch, A., Böning, C., Bozec, A., Canuto, V. M., Cassou, C., Chassignet, E., Coward, A. C., Danilov, S., Diansky, N., Drange, H., Farneti, R., Fernandez, E., Fogli, P. G., Forget, G., Fujii, Y., Griffies, S. M., Gusev, A., Heimbach, P., Howard, A., Jung, T., Kelley, M., Large, W. G., Leboissetier, A., Lu, J., Madec, G., Marsland, S. J., Masina, S., Navarra, A., George Nurser, A., Pirani, A., Y Mélia, D. S., Samuels, B. L., Scheinert, M., Sidorenko, D., Treguier, A.-M., Tsujino, H., Uotila, P., Valcke, S., Voldoire, A., & Wang, Q. (2014). North Atlantic simulations in Coordinated Ocean-ice Reference Experiments phase II (CORE-II). Part I: Mean states. *Ocean Modelling*, 73, 76–107. https://doi.org/10.1016/j.ocemod.2013.10.005

Danabasoglu, G., Yeager, S. G., Kim, W. M., Behrens, E., Bentsen, M., Bi, D., Biastoch, A., Bleck, R., Böning, C., Bozec, A., Canuto, V. M., Cassou, C., Chassignet, E., Coward, A. C., Danilov, S., Diansky, N., Drange, H., Farneti, R., Fernandez, E., Fogli, P. G., Forget, G., Fujii, Y., Griffies, S. M., Gusev, A., Heimbach, P., Howard, A., Ilicak, M., Jung, T., Karspeck, A. R., Kelley, M., Large, W. G., Leboissetier, A., Lu, J., Madec, G., Marsland, S. J., Masina, S., Navarra, A., Nurser, A. G., Pirani, A., Romanou, A., Salas Y Mélia, D., Samuels, B. L., Scheinert, M., Sidorenko, D., Sun, S., Treguier, A.-M., Tsujino, H., Uotila, P., Valcke, S., Voldoire, A., Wang, Q., & Yashayaev, I. (2016). North Atlantic simulations in Coordinated Ocean-ice Reference Experiments phase II (CORE-II). Part II: Inter-annual to decadal variability. *Ocean Modelling*, 97, 65–90. https://doi.org/10.1016/j.ocemod.2015.11.007

Daniault, N., Lherminier, P., & Mercier, H. (2011). Circulation and Transport at the Southeast Tip of Greenland. *Journal of Physical Oceanography*, 41(3), 437–457. https://doi.org/10.1175/2010JPO4428.1

Danilov, S. (2013). Ocean modeling on unstructured meshes. *Ocean Modelling*, 69, 195–210. https://doi.org/10.1016/j.ocemod.2013.05.005

De Jong, M. F., Bower, A. S., & Furey, H. H. (2016). Seasonal and Interannual Variations of Irminger Ring Formation and Boundary–Interior Heat Exchange in FLAME. *Journal of Physical Oceanography*, 46(6), 1717–1734. https://doi.org/10.1175/JPO-D-15-0124.1

Desbiolles, F., Bentamy, A., Blanke, B., Roy, C., Mestas-Nuñez, A. M., Grodsky, S. A., Herbette, S., Cambon, G., & Maes, C. (2017). Two decades [1992–2012] of surface wind analyses based on satellite scatterometer observations. *Journal of Marine Systems*, 168, 38–56. https://doi.org/10.1016/j.jmarsys.2017.01.003

Desbruyères, D. G., Mercier, H., Maze, G., & Daniault, N. (2019). Surface predictor of overturning circulation and heat content change in the subpolar North Atlantic. *Ocean Science*, 15(3), 809–817. https://doi.org/10.5194/os-15-809-2019

Diabaté, S. T., Swingedouw, D., Hirschi, J. J.-M., Duchez, A., Leadbitter, P. J., Haigh, I. D., & McCarthy, G. D. (2021). Western boundary circulation and coastal sea-level variability in northern hemisphere oceans. *Ocean Science*, 17, 1449–1471. https://doi.org/10.5194/os-17-1449-2021

Ditlevsen, P. & Ditlevsen, S. (2023). Warning of a forthcoming collapse of the Atlantic meridional overturning circulation. *Nature Communications*, 14(1), 4254. https://doi.org/10.1038/s41467-023-39810-w

Dong, S., Baringer, M. O., Goni, G. J., Meinen, C. S., & Garzoli, S. L. (2014). Seasonal variations in the South Atlantic Meridional Overturning Circulation from observations and numerical models. *Geophysical Research Letters*, 41(13), 4611–4618. https://doi.org/10.1002/2014GL060428

Drijfhout, S., Van Oldenborgh, G. J., & Cimatoribus, A. (2012). Is a Decline of AMOC Causing the Warming Hole above the North Atlantic in Observed and Modeled Warming Patterns? *Journal of Climate*, 25(24), 8373–8379. https://doi.org/10.1175/JCLI-D-12-00490.1

Drijfhout, S. S., Weber, S. L., & Van Der Swaluw, E. (2010). The stability of the MOC as diagnosed from model projections for pre-industrial, present and future climates. *Climate Dynamics*, 37(7-8), 1575–1586. https://doi.org/10.1007/s00382-010-0930-z

Dussin, R., Barnier, B., Brodeau, L., & Molines, J.-M. (2016). The Making Of The Drakkar Forcing Set Dfs5. Technical report, Zenodo. https://doi.org/10.5281/ZENODO.1209243

Ebisuzaki, W. (1997). A Method to Estimate the Statistical Significance of a Correlation When the Data Are Serially Correlated. *Journal of Climate*, 10(9), 2147–2153. https://doi.org/10.1175/1520-0442(1997)010<2147:AMTETS>2.0.CO;2

Elipot, S., Frajka-Williams, E., Hughes, C. W., Olhede, S., & Lankhorst, M. (2017). Observed Basin-Scale Response of the North Atlantic Meridional Overturning Circulation to Wind Stress Forcing. *Journal of Climate*, 30(6), 2029–2054. https://doi.org/10.1175/JCLI-D-16-0664.1

Elipot, S., Frajka-Williams, E., Hughes, C. W., & Willis, J. K. (2014). The Observed North Atlantic Meridional Overturning Circulation: Its Meridional Coherence and Ocean Bottom Pressure. *Journal of Physical Oceanography*, 44(2), 517–537. https://doi.org/10.1175/JPO-D-13-026.1

Emery, W. J. & Thomson, R. E. (1998). *Data Analysis Methods in Physical Oceanography* (1st ed.). Pergamon.

Feucher, C., Garcia-Quintana, Y., Yashayaev, I., Hu, X., & Myers, P. G. (2019). Labrador Sea Water Formation Rate and Its Impact on the Local Meridional Overturning Circulation. *Journal of Geophysical Research: Oceans*, 124(8), 5654–5670. https://doi.org/10.1029/2019JC015065

Foley, A., Fealy, R., & Sweeney, J. (2013). Model skill measures in probabilistic regional climate projections for Ireland. *Climate Research*, 56(1), 33–49. https://doi.org/10.3354/cr01140

Forget, G., Campin, J.-M., Heimbach, P., Hill, C. N., Ponte, R. M., & Wunsch, C. (2015). ECCO version 4: an integrated framework for non-linear inverse modeling and global ocean state estimation. *Geoscientific Model Development*, 8(10), 3071–3104. https://doi.org/10.5194/gmd-8-3071-2015

Foukal, N. P. & Chafik, L. (2022). The AMOC needs a universally-accepted definition. preprint, Oceanography. https://doi.org/10.1002/essoar.10512765.1

Fox, A. D., Handmann, P., Schmidt, C., Fraser, N., Rühs, S., Sanchez-Franks, A., Martin, T., Oltmanns, M., Johnson, C., Rath, W., Holliday, N. P., Biastoch, A., Cunningham, S. A., & Yashayaev, I. (2022). Exceptional freshening and cooling in the eastern subpolar North Atlantic caused by reduced Labrador Sea surface heat loss. *Ocean Science*, 18(5), 1507–1533. https://doi.org/10.5194/os-18-1507-2022

Fox-Kemper, B., Adcroft, A., Böning, C. W., Chassignet, E. P., Curchitser, E., Danabasoglu, G., Eden, C., England, M. H., Gerdes, R., Greatbatch, R. J., Griffies, S. M., Hallberg, R. W., Hanert, E., Heimbach, P., Hewitt, H. T., Hill, C. N., Komuro, Y., Legg, S., Le Sommer, J., Masina, S., Marsland, S. J., Penny, S. G., Qiao, F., Ringler, T. D., Treguier, A. M., Tsujino, H., Uotila, P., & Yeager, S. G. (2019). Challenges and Prospects in Ocean Circulation Models. *Frontiers in Marine Science*, 6, 65. https://doi.org/10.3389/fmars.2019.00065

Frajka-Williams, E. (2015). Estimating the Atlantic overturning at 26°N using satellite altimetry and cable measurements. *Geophysical Research Letters*, 42(9), 3458–3464. https://doi.org/10.1002/2015GL063220

Frajka-Williams, E., Ansorge, I. J., Baehr, J., Bryden, H. L., Chidichimo, M. P., Cunningham, S. A., Danabasoglu, G., Dong, S., Donohue, K. A., Elipot, S., Heimbach, P., Holliday, N. P., Hummels, R., Jackson, L. C., Karstensen, J., Lankhorst, M., Le Bras, I. A., Lozier, M. S., McDonagh, E. L., Meinen, C. S., Mercier, H., Moat, B. I., Perez, R. C., Piecuch, C. G., Rhein, M., Srokosz, M. A., Trenberth, K. E., Bacon, S., Forget, G., Goni, G., Kieke, D., Koelling, J., Lamont, T., McCarthy, G. D., Mertens, C., Send, U., Smeed, D. A., Speich, S., van den Berg, M., Volkov, D., & Wilson, C. (2019). Atlantic Meridional Overturning Circulation: Observed Transport and Variability. *Frontiers in Marine Science*, 6, 260. https://doi.org/10.3389/fmars.2019.00260

Frajka-Williams, E., Foukal, N., & Danabasoglu, G. (2023). Should AMOC observations continue: how and why? *Philosophical Transactions of the Royal Society A: Mathematical, Physical and Engineering Sciences*, 381(2262), 20220195. https://doi.org/10.1098/rsta.2022.0195

Frajka-Williams, E., Meinen, C. S., Johns, W. E., Smeed, D. A., Duchez, A., Lawrence, A. J., Cuthbertson, D. A., McCarthy, G. D., Bryden, H. L., Baringer, M. O., Moat, B. I., & Rayner, D. (2016). Compensation between meridional flow components of the Atlantic MOC at 26° N. *Ocean Science*, 12(2), 481–493. https://doi.org/10.5194/os-12-481-2016

Frajka-Williams, E., Lankhorst, M., Koelling, J., & Send, U. (2018). Coherent Circulation Changes in the Deep North Atlantic From 16°N and 26°N Transport Arrays. *Journal of Geophysical Research: Oceans*, 123(5), 3427–3443. https://doi.org/10.1029/2018JC013949

Fu, Y. & Li, F. (2023). OSNAP technical report, Calculation method summary. Technical report. url: https://duke.app.box.com/v/2023OSNAPtechnicalreport.

Fu, Y., Lozier, M. S., Biló, T. C., Bower, A. S., Cunningham, S. A., Cyr, F., De Jong, M. F., deYoung, B., Drysdale, L., Fraser, N., Fried, N., Furey, H. H., Han, G., Handmann, P., Holliday, N. P., Holte, J., Inall, M. E., Johns, W. E., Jones, S., Karstensen, J., Li, F., Pacini, A., Pickart, R. S., Rayner, D., Straneo, F., & Yashayaev, I. (2023). Seasonality of the Meridional Overturning Circulation in the subpolar North Atlantic. *Communications Earth & Environment*, 4(1), 181. https://doi.org/10.1038/s43247-023-00848-9

Galbraith, E. D., Gnanadesikan, A., Dunne, J. P., & Hiscock, M. R. (2010). Regional impacts of iron-light colimitation in a global biogeochemical model.

Ganachaud, A. & Wunsch, C. (2003). Large-Scale Ocean Heat and Freshwater Transports during the World Ocean Circulation Experiment. *Journal of Climate*, 16(4), 696–705. https://doi.org/10.1175/1520-0442(2003)016<0696:LSOHAF>2.0.CO;2

Garcia-Quintana, Y., Courtois, P., Hu, X., Pennelly, C., Kieke, D., & Myers, P. G. (2019). Sensitivity of Labrador Sea Water Formation to Changes in Model Resolution, Atmospheric Forcing, and Freshwater Input. *Journal of Geophysical Research: Oceans*, 124(3), 2126–2152. https://doi.org/10.1029/2018JC014459

Gasparin, F., Hamon, M., Rémy, E., & Le Traon, P.-Y. (2020). How Deep Argo Will Improve the Deep Ocean in an Ocean Reanalysis. *Journal of Climate*, 33(1), 77–94. https://doi.org/10.1175/JCLI-D-19-0208.1

Good, S. A., Martin, M. J., & Rayner, N. A. (2013). EN4: Quality controlled ocean temperature and salinity profiles and monthly objective analyses with uncertainty estimates. *Journal of Geophysical Research: Oceans*, 118(12), 6704–6716. https://doi.org/10.1002/2013JC009067

Gouretski, V. & Reseghetti, F. (2010). On depth and temperature biases in bathythermograph data: Development of a new correction scheme based on analysis of a global ocean database. *Deep Sea Research Part I: Oceanographic Research Papers*, 57(6), 812–833. https://doi.org/10.1016/j.dsr.2010.03.011

Greiner, E., Verbrugge, N., Mulet, S., & Guinehut, S. (2021). Multi Observation Global Ocean 3D Temperature Salinity Heights Geostrophic Currents and MLD Product MULTIOBS_glo_phy_tsuv_3d_mynrt_015_012. (1.1), 31.

Griffies, S. M., Biastoch, A., Böning, C., Bryan, F., Danabasoglu, G., Chassignet, E. P., England, M. H., Gerdes, R., Haak, H., Hallberg, R. W., Hazeleger, W., Jungclaus, J., Large, W. G., Madec, G., Pirani, A., Samuels, B. L., Scheinert, M., Gupta, A. S., Severijns, C. A., Simmons, H. L., Treguier, A. M., Winton, M., Yeager, S., & Yin, J. (2009). Coordinated Ocean-ice Reference Experiments (COREs). *Ocean Modelling*, 26(1-2), 1–46. https://doi.org/10.1016/j.ocemod.2008.08.007

Griffies, S. M., Danabasoglu, G., Durack, P. J., Adcroft, A. J., Balaji, V., Böning, C. W., Chassignet, E. P., Curchitser, E., Deshayes, J., Drange, H., Fox-Kemper, B., Gleckler, P. J., Gregory, J. M., Haak, H., Hallberg, R. W., Heimbach, P., Hewitt, H. T., Holland, D. M., Ilyina, T., Jungclaus, J. H., Komuro, Y., Krasting, J. P., Large, W. G., Marsland, S. J., Masina, S., McDougall, T. J., Nurser, A. J. G., Orr, J. C., Pirani, A., Qiao, F., Stouffer, R. J., Taylor, K. E., Treguier, A. M., Tsujino, H., Uotila, P., Valdivieso, M., Wang, Q., Winton, M., & Yeager, S. G. (2016). OMIP contribution to CMIP6: experimental and diagnostic protocol for the physical component of the Ocean Model Intercomparison Project. *Geoscientific Model Development*, 9(9), 3231–3296. https://doi.org/10.5194/gmd-9-3231-2016

Gu, S., Liu, Z., & Wu, L. (2020). Time Scale Dependence of the Meridional Coherence of the Atlantic Meridional Overturning Circulation. *Journal of Geophysical Research: Oceans*, 125(3). https://doi.org/10.1029/2019JC015838

Guinehut, S. (2021). Multi Observation Global Ocean 3D Temperature Salinity Heights Geostrophic Currents and MLD Product. *Copernicus Marine Service*, (1.1), 15.

Guinehut, S., Dhomps, A.-L., Larnicol, G., & Le Traon, P.-Y. (2012). High resolution 3-D temperature and salinity fields derived from in situ and satellite observations. *Ocean Science*, 8(5), 845–857. https://doi.org/10.5194/os-8-845-2012

Hallberg, R. (2013). Using a resolution function to regulate parameterizations of oceanic mesoscale eddy effects. *Ocean Modelling*, 72, 92–103. https://doi.org/10.1016/j.ocemod.2013.08.007

Han, L. (2023). Exploring the AMOC Connectivity Between the RAPID and OSNAP Lines With a Model-Based Data Set. *Geophysical Research Letters*, 50(19), e2023GL105225. https://doi.org/10.1029/2023GL105225

Hansen, B., Húsgarð Larsen, K. M., Hátún, H., & Østerhus, S. (2016). A stable Faroe Bank Channel overflow 1995–2015. *Ocean Science*, 12(6), 1205–1220. https://doi.org/10.5194/os-12-1205-2016

Hansen, J., Ruedy, R., Glascoe, J., & Sato, M. (1999). GISS analysis of surface temperature change. *Journal of Geophysical Research: Atmospheres*, 104(D24), 30997–31022. https://doi.org/10.1029/1999JD900835

Harden, B., Pickart, R., Valdimarsson, H., Våge, K., De Steur, L., Richards, C., Bahr, F., Torres, D., Børve, E., Jónsson, S., Macrander, A., Østerhus, S., Håvik, L., & Hattermann, T. (2016). Upstream sources of the Denmark Strait Overflow: Observations from a high-resolution mooring array. *Deep Sea Research Part I: Oceanographic Research Papers*, 112, 94–112. https://doi.org/10.1016/j.dsr.2016.02.007

Henry, L. G., McManus, J. F., Curry, W. B., Roberts, N. L., Piotrowski, A. M., & Keigwin, L. D. (2016). North Atlantic ocean circulation and abrupt climate change during the last glaciation. *Science*, 353(6298), 470–474. https://doi.org/10.1126/science.aaf5529

Hersbach, H., Bell, B., Berrisford, P., Hirahara, S., Horányi, A., Muñoz-Sabater, J., Nicolas, J., Peubey, C., Radu, R., Schepers, D., Simmons, A., Soci, C., Abdalla, S., Abellan, X., Balsamo, G., Bechtold, P., Biavati, G., Bidlot, J., Bonavita, M., De Chiara, G., Dahlgren, P., Dee, D., Diamantakis, M., Dragani, R., Flemming, J., Forbes, R., Fuentes, M., Geer, A., Haimberger, L., Healy, S., Hogan, R. J., Hólm, E., Janisková, M., Keeley, S., Laloyaux, P., Lopez, P., Lupu, C., Radnoti, G., De Rosnay, P., Rozum, I., Vamborg, F., Villaume, S., & Thépaut, J. (2020). The ERA5 global reanalysis. *Quarterly Journal of the Royal Meteorological Society*, 146(730), 1999–2049. https://doi.org/10.1002/qj.3803

Heuzé, C. (2020). Antarctic Bottom Water and North Atlantic Deep Water in CMIP6 models. preprint, Deep Ocean/Numerical Models/All Geographic Regions/Temperature, Salinity and Density Fields. https://doi.org/10.5194/os-2020-66

Hewitt, H. T., Roberts, M., Mathiot, P., Biastoch, A., Blockley, E., Chassignet, E. P., Fox-Kemper, B., Hyder, P., Marshall, D. P., Popova, E., Treguier, A.-M., Zanna, L., Yool, A., Yu, Y., Beadling, R., Bell, M., Kuhlbrodt, T., Arsouze, T., Bellucci, A., Castruccio, F., Gan, B., Putrasahan, D., Roberts, C. D., Van Roekel, L., & Zhang, Q. (2020). Resolving and Parameterising the Ocean Mesoscale in Earth System Models. *Current Climate Change Reports*, 6(4), 137–152. https://doi.org/10.1007/s40641-020-00164-w

Hirschi, J. J., Barnier, B., Böning, C., Biastoch, A., Blaker, A. T., Coward, A., Danilov, S., Drijfhout, S., Getzlaff, K., Griffies, S. M., Hasumi, H., Hewitt, H., Iovino, D., Kawasaki, T., Kiss, A. E., Koldunov, N., Marzocchi, A., Mecking, J. V., Moat, B., Molines, J., Myers, P. G., Penduff, T., Roberts, M., Treguier, A., Sein, D. V., Sidorenko, D., Small, J., Spence, P., Thompson, L., Weijer, W., & Xu, X. (2020). The Atlantic Meridional Overturning Circulation in High-Resolution Models. *Journal of Geophysical Research: Oceans*, 125(4). https://doi.org/10.1029/2019JC015522

Holliday, N. P., Bersch, M., Berx, B., Chafik, L., Cunningham, S., Florindo-López, C., Hátún, H., Johns, W., Josey, S. A., Larsen, K. M. H., Mulet, S., Oltmanns, M., Reverdin, G., Rossby, T., Thierry, V., Valdimarsson, H., & Yashayaev, I. (2020). Ocean circulation causes the largest freshening event for 120 years in eastern subpolar North Atlantic. *Nature Communications*, 11(1), 585. https://doi.org/10.1038/s41467-020-14474-y

Hopkins, J. E., Holliday, N. P., Rayner, D., Houpert, L., Le Bras, I., Straneo, F., Wilson, C., & Bacon, S. (2019). Transport Variability of the Irminger Sea Deep Western Boundary Current From a Mooring Array. *Journal of Geophysical Research: Oceans*, 124(5), 3246–3278. https://doi.org/10.1029/2018JC014730

Hoshyar, P., Pennelly, C., & Myers, P. G. (2024). The Impacts of Air-Sea Fluxes and

Model Resolution on Seasonal and Inter-Annual Variability of the Atlantic Meridional Overturning Circulation across the OSNAP West Section. *Ocean Modelling*, 187, 102307. https://doi.org/10.1016/j.ocemod.2023.102307

Hu, X., Sun, J., Chan, T. O., & Myers, P. G. (2018). Thermodynamic and dynamic ice thickness contributions in the Canadian Arctic Archipelago in NEMO-LIM2 numerical simulations. *The Cryosphere*, 12(4), 1233–1247. https://doi.org/10.5194/tc-12-1233-2018

Hughes, C. W., Williams, J., Blaker, A., Coward, A., & Stepanov, V. (2018). A window on the deep ocean: The special value of ocean bottom pressure for monitoring the large-scale, deep-ocean circulation. *Progress in Oceanography*, 161, 19–46. https://doi.org/10.1016/j.pocean.2018.01.011

Hui-Er, M. & Yong-Qiang, Y. (2012). Simulation of Volume and Heat Transport along 26.5°N in the Atlantic. *Atmospheric and Oceanic Science Letters*, 5(5), 373–378. https://doi.org/10.1080/16742834.2012.11447019

Hurrell, J. W. (1995). Decadal Trends in the North Atlantic Oscillation: Regional Temperatures and Precipitation. *Science*, 269(5224), 676–679. https://doi.org/10.1126/science.269.5224.676

Hátún, H., Eriksen, C. C., & Rhines, P. B. (2007). Buoyant Eddies Entering the Labrador Sea Observed with Gliders and Altimetry. *Journal of Physical Oceanography*, 37(12), 2838–2854. https://doi.org/10.1175/2007JPO3567.1

Häkkinen, S., Rhines, P. B., & Worthen, D. L. (2016). Warming of the Global Ocean: Spatial Structure and Water-Mass Trends. *Journal of Climate*, 29(13), 4949–4963. https://doi.org/10.1175/JCLI-D-15-0607.1

Iakovleva, D. A. & Bashmachnikov, I. L. (2021). On the seesaw in interannual variability of upper ocean heat advection between the North Atlantic Subpolar Gyre and the Nordic Seas. *Dynamics of Atmospheres and Oceans*, 96, 101263. https://doi.org/10.1016/j.dynatmoce.2021.101263

IPCC (2013). Climate Change 2013: The Physical Science Basis. Contribution of Working Group I to the Fifth Assessment Report of the Intergovernmental Panel on Climate Change. *Cambridge University Press, Cambridge, United Kingdom and New York, NY, USA, 1535 pp.* https://doi.org/10.1017/CBO9781107415324

IPCC (2021). Climate Change 2021: The Physical Science Basis. Contribution of Working Group I to the Sixth Assessment Report of the Intergovernmental Panel on Climate Change. *Cambridge University Press, Cambridge, United Kingdom and New York, NY, USA, In press.* https://doi.org/10.1017/9781009157896

Iqbal, M. J., Rehman, S. U., Hameed, S., & Qureshi, M. A. (2019). Changes in Hadley circulation: the Azores high and winter precipitation over tropical northeast Africa. *Theoretical and Applied Climatology*, 137(3-4), 2941–2948. https://doi.org/10.1007/s00704-019-02765-4

Ishii, M., Kimoto, M., & Kachi, M. (2003). Historical Ocean Subsurface Temperature Analysis with Error Estimates. *Monthly Weather Review*, 131(1), 51–73. https://doi.org/10.1175/1520-0493(2003)131<0051:HOSTAW>2.0.CO;2

Jackson, L. C., Biastoch, A., Buckley, M. W., Desbruyères, D. G., Frajka-Williams, E., Moat, B., & Robson, J. (2022). The evolution of the North Atlantic Meridional Overturning Circulation since 1980. *Nature Reviews Earth & Environment*, 3(4), 241–254. https://doi.org/10.1038/s43017-022-00263-2

Jackson, L. C., Dubois, C., Forget, G., Haines, K., Harrison, M., Iovino, D., Köhl, A., Mignac, D., Masina, S., Peterson, K. A., Piecuch, C. G., Roberts, C. D., Robson, J., Storto, A., Toyoda, T., Valdivieso, M., Wilson, C., Wang, Y., & Zuo, H. (2019). The Mean State and Variability of the North Atlantic Circulation: A Perspective From Ocean Reanalyses. *Journal of Geophysical Research: Oceans*, 124(12), 9141–9170. https://doi.org/10.1029/2019JC015210

Jackson, L. C., Hewitt, H. T., Bruciaferri, D., Calvert, D., Graham, T., Guiavarc'h, C., Menary, M. B., New, A. L., Roberts, M., & Storkey, D. (2023). Challenges simulating the AMOC in climate models. *Philosophical Transactions of the Royal Society A: Mathematical, Physical and Engineering Sciences*, 381(2262), 20220187. https://doi.org/10.1098/rsta.2022.0187

Jackson, L. C., Kahana, R., Graham, T., Ringer, M. A., Woollings, T., Mecking, J. V., & Wood, R. A. (2015). Global and European climate impacts of a slowdown of the AMOC in a high resolution GCM. *Climate Dynamics*, 45(11-12), 3299–3316. https://doi.org/10.1007/s00382-015-2540-2

Jackson, L. C., Peterson, K., Roberts, C. D., & Wood, R. A. (2016). Recent slowing of Atlantic overturning circulation as a recovery from earlier strengthening. *Nature Geoscience*, 9(7), 518–522. https://doi.org/10.1038/ngeo2715

Jackson, L. C., Roberts, M. J., Hewitt, H. T., Iovino, D., Koenigk, T., Meccia, V. L., Roberts, C. D., Ruprich-Robert, Y., & Wood, R. A. (2020). Impact of ocean resolution and mean state on the rate of AMOC weakening. *Climate Dynamics*, 55(7-8), 1711–1732. https://doi.org/10.1007/s00382-020-05345-9

Jackson, L. C. & Wood, R. A. (2018). Timescales of AMOC decline in response to fresh water forcing. *Climate Dynamics*, 51(4), 1333–1350. https://doi.org/10.1007/s00382-017-3957-6

Jeon, C., Park, J.-H., Kennelly, M., Sousa, E., Watts, D. R., Lee, E.-J., Park, T., & Peacock, T. (2021). Advanced Remote Data Acquisition Using a Pop-Up Data Shuttle (PDS) to Report Data From Current- and Pressure-Recording Inverted Echo Sounders (CPIES). *Frontiers in Marine Science*, 8, 679534. https://doi.org/10.3389/fmars.2021.679534

Johns, W. E., Baringer, M. O., Beal, L. M., Cunningham, S. A., Kanzow, T., Bryden, H. L., Hirschi, J. J. M., Marotzke, J., Meinen, C. S., Shaw, B., & Curry, R. (2011). Continuous, Array-Based Estimates of Atlantic Ocean Heat Transport at 26.5°N. *Journal of Climate*, 24(10), 2429–2449. https://doi.org/10.1175/2010JCLI3997.1

Joyce, T. M. & Zhang, R. (2010). On the Path of the Gulf Stream and the Atlantic Meridional Overturning Circulation. *Journal of Climate*, 23(11), 3146–3154. https://doi.org/10.1175/2010JCLI3310.1

Kanzow, T., Cunningham, S. A., Johns, W. E., Hirschi, J. J.-M., Marotzke, J., Baringer, M. O., Meinen, C. S., Chidichimo, M. P., Atkinson, C., Beal, L. M., Bryden, H. L., &

Collins, J. (2010). Seasonal Variability of the Atlantic Meridional Overturning Circulation at 26.5°N. *Journal of Climate*, 23(21), 5678–5698. https://doi.org/10.1175/2010JCLI3389.1

Kanzow, T., Cunningham, S. A., Rayner, D., Hirschi, J. J.-M., Johns, W. E., Baringer, M. O., Bryden, H. L., Beal, L. M., Meinen, C. S., & Marotzke, J. (2007). Observed Flow Compensation Associated with the MOC at 26.5°N in the Atlantic. *Science*, 317(5840), 938–941. https://doi.org/10.1126/science.1141293

Kanzow, T., Johnson, H. L., Marshall, D. P., Cunningham, S. A., Hirschi, J. J.-M., Mujahid, A., Bryden, H. L., & Johns, W. E. (2009). Basinwide Integrated Volume Transports in an Eddy-Filled Ocean. *Journal of Physical Oceanography*, 39(12), 3091–3110. https://doi.org/10.1175/2009JPO4185.1

Keil, P., Mauritsen, T., Jungclaus, J., Hedemann, C., Olonscheck, D., & Ghosh, R. (2020). Multiple drivers of the North Atlantic warming hole. *Nature Climate Change*, 10(7), 667–671. https://doi.org/10.1038/s41558-020-0819-8

Kelly, K. A., Thompson, L., & Lyman, J. (2014). The Coherence and Impact of Meridional Heat Transport Anomalies in the Atlantic Ocean Inferred from Observations. *Journal of Climate*, 27(4), 1469–1487. https://doi.org/10.1175/JCLI-D-12-00131.1

Kieke, D., Klein, B., Stramma, L., Rhein, M., & Koltermann, K. P. (2009). Variability and propagation of Labrador Sea Water in the southern subpolar North Atlantic. *Deep Sea Research Part I: Oceanographic Research Papers*, 56(10), 1656–1674. https://doi.org/10.1016/j.dsr.2009.05.010

Kieke, D. & Yashayaev, I. (2015). Studies of Labrador Sea Water formation and variability in the subpolar North Atlantic in the light of international partnership and collaboration. *Progress in Oceanography*, 132, 220–232. https://doi.org/10.1016/j.pocean.2014.12.010

Kilbourne, K. H., Wanamaker, A. D., Moffa-Sanchez, P., Reynolds, D. J., Amrhein, D. E., Butler, P. G., Gebbie, G., Goes, M., Jansen, M. F., Little, C. M., Mette, M., Moreno-Chamarro, E., Ortega, P., Otto-Bliesner, B. L., Rossby, T., Scourse, J., & Whitney, N. M. (2022). Atlantic circulation change still uncertain. *Nature Geoscience*, 15(3), 165–167. https://doi.org/10.1038/s41561-022-00896-4

Knight, J. R. (2005). A signature of persistent natural thermohaline circulation cycles in observed climate. *Geophysical Research Letters*, 32(20), L20708. https://doi.org/10.1029/2005GL024233

Koltermann, K., Sokov, A., Tereschenkov, V., Dobroliubov, S., Lorbacher, K., & Sy, A. (1999). Decadal changes in the thermohaline circulation of the North Atlantic. *Deep Sea Research Part II: Topical Studies in Oceanography*, 46(1-2), 109–138. https://doi.org/10.1016/S0967-0645(98)00115-5

Kostov, Y., Johnson, H. L., Marshall, D. P., Heimbach, P., Forget, G., Holliday, N. P., Lozier, M. S., Li, F., Pillar, H. R., & Smith, T. (2021). Distinct sources of interannual subtropical and subpolar Atlantic overturning variability. *Nature Geoscience*, 14(7), 491–495. https://doi.org/10.1038/s41561-021-00759-4

Kostov, Y., Messias, M.-J., Mercier, H., Johnson, H. L., & Marshall, D. P. (2022). Fast mechanisms linking the Labrador Sea with subtropical Atlantic overturning. *Climate Dynamics*. https://doi.org/10.1007/s00382-022-06459-y

Krauss, W. (1986). The North Atlantic Current. *Journal of Geophysical Research: Oceans*, 91(C4), 5061–5074. https://doi.org/10.1029/JC091iC04p05061

Kuhlbrodt, T., Griesel, A., Montoya, M., Levermann, A., Hofmann, M., & Rahmstorf, S. (2007). On the driving processes of the Atlantic meridional overturning circulation. *Reviews of Geophysics*, 45(2), 2004RG000166. https://doi.org/10.1029/2004RG000166

Lazier, J., Hendry, R., Clarke, A., Yashayaev, I., & Rhines, P. (2002). Convection and restratification in the Labrador Sea, 1990–2000. *Deep Sea Research Part I: Oceanographic Research Papers*, 49(10), 1819–1835. https://doi.org/10.1016/S0967-0637(02)00064-X

Lenton, T. M., Held, H., Kriegler, E., Hall, J. W., Lucht, W., Rahmstorf, S., & Schellnhuber, H. J. (2008). Tipping elements in the Earth's climate system. *Proceedings of the National Academy of Sciences*, 105(6), 1786–1793. https://doi.org/10.1073/pnas.0705414105

Li, F., Lozier, M. S., Bacon, S., Bower, A. S., Cunningham, S. A., de Jong, M. F., deYoung, B., Fraser, N., Fried, N., Han, G., Holliday, N. P., Holte, J., Houpert, L., Inall, M. E., Johns, W. E., Jones, S., Johnson, C., Karstensen, J., Le Bras, I. A., Lherminier, P., Lin, X., Mercier, H., Oltmanns, M., Pacini, A., Petit, T., Pickart, R. S., Rayner, D., Straneo, F., Thierry, V., Visbeck, M., Yashayaev, I., & Zhou, C. (2021). Subpolar North Atlantic western boundary density anomalies and the Meridional Overturning Circulation. *Nature Communications*, 12(1), 3002. https://doi.org/10.1038/s41467-021-23350-2

Li, F., Lozier, M. S., & Johns, W. E. (2017). Calculating the Meridional Volume, Heat, and Freshwater Transports from an Observing System in the Subpolar North Atlantic: Observing System Simulation Experiment. *Journal of Atmospheric and Oceanic Technology*, 34(7), 1483–1500. https://doi.org/10.1175/JTECH-D-16-0247.1

Lilly, J. M. (2022). Ocean/Atmosphere Time Series Analysis. https://doi.org/10.5281/ZENODO.5977995

Lilly, J. M. & Elipot, S. (2021). jLab: A data analysis package for Matlab. *v.1.7.1*. https://doi.org/10.5281/zenodo.4547006. http://www.jmlilly.net/software

Lippold, J., Pöppelmeier, F., Süfke, F., Gutjahr, M., Goepfert, T. J., Blaser, P., Friedrich, O., Link, J. M., Wacker, L., Rheinberger, S., & Jaccard, S. L. (2019). Constraining the Variability of the Atlantic Meridional Overturning Circulation During the Holocene. *Geophysical Research Letters*, 46(20), 11338–11346. https://doi.org/10.1029/2019GL084988

Little, C. M., Hu, A., Hughes, C. W., McCarthy, G. D., Piecuch, C. G., Ponte, R. M., & Thomas, M. D. (2019). The Relationship Between U.S. East Coast Sea Level and the Atlantic Meridional Overturning Circulation: A Review. *Journal of Geophysical Research: Oceans*, 124(9), 6435–6458. https://doi.org/10.1029/2019JC015152

Little, C. M., Zhao, M., & Buckley, M. W. (2020). Do Surface Temperature Indices Reflect Centennial-Timescale Trends in Atlantic Meridional Overturning Circulation Strength?

Geophysical Research Letters, 47(22), e2020GL090888. https://doi.org/10.1029/2020GL090888

Liu, W., Xie, S.-P., Liu, Z., & Zhu, J. (2017). Overlooked possibility of a collapsed Atlantic Meridional Overturning Circulation in warming climate. *Science Advances*, 3(1), e1601666. https://doi.org/10.1126/sciadv.1601666

Lohmann, J. & Ditlevsen, P. D. (2021). Risk of tipping the overturning circulation due to increasing rates of ice melt. *Proceedings of the National Academy of Sciences*, 118(9), e2017989118. https://doi.org/10.1073/pnas.2017989118

Lozier, M. S. (2023). Overturning in the subpolar North Atlantic: a review. *Philosophical Transactions of the Royal Society A: Mathematical, Physical and Engineering Sciences*, 381(2262), 20220191. https://doi.org/10.1098/rsta.2022.0191

Lozier, M. S., Bacon, S., Bower, A. S., Cunningham, S. A., Femke de Jong, M., de Steur, L., deYoung, B., Fischer, J., Gary, S. F., Greenan, B. J. W., Heimbach, P., Holliday, N. P., Houpert, L., Inall, M. E., Johns, W. E., Johnson, H. L., Karstensen, J., Li, F., Lin, X., Mackay, N., Marshall, D. P., Mercier, H., Myers, P. G., Pickart, R. S., Pillar, H. R., Straneo, F., Thierry, V., Weller, R. A., Williams, R. G., Wilson, C., Yang, J., Zhao, J., & Zika, J. D. (2017). Overturning in the Subpolar North Atlantic Program: A New International Ocean Observing System. *Bulletin of the American Meteorological Society*, 98(4), 737–752. https://doi.org/10.1175/BAMS-D-16-0057.1

Lozier, M. S., Li, F., Bacon, S., Bahr, F., Bower, A. S., Cunningham, S. A., de Jong, M. F., de Steur, L., deYoung, B., Fischer, J., Gary, S. F., Greenan, B. J. W., Holliday, N. P., Houk, A., Houpert, L., Inall, M. E., Johns, W. E., Johnson, H. L., Johnson, C., Karstensen, J., Koman, G., Le Bras, I. A., Lin, X., Mackay, N., Marshall, D. P., Mercier, H., Oltmanns, M., Pickart, R. S., Ramsey, A. L., Rayner, D., Straneo, F., Thierry, V., Torres, D. J., Williams, R. G., Wilson, C., Yang, J., Yashayaev, I., & Zhao, J. (2019). A sea change in our view of overturning in the subpolar North Atlantic. *Science*, 363(6426), 516–521. https://doi.org/10.1126/science.aau6592

Lynch-Stieglitz, J. (2017). The Atlantic Meridional Overturning Circulation and Abrupt Climate Change. *Annual Review of Marine Science*, 9(1), 83–104. https://doi.org/10.1146/annurev-marine-010816-060415

Madec, G., Bell, M., Blaker, A., Bricaud, C., Bruciaferri, D., Castrillo, M., Calvert, D., Jérômeme Chanut, Clementi, E., Coward, A., Epicoco, I., Éthé, C., Ganderton, J., Harle, J., Hutchinson, K., Iovino, D., Lea, D., Lovato, T., Martin, M., Martin, N., Mele, F., Martins, D., Masson, S., Mathiot, P., Mele, F., Mocavero, S., Müller, S., Nurser, A. G., Paronuzzi, S., Peltier, M., Person, R., Rousset, C., Rynders, S., Samson, G., Téchené, S., Vancoppenolle, M., & Wilson, C. (2023). NEMO Ocean Engine Reference Manual. https://doi.org/10.5281/ZENODO.8167700. Publisher: Zenodo Version Number: v4.2.1

Mann, M. E., Zhang, Z., Hughes, M. K., Bradley, R. S., Miller, S. K., Rutherford, S., & Ni, F. (2008). Proxy-based reconstructions of hemispheric and global surface temperature variations over the past two millennia. *Proceedings of the National Academy of Sciences*, 105(36), 13252–13257. https://doi.org/10.1073/pnas.0805721105

Mann, M. E., Zhang, Z., Rutherford, S., Bradley, R. S., Hughes, M. K., Shindell, D., Ammann, C., Faluvegi, G., & Ni, F. (2009). Global Signatures and Dynamical Origins of the Little Ice Age and Medieval Climate Anomaly. *Science*, 326(5957), 1256–1260. https://doi.org/10.1126/science.1177303

Marshall, J. & Schott, F. (1999). Open-ocean convection: Observations, theory, and models. *Reviews of Geophysics*, 37(1), 1–64. https://doi.org/10.1029/98RG02739

Marshall, J., Scott, J. R., Romanou, A., Kelley, M., & Leboissetier, A. (2017). The dependence of the ocean's MOC on mesoscale eddy diffusivities: A model study. *Ocean Modelling*, 111, 1–8. https://doi.org/10.1016/j.ocemod.2017.01.001

Marshall, J. & Speer, K. (2012). Closure of the meridional overturning circulation through Southern Ocean upwelling. *Nature Geoscience*, 5(3), 171–180. https://doi.org/10.1038/ngeo1391

Martin, T. & Biastoch, A. (2023). On the ocean's response to enhanced Greenland runoff in model experiments: relevance of mesoscale dynamics and atmospheric coupling. *Ocean Science*, 19(1), 141–167. https://doi.org/10.5194/os-19-141-2023

McCarthy, G., Brown, P., Flagg, C. N., Goni, G., Houpert, L., Hughes, C. W., Hummels, R., Inall, M., Jochumsen, K., Larsen, K., Lherminier, P., Meinen, C., Moat, B. I., Rayner, D., Rhein, M., Roessler, A., Schmid, C., & Smeed, D. (2020). Sustainable Observations of the AMOC: Methodology and Technology. *Reviews of Geophysics*, 58(1). https://doi.org/10.1029/2019RG000654

McCarthy, G., Haigh, I. D., Hirschi, J. J.-M., Grist, J. P., & Smeed, D. A. (2015a). Ocean impact on decadal Atlantic climate variability revealed by sea-level observations. *Nature*, 521(7553), 508–510. https://doi.org/10.1038/nature14491

McCarthy, G., Smeed, D., Johns, W., Frajka-Williams, E., Moat, B., Rayner, D., Baringer, M., Meinen, C., Collins, J., & Bryden, H. (2015b). Measuring the Atlantic Meridional Overturning Circulation at 26°N. *Progress in Oceanography*, 130, 91–111. https://doi.org/10.1016/j.pocean.2014.10.006

McCarthy, G. D. & Caesar, L. (2023). Can we trust projections of AMOC weakening based on climate models that cannot reproduce the past? *Philosophical Transactions of the Royal Society A: Mathematical, Physical and Engineering Sciences*, 381(2262), 20220193. https://doi.org/10.1098/rsta.2022.0193

Meinen, C. S., Garzoli, S. L., Johns, W. E., & Baringer, M. O. (2004). Transport variability of the Deep Western Boundary Current and the Antilles Current off Abaco Island, Bahamas. *Deep Sea Research Part I: Oceanographic Research Papers*, 51(11), 1397–1415. https://doi.org/10.1016/j.dsr.2004.07.007

Menary, M. B., Robson, J., Allan, R. P., Booth, B. B. B., Cassou, C., Gastineau, G., Gregory, J., Hodson, D., Jones, C., Mignot, J., Ringer, M., Sutton, R., Wilcox, L., & Zhang, R. (2020). Aerosol-Forced AMOC Changes in CMIP6 Historical Simulations. *Geophysical Research Letters*, 47(14), e2020GL088166. https://doi.org/10.1029/2020GL088166

Meng, L., Yan, C., Zhuang, W., Zhang, W., & Yan, X. (2021). Reconstruction of Three-Dimensional Temperature and Salinity Fields From Satellite Observations. *Journal of Geophysical Research: Oceans*, 126(11), e2021JC017605. https://doi.org/10.1029/2021JC017605

Mercier, H., Lherminier, P., Sarafanov, A., Gaillard, F., Daniault, N., Desbruyères, D., Falina, A., Ferron, B., Gourcuff, C., Huck, T., & Thierry, V. (2015). Variability of the meridional overturning circulation at the Greenland–Portugal OVIDE section from 1993 to 2010. *Progress in Oceanography*, 132, 250–261. https://doi.org/10.1016/j.pocean.2013.11.001

Mertens, C., Rhein, M., Walter, M., Böning, C. W., Behrens, E., Kieke, D., Steinfeldt, R., & Stöber, U. (2014). Circulation and transports in the Newfoundland Basin, western subpolar North Atlantic. *Journal of Geophysical Research: Oceans*, 119(11), 7772–7793. https://doi.org/10.1002/2014JC010019

Mielke, C., Frajka-Williams, E., & Baehr, J. (2013). Observed and simulated variability of the AMOC at 26°N and 41°N. *Geophysical Research Letters*, 40(6), 1159–1164. https://doi.org/10.1002/grl.50233

Moat, B., Frajka-Williams, E., Smeed, D., Rayner, D., Johns, W. E., Baringer, M. O., Volkov, D., & Collins, J. (2022). *Atlantic meridional overturning circulation observed by the RAPID-MOCHA-WBTS (RAPID-Meridional Overturning Circulation and Heat-flux Array-Western Boundary Time Series) array at 26N from 2004 to 2020 (v2020.1) [data set]*. https://www.doi.org/10.5285/e91b10af-6f0a-7fa7-e053-6c86abc05a09

Moat, B., Smeed, D. A., Frajka-Williams, E., Desbruyères, D. G., Beaulieu, C., Johns, W. E., Rayner, D., Sanchez-Franks, A., Baringer, M. O., Volkov, D., Jackson, L. C., & Bryden, H. L. (2020). Pending recovery in the strength of the meridional overturning circulation at 26° N. *Ocean Science*, 16(4), 863–874. https://doi.org/10.5194/os-16-863-2020

Morice, C. P., Kennedy, J. J., Rayner, N. A., & Jones, P. D. (2012). Quantifying uncertainties in global and regional temperature change using an ensemble of observational estimates: The HadCRUT4 data set. *Journal of Geophysical Research: Atmospheres*, 117(D8), 2011JD017187. https://doi.org/10.1029/2011JD017187

Moritz, M., Jochumsen, K., Kieke, D., Klein, B., Klein, H., Köllner, M., & Rhein, M. (2021a). *Current meter measurement data and volume transport time series from deep-sea moorings deployed in the North Atlantic Eastern Boundary (EB) region at Goban Spur [data set]*. https://doi.pangaea.de/10.1594/PANGAEA.932566

Moritz, M., Jochumsen, K., Kieke, D., Klein, B., Klein, H., Köllner, M., & Rhein, M. (2021b). Volume Transport Time Series and Variability of the North Atlantic Eastern Boundary Current at Goban Spur. *Journal of Geophysical Research: Oceans*, 126(9). https://doi.org/10.1029/2021JC017393

Morrow, R., Fu, L.-L., Rio, M.-H., Ray, R., Prandi, P., Le Traon, P.-Y., & Benveniste, J. (2023). Ocean Circulation from Space. *Surveys in Geophysics*. https://doi.org/10.1007/s10712-023-09778-9

Msadek, R., Johns, W. E., Yeager, S. G., Danabasoglu, G., Delworth, T. L., & Rosati, A. (2013). The Atlantic Meridional Heat Transport at 26.5°N and Its Relationship with the MOC in the RAPID Array and the GFDL and NCAR Coupled Models. *Journal of Climate*, 26(12), 4335–4356. https://doi.org/10.1175/JCLI-D-12-00081.1

Mulet, S., Rio, M.-H., Mignot, A., Guinehut, S., & Morrow, R. (2012). A new estimate of the global 3D geostrophic ocean circulation based on satellite data and in-situ measurements. *Deep Sea Research Part II: Topical Studies in Oceanography*, 77-80, 70–81. https://doi.org/10.1016/j.dsr2.2012.04.012

Myers, P. G. & Kulan, N. (2012). Changes in the Deep Western Boundary Current at 53°N. *Journal of Physical Oceanography*, 42(7), 1207–1216. https://doi.org/10.1175/JPO-D-11-090.1

Müller, V., Kieke, D., Myers, P. G., Pennelly, C., & Mertens, C. (2017). Temperature flux carried by individual eddies across 47°N in the Atlantic Ocean. *Journal of Geophysical Research: Oceans*, 122(3), 2441–2464. https://doi.org/10.1002/2016JC012175

Müller, V., Kieke, D., Myers, P. G., Pennelly, C., Steinfeldt, R., & Stendardo, I. (2019). Heat and Freshwater Transport by Mesoscale Eddies in the Southern Subpolar North Atlantic. *Journal of Geophysical Research: Oceans*, 124, 5565–5585. https://doi.org/10.1029/2018JC014697

NOAA (2006). *2-minute Gridded Global Relief Data (ETOPO2) v2. [data set]. National Centers for Environmental Information.* https://doi.org/10.7289/V5J1012Q

Nowitzki, H., Rhein, M., Roessler, A., Kieke, D., & Mertens, C. (2020). *Absolute baroclinic PIES transport expanded with satellite altimetry [data set]*. https://doi.pangaea.de/10.1594/PANGAEA.925089

Nowitzki, H., Rhein, M., Roessler, A., Kieke, D., & Mertens, C. (2021). Trends and Transport Variability of the Circulation in the Subpolar Eastern North Atlantic. *Journal of Geophysical Research: Oceans*, 126(2). https://doi.org/10.1029/2020JC016693

Oldenburg, D., Wills, R. C. J., Armour, K. C., & Thompson, L. (2022). Resolution Dependence of Atmosphere–Ocean Interactions and Water Mass Transformation in the North Atlantic. *Journal of Geophysical Research: Oceans*, 127(4), e2021JC018102. https://doi.org/10.1029/2021JC018102

Pennelly, C. (2021). *Modelling Sources of Stratification within the Labrador Sea [Ph.D. thesis]*. University of Alberta.

Pennelly, C., Hu, X., & Myers, P. G. (2019). Cross-Isobath Freshwater Exchange Within the North Atlantic Subpolar Gyre. *Journal of Geophysical Research: Oceans*, 124(10), 6831–6853. https://doi.org/10.1029/2019JC015144

Pennelly, C. & Myers, P. G. (2020). Introducing LAB60: A 1/60° NEMO 3.6 numerical simulation of the Labrador Sea. *Geoscientific Model Development*, 13(10), 4959–4975. https://doi.org/10.5194/gmd-13-4959-2020

Pennelly, C. & Myers, P. G. (2022). Tracking Irminger Rings' properties using a submesoscale ocean model. *Progress in Oceanography*, 201, 102735. https://doi.org/10.1016/j.pocean.2021.102735

Pickart, R. S. (1992). Water mass components of the North Atlantic deep western boundary current. *Deep Sea Research Part A. Oceanographic Research Papers*, 39(9), 1553–1572. https://doi.org/10.1016/0198-0149(92)90047-W

Piecuch, C. G. (2020). Likely weakening of the Florida Current during the past century revealed by sea-level observations. *Nature Communications*, 11(1), 3973. https://doi.org/10.1038/s41467-020-17761-w

Rahmstorf, S. (2002). Ocean circulation and climate during the past 120,000 years. *Nature*, 419(6903), 207–214. https://doi.org/10.1038/nature01090

Rahmstorf, S., Box, J. E., Feulner, G., Mann, M. E., Robinson, A., Rutherford, S., & Schaffernicht, E. J. (2015). Exceptional twentieth-century slowdown in Atlantic Ocean overturning circulation. *Nature Climate Change*, 5(5), 475–480. https://doi.org/10.1038/nclimate2554

Rahmstorf, S. & Willebrand, J. (1995). The Role of Temperature Feedback in Stabilizing the Thermohaline Circulation. *Journal of Physical Oceanography*, 25(5), 787–805. https://doi.org/10.1175/1520-0485(1995)025<0787:TROTFI>2.0.CO;2

Rhein, M., Kieke, D., Hüttl-Kabus, S., Roessler, A., Mertens, C., Meissner, R., Klein, B., Böning, C. W., & Yashayaev, I. (2011). Deep water formation, the subpolar gyre, and the meridional overturning circulation in the subpolar North Atlantic. *Deep Sea Research Part II: Topical Studies in Oceanography*, 58(17-18), 1819–1832. https://doi.org/10.1016/j.dsr2.2010.10.061

Rhein, M., Kieke, D., & Steinfeldt, R. (2015). Advection of North Atlantic Deep Water from the Labrador Sea to the southern hemisphere. *Journal of Geophysical Research: Oceans*, 120(4), 2471–2487. https://doi.org/10.1002/2014JC010605

Rhein, M., Mertens, C., & Roessler, A. (2019a). *Lowered ADCP, current meter data and PIES time series measurements in the western subpolar North Atlantic (47°N) [data set]*. https://doi.pangaea.de/10.1594/PANGAEA.903211

Rhein, M., Mertens, C., & Roessler, A. (2019b). Observed Transport Decline at 47°N, Western Atlantic. *Journal of Geophysical Research: Oceans*, 124(7), 4875–4890. https://doi.org/10.1029/2019JC014993

Rhein, M., Steinfeldt, R., Kieke, D., Stendardo, I., & Yashayaev, I. (2017). Ventilation variability of Labrador Sea Water and its impact on oxygen and anthropogenic carbon: a review. *Philosophical Transactions of the Royal Society A: Mathematical, Physical and Engineering Sciences*, 375(2102), 20160321. https://doi.org/10.1098/rsta.2016.0321

Rinke, A., Dethloff, K., Cassano, J. J., Christensen, J. H., Curry, J. A., Du, P., Girard, E., Haugen, J.-E., Jacob, D., Jones, C. G., Køltzow, M., Laprise, R., Lynch, A., Pfeifer, S., Serreze, M. C., Shaw, M. J., Tjernström, M., Wyser, K., & Žagar, M. (2006). Evaluation of an ensemble of Arctic regional climate models: spatiotemporal fields during the SHEBA year. *Climate Dynamics*, 26(5), 459–472. https://doi.org/10.1007/s00382-005-0095-3

Roberts, M. J., Jackson, L. C., Roberts, C. D., Meccia, V., Docquier, D., Koenigk, T., Ortega, P., Moreno-Chamarro, E., Bellucci, A., Coward, A., Drijfhout, S., Exarchou, E., Gutjahr, O., Hewitt, H., Iovino, D., Lohmann, K., Putrasahan, D., Schiemann, R., Seddon, J., Terray, L., Xu, X., Zhang, Q., Chang, P., Yeager, S. G., Castruccio, F. S., Zhang, S., & Wu, L. (2020). Sensitivity of the Atlantic Meridional Overturning Circulation to Model Resolution in CMIP6 HighResMIP Simulations and Implications for Future Changes. *Journal of Advances in Modeling Earth Systems*, 12(8), e2019MS002014. https://doi.org/10.1029/2019MS002014

Robson, J., Ortega, P., & Sutton, R. (2016). A reversal of climatic trends in the North

Atlantic since 2005. *Nature Geoscience*, 9(7), 513–517. https://doi.org/10.1038/ngeo2727

Roemmich, D., Boebel, O., Freeland, H., King, B., LeTraon, P.-Y., Molinari, R., Owens, W. B., Riser, S., Send, U., Takeuchi, K., & Wijffels, S. (1998). *On The Design and Implementation of Argo*. https://argo.ucsd.edu/wp-content/uploads/sites/361/2020/05/argo-design.pdf

Roemmich, D., Sherman, J. T., Davis, R. E., Grindley, K., McClune, M., Parker, C. J., Black, D. N., Zilberman, N., Purkey, S. G., Sutton, P. J. H., & Gilson, J. (2019). Deep SOLO: A Full-Depth Profiling Float for the Argo Program. *Journal of Atmospheric and Oceanic Technology*, 36(10), 1967–1981. https://doi.org/10.1175/JTECH-D-19-0066.1

Roessler, A., Rhein, M., Kieke, D., & Mertens, C. (2015). Long-term observations of North Atlantic Current transport at the gateway between western and eastern Atlantic. *Journal of Geophysical Research: Oceans*, 120(6), 4003–4027. https://doi.org/10.1002/2014JC010662

Roquet, F. & Wunsch, C. (2022). The Atlantic Meridional Overturning Circulation and its Hypothetical Collapse. *Tellus A: Dynamic Meteorology and Oceanography*, 74(1), 393–398. https://doi.org/10.16993/tellusa.679

Rossby, T. (1996). The North Atlantic Current and surrounding waters: At the crossroads. *Reviews of Geophysics*, 34(4), 463–481. https://doi.org/10.1029/96RG02214

Rossby, T., Chafik, L., & Houpert, L. (2020). What can Hydrography Tell Us About the Strength of the Nordic Seas MOC Over the Last 70 to 100 Years? *Geophysical Research Letters*, 47(12), e2020GL087456. https://doi.org/10.1029/2020GL087456

Rühs, S., Oliver, E. C. J., Biastoch, A., Böning, C. W., Dowd, M., Getzlaff, K., Martin, T., & Myers, P. G. (2021). Changing Spatial Patterns of Deep Convection in the Subpolar North Atlantic. *Journal of Geophysical Research: Oceans*, 126(7), e2021JC017245. https://doi.org/10.1029/2021JC017245

Saenko, O. A., Dupont, F., Yang, D., Myers, P. G., Yashayaev, I., & Smith, G. C. (2014). Role of Resolved and Parameterized Eddies in the Labrador Sea Balance of Heat and Buoyancy. *Journal of Physical Oceanography*, 44(12), 3008–3032. https://doi.org/10.1175/JPO-D-14-0041.1

Sanchez-Franks, A., Frajka-Williams, E., Moat, B. I., & Smeed, D. A. (2021). A dynamically based method for estimating the Atlantic meridional overturning circulation at 26° N from satellite altimetry. *Ocean Science*, 17(5), 1321–1340. https://doi.org/10.5194/os-17-1321-2021. doi:10.5194/os-17-1321-2021

Sanchez-Franks, A., Holliday, N. P., Evans, D. G., Fried, N., Tooth, O. J., Chafik, L., Fu, Y., Li, F., Jong, M. F. D., & Johnson, H. L. (2023). The Irminger Gyre as a key driver of the subpolar North Atlantic overturning on monthly timescales. Preprint. https://doi.org/10.22541/essoar.168182248.82025084/v1

Seager, R., Battisti, D. S., Yin, J., Gordon, N., Naik, N., Clement, A. C., & Cane, M. A. (2002). Is the Gulf Stream responsible for Europe's mild winters? *Quarterly Journal of the Royal Meteorological Society*, 128(586), 2563–2586. https://doi.org/10.1256/qj.01.128

Send, U., Lankhorst, M., & Kanzow, T. (2011). Observation of decadal change in the Atlantic meridional overturning circulation using 10 years of continuous transport data. *Geophysical Research Letters*, 38(24), n/a–n/a. https://doi.org/10.1029/2011GL049801

Shannon, C. (1949). Communication in the Presence of Noise. *Proceedings of the IRE*, 37(1), 10–21. https://doi.org/10.1109/JRPROC.1949.232969

Sinha, B., Smeed, D., McCarthy, G., Moat, B., Josey, S., Hirschi, J.-M., Frajka-Williams, E., Blaker, A., Rayner, D., & Madec, G. (2018). The accuracy of estimates of the overturning circulation from basin-wide mooring arrays. *Progress in Oceanography*, 160, 101–123. https://doi.org/10.1016/j.pocean.2017.12.001

Smeed, D. A., Josey, S. A., Beaulieu, C., Johns, W. E., Moat, B. I., Frajka-Williams, E., Rayner, D., Meinen, C. S., Baringer, M. O., Bryden, H. L., & McCarthy, G. D. (2018). The North Atlantic Ocean Is in a State of Reduced Overturning. *Geophysical Research Letters*, 45(3), 1527–1533. https://doi.org/10.1002/2017GL076350

Smeed, D. A., McCarthy, G. D., Cunningham, S. A., Frajka-Williams, E., Rayner, D., Johns, W. E., Meinen, C. S., Baringer, M. O., Moat, B. I., Duchez, A., & Bryden, H. L. (2014). Observed decline of the Atlantic meridional overturning circulation 2004–2012. *Ocean Science*, 10(1), 29–38. https://doi.org/10.5194/os-10-29-2014

Smith, G. C., Roy, F., Mann, P., Dupont, F., Brasnett, B., Lemieux, J., Laroche, S., & Bélair, S. (2014). A new atmospheric dataset for forcing ice–ocean models: Evaluation of reforecasts using the Canadian global deterministic prediction system. *Quarterly Journal of the Royal Meteorological Society*, 140(680), 881–894. https://doi.org/10.1002/qj.2194

Spall, M. A. & Pickart, R. S. (2001). Where Does Dense Water Sink? A Subpolar Gyre Example. *Journal of Physical Oceanography*, 31(3), 810–826. https://doi.org/10.1175/1520-0485(2001)031<0810:WDDWSA>2.0.CO;2

Srokosz, M. A. & Bryden, H. L. (2015). Observing the Atlantic Meridional Overturning Circulation yields a decade of inevitable surprises. *Science*, 348(6241), 1255575. https://doi.org/10.1126/science.1255575

Stendardo, I., Rhein, M., & Steinfeldt, R. (2020). The North Atlantic Current and its Volume and Freshwater Transports in the Subpolar North Atlantic, Time Period 1993–2016. *Journal of Geophysical Research: Oceans*, 125(9), e2020JC016065. https://doi.org/10.1029/2020JC016065

Stepanov, V. N., Iovino, D., Masina, S., Storto, A., & Cipollone, A. (2016). Methods of calculation of the Atlantic meridional heat and volume transports from ocean models at 26.5°N. *Journal of Geophysical Research: Oceans*, 121(2), 1459–1475. https://doi.org/10.1002/2015JC011007

Stommel, H. (1961). Thermohaline Convection with Two Stable Regimes of Flow. *Tellus*, 13(2), 224–230. https://doi.org/10.1111/j.2153-3490.1961.tb00079.x

Storto, A., Alvera-Azcárate, A., Balmaseda, M. A., Barth, A., Chevallier, M., Counillon, F., Domingues, C. M., Drevillon, M., Drillet, Y., Forget, G., Garric, G., Haines, K., Hernandez, F., Iovino, D., Jackson, L. C., Lellouche, J.-M., Masina, S., Mayer, M., Oke, P. R., Penny, S. G., Peterson, K. A., Yang, C., & Zuo, H. (2019). Ocean Reanalyses:

Recent Advances and Unsolved Challenges. *Frontiers in Marine Science*, 6, 418. https://doi.org/10.3389/fmars.2019.00418

Sutton, R. T. & Hodson, D. L. R. (2005). Atlantic Ocean Forcing of North American and European Summer Climate. *Science*, 309(5731), 115–118. https://doi.org/10.1126/science.1109496

Talley, L. D., Pickard, G. L., Emery, W. J., & Swift, J. H., editors (2011). *Descriptive physical oceanography: an introduction* (6. ed ed.). Elsevier, AP.

Tanguy, S., Gourrion, J., Pouliquen, S., & Gilles, R. (2023). *CORA, Coriolis Ocean Dataset for Reanalysis [data set]*. https://www.doi.org/10.17882/46219

Treguier, A. M., Deshayes, J., Lique, C., Dussin, R., & Molines, J. M. (2012). Eddy contributions to the meridional transport of salt in the North Atlantic. *Journal of Geophysical Research: Oceans*, 117(C5), 2012JC007927. https://doi.org/10.1029/2012JC007927

Trenberth, K. E. & Caron, J. M. (2001). Estimates of Meridional Atmosphere and Ocean Heat Transports. *Journal of Climate*, 14(16), 3433–3443. https://doi.org/10.1175/1520-0442(2001)014<3433:EOMAAO>2.0.CO;2

Trenberth, K. E. & Fasullo, J. T. (2017). Atlantic meridional heat transports computed from balancing Earth's energy locally. *Geophysical Research Letters*, 44(4), 1919–1927. https://doi.org/10.1002/2016GL072475

Trenberth, K. E. & Solomon, A. (1994). The global heat balance: heat transports in the atmosphere and ocean. 10, 107–134. https://doi.org/https://doi.org/10.1007/BF00210625

Tsujino, H., Urakawa, S., Nakano, H., Small, R. J., Kim, W. M., Yeager, S. G., Danabasoglu, G., Suzuki, T., Bamber, J. L., Bentsen, M., Böning, C. W., Bozec, A., Chassignet, E. P., Curchitser, E., Boeira Dias, F., Durack, P. J., Griffies, S. M., Harada, Y., Ilicak, M., Josey, S. A., Kobayashi, C., Kobayashi, S., Komuro, Y., Large, W. G., Le Sommer, J., Marsland, S. J., Masina, S., Scheinert, M., Tomita, H., Valdivieso, M., & Yamazaki, D. (2018). JRA-55 based surface dataset for driving ocean–sea-ice models (JRA55-do). *Ocean Modelling*, 130, 79–139. https://doi.org/10.1016/j.ocemod.2018.07.002

Wang, Z., Brickman, D., & Greenan, B. J. (2019). Characteristic evolution of the Atlantic Meridional Overturning Circulation from 1990 to 2015: An eddy-resolving ocean model study. *Deep Sea Research Part I: Oceanographic Research Papers*, 149, 103056. https://doi.org/10.1016/j.dsr.2019.06.002

Wang, Z., Lu, Y., Dupont, F., W. Loder, J., Hannah, C., & G. Wright, D. (2015). Variability of sea surface height and circulation in the North Atlantic: Forcing mechanisms and linkages. *Progress in Oceanography*, 132, 273–286. https://doi.org/10.1016/j.pocean.2013.11.004

Watts, D. R. & Kontoyiannis, H. (1990). Deep-Ocean Bottom Pressure Measurement: Drift Removal and Performance. *Journal of Atmospheric and Oceanic Technology*, 7(2), 296–306. https://doi.org/10.1175/1520-0426(1990)007<0296:DOBPMD>2.0.CO;2

Watts, D. R. & Rossby, H. T. (1977). Measuring Dynamic Heights with Inverted Echo

Sounders: Results from MODE. *Journal of Physical Oceanography*, 7(3), 345–358. https://doi.org/10.1175/1520-0485(1977)007<0345:MDHWIE>2.0.CO;2

Weijer, W., Cheng, W., Drijfhout, S. S., Fedorov, A. V., Hu, A., Jackson, L. C., Liu, W., McDonagh, E. L., Mecking, J. V., & Zhang, J. (2019). Stability of the Atlantic Meridional Overturning Circulation: A Review and Synthesis. *Journal of Geophysical Research: Oceans*, 124(8), 5336–5375. https://doi.org/10.1029/2019JC015083

Wett, S., Rhein, M., Kieke, D., Mertens, C., & Moritz, M. (2023a). Meridional Connectivity of a 25-Year Observational AMOC Record at 47°N. *Geophysical Research Letters*, 50(16), e2023GL103284. https://doi.org/10.1029/2023GL103284

Wett, S., Rhein, M., Kieke, D., Mertens, C., Moritz, M., & Nowitzki, H. (2023b). *Basin-wide AMOC volume transport from the NOAC array at 47°N in the subpolar North Atlantic (1993-2018) [data set]*. https://doi.pangaea.de/10.1594/PANGAEA.959558

Wiegand, K. (2023). *Characteristics and causes of Irminger Water variability in the subpolar North Atlantic between 1993 and 2022 [Ph.D. thesis]*. University of Bremen.

Willis, J. K. (2010). Can in situ floats and satellite altimeters detect long-term changes in Atlantic Ocean overturning? *Geophysical Research Letters*, 37(6). https://doi.org/10.1029/2010GL042372

Willis, J. K. & Fu, L. (2008). Combining altimeter and subsurface float data to estimate the time-averaged circulation in the upper ocean. *Journal of Geophysical Research: Oceans*, 113(C12), 2007JC004690. https://doi.org/10.1029/2007JC004690

Wong, A. P. S., Wijffels, S. E., Riser, S. C., Pouliquen, S., Hosoda, S., Roemmich, D., Gilson, J., Johnson, G. C., Martini, K., Murphy, D. J., Scanderbeg, M., Bhaskar, T. V. S. U., Buck, J. J. H., Merceur, F., Carval, T., Maze, G., Cabanes, C., André, X., Poffa, N., Yashayaev, I., Barker, P. M., Guinehut, S., Belbéoch, M., Ignaszewski, M., Baringer, M. O., Schmid, C., Lyman, J. M., McTaggart, K. E., Purkey, S. G., Zilberman, N., Alkire, M. B., Swift, D., Owens, W. B., Jayne, S. R., Hersh, C., Robbins, P., West-Mack, D., Bahr, F., Yoshida, S., Sutton, P. J. H., Cancouët, R., Coatanoan, C., Dobbler, D., Juan, A. G., Gourrion, J., Kolodziejczyk, N., Bernard, V., Bourlès, B., Claustre, H., D'Ortenzio, F., Le Reste, S., Le Traon, P.-Y., Rannou, J.-P., Saout-Grit, C., Speich, S., Thierry, V., Verbrugge, N., Angel-Benavides, I. M., Klein, B., Notarstefano, G., Poulain, P.-M., Vélez-Belchí, P., Suga, T., Ando, K., Iwasaska, N., Kobayashi, T., Masuda, S., Oka, E., Sato, K., Nakamura, T., Sato, K., Takatsuki, Y., Yoshida, T., Cowley, R., Lovell, J. L., Oke, P. R., Van Wijk, E. M., Carse, F., Donnelly, M., Gould, W. J., Gowers, K., King, B. A., Loch, S. G., Mowat, M., Turton, J., Rama Rao, E. P., Ravichandran, M., Freeland, H. J., Gaboury, I., Gilbert, D., Greenan, B. J. W., Ouellet, M., Ross, T., Tran, A., Dong, M., Liu, Z., Xu, J., Kang, K., Jo, H., Kim, S.-D., & Park, H.-M. (2020). Argo Data 1999–2019: Two Million Temperature-Salinity Profiles and Subsurface Velocity Observations From a Global Array of Profiling Floats. *Frontiers in Marine Science*, 7, 700. https://doi.org/10.3389/fmars.2020.00700

Woodgate, R. A. (2018). Increases in the Pacific inflow to the Arctic from 1990 to 2015, and insights into seasonal trends and driving mechanisms from year-round Bering Strait mooring data. *Progress in Oceanography*, 160, 124–154. https://doi.org/10.1016/j.pocean.2017.12.007

Worthington, E. L., Moat, B. I., Smeed, D. A., Mecking, J. V., Marsh, R., & McCarthy,

G. D. (2021). A 30-year reconstruction of the Atlantic meridional overturning circulation shows no decline. *Ocean Science*, 17(1), 285–299. https://doi.org/10.5194/os-17-285-2021

Wunsch, C. (1999). Where do ocean eddy heat fluxes matter? *Journal of Geophysical Research: Oceans*, 104(C6), 13235–13249. https://doi.org/10.1029/1999JC900062

Wunsch, C. & Ferrari, R. (2004). Vertical Mixing, Energy, and the General Circulation of the Oceans. *Annual Review of Fluid Mechanics*, 36(1), 281–314. https://doi.org/10.1146/annurev.fluid.36.050802.122121

Yan, X., Zhang, R., & Knutson, T. R. (2017). The role of Atlantic overturning circulation in the recent decline of Atlantic major hurricane frequency. *Nature Communications*, 8(1), 1695. https://doi.org/10.1038/s41467-017-01377-8

Yan, X., Zhang, R., & Knutson, T. R. (2018). Underestimated AMOC Variability and Implications for AMV and Predictability in CMIP Models. *Geophysical Research Letters*, 45(9), 4319–4328. https://doi.org/10.1029/2018GL077378

Yashayaev, I. & Loder, J. W. (2017). Further intensification of deep convection in the Labrador Sea in 2016. *Geophysical Research Letters*, 44(3), 1429–1438. https://doi.org/10.1002/2016GL071668

Yeager, S., Castruccio, F. S., Chang, P., Danabasoglu, G., Maroon, E., Small, J., Wang, H., Wu, L., & Zhang, S. (2021). An outsized role for the Labrador Sea in the multidecadal variability of the Atlantic overturning circulation. *SCIENCE ADVANCES*, 7. https://doi.org/10.1126/sciadv.abh3592

Yeager, S. & Danabasoglu, G. (2014). The Origins of Late-Twentieth-Century Variations in the Large-Scale North Atlantic Circulation. *Journal of Climate*, 27(9), 3222–3247. https://doi.org/10.1175/JCLI-D-13-00125.1

Zantopp, R., Fischer, J., Visbeck, M., & Karstensen, J. (2017). From interannual to decadal: 17 years of boundary current transports at the exit of the Labrador Sea. *Journal of Geophysical Research: Oceans*, 122(3), 1724–1748. https://doi.org/10.1002/2016JC012271

Zhang, R. (2010). Latitudinal dependence of Atlantic meridional overturning circulation (AMOC) variations. *Geophysical Research Letters*, 37(16). https://doi.org/10.1029/2010GL044474

Zhang, R., Sutton, R., Danabasoglu, G., Kwon, Y., Marsh, R., Yeager, S. G., Amrhein, D. E., & Little, C. M. (2019). A Review of the Role of the Atlantic Meridional Overturning Circulation in Atlantic Multidecadal Variability and Associated Climate Impacts. *Reviews of Geophysics*, 57(2), 316–375. https://doi.org/10.1029/2019RG000644

Zhao, J. (2017). Basinwide response of the Atlantic Meridional Overturning Circulation to interannual wind forcing. *Climate Dynamics*, 49(11-12), 4263–4280. https://doi.org/10.1007/s00382-017-3568-2

Zhao, J. & Johns, W. (2014). Wind-forced interannual variability of the Atlantic Meridional Overturning Circulation at 26.5°N. *Journal of Geophysical Research: Oceans*, 119(4), 2403–2419. https://doi.org/10.1002/2013JC009407

Zhu, C., Liu, Z., Zhang, S., & Wu, L. (2023). Likely accelerated weakening of Atlantic overturning circulation emerges in optimal salinity fingerprint. *Nature Communications*, 14(1), 1245. https://doi.org/10.1038/s41467-023-36288-4

Zou, S., Lozier, M. S., & Buckley, M. (2019). How Is Meridional Coherence Maintained in the Lower Limb of the Atlantic Meridional Overturning Circulation? *Geophysical Research Letters*, 46(1), 244–252. https://doi.org/10.1029/2018GL080958

Funding and Data Availability

This thesis was funded by the German Research Foundation through the International Research Training Group ArcTrain "Processes and impacts of climate change in the North Atlantic Ocean and the Canadian Arctic" (IRTG, 1904 ArcTrain to M. Rhein).

Moored Data

The basin-wide AMOC volume transport time series from the NOAC array at 47°N, displayed in Figure 3.2 a, is freely available from PANGAEA under the CC-BY license (Wett et al., 2023b, `https://doi.org/10.1594/PANGAEA.959558`).

Top-bottom PIES transport time series from the eastern Atlantic basin, published in Nowitzki et al. (2021) are available from PANGAEA (Nowitzki et al., 2020, `https://doi.org/10.1594/PANGAEA.925089`).

Mooring current meter data and transport time series, published in Moritz et al. (2021b) are available from PANGAEA (Moritz et al., 2021a, `https://doi.org/10.1594/PANGAEA.932566`).

Lowered ADCP, current meter data, and PIES time series measurements from the western Atlantic basin, published in Rhein et al. (2019b) are available from PANGAEA (Rhein et al., 2019a, `https://doi.org/10.1594/PANGAEA.903211`).

Data from the RAPID AMOC monitoring project (Moat et al., 2022, `https://www.doi.org/10.5285/e91b10af-6f0a-7fa7-e053-6c86abc05a09`) is funded by the Natural Environment Research Council and freely available from `www.rapid.ac.uk/rapidmoc` (downloaded on 25 January 2023).

Copernicus Marine Service

This thesis has been conducted using E.U. Copernicus Marine Service Information

ARMOR3D: Product identifier: MULTIOBS_GLO_PHY_TSUV_3D_MYNRT_015_012 (downloaded on May 20/21,2021, `https://www.doi.org/10.48670/moi-00052`)

IFREMER CERSAT Global Blended Mean Wind Fields: Product identifier: WIND_GLO_WIND_L4_REP_OBSERVATIONS_012_006 (downloaded in August 2022).

Global Ocean Gridded Sea surface Heights: Product identifier: SEALEVEL_GLO_PHY_L4_REP_OBSERVATIONS_008_047 (downloaded in August 2020).

EN4

EN.4.2.1 data were obtained from `https://www.metoffice.gov.uk/hadobs/en4/` (downloaded on 01 September 2020) and are © British Crown Copyright, Met Office, 2013, provided under a Non-Commercial Government Licence `http://www.nationalarchives.gov.uk/doc/non-commercial-government-licence/version/2/`.

NAO index

The monthly mean NAO index data is available at `https://www.cpc.ncep.noaa.gov/products/precip/CWlink/pna/nao.shtml#current` (downloaded on 15 December 2022).

ETOPO

The topography in Figure 1 is from ETOPO2v2 (NOAA National Geophysical Data Center, 2006 (downloaded on 04 November 2020), `https://www.ncei.noaa.gov/products/etopo-global-relief-model`).

NEMO models

The model simulations, discussed in this thesis are implemented in the NEMO framework. For more information, refer to Madec et al. (2023).

VIKING20X

Output from the VIKING20X model simulation (VIKING20X-JRA-OMIP) was kindly provided by Arne Biastoch and the ocean dynamics group at Geomar. The implementation follows Biastoch et al. (2021).

ANHA

Output from the ANHA model simulations (ANHA4: EXH006, ANHA12: EXH006, LAB60+SPG12: ECP017) was kindly provided by Paul G. Myers and the ocean modeling group at the University of Alberta. The implementation follows Hu et al. (2018) for ANHA4 and ANHA12, and Pennelly & Myers (2020) for LAB60+SPG12.

Personal Communication

Alejandra Sanchez-Franks kindly provided the extended AMOC volume transport time series from the RAPID array at 26°N, published in Sanchez-Franks et al. (2021)

Damien Desbruyères kindly provided the AMOC volume transport time series at 45°N, published in Desbruyères et al. (2019).

Acknowledgements

Throughout my Ph.D. project, I have experienced the support of multiple people, without whom this thesis would not have been possible and to whom I owe special thanks.

First and foremost, I want to express my thanks to my supervisor, Monika Rhein. Monika, your support and guidance throughout all stages of my Ph.D. project have been a huge motivation, and your optimism always left me feeling that my project was going in the right direction. I am grateful for your support in developing my own ideas and critically assessing the results in fruitful discussions with you. Your encouragement to engage with the scientific community outside the office, be it at research cruises, scientific conferences, or research stays, helped me reach a wider audience and benefit from scientific discussions with international experts. Furthermore, your continued efforts to secure the funding for my work have provided me the security to focus on the science of my project.

I also thank my co-supervisor, Paul G. Myers, from the University of Alberta in Edmonton. Though the global pandemic delayed my stay in Edmonton, it was a very productive and pleasant time and helped me look at the North Atlantic from the perspective of the different ANHA model configurations. Thank you for the warm welcome to the University of Alberta and for always providing feedback on my project, whether in daily updates during my stay in Edmonton or during remote group meetings throughout my project. I would like to thank the whole modeling group at the University of Alberta for welcoming me to the lab and providing support and scientific discussions that helped advance my project.

I extend my gratitude to my whole scientific committee: Monika Rhein, Paul G. Myers, Arne Biastoch, Christian Mertens, and Dagmar Kieke. Thank you for shaping my project by asking the right questions during committee meetings and providing valuable feedback throughout all stages of my Ph.D. project. I would like to include Martin Moritz here, who has not been part of my committee but is a co-author of our paper and provided valuable support and advice.

For my research on the VIKING20X model simulation, Arne Biastoch welcomed me to the ocean dynamics group at the Geomar in Kiel. Thank you for your great collaboration, continued advice regarding all things related to numerical modeling, and helpful comments on my thesis draft. I also thank Klaus Getzlaff, Markus Scheinert, Tobias Schulzki, and Franziska Schwarzkopf, who gave technical advice.

This thesis was only possible with all the previous work I could build upon, for which I am thankful. Hannah Nowitzki provided the transport estimates from the eastern PIES at the NOAC array and advice on my questions regarding the PIES transport calculation. Christian Mertens calculated the transports at the western side of the NOAC array and provided advice on statistical questions. Reiner Steinfeldt calibrated the CTD data from various cruises along 47°N. Alejandra Sanchez-Franks kindly provided the extended transport time series at 26°N. Damien Desbruyères kindly provided the AMOC estimate from 45°N. I would like to express my thanks to all crew members and scientists onboard the research vessels MARIA S. MERIAN, METEOR, Celtic Explorer, Sarmiento de Gamboa, and Thalassa, who have contributed to acquiring data used for the present thesis.

From the beginning of my Ph.D. project, I have been a part of the ArcTrain and GLOMAR graduate schools, which provided funding, mentoring, courses, and leisure time activities. I want to thank all organizers involved in these graduate schools for making my Ph.D. project a great experience and the opportunity to make new friends.

I thank the whole oceanography group at the University of Bremen for providing an enjoyable and productive working environment. Though I spent part of my Ph.D. project in home office due to the pandemic, I always felt connected to the group through on- and offline seminars, North Atlantic meetings, and lunch breaks. I owe special thanks to my office colleagues Kevin and Wiebke, with whom I enjoyed scientific and non-scientific discussions and who provided mental support throughout my Ph.D. project.

I want to thank all my friends and family who have supported me throughout this Ph.D. project and before, providing advice, understanding, distraction, and mental support whenever necessary. Special thanks go to Kevin for being Miri's and my only in-person contact in lockdown times, leaving us wondering what to do with our Friday evening now. Additionally, I thank Andrea, Birte, Kevin, Ria, and Tim for providing feedback on my thesis draft. Finally, I thank you, Miri, for providing incredible support in every possible way throughout this fun but challenging project. Thank you for being home office colleague, best friend, and now wife, who has been married to a very busy husband lately.

Declaration of originality

I, Simon Wett, certify that the work presented here is, to the best of my knowledge and belief, original and the result of my own investigations, except as acknowledged, and has not been submitted, either in part or whole, for a degree at this or any other University. Parts of Chapter 1, Chapter 2, Chapter 3, and Chapter 5 are part of a publication that has been published in the peer-reviewed Journal Geophysical Research Letters (Wett et al., 2023b). The figures, tables, and text of this publication and the corresponding supplementary material have been partially adapted to fit the context of this thesis.

Place, Date	Simon Wett